Developing Chalcogenide Materials for Photovoltaic Applications

Yuchen Fu

Worcester College

Inorganic Chemistry Laboratory, Department of Chemistry

University of Oxford

This thesis is submitted for the degree of

Doctor of Philosophy

September 2025

Declaration of Originality

I declare that the contents of this thesis are the result of my own work, except where specific reference is made to the work of others. This thesis has not been submitted in whole or in part for consideration for any other degree or qualification in this, or any other university. All figures from literature are obtained with permission as described in the captions.

Yuchen Fu

September 2025

Abstract

Lead halide perovskites (LHPs) have shown great potential for optoelectronic applications, including solar cells, photodetectors and light-emitting diodes, but face challenges due to the toxicity of the lead and the limited stability of these materials. These concerns motivate the search for lead-free and more stable alternatives with similar optoelectronic properties to LHPs, and these materials are collectively referred to as 'perovskite-inspired materials (PIMs)'. Among the studied PIMs, chalcogenide semiconductors based on heavy pnictogen cations (Sb^{3+} and Bi^{3+}) have gained increasing attention due to the similar electronic structure of Sb^{3+} and Bi^{3+} to that of Pb^{2+}, which is believed to be important for the defect tolerance found in LHPs. Chalcogenides also generally have improved stability compared to halide compounds. However, a limitation of pnictogen-based halide and chalcogenide semiconductors is the prevalence of charge-carrier localisation, which severely reduces mobilities and diffusion lengths. Therefore, the discovery of pnictogen-based semiconductors with delocalised charge-carriers, and understanding the principles behind how band-like transport could be found, are important for the future development of these PIMs.

In my first project, through optical pump terahertz probe spectroscopy and temperature-dependent mobility measurements, the pnictogen-based semiconductor $CuSbSe_2$ was discovered to have delocalised free charge-carriers, which is different to many other Sb- and Bi-based PIMs explored thus far. Charge-carrier localisation in this family of materials has been so prevalently found that it is being referred to as a "hallmark" of these materials, and

fundamentally prevents these materials from reaching their optical limits in efficiency. Therefore, the discovery of delocalised charge-carriers in $CuSbSe_2$ and the understanding of the enabling factors can provide valuable suggestions on how the chemistry of heavy pnictogen-based materials could be changed to avoid this limitation. Through theoretical and experimental studies, I find that the critical factors enabling delocalised charge-carriers are: 1) the presence of regular free volume in the layered structure that can relax the lattice distortions caused by the propagation of acoustic waves in the interlayer gaps, such that bond lengths negligibly change, leading to low deformation potentials; 2) higher electronic dimensionality at band extrema due to quasi-bonding across these interlayer gaps; 3) a low ionic contribution to the dielectric constant compared to the electronic contribution caused by relatively low Born effective charges, as well as the small bandgap ($\leq$1.2 eV), thus leading to weak Fröhlich coupling. These findings could be generalisable to other pnictogen-based semiconductors.

As $CuSbSe_2$ has been shown to exhibit delocalised charge-carriers, I next investigate two techniques to deposit $CuSbSe_2$ thin films: solution processing and chemical vapour deposition, with the aim of developing these materials into photovoltaics. The novel thiol-amine-based solution processing method is safer than the previously-reported method employing hydrazine as the solvent. Meanwhile, compared to the co-sputtering of metal selenides, which was previously used to achieve the highest efficiency $CuSbSe_2$ solar cells thus far, solution processing may be more cost-effective, since it does not require expensive equipment or vacuum systems. The simpler operation of solution processing also allows the efficient exploration of different parameters. After achieving phase-pure $CuSbSe_2$ thin films via the

thiol-amine-based solution processing route, through morphological studies, I found that the heat treatment and the underlayer (compact TiO_2, meso-porous TiO_2, SnO_2 or NiO_x) can influence the morphology of solution-processed $CuSbSe_2$ thin films, while the morphology of chemical-vapour-deposited $CuSbSe_2$ thin films is mainly determined by the substrate temperature. Solution-processed $CuSbSe_2$ thin film-based solar cells were all shunted, which can be attributed to the high density of pinholes and small grains present in these films. Some pixels based on CVD $CuSbSe_2$ thin films showed diode-like J-V curves, but exhibited unmeasurable PCEs. This project found that moderate thermal energy input at the beginning of the heat treatment could improve the microscopic morphology of the solution-processed $CuSbSe_2$ thin films. The layer under $CuSbSe_2$ was also found to influence the morphology of the solution-processed $CuSbSe_2$ thin films. To further improve the film morphology, future studies can focus on the underlayers, different solvents (thiols and amines), and heat treatment methods.

In the third section, I investigate Sb_2S_3, grown by chemical bath deposition (CBD). This has been studied for photovoltaics well before the interest in LHPs grew, and has a bandgap (~1.7 eV) that is well-matched with the spectrum from indoor light sources (*e.g.*, white light emitting diodes (WLEDs)). We achieved 17.55%-efficient Sb_2S_3 indoor photovoltaics (IPVs) under 1000 lux WLED illumination, which was the record value for this material at the time of publication in 2024. However, one key challenge of Sb_2S_3 photovoltaics is the use of CdS as the buffer layer. Cd is more toxic than Pb, and may impede the commercial development of Sb_2S_3 photovoltaics. Therefore, in my third project, I focus on developing Cd-free electron

transport layers (ETLs). As deposition on CBD-grown SnO_2 resulted in discontinuous Sb_2S_3 films with pinholes, the morphology evolution of Sb_2S_3 thin films deposited on CdS and SnO_2 are compared to understand the fundamental reasons. Microscopic analysis showed that isolated spherical Sb_2S_3 clusters tend to form on the SnO_2 surface. In-depth XPS analysis further reveals that Sb primarily bonds with oxygen on the surface of SnO_2, forming Sb_2O_3, which hinders the heterogeneous nucleation of Sb_2S_3 on the surface of SnO_2, and results in the discontinuous Sb_2S_3 films. Also, introducing CdS as an interfacial layer between SnO_2 and Sb_2S_3 improved the Sb_2S_3 film morphology, while significantly reducing the overall Cd content in the device. This suggests that alternative sulphide interfacial layers could optimise Sb_2S_3 film morphology and enable the development of Cd-free solar cells. Furthermore, our Sb_2S_3 solar cells exhibited excellent performance under 1-sun illumination, with open-circuit voltage (V_{OC}) values (0.748 V) comparable to the highest reported in the literature (0.796 V). Optical loss analysis identifies device reflection and window layer parasitic absorption as key factors limiting the short-circuit current density, suggesting anti-reflection coatings and more transparent buffer layers as promising strategies for improvement. Overall, this work unravels the mechanisms enabling CdS to outperform SnO_2 as the buffer layer for Sb_2S_3 solar cells, and offers insight into designing more benign buffer layers to improve performance.

These three projects not only investigate the fundamental limitations of pnictogen-based chalcogenide semiconductors, such as charge-carrier localisation, but also make contributions to the practical applications and optimisation of these materials as solar absorbers. Based on the understanding of mechanisms enabling delocalised charge-carriers in $CuSbSe_2$, more

perovskite-inspired materials with band-like transport can be discovered in the future. Meanwhile, the novel methods to synthesize $CuSbSe_2$ are expected to promote the development of more efficient solar cells with improved safety and cost-efficiency. Moreover, the investigation on the buffer layers for Sb_2S_3 solar cells highlights the critical properties determining the quality of Sb_2S_3 films, providing guidance for designing more benign buffer layers. As we have demonstrated the exceptional potential of Sb_2S_3 solar cells for indoor light harvesting, replacing CdS with other environmentally friendly sulphide buffer layers is expected to contribute to the commercial development of Sb_2S_3 solar cells for IPV. With more efforts and understanding, it is believed that chalcogenide materials can be suitable for sustainable, stable and high-efficiency photovoltaic devices.

Acknowledgements

This incredible four-year journey is now drawing to a close. Since beginning my PhD, my life has been filled with surprises, achievements, and challenges. More importantly, I have received countless love and support. From dealing with the uncertainties of COVID-19 to setting up the lab, and even the multiple packing and unpacking of both the lab and my own home, this journey has truly been a transformative experience. As I reflect on these fruitful years, I wish to begin by expressing my deepest gratitude to my supervisor, Prof. Robert Hoye, for his invaluable guidance, steadfast support, and constant encouragement throughout this research journey. His expertise and insightful advice have been pivotal in shaping this thesis, and I am deeply thankful for his patience and confidence in my abilities. I would also like to thank him for offering me the opportunity to continue my PhD in Oxford, which is one of the most meaningful places in my life and is filled with countless unforgettable memories.

I am also immensely grateful to the Hoye group for their support and collaboration during this journey. The stimulating discussions, constructive feedback, and camaraderie within the group have enriched my academic experience. I would like to express my heartfelt gratitude to Dr. Yi-Teng Huang, Prof. Ru Zhou, Hugh Lohan and Emma Setzer for their generous help and invaluable assistance, which were critical to my research. I am also deeply thankful to Dr. Jason Ye, Dr. Huimin Zhu, Dr. Kaiwen Zhang, Dr. Daniel Price, Dr. Sachin R. Rondiya, Ivy Liu, Xiaoyu Guo, Kavya Reddy Dudipala, Minette Chang, Yixin Wang, and Eilidh Quinn for their guidance and expertise throughout my PhD journey. I also cherish the memory of Christina

Kong.

I sincerely thank all my collaborators for providing the resources and infrastructure essential to my research. These achievements would not have been possible without their support and assistance.

My special thanks go to my badminton mate, Jing, who has always covered my mistakes on the court but also supported me throughout my entire life in Oxford. You always cheer me up and inspire me from all perspectives. My gratitude also goes to Jiaxing, who often challenges me on the court and motivates us to play badminton with passion and dedication. I am incredibly lucky to meet you and have you as a valuable part of my world. Wishing you all the very best in everything you do.

Finally, my deepest gratitude goes to my family for their unconditional love, patience, and unwavering faith in me. To my parents, Yongjun Fu and Shufeng Xing, thank you for your sacrifices and for instilling in me the values of hard work and perseverance. To my wife, Dr. Xiyao Li, thank you for standing by my side all the time. Maintaining a long-distance relationship was not easy, but thankfully, we made it through together.

This thesis is dedicated to my loved ones who have inspired, supported, and encouraged me throughout this journey. Thank you for believing in me.

Table of Contents

List of Publications

1. **Fu, Y.**, Lohan, H., Righetto, M. *et al.* Structural and electronic features enabling delocalized charge-carriers in $CuSbSe_2$. *Nat Commun* **16**, 65 (2025).
2. Chen, X., Shu, X., Zhou, J., Wan, L., Xiao, P., **Fu, Y.** *et al.* Additive engineering for Sb_2S_3 indoor photovoltaics with efficiency exceeding 17%. *Light Sci Appl* **13**, 281 (2024).

List of Figures

List of Tables

Chapter 1: Introduction

Ensuring access to affordable, reliable and sustainable energy is the aim of United Nations Sustainable Development Goal (UN-SDG) 7, which is also critical to addressing the challenges posed by the continuous rise in global energy consumption[1,2]. Nowadays, the dominant energy sources globally are still based on fossil fuels, whose combustion results in the harmful emission of CO_2 and other greenhouse gases, accelerating the negative impact of climate change. Furthermore, the finite nature of these reserves raises concerns about long-term energy security. These challenges emphasise the pressing need for clean, sustainable, and reliable energy alternatives. Among the various renewable energy technologies, photovoltaic (PV) systems, which directly convert sunlight into electricity, are one of the most promising solutions. It is estimated that the amount of solar energy reaching the Earth in a single year is nearly two hundred times greater than the total energy stored in all known fossil fuel reserves[3]. This extraordinary potential highlights the important role of solar energy in addressing global energy demands sustainably. To further increase PV capacities, both reductions in capital expenditures and increases in power conversion efficiency (PCE, the ratio between electrical power produced and incident light power) will be required[4]. Currently, the PV market is dominated by crystalline silicon (c-Si) solar cells (~ 97% of the global production[5]), but the present PCE of c-Si solar cells (27.30%) is approaching their Shockley–Queisser limit (29.4%[6-8]). Beyond this efficiency concern, silicon solar cells face additional challenges, including the high energy demands of their manufacturing and the requirement for relatively thick wafers to

ensure sufficient light absorption. Furthermore, their opaqueness, rigidity and material properties make them less suitable for emerging applications such as portable, building-integrated, and indoor PVs. These limitations highlight the urgent need for the development of novel solar absorber materials that can expand the scope of photovoltaic technologies.

Among all other solar absorber materials, lead-halide perovskites (LHPs) have shown the most impressive performance. Perovskite solar cells (PSCs) have not only achieved a PCE comparable to Si solar cells within a short research period, but also demonstrated promising potentials for novel applications, such as flexible solar cells and indoor PVs. Nevertheless, the concerns on the toxicity of lead and the limited stability of LHPs still impede the widespread applications of PSCs. At the same time, these challenges drive the search for lead-free alternatives capable of replicating the exceptional optoelectronic properties of LHPs, and are referred to as perovskite-inspired materials (PIMs)[9]. Among the studied PIMs, chalcogenide materials have gained increasing attention, owing to the successful development of solar cells based on compounds such as CdTe and Cu(In, Ga)Se_2, as well as their enhanced stability compared to halides. Advancing the potential of chalcogenide materials for photovoltaic applications requires a deeper understanding of both their fundamental properties and device-level optimisations.

This thesis focuses on two promising chalcogenide materials, $CuSbSe_2$ and Sb_2S_3, investigating the fundamental charge-carrier kinetics, deposition techniques and device development. Chapter 2 will firstly introduce the basic mechanisms of solar cells, then review the progress

and limitations of PIMs studied so far, and finally discuss different thin film deposition techniques and summarize the overall aim of this thesis. In Chapter 3, the experimental details used in the thesis will be given. Chapter 4 will focus on the investigation of charge-carrier-phonon coupling in $CuSbSe_2$. Through both optical pump terahertz probe (OPTP) spectroscopy and temperature-dependent Hall effect measurements, it was demonstrated that $CuSbSe_2$ could avoid charge-carrier localisation, which is different from many other pnictogen-based semiconductors. The conclusion was further supported by density functional theory (DFT) calculations, which subsequently unravelled the critical properties of $CuSbSe_2$, enabling its delocalised charge-carriers. The analysis of the underlying mechanisms can provide important guidance for the design of semiconductors with band-like transport. Chapter 5 investigated two deposition techniques for $CuSbSe_2$, a thiol-amine-based solution processing method and a chemical vapour deposition (CVD) method. It was found that heat treatment parameters and underlayers could have significant effects on the solution-processed $CuSbSe_2$ films, while the sharp temperature gradient was the key limitation of the CVD method. After establishing the optimal conditions for both methods, $CuSbSe_2$ solar cells were fabricated. Due to the different density of structural defects and grain boundaries, as well as different device structures, solar cells based on solution-processed $CuSbSe_2$ films exhibited resistor-like J-V curves while those based on CVD films showed diode-like J-V curves. Chapter 6 explored the use of SnO_2 as a benign buffer layer for Sb_2S_3 solar cells to replace CdS, but observed the discontinuous Sb_2S_3 films on the SnO_2 surface. Through EDX and XPS analysis, the effects of buffer layers on the nucleation behaviour and growth mode of Sb_2S_3 were demonstrated, and the underlying reason was revealed to be the preferential Sb-O bonding at the SnO_2/Sb_2S_3 interface. By inserting a

CdS interfacial layer, the morphology of Sb_2S_3 films was effectively improved. Finally, the main mechanisms of optical loss for Sb_2S_3 solar cells were analysed. Chapter 7 will summarise the key conclusions from these three projects and propose some future research directions for $CuSbSe_2$ and Sb_2S_3, as well as the broader family of solar absorber materials.

Chapter 2: Background

2.1 Semiconductor physics

2.1.1 Fundamentals

For an isolated atom, the electrons can have discrete energy levels. When two identical atoms are brought closer, one discrete energy level will split into two levels by the interactions between the atoms. As a large number of atoms are brought together to form a solid, the discrete energy levels will form an essentially continuous energy band. Fig. 2.1 shows the formation of energy bands of a silicon crystal. At the equilibrium interatomic distance, the continuous energy band will split again to form the lower and upper bands. At the temperature of absolute zero, all states in the lower band (the valence band, VB) will be occupied by electrons, while all states in the upper band (the conduction band, CB) will be empty. Electrons in the VB are strongly constrained by the bonding, thereby not available for conduction. When a bond is broken due to increased temperature or other energy input, an electron will be excited to the CB and leave a hole in the VB. The energy required to create the electron-hole pair is called the bandgap energy, E_g, and defined as

$$E_g = E_C - E_V \tag{2.1}$$

where E_C and E_V are the energy of the conduction band minimum (CBM) and valence band maximum (VBM), respectively. For conductors, their CB may overlap with VB or be partially filled[10]. As for materials with a positive bandgap energy, those having E_g > 3 eV are usually

regarded as insulators while semiconductors usually have a bandgap energy of 0.5-3 eV, making it possible to excite an electron by visible light.

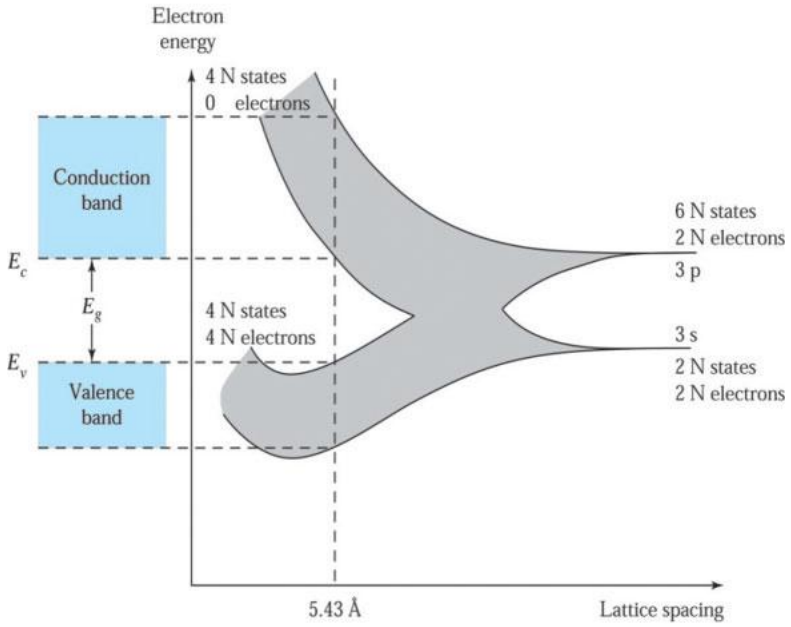

Fig. 2.1 | Schematic of formation of energy bands of a silicon crystal. 5.43 Å is the equilibrium interatomic distance. Reproduced with permission from Ref. 10. Copyright 2011 McGraw-Hill.

The Bloch wavefunction can be used to describe the electrons in a periodic structure as

$$\varphi(\boldsymbol{k},\boldsymbol{r}) = u_i(\boldsymbol{r})e^{i\boldsymbol{k}\cdot\boldsymbol{r}} \tag{2.2}$$

where $\boldsymbol{k}$ is the electron wave vector and $u_i(\boldsymbol{r})$ is a periodic factor. By substituting a Bloch wavefunction into Schrödinger's equation, we can calculate the energy E in a specific $\boldsymbol{k}$ direction as an eigenvalue of the equation. A 2D band diagram can be plotted based on such $E(\boldsymbol{k})$ relation with the most important directions in the lattice displayed along the x axis. The x axis is usually labelled by Miller indices $\langle hkl \rangle$ or highly symmetric points in $\boldsymbol{k}$-space such as W, X or Γ. The band structure diagram is displayed within the first Brillouin zone, which

describes a primitive cell in the reciprocal lattice space. All wavevectors within a lattice can be found in the first Brillouin zone. As shown in Fig. 2.2, if the VBM and CBM are positioned at the same $\boldsymbol{k}$ position, the material exhibits a direct bandgap (such as GaAs), where the absorption of light can directly create electron-hole pairs. By contrast, materials with the VBM and CBM at different $\boldsymbol{k}$ positions have an indirect bandgap (such as Si), and an extra phonon along with photon absorption is required for such materials to excite electrons. Therefore, materials with indirect band gaps exhibit weaker optical absorption and thicker films are needed for sufficient light absorption.

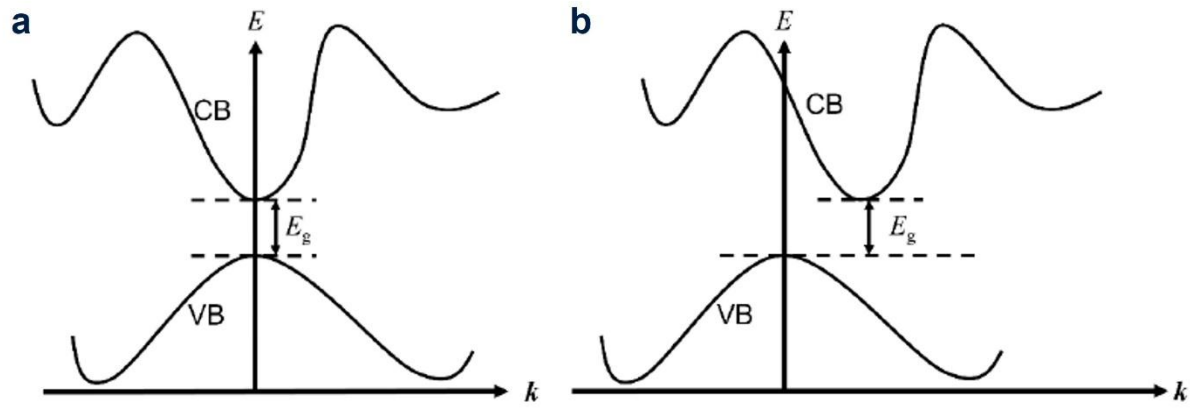

Fig. 2.2 | The band structure of a semiconductor with a, a direct bandgap and b, an indirect bandgap. Figure courtesy of Dr. Yi-Teng Huang.

The probability of finding an electron at an energy state with energy E follows the Fermi-Dirac distribution,

$$F(E) = \frac{1}{1 + e^{\frac{E - E_F}{kT}}} \tag{2.3}$$

where k is the Boltzmann constant, T is the temperature in degrees Kelvin, while E_F is the

energy of the Fermi level. The Fermi level is the energy level where the probability of being occupied by an electron is exactly 1/2. It should also be noted that, at 0 K, no electrons can be found in the states above E_F. As temperature increases, more electrons will occupy higher energy states (Fig. 2.3). In intrinsic semiconductors, E_F is approximately positioned at the middle of the bandgap, while E_F will shift towards the CBM or VBM for *n*-type or *p*-type semiconductors, respectively.

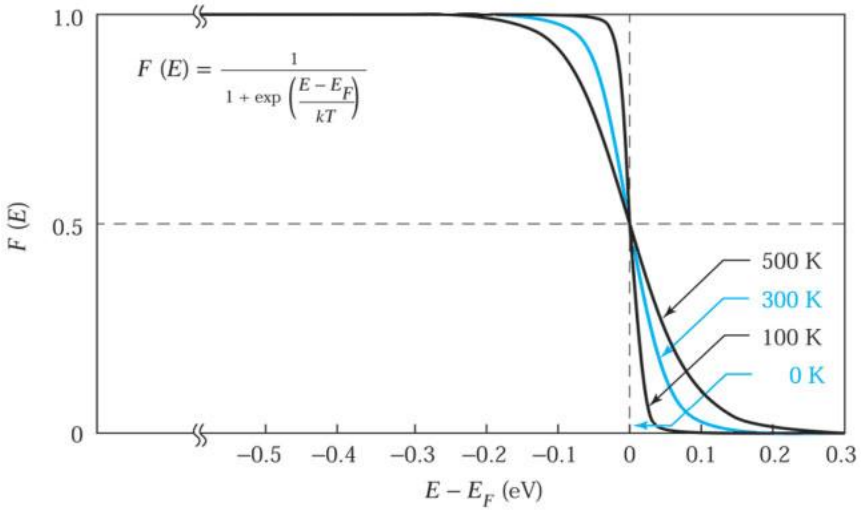

Fig. 2.3 | Fermi-Dirac distribution versus $(E - E_F)$ for different temperatures. Reproduced with permission from Ref. 10. Copyright 2011 McGraw-Hill.

In the vicinity of the CBM, the energy can be described as

$$E_c(\boldsymbol{k}) = E_{c0} + \frac{\hbar^2|\boldsymbol{k} - \boldsymbol{k}_{c0}|^2}{2m_c^*} \tag{2.4}$$

with parabolic approximation, where $E_{c0} = E_c(\boldsymbol{k}_{c0})$ is the energy at the CBM with a wavevector $\boldsymbol{k}_{c0}$. m_c^* is the effective mass of the electron, and $\hbar$ is the reduced Planck constant. Due to the periodic potential of the nuclei, the effective mass of the electron m_c^* is different from the free mass m_0. Thus, the effective mass m_c^* can be defined as

$$m_c^* = \left(\frac{1}{\hbar^2}\frac{\partial^2 E_c}{\partial k^2}\right)^{-1}. \tag{2.5}$$

Similarly, the energy near the VBM $E_v(\boldsymbol{k})$ can be given by

$$E_v(\boldsymbol{k}) = E_{v0} - \frac{\hbar^2|\boldsymbol{k} - \boldsymbol{k}_{v0}|^2}{2m_v^*}, \tag{2.6}$$

and the effective mass of the hole as

$$m_v^* = \left(-\frac{1}{\hbar^2}\frac{\partial^2 E_v}{\partial k^2}\right)^{-1}. \tag{2.7}$$

Therefore, a more dispersive band edge with a larger $\frac{\partial^2 E}{\partial k^2}$ value results in a smaller effective mass.

2.1.2 Charge-carrier generation and recombination

The charge-carrier density in a semiconductor can be changed via the generation and recombination processes. Generation refers to the creation of excess charge-carriers through an energy input. The sources of energy input can be the vibrational energies of the lattice (phonons) or the light illumination (photons). As mentioned in the previous section, a semiconductor can absorb photons with energy exceeding its bandgap, generating additional charge-carriers. The photo-generation process is the primary source of excess charge-carriers in solar cells. To describe the absorption of light, the absorption coefficient α is introduced and the light intensity at a distance x below the semiconductor surface is given by:

$$I(x) = I_0 e^{-\int_0^x \alpha(x')dx'} \tag{2.8}$$

where I_0 is the incident light intensity at the surface. If the absorption coefficient is constant, equation (2.8) can be simplified to the Beer-Lambert Law:

$$I(x) = I_0 e^{-\alpha x}. \tag{2.9}$$

On the contrary, free charge-carriers are eliminated via the recombination process. A recombination process can be either radiative or non-radiative, while non-radiative recombination includes Auger-Meitner and Shockley-Read-Hall (SRH) recombination processes, as illustrated in Fig. 2.4.

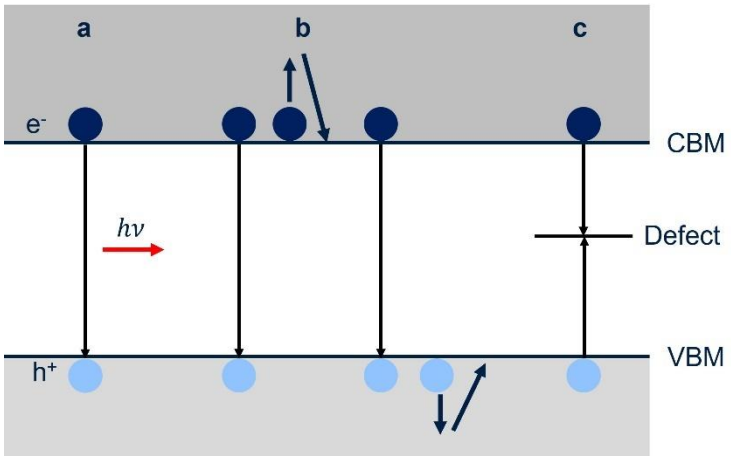

Fig. 2.4 | Schematics of different recombination processes. a, radiative recombination; **b,** Auger-Meitner recombination, and **c,** SRH recombination.

Radiative recombination is caused by band-to-band transition of charge-carriers. An electron in the CB recombines with a hole in the VB and emits a photon with the energy equal to the energy difference between the initial and final states (Fig. 2.4a). Since most radiative recombination processes involve the charge-carriers near the band edges, the energy of emitted photon is close to the bandgap energy. The radiative recombination rate U_{rad} is given by

$$U_{rad} = \beta np \tag{2.10}$$

where β is the proportionality constant while n and p are the density of electrons and holes,

respectively. Since the CBM and VBM are located at different $\boldsymbol{k}$ positions, the radiative recombination in semiconductors with an indirect bandgap requires extra phonons to be absorbed or emitted, making the radiative recombination less likely to occur.

Fig. 2.4b describes Auger-Meitner recombination processes where the energy released by the band-to-band transition is used to excite another charge-carrier to a higher energy state, then the excited charge-carrier will thermalise to the band edge. In this case, the released energy will be lost as heat. In this process, three charge-carriers (two electrons with one hole or two holes with one electron) are involved. Thus, the Auger-Meitner recombination rate U_{Aug} can be given by

$$U_{Aug} = An^2p \tag{2.11}$$

$$U_{Aug} = Ap^2n \tag{2.12}$$

depending on the involved charge-carriers, with A as a constant.

Shockley-Read-Hall (SRH) recombination, also known as trap-assisted recombination, involves a defect state capturing free charge-carriers (Fig. 2.4c). If a defect state is located close to the band edge or within the band, captured charge-carriers are easily re-emitted back to the band due to thermal energy. Such defect state is regarded as a shallow defect and does not have significant effects on charge-carrier recombination. On the other hand, a defect state located near the middle of the bandgap is called a deep defect since its captured charge-carrier is more likely to recombine with another opposite charge-carrier captured by this defect before re-emitted. This process reduces the density of free charge-carriers and dissipates the energy of

recombined charge-carriers as heat. The SRH recombination rate U_{SRH} can be calculated by

$$U_{SRH} = \frac{np - n_i^2}{\tau_p(n + n_t) + \tau_n(p + p_t)} \tag{2.13}$$

Where n_i is the intrinsic charge-carrier density while τ_p and τ_n are the reciprocal of the defect capture rate for electrons and holes, respectively. The defect capture rate depends on the density and the capture cross section of the defect state. Meanwhile, n_t and p_t are defined as

$$n_t = N_c e^{\frac{-(E_c - E_t)}{kT}} \tag{2.14}$$

$$p_t = N_v e^{\frac{-(E_t - E_v)}{kT}} \tag{2.15}$$

with N_c and N_v as the effective density of states for electrons and holes. E_c, E_v and E_t correspond to the energy of the CBM, VBM and defect state, respectively. The largest U_{SRH} is obtained when $E_t = (E_c + E_v)/2$ (*i.e.*, defect state located at the middle of the bandgap).

Overall, the change rate of charge-carrier density can be derived by combining both the generation and recombination process. For an intrinsic semiconductor ($n \sim p$), the rate can be approximated as[11]

$$\frac{dn}{dt} = G - U_{SRH}n - U_{rad}n^2 - U_{Aug}n^3. \tag{2.16}$$

If considering the current flow as well, the continuity equations for electrons and holes can be derived:

$$\frac{\partial n}{\partial t} = \frac{1}{q}\frac{\partial J_n}{\partial x} + G_n - R_n \tag{2.17}$$

$$\frac{\partial p}{\partial t} = -\frac{1}{q}\frac{\partial J_p}{\partial x} + G_p - R_p \tag{2.18}$$

with q as the elementary charge, J_n and J_p as the electron and hole current density, G as the generation rate and U as the recombination rate.

2.1.3 Charge-carrier transport

The current densities included in the continuity equations (2.17) and (2.18) are caused by charge-carrier transport, which refers to the net movement of electrons or holes. The driving force of charge-carrier transport can be either an external electric field (drift) or a concentration gradient (diffusion).

When applying an external electric field E, the drift velocity of electrons (v_n) or holes (v_p) is given by

$$v_n = \mu_n E \tag{2.19}$$

$$v_p = \mu_p E \tag{2.20}$$

with μ_n and μ_p as the mobility of electrons and holes, respectively. Mobility is an important parameter because it describes how strongly the motion of an electron is influenced by an applied electric field. Since the applied field results in the opposite movement of electrons and holes, the total drift current density J_{drf} can be obtained by

$$J_{drf} = q(n\mu_n + p\mu_p)E = \sigma E \tag{2.21}$$

with $\sigma = q(n\mu_n + p\mu_p)$ defined as the conductivity. The corresponding resistivity of the semiconductor is given by $\rho = 1/\sigma$.

Another current component, diffusion current, arises from the spatial variation of charge-carrier concentration in a semiconductor. For the electron/hole concentration gradient $\frac{dn}{dx}$ or $\frac{dp}{dx}$, the

current density J_n/J_p is expressed as

$$J_n = qD_n \frac{dn}{dx} \tag{2.22}$$

$$J_p = -qD_p \frac{dp}{dx} \tag{2.23}$$

where D_n or D_p is the diffusion coefficient of electrons/holes. The diffusion coefficient is related to the charge-carrier mobility via the Einstein relation

$$D = \left(\frac{kT}{q}\right)\mu. \tag{2.24}$$

Another important parameter for the diffusion transport is the diffusion length, which is the average length that charge-carriers can diffuse before recombination, defined as

$$L = \sqrt{D\tau} \tag{2.25}$$

with τ as the charge-carrier lifetime.

2.1.4 Charge-carrier-phonon interaction

In real semiconductors, charge-carriers are also influenced by the thermal vibrations of atoms from their equilibrium positions, which are described by phonons. Phonons can be categorized into optical or acoustic phonons, describing out-of-phase and in-phase atomic displacements, respectively[12]. Since lattices are deformable, introducing a charge-carrier leads to the ionic lattice being distorted due to the interaction with the charge-carrier. As the charge-carrier moves, the phonons will be coupled to it, resulting in the formation of a polaron[13] (Fig. 2.5a). Compared to free charge-carriers, polarons exhibit increased effective mass. According to the coupling range, polarons can be classified as large and small polarons. Large polarons tend to have long-range and weak interactions with phonons, while smaller polarons are strongly

coupled to phonons, confining their wavefunctions to within a unit cell or smaller[14-17]. Strong charge-carrier-phonon coupling can severely reduce the carrier mobility, such that it is referred to as being "self-trapped" or undergoing "charge-carrier localisation"[18]. For ideal photovoltaic materials, strong charge-carrier localisation should be avoided, while other properties such as the bandgap, optical absorption coefficient and charge-carrier lifetime should also be considered.

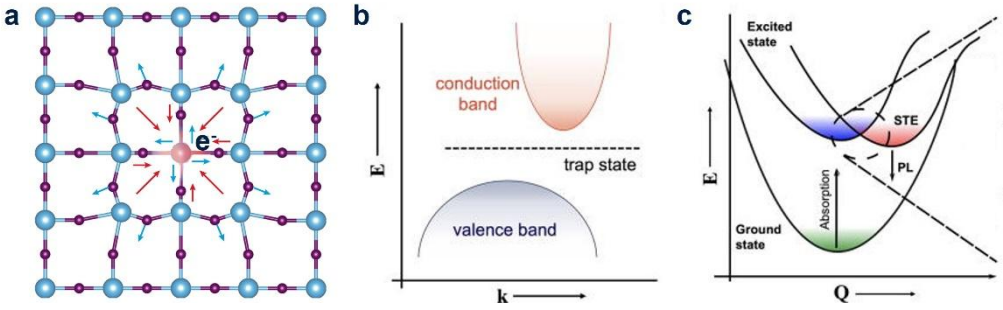

Fig. 2.5 | Schematics of charge-carrier-phonon interactions. a, Schematic of the interactions between the lattice and an electron, which then forms a small electron polaron. Red and blue arrows represent attractive and repulsive forces, respectively. Reproduced with permission from Ref. 12. Copyright 2021 Springer Nature. **b,** Standard electronic band structure of a semiconductor. **c,** Configuration coordinate diagram for a semiconductor exhibiting a self-trapped exciton (STE). Q is the configuration coordinate. Fig. 2.5a and c are adapted with permission from Ref. 19. Copyright 2021 Author(s), licensed under a Creative Commons Attribution (CC BY) license.

The formation of small polarons (or localised charge-carriers) can be caused by strong coupling to either acoustic or longitudinal optical (LO) phonons. The strength of coupling between

charge-carriers and acoustic phonons can be characterised by the acoustic coupling constant g_{ac}, given by

$$g_{ac} = \frac{E_d^2}{C a_0} . \frac{m}{3\pi\hbar^2} \tag{2.26}$$

where E_d is the acoustic deformation potential, C the elastic constant, m the mass of the charge-carrier considered and $\hbar$ the reduced Planck's constant. Based on the assumption that the propagating acoustic wave has a wavelength larger than the size of the unit cell, the acoustic wave can be regarded as a homogeneous strain to the unit cell. Therefore the acoustic deformation potential E_d can be described by this equation:

$$E_{\mathrm{d}}^{\mathbf{nk}} = \frac{\delta \mathcal{E}_{n\boldsymbol{k}}}{\delta S_{\alpha\beta}} . \tag{2.27}$$

In this equation, $\mathcal{E}_{n\boldsymbol{k}}$ is the energy of band n at wavevector $\mathbf{k}$, while $S_{\alpha\beta}$ is the uniform stress tensor. The schematic of determining the acoustic deformation potential is illustrated in Fig. 2.6. According to equation 2.26, materials with a lower acoustic deformation potential are more likely to exhibit lower g_{ac} value, thereby weaker coupling to acoustic phonons. Materials with the g_{ac} value much lower than one are expected to avoid charge-carrier localisation.

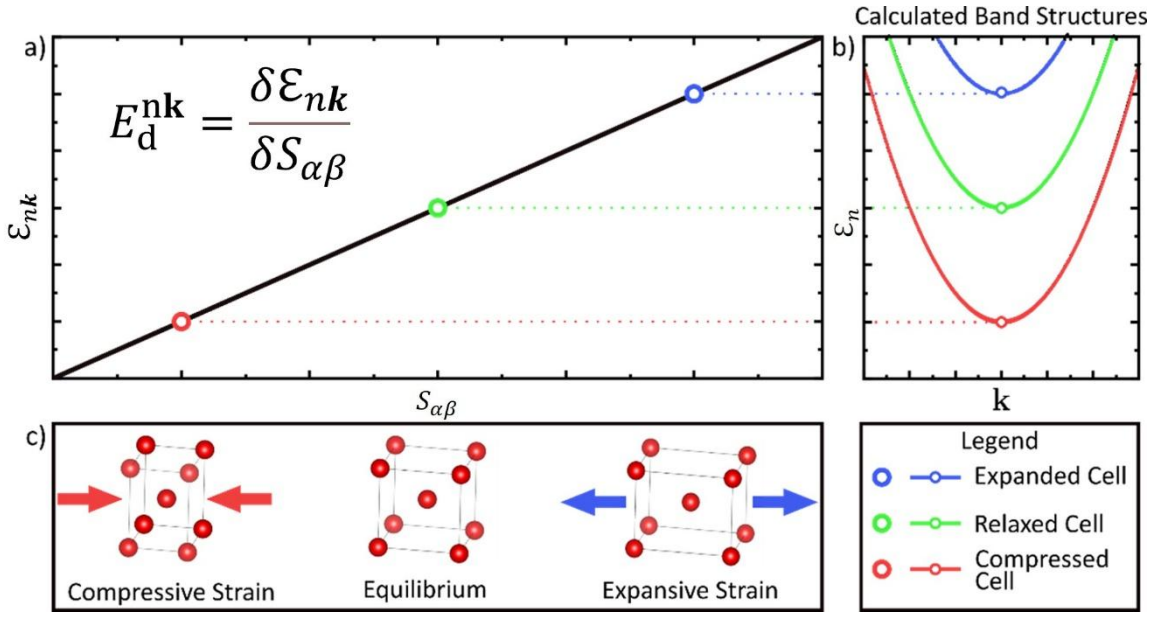

Fig. 2.6 | Schematic illustrating how the acoustic deformation potential of band n at point k was calculated using a modified method of Wei and Zunger[20]. a, Plot of band energy $\mathcal{E}_{nk}$ as a function of homogenous strain $S_{\alpha\beta}$. The acoustic deformation potential is defined as the change in $\mathcal{E}_{nk}$ with respect to $S_{\alpha\beta}$ **b,** Band edge energy of a simple parabolic band under axial compression (red) and expansion (blue). **c,** Uniaxial compression (red) and expansion (blue) of a BCC unit cell. Note, it is implicitly assumed in this schematic that the change in energy of core levels is negligible, and that the band edges are in equivalent electrostatic reference frames. Figure courtesy of Mr. Hugh Lohan.

On the other hand, coupling between charge-carriers and LO phonons (known as Fröhlich coupling) can also result in charge-carrier localisation if this is strong. To describe the coupling strength, the Fröhlich coupling constant, α, is expressed as:

$$\alpha = \frac{q^2}{4\pi\epsilon_0}\left(\frac{1}{\epsilon_\infty} - \frac{1}{\epsilon_{\mathrm{stat}}}\right)\sqrt{\frac{m^*}{2\omega_{\mathrm{LO}}\hbar^3}} \tag{2.28}$$

where ϵ_0 is the vacuum permittivity while ϵ_∞ and ϵ_{stat} are the optical and static dielectric

constants, respectively. m^* is the effective mass of the free charge-carrier, while ω_{LO} is the effective longitudinal optical (LO) phonon frequency, and $\hbar$ is the reduced Planck's constant. In cases where multiple LO phonon modes are acting, the effective weighted average is taken[21]. The α value over 10 is usually regarded as the sign of strong coupling, while the value below 1 is the weak coupling limit[22,23]. LHPs have been reported to exhibit an α value between 1.7 and 2.2[24], indicating intermediate Fröhlich coupling strength, and resulting in the mobility of ~200 $cm^2 \cdot V^{-1} \cdot s^{-1}$ [25], lower than the mobility of GaAs, of which α is only 0.06 to 0.07[26].

Besides reducing the mobility value, charge-carrier localisation also influences the temperature dependence of the mobilities. Large polarons tend to show decreased mobility as temperature increases, because of more phonons that charge-carriers can be coupled to[12,14,17,21]. However, small polarons are transported via phonon-assisted hopping between lattice sites. Therefore, higher temperatures lead to increases in thermal energy, which promotes the hopping of small polarons, thus giving rise to higher mobilities[12,17,27,28]. However, such mobilities still remain smaller than materials without charge-carrier localisation.

Moreover, charge-carrier localisation can change the electronic band structure. Fig. 2.5b and c compare the standard electronic band structure with the configuration coordinate diagram for a material undergoing charge-carrier localisation. Due to the local lattice distortions (Q in Fig. 2.5c) caused by the coupling between charge-carriers and LO or acoustic phonons, self-trapped states appear. Q is defined as $Q = \sqrt{\sum_i m_i \Delta r_i^2}$ where m_i and Δr_i represent the mass and the distance away from the equilibrium position of the atom, respectively. Q hence describes

the atomic displacement in a certain vibrational mode, known as the configuration coordinate. The curves in Fig. 2.5c therefore illustrate the energy of both the lattice and charge-carriers as a function of lattice distortions. When a photon is absorbed, an electron will be excited from the ground state to the excited state. Due to the charge-carrier-phonon interaction, a self-trapped state (STE in Fig. 2.5c) with an even lower energy, will be created. The energy difference between the minimum of the excited state and the point where the energy of the excited state and STE are equal depicts the energy barrier against the self-trapping. By overcoming this barrier, excited charge-carriers can reach the minimum of STE, releasing excess energy and becoming localised. Finally, self-trapped charge-carriers can relax to the ground state through either a radiative or non-radiative recombination process.

In addition to electron-phonon coupling, there are also interactions between charge-carriers themselves. In this thesis, I focus on the Coulomb attraction between photo-generated electrons and holes, leading to the formation of excitons. Excitons can be classified into two types, Frenkel and Wannier-Mott excitons. Frenkel excitons are strongly bound within a single unit cell and are typically observed in organic materials with low dielectric constants, which are unable to effectively screen the strong Coulomb attraction between charge-carriers. In contrast, Wannier-Mott excitons are highly delocalised, spreading across multiple unit cells. These excitons are commonly found in inorganic semiconductors, where a significant screening effect arises from relatively high dielectric constants. Consequently, our focus will be on Wannier-Mott excitons in the following discussion.

The excitonic effects can be reflected in the optical absorption spectrum, and the most common model was first established by Elliott[29]. For an excitonic system, the total optical absorption coefficient can be expressed as

$$\alpha(E) = \alpha_X(E) + \alpha_C(E) \tag{2.29}$$

where $\alpha_X(E)$ and $\alpha_C(E)$ are the contributions from excitons and continuum, respectively.

2.2 Solar cells

2.2.1 Working mechanism

Solar cells can convert incident light into electricity. The primary component of a typical solar cell is a *p*-*n* junction, forming near the interface between a *p*-type and an *n*-type semiconductor. When the interface forms, due to the gradient of the charge-carrier density, the majority charge-carriers in both semiconductors will diffuse across the interface, leading to positively-charged donor atoms in the *n* region and negatively-charged acceptor atoms in the *p* region. The charge-carriers arriving at the opposite region will recombine with the complementary charge-carriers, resulting in a space charge region (also known as a depletion region) with no free charge-carrier, as illustrated in Fig. 2.7.

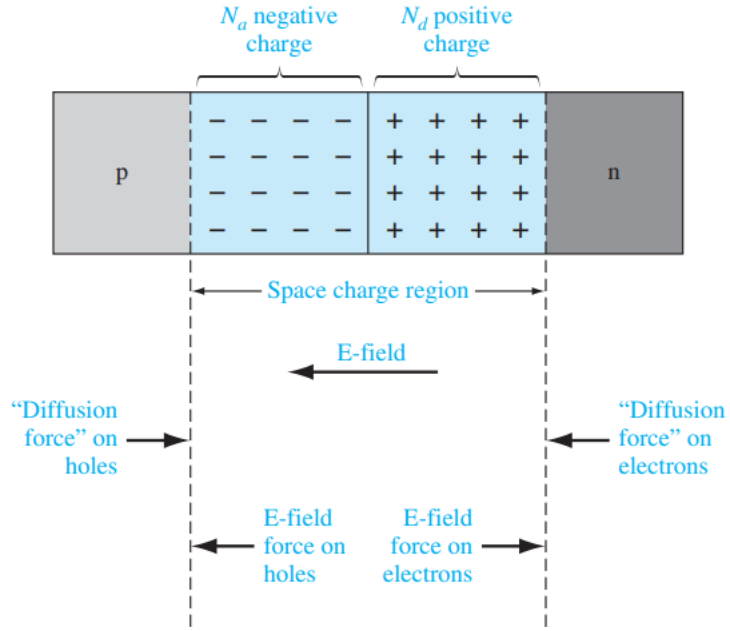

Fig. 2.7 | Schematic of a *p-n* junction. Reproduced with permission from Ref. 10. Copyright 2011 McGraw-Hill.

Meanwhile, the space charges will create a built-in electric field across the depletion region, which will cause drift to occur in the opposite direction to diffusion. At thermal equilibrium, these two forces will finally reach a balance. For the condition of zero current flow across the junction, the Fermi level must be constant (*i.e.*, $\frac{dE_F}{dx} = 0$), so the energy band will be bent as shown in Fig. 2.8. Due to the built-in electric field, an electric potential eV_{bi} will be created, preventing any charge-carrier diffusion at thermal equilibrium.

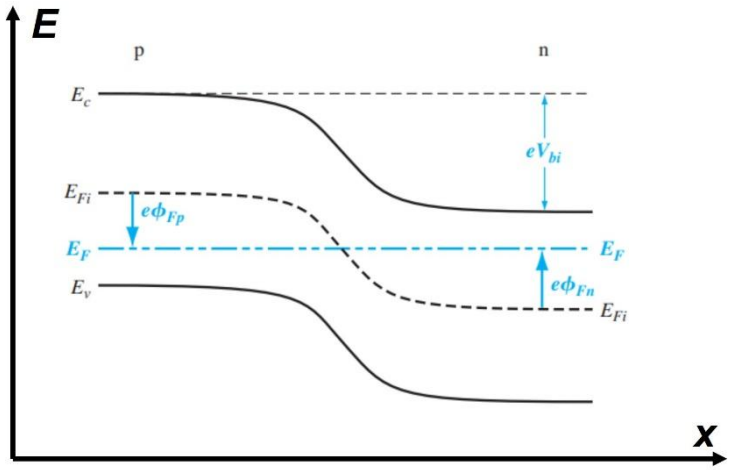

Fig. 2.8 | The energy band diagram of a *p-n* junction. Reproduced with permission from Ref. 10. Copyright 2011 McGraw-Hill.

The key characteristic of *p*–*n* junctions is their rectifying behaviour that they allow current to flow easily in only one direction, as the typical current-voltage characteristics of a *p*–*n* junction shown in Fig. 2.9. When a "forward bias" (positive voltage on the *p*-region) is applied, the built-in electric potential, as well as the width of the depletion region, will be reduced, making it easier for the majority charge-carriers in each region to diffuse across the junction. Therefore, the current will increase exponentially as the forward bias increases. By contrast, when a "reverse bias" is applied, the built-in electric potential will be increased and the depletion region will be wider, further reducing the diffusion current until a critical voltage is reached to break down the junction. At this point, the current will suddenly increase. For an ideal *p*–*n* junction (or diode), the total current I_D under the voltage V can be expressed as

$$I_D = I_S\left(e^{\frac{qV}{kT}} - 1\right) \tag{2.30}$$

where I_S is called the saturation current.

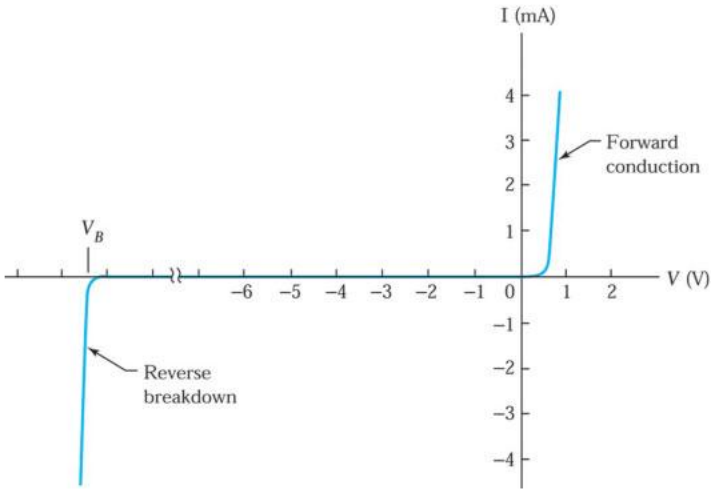

Fig. 2.9 | Current-voltage characteristics of a typical *p-n* junction. Reproduced with permission from Ref. 10. Copyright 2011 McGraw-Hill.

While the *p-n* junction has been widely used for Si solar cells, the *n-i-p* or *p-i-n* structure, where an intrinsic semiconductor is sandwiched by a *p*-type and *n*-type semiconductor, is preferred in thin-film solar cells, including the solar cells investigated in this thesis. The intrinsic semiconductor will be the main region where incident light is absorbed and charge-carriers are generated. In such a structure, the built-in electric field can extend throughout the whole intrinsic semiconductor, thus driving the photo-generated charge-carriers towards the ends of the junction more efficiently by drift. The *n*-type semiconductor is also known as the electron transport layer (ETL, such as TiO_2, ZnO and CdS), while the *p*-type semiconductor is called as hole transport layer (HTL, such as NiO_x and polymers). These transport layers exhibit high charge-carrier mobilities, promoting the collection of charge-carriers.

As Fig. 2.10 shows, when light illumination is applied to an ideal *p-n* junction solar cell, a photocurrent I will be generated since excess charge-carriers are excited by solar radiation. If

an external load R is connected to the solar cell, a voltage difference will be created across the load, applying a forward bias V on the *p-n* junction. Consequently, a current I_F opposite to the photocurrent will flow across the junction. Therefore, the total current I_t can be given by

$$I_t = I - I_F = I_{SC} - I_S\left(e^{\frac{qV}{kT}} - 1\right) \tag{2.31}$$

where I_{SC} is the short-circuit current (*i.e.*, the photocurrent with no external load), and I_S is the diode saturation current. It should be noted that both the short-circuit current (I_{SC}) and the short-circuit current density (J_{SC}) can be used to characterise the current under short-circuit conditions. I_{SC} refers to the total current that flows through the *p-n* junction under short-circuit conditions, while J_{SC} is the current normalised by the active device area, which allows direct comparison between devices of different sizes. In this work, I_{SC} is used consistently for clarity.

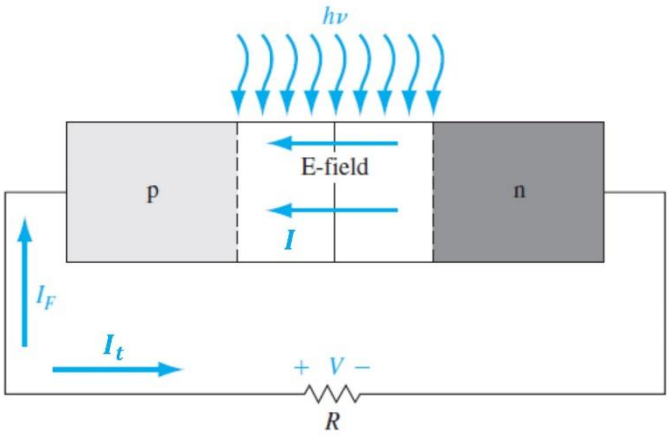

Fig. 2.10 | Schematic of an ideal *p-n* junction solar cell under light illumination. Reproduced with permission from Ref. 10. Copyright 2011 McGraw-Hill.

According to equation (2.31), as the voltage V increases, I_t will gradually decrease. When

I_t reaches zero (*i.e.*, open circuit condition), the corresponding voltage V_{OC} is referred to the open-circuit voltage as:

$$V_{OC} = \frac{kT}{q}\ln\left(\frac{I_{SC}}{I_S}+1\right). \tag{2.32}$$

It should be noted that V_{OC} also stands for the largest voltage achieved by a solar cell, which is determined by the quasi-Fermi level splitting. When excess charge-carriers are photo-generated, the thermal equilibrium is shifted, and the Fermi level of an intrinsic semiconductor E_{Fi} is not meaningful anymore. Instead, the quasi-Fermi levels E_{Fn} and E_{Fp} are used to express the electron and hole concentrations in a nonequilibrium state as:

$$n = n_i e^{\frac{E_{Fn}-E_{Fi}}{kT}} \tag{2.33}$$

$$p = n_i e^{\frac{E_{Fi}-E_{Fp}}{kT}}. \tag{2.34}$$

The open-circuit voltage V_{OC} is equal to the maximum potential difference built up by quasi-Fermi level splitting in the *p*-*n* junction.

Equation (2.31) describes the current-voltage characteristics of a solar cell under illumination, as plotted in Fig. 2.11. At certain point, the maximum power output P_{MP} can be achieved, and the fill factor FF is defined as

$$FF = \frac{P_{MP}}{I_{SC}V_{OC}}, \tag{2.35}$$

while the power conversion efficiency (PCE) is defined as

$$PCE = \frac{P_{MP}}{P_{in}} = \frac{I_{SC}V_{OC}FF}{P_{in}} \tag{2.36}$$

with P_{in} as the incident light intensity. Two additional parameters commonly used to evaluate solar cell performance are the internal and external quantum efficiency ($IQE(\lambda)$ and $EQE(\lambda)$), which can be calculated as functions of the wavelength λ:

$$IQE(\lambda) = \frac{\text{total electrons collected from device at wavelength } \lambda}{\text{total absorbed photons at wavelength } \lambda} \tag{2.37}$$

$$EQE(\lambda) = \frac{\text{total electrons collected from device at wavelength } \lambda}{\text{total incident photons at wavelength } \lambda}. \tag{2.38}$$

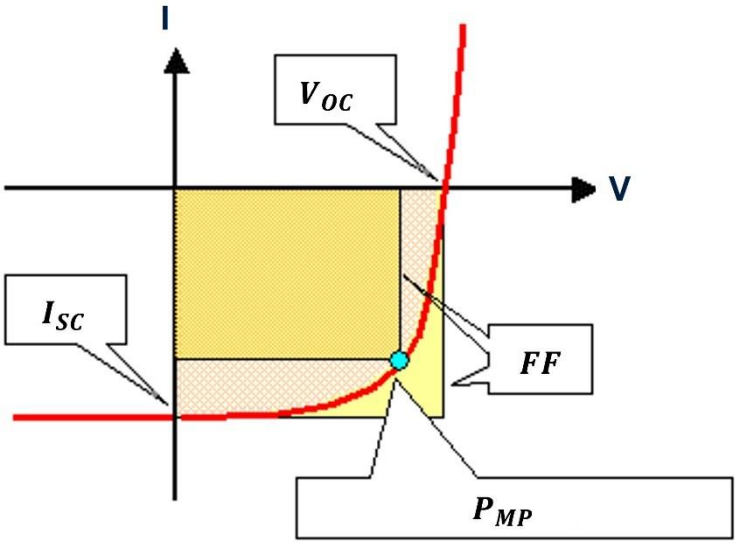

Fig. 2.11 | Typical I-V curve of a solar cell. V_{OC}, I_{SC}, P_{MP} and FF represent the open-circuit voltage, short-circuit current, maximum power output and fill factor, respectively. Reproduced with permission from pvdeucation.org.

For realistic solar cells, the ideal diode model needs modifications to consider the effects of parasitic resistances. Fig. 2.12 displays the equivalent circuit of a non-ideal solar cell, where the series resistance R_s and the shunt resistance R_{sh} are included. R_s can result from the contact resistances between the electrodes and the semiconductor, while R_{sh} is commonly caused by the connection between electrodes or transport layers, providing extra paths for charge-carrier recombination and power loss. In this case, the I-V characteristics of a non-ideal solar cell can be expressed as

$$I_t = I_{SC} - I_0\left[e^{\frac{q(V+IR_s)}{mkT}} - 1\right] - \frac{V + IR_s}{R_{sh}} \tag{2.39}$$

where m is the ideality factor.

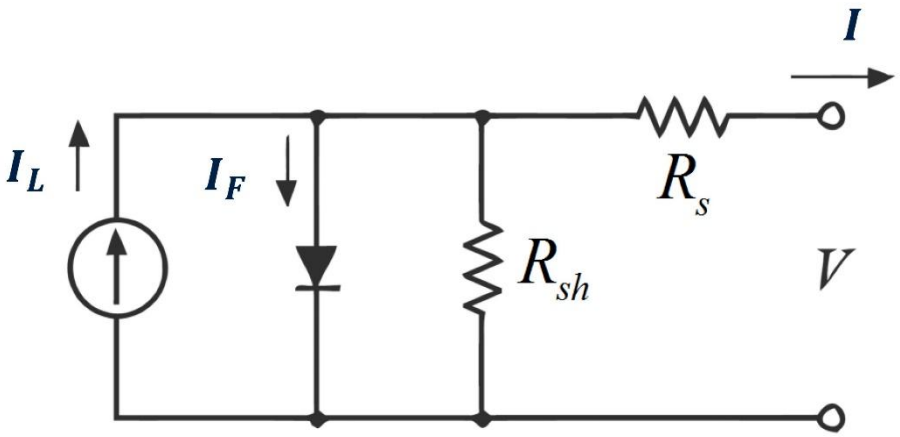

Fig. 2.12 | Equivalent circuit of a solar cell. R_s and R_{sh} represent the series resistance and the shunt resistance, respectively. Reproduced with permission from pvdeucation.org.

2.2.2 Efficiency limit

The Shockley-Queisser (SQ) limit gives the theoretical maximum PCE of a single junction solar cell[30]. The model was established based on the following assumptions:

(1) The sun and the solar cell are both blackbodies with temperatures of 6000 K and 300 K, respectively.

(2) All photons with energies exceeding the bandgap E_g of the semiconductor can be absorbed to generate an electron-hole pair, while no photons with an energy lower than E_g can be absorbed. Namely, the optical absorption coefficient is a step function with the onset at E_g.

(3) Radiative recombination is the only recombination mechanism.

As a result, the theoretical PCEs can be expressed as a function of E_g, reaching a maximum value of 30% at 1.1 eV. When the blackbody radiation is substituted with the standard solar spectrum (AM 1.5G), the maximum PCE increases to 33.7% at 1.34 eV[31]. If replacing the simple step function with an energy-dependent absorption spectrum $a(E)$, spectroscopic limited maximum efficiency (SLME) could be derived. By employing $a(E)$ measured by experiments, SLME can estimate the theoretical PCE limit more accurately[32].

2.2.3 Development history

The development of solar cells started with the first observation of the photovoltaic effect in 1839, then the first solar cell was built by coating selenium with two metal thin layers in 1878[33]. A major breakthrough was the invention of the first practical silicon solar cell with a PCE of 6% in 1954, which has since dominated the solar cell market. By the late 20th century, advancements in thin-film technologies, including cadmium telluride (CdTe) and copper indium gallium selenide (CIGS), offered cost-effective alternatives. Therefore, c-Si and III-V solar cells based on wafer technologies are regarded as the first-generation solar cells, while those employing thin-film technologies have been defined as the second generation. The invention of dye-sensitized solar cells (DSSCs) in 1991 further diversified the field[34]. In the early 2000s, quantum dot solar cells were developed[35], while the first perovskite solar cell (PSC) was demonstrated and achieved a PCE over 3% in 2009[36]. These novel technologies are classified as third-generation solar cells. Over the past decade, the efficiency of PSCs has been improved rapidly and recently reached 26.7%[37]. The perovskite-Si tandem solar cell has even

achieved the impressive PCE of 34.6%. However, even if PSC might be the most popular field for research on solar cells, concerns such as the toxicity of lead element and the solvents used in the production (*e.g.*, *N*, *N*-dimethylformamide), as well as the limited stability of LHPs still urge further material development.

Since solar cells were invented, various applications have emerged. In addition to the most common outdoor solar energy conversion, novel applications such as flexible electronics[38-40], building-integrated photovoltaics (BIPV)[41], and indoor PVs (IPV)[32,42-44] have gained increasing attention. In the third project of this thesis, the potentials for Sb_2S_3 solar cells for IPV applications were investigated. The progress and challenges for IPV will be reviewed in the next section.

2.2.4 Indoor photovoltaics (IPV)

Different from outdoor solar panels which convert solar radiation into electricity, indoor photovoltaic devices harvest ambient light inside buildings to power electronics. To achieve "smart life", the Internet of Things (IoT) electronics are attracting increasing interest as they enable daily objects and environments to acquire data connectivity and "intelligence", enhancing the quality and efficiency of daily lives[42,45]. Autonomous IoT nodes are commonly powered by batteries, but their limited lifespan and the need for frequent replacement and maintenance make long-term reliance on them unsustainable[46]. On the other hand, IPV can efficiently harvest energy from artificial lighting, commonly available inside buildings.

Meanwhile, IPV devices can be fabricated from the sub-mm^2 to >100 cm^2 area to meet the power requirement of various IoT electronics[42]. Additionally, IPV provides a higher power density than other indoor energy harvesting technologies, making it an ideal choice for sustainably powering IoT devices. So far, IPVs have been successfully employed to power electronics such as environment- and bio-sensors[44,47,48], as well as machine learning on wireless nodes[45] and lithium batteries[49].

Fig. 2.13 compares the AM1.5G solar spectrum with the spectra of two common indoor light sources, WLEDs and fluorescent lamps (FL). Indoor lighting levels usually range from 50 to 500 lux illuminance in residential settings, and from 500 to 1500 lux in offices, commercial, and industrial spaces. For common cold white light-emitting diodes (WLEDs), an illuminance of 500-1000 lux (0.14-0.28 mW/cm^2) is approximately 300–700 times lower than the intensity of "1-sun" (AM1.5G, 100 mW/cm^2)[50]. As mentioned above, the Shockley-Queisser limit under the AM 1.5G spectrum is obtained with a bandgap of 1.34 eV. On the contrary, due to the different spectra, the optimal bandgap value for IPVs under white light illumination is 1.9-2.0 eV[51]. Materials which have been demonstrated for IPVs include hydrogenated amorphous silicon (a-Si:H)[52-54], dye-sensitised solar cells[45,55], organic photovoltaics[54,56], LHPs[57-59], BiOI[32], Sb_2S_3[43,44] and so on. Due to their exceptional optoelectronic properties and easily tuneable bandgap, LHPs have achieved the current record reported PCE for IPV (44.72%). However, the toxicity of lead remains a significant barrier to the commercialisation of PSCs, particularly for indoor applications. In contrast, Sb_2S_3 solar cells offer a more environmentally friendly alternative. Following the initial study demonstrating an impressive PCE of 16.37% for Sb_2S_3

solar cells under indoor lighting, we have recently enhanced the efficiency to 17.55% under 1000 lux WLED illumination, highlighting their strong potential.

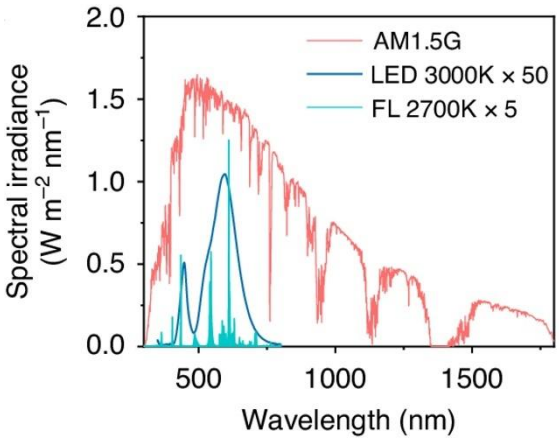

Fig. 2.13 | Comparison of the emission spectra of AM 1.5 G solar (red), 3000 K WLED at 1000 lux (blue), and 2700 K FL at 1000 lux (green). The spectral intensities of WLED and FL are amplified by 50 and 5 times, respectively. Reproduced with permission from Ref. 44. Copyright 2024 Springer Nature.

2.3 Perovskite-inspired materials (PIMs)

2.3.1 Introduction

The remarkable optoelectronic properties of LHPs have enabled their exceptional performance as solar absorbers. However, their industrial application remains hindered by lead toxicity and limited stability. To address these challenges while preserving the desirable properties of LHPs, lead-free alternatives, also referred to as perovskite-inspired materials (PIMs)[60,61], have garnered growing interest for photovoltaic applications.

Research on PIMs has primarily focused on three common types: (i) structurally analogous materials, which exhibit the perovskite crystal structure (*e.g.*, $Cs_2AgBiBr_6$); (ii) chemically analogous materials (*e.g.*, caesium bismuth iodide); and (iii) electronically analogous materials. The third category comprises compounds like bismuth oxyiodide (BiOI) that, despite being structurally and chemically distinct from LHPs, exhibit similar electronic characteristics at their band extrema[9,18,62]. These characteristics primarily arise from the hybridisation of the metal cation valence *s* and *p* orbitals with the anion *p* orbitals, resulting in bonding–antibonding states in the upper valence band and an antibonding state at the conduction band minimum[60].

One of the most outstanding properties of LHPs is their defect tolerance, which occurs when the most common trap states are shallow and exhibit low capture cross sections, resulting in low non-radiative recombination rates even in the presence of high defect densities[63]. The shallow trapping model shows that defect tolerance in LHPs is related to the $6s^2$ lone electron pair in Pb^{2+} [64-66], motivating the development of materials with heavy cations that have stable valence ns^2 electron pairs (In^+, Sn^{2+}, Sb^{3+} and Bi^{3+}). By sharing similar electronic characteristics with LHPs, these PIMs are also anticipated to exhibit defect tolerance. The following sections will first explore the concept of defect tolerance in detail, then introduce a specific family of PIMs: ABZ_2 materials.

2.3.2 Defect tolerance

Herein, defect tolerance is defined as the semiconductor maintaining free charge carriers, low non-radiative recombination rates and high mobilities, despite the presence of defects. This capability enables long charge-carrier transport lengths, allowing the material to operate near its optical performance limits[66-72]. To analyse the defect tolerance of semiconductors, the defect formation energy diagrams are commonly constructed via calculations based on the equation:

$$\Delta H_{X,q} = \left(E_{X,q} - E_H\right) - \sum_i n_i \mu_i + qE_F + E_{corr}(q), \quad (2.40)$$

where $\Delta H_{X,q}$ refers to the formation energy of certain defect state, while $E_{X,q}$ and E_H represent the energy for a supercell with and without the investigated defect, respectively. $\sum_i n_i \mu_i$ accounts for the Gibbs free energy change when the defect is formed by adding or removing n_i atoms with a chemical potential μ_i. The term qE_F stands for the energy cost to change the charge state of the defect by adding q charges, while E_F is the Fermi level. Due to the existence of this term, the defect formation energy can be described as a function of the Fermi level. Finally, $E_{corr}(q)$ is the correction term to reduce the spurious charge-charge interaction between the finite-sized supercells.

The left panel of Fig. 2.14 depicts a typical defect formation energy diagram of a defect state with two transition levels, $\varepsilon(+1/0)$ and $\varepsilon(0/-1)$, as a function of the Fermi level E_F. The transition levels ε represent the points where the formation energies of two charge states, $q1$ and $q2$, are equal (*i.e.*, $\Delta H_{X,q}(q1) = \Delta H_{X,q}(q2)$). These levels also correspond to the energy positions of donor or acceptor defects. For instance, the transition level $\varepsilon(+1/0)$ denotes the energy level of a donor defect, which is more stable (due to a lower defect formation energy) when it loses one electron to form a +1 charge state at energy levels below $\varepsilon(+1/0)$. Therefore,

the formation of this defect makes the material more *n*-type. Conversely, the transition level $\varepsilon(0/-1)$ represents the energy level of an acceptor defect, which becomes more stable upon capturing an electron (resulting in a -1 charge state) at energy levels above $\varepsilon(0/-1)$. These two transition levels can also be interpreted as defect states located within the bandgap, as illustrated in the right panel of Fig. 2.14.

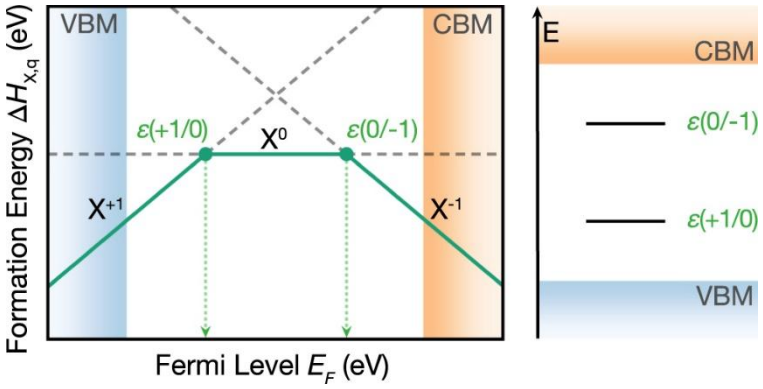

Fig. 2.14 | The two defect transition levels (ε(+1/0) and ε(0/−1)) on a defect formation energy diagram and an energy band diagram. Reproduced with permission from Ref. 9. Open access, CC BY.

At room temperature (300 K), the thermal energy of charge-carriers kT is about 0.026 eV. In this case, defect states located about 0.03 eV away from the band edges can be regarded as shallow defects because the trapped charge-carriers can be thermally activated back to the CB or VB. On the other hand, defect states with the formation energies $\Delta H_{X,q}$ higher than 1 eV have relatively low concentration according to the equation:

$$N_t = Ne^{-\frac{\Delta H_{X,q}}{kT}} \tag{2.41}$$

where N_t and N represent the concentration of defects and forming atoms, respectively.

Therefore, defects with either energy levels close to band edges or high formation energies can be treated as benign, as they will not significantly reduce the charge-carrier lifetime.

Defect tolerance has been found in compounds such as Cu_3N[73], where the *p-d* orbital interactions contribute to the bonding and antibonding states at the CBM and VBM, respectively. These electronic characteristics at the band extrema make defect states located within the bands or shallow to the band edges. On the contrary, semiconductors with anti-bonding CBM and bonding VBM (*e.g.*, Si or GaAs) tend to exhibit defects near the middle of their band gaps. Such materials are less defect-tolerant and require reduced defect concentrations to achieve high efficiencies. Fig. 2.15 compares the electronic structures of defect-intolerant materials (Fig. 2.15a) and LHP (Fig. 2.15b), which is also defect-tolerant. Similar to other defect-tolerant materials discussed earlier, the Pb 6*s*-I 5*p* hybridisation in LHP leads to the anti-bonding states at the VBM, making defect states shallower. This highlights the importance of the $6s^2$ lone electron pair in Pb^{2+}. Also, due to the significant relativistic spin-orbit coupling (SOC) resulting from the large nuclear charges, the CBM of LHPs exhibits high dispersion. This high dispersion pushes the band edges closer to most defect states[60]. Based on these characteristics, the shallow trapping model has emerged as one of the most widely accepted explanations for defect tolerance in LHPs[63,74]. However, deep states can still form, and a wide range of models have been proposed, including dielectric screening[60,65], defect self-compensation[75], formation of large polarons[76-78], and self-healing[79,80]. The development of different theoretical models indicates that the defect tolerance in LHPs is complex and can be related to various properties. Potential PIMs sharing similar features are expected to be able to

tolerate defects.

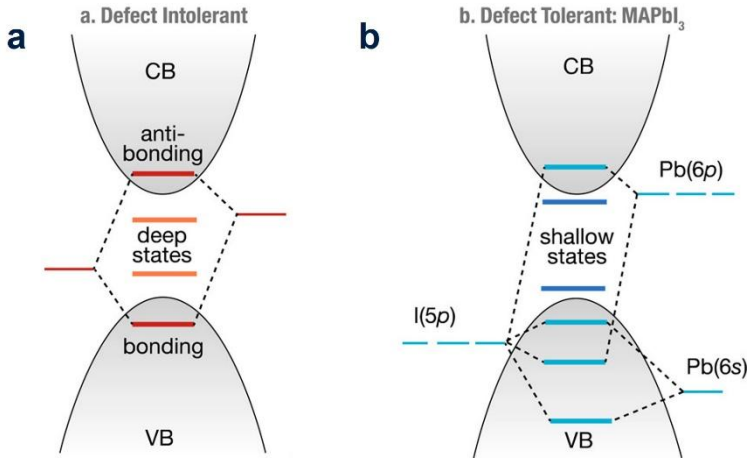

Fig. 2.15 | The electronic band structure of a, typical defect intolerant materials (*e.g.*, III-V, II-VI, and group IV semiconductors) and b, typical defect tolerant materials (*e.g.*, LHPs). Reproduced with permission from Ref. 81. Copyright 2017 American Chemical Society.

2.3.3 ABZ_2 materials

As discussed in the previous section, the $6s^2$ lone electron pair in Pb^{2+} is critical for the defect tolerance of LHPs. Therefore, lead-free PIMs containing cations with similar valence ns^2 electrons (*e.g.*, In^+, Sn^{2+}, Sb^{3+}, and Bi^{3+}) have gained increasing attention. More specifically, the ABZ_2 family of materials (A = monovalent cation, B = Sb^{3+} or Bi^{3+}, Z = chalcogen) is promising solar absorber materials because Sb^{3+} or Bi^{3+} avoids the scarcity of In[82] and the self-doping that is prevalent in Sn perovskites[83-86]. Moreover, chalcogenides exhibit generally improved stability than halides. In this section, I will review important research progress of some representative ABZ_2 materials with the focus on $CuSbSe_2$, which is the material

investigated in Chapter 4 and 5 of this thesis.

Thanks to the high absorption coefficient (10^4-10^5 cm^{-1}), the highest PCE of solar cells based on ABZ_2 materials was achieved by $AgBiS_2$ solar cells in 2024 (10.8%)[87]. Early work employed the SILAR (sequential ionic layer adsorption reaction) process[88] or spray pyrolysis[89] to synthesize $AgBiS_2$, while the hot-injection method has been widely used to grow $AgBiS_2$ nanocrystals (NCs) since 2016[90-95], facilitating the increased PCE of $AgBiS_2$ solar cells. However, OPTP measurements reported a low charge-carrier mobility (0.46 ± 0.05 $cm^2 \cdot V^{-1} \cdot s^{-1}$) and a short diffusion length (≈ 50 nm) for $AgBiS_2$ NC thin films[94]. Thus, the best performance of $AgBiS_2$ solar cells was achieved by ultrathin (30 nm) films[93]. It has been further demonstrated that the low charge-carrier mobility and diffusion length of $AgBiS_2$ NCs are caused by charge-carrier localisation, which results from the Ag and Bi cation disorder. Through heat treatment, the cation disorder in $AgBiS_2$ can be engineered from the cation-segregated structure (middle panel of Fig. 2.16a) to the homogeneously cation-disordered structure (bottom panel of Fig. 2.16a). With the engineered cation disorder, the charge-carrier localisation in $AgBiS_2$ can be mitigated and the mobility is increased to 2.7 ± 0.1 $cm^2 \cdot V^{-1} \cdot s^{-1}$, enabling efficient charge-carrier transport[94].

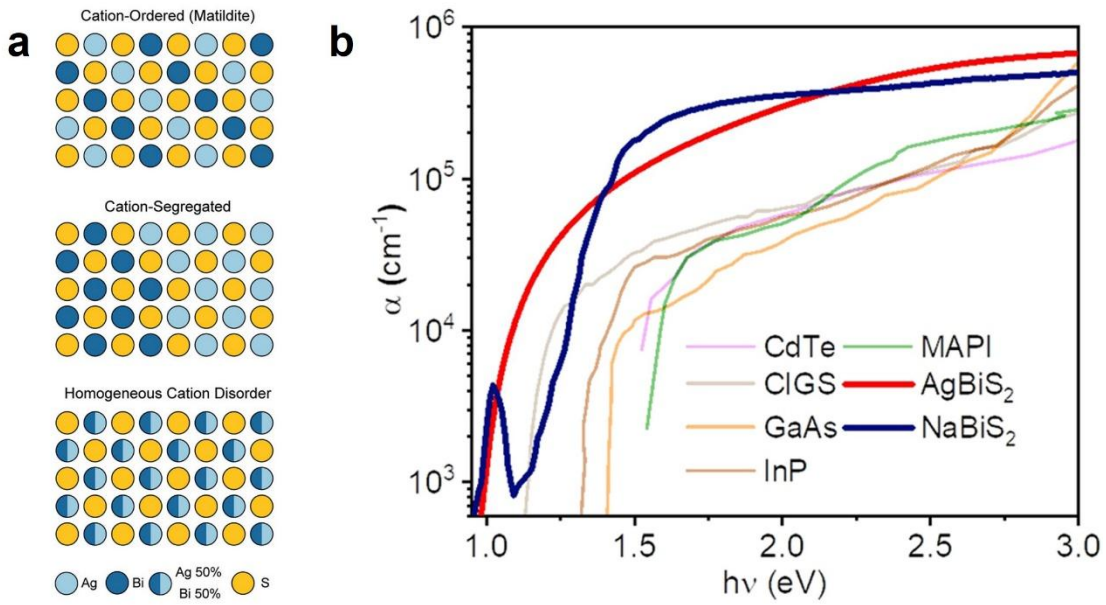

Fig. 2.16 | Cation disorder and optical absorption coefficients of $AgBiS_2$ and $NaBiS_2$. a, Schematic of $AgBiS_2$ crystal structures with different types of cation ordering. Top: perfectly cation-ordered; middle: cation-segregated; bottom: fully homogeneous cation-disordered structures. Reproduced with permission from Ref. 94. Open access, CC BY. **b,** Optical absorption coefficient (α) spectrum of $AgBiS_2$ and $NaBiS_2$ NC films compared with other PV absorbers. Reproduced with permission from Ref. 96. Open access, CC BY.

$NaBiS_2$ is another ABZ_2 material exhibiting a high optical absorption coefficient (Fig. 2.16b), thus attracting attention for its photovoltaic applications. However, since $NaBiS_2$ has a similar rock salt crystal structure to $AgBiS_2$, where the Na^+ and Bi^{3+} cations randomly occupy the same lattice sites, cation disorder has also been reported for $NaBiS_2$ NCs. The formation of Na^+-rich clusters leads to charge-carrier localisation in $NaBiS_2$, thereby reducing the charge-carrier mobility and diffusion length[96]. The cation disorder in $NaBiS_2$ has not yet been as effectively engineered as in $AgBiS_2$, resulting in the suboptimal performance of $NaBiS_2$ solar cells, with a highest-reported PCE reaching only 0.74%[97]. Beyond these two materials, charge-carrier

localisation has been prevalently observed in the family of bismuth-halide and bismuth-chalcogenide semiconductors, so that it is being regarded as a hallmark of these materials[27,28,98,99]. The limited performance of these Bi-based materials suggests that future development of PIMs should prioritise materials which do not undergo charge-carrier localisation. Thus, it is critical to better understand how to design PIMs with delocalised charge-carriers.

Recent studies on BiOI revealed its band-like transport[100,101], unlike many other Bi-based semiconductors. The change-carrier mobility of BiOI can reach up to 83 $cm^2 \cdot V^{-1} \cdot s^{-1}$, far exceeding the mobilities of localised charge-carriers (typically $\approx$10 $cm^2 \cdot V^{-1} \cdot s^{-1}$ or lower)[14,18,27,28,96,102]. It is supposed that this is related to both the layered structure of BiOI and its large layer thickness. Considering that the charge-carrier localisation of Sb-based compounds is not as well established as Bi-based compounds, I investigate a related layered Sb-based ABZ_2 material, $CuSbSe_2$.

$CuSbSe_2$ is a příbramite, which is the Se analogue to the chalcostibite $CuSbS_2$, having an orthorhombic unit cell (*Pnma* space group). The crystal structure of $CuSbSe_2$ is shown in Fig. 2.17a, where each Sb atom is bonded to three Se atoms forming a trigonal pyramidal geometry, while each Cu atom is bonded with four Se atoms in a tetrahedral arrangement. The $CuSbSe_2$ layers are held together by *van der Waals* interactions. The $5s^2$ lone electron pairs of Sb^{3+} are projected towards the interlayer space, as shown at the lower right corner of Fig. 2.17a. The stereochemical activity of the $5s^2$ lone electron pair has been reported for Sb^{3+} in both

$CuSbS_2$[103-105] and Sb_2Se_3[106,107], indicating that the orbital energy levels of the Sb 5*s* and Se 4*p* states are close enough to interact. The bandgap of $CuSbSe_2$ has been reported to range from 0.9 to 1.2 eV[108-113], making it suitable for harvesting the near-infrared portion of the solar spectrum. Also, both $CuSbS_2$ and $CuSbSe_2$ exhibit optical absorption coefficients higher than 10^4 cm^{-1} [112,114], as well as exceptional charge-carrier mobilities (64.6 $cm^2 \cdot V^{-1} \cdot s^{-1}$ for polycrystalline $CuSbS_2$[115]; 87 $cm^2 \cdot V^{-1} \cdot s^{-1}$ for single crystal $CuSbSe_2$[108]). These properties make both materials promising for photovoltaic applications. So far, a record PCE of 3.22% (with a V_{OC} of 0.47 V and a J_{SC} of 15.64 mA/cm^2) and 4.7% (with a V_{OC} of 0.34 V and a J_{SC} of 26 mA/cm^2) have been achieved for $CuSbS_2$[116] and $CuSbSe_2$[117] solar cells, respectively.

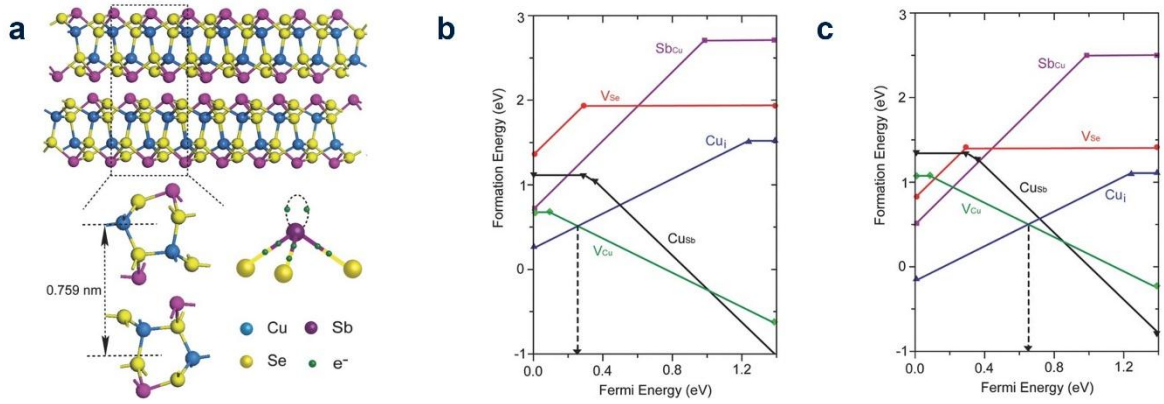

Fig. 2.17 | Crystal structure and defect formation energy diagrams of $CuSbSe_2$. a, Crystal structure $CuSbSe_2$. The interlayer gap and $5s^2$ lone electron pair of Sb^{3+} are displayed at the bottom. The defect formation energy as a function of the Fermi level under **b,** Se-rich and **c,** Se-poor condition. Reproduced with permission from Ref. 112. Copyright 2015 John Wiley and Sons.

The defect properties of both materials have also been studied computationally. Fig. 2.17b and

c show the defect formation energy diagram of $CuSbSe_2$ under Se-rich and Se-poor conditions, respectively[112]. Under the Se-rich condition (Fig. 2.17b), the acceptor defect V_{Cu} has the lowest formation energy, leading to the *p*-type conductivity and shifting the Fermi energy closer to the VBM. However, the shift of the Fermi energy towards the VBM also results in the decreased formation energy of the donor defect Cu_i. When the balance between V_{Cu} and Cu_i is reached, the Fermi level is set at about 0.2 eV above VBM. On the other hand, under the Se-poor condition, V_{Cu} and Cu_i are still the two dominant defects, but their formation energies are changed. In this case, the competition between V_{Cu} and Cu_i determines the Fermi level near the middle of the bandgap. This comparison indicates that the synthesis condition can influence the conductivity of $CuSbSe_2$. However, under both conditions, both V_{Cu} (0.08 eV above the VBM) and Cu_i (0.15 eV below the CBM) have shallow transition energy levels, so they are expected not to affect the charge-carrier lifetimes significantly. The acceptor defect Cu_{Sb} is located at 0.29 eV above the VBM, which is not very deep. Considering its relatively high formation energy, its concentration should be low, and its negative effects on charge-carriers should be negligible. The other defects V_{Se} and Sb_{Cu} have deeper transition levels, but their formation energies higher than 1 eV result in even lower concentrations, so they will not dramatically assist the charge-carrier recombination. Given that all low-energy defects have shallow transition levels, $CuSbSe_2$ is expected to be a defect-tolerant semiconductor, but this needs more experimental examination in the future. Similar defect characteristics have also been proposed for $CuSbS_2$[114].

Due to its outstanding optoelectronic properties and promising photovoltaic applications,

various techniques have been employed to grow $CuSbSe_2$, such as sputter deposition[117], close-space sublimation[118], fusion method[119], selenization of metal precursors[120] and hydrazine-based solution processing[112,121]. Among these methods, solution processing requires less capital-intensive equipment and shorter reaction time[122], but the highly dangerous hydrazine is another concern to address, urging the development of more benign solvents to synthesize $CuSbSe_2$. A recently explored solvent system for solution processing of chalcogenides, a thiol-amine solvent system, will be introduced later. Moreover, to overcome the limited scalability of solution processing method, especially spin coating, other synthesis techniques such as CVD are also worth studying.

2.4 Sb_2S_3-based solar cells

As c-Si solar cells are leading the photovoltaic market, the bulkiness of Si makes them unsuitable for light-weight or flexible applications. Among alternative thin-film solar cells, CIGS technology is limited by the scarcity of In[123], while CdTe contains the toxic Cd element. Therefore, novel solar absorbers comprising earth-abundant, non-toxic constituents are needed. Sb_2S_3, as an emerging photovoltaic material, consists of earth-abundant and benign elements and has a high optical absorption coefficient ($> 10^4$ cm^{-1})[124]. Moreover, Sb_2S_3 only presents one single stable phase, avoiding the formation of undesired impurity phases. Also, the relatively low melting point of Sb_2S_3 ($\approx$550 °C) makes it possible to synthesize crystalline films at low temperatures (< 400 °C)[125]. These properties enable Sb_2S_3 to be an attractive material for thin-film solar cells. In particular, the bandgap value of Sb_2S_3 (1.7-1.8 eV) matches

well with the requirement for top cells of tandem solar cells, as well as indoor light harvesting discussed in Section 2.2.4. The SLME of Sb_2S_3 solar cell has been predicted to reach 47% under 1000 lux WLED illumination[42].

Sb_2S_3 has an orthorhombic crystal structure (*Pnma* or *Pbnm* space group depending on axis assignment), as shown in Fig. 2.18. The structure is composed of covalently bonded quasi-1D $[Sb_4X_6]_n$ ribbons, while the ribbons are stacked together by weak *van der Waals* interactions. Such inter-ribbon free volumes may accommodate the lattice distortions caused by acoustic wave propagation, thereby reducing the acoustic deformation potential. However, whether Sb_2S_3 undergoes charge-carrier localisation or not is still under debate[107,126].

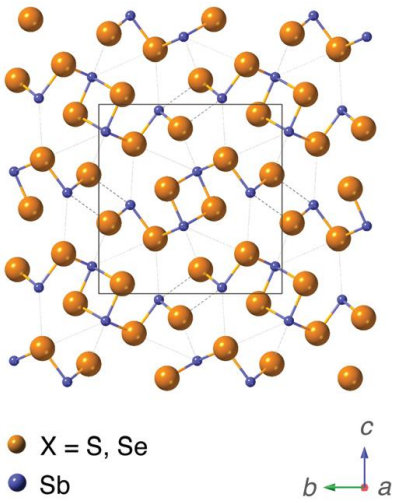

Fig. 2.18 | Crystal structure of Sb_2S_3. Reproduced from Ref. 107 with permission from the Royal Society of Chemistry.

Due to its exceptional properties, different techniques have been developed to synthesize Sb_2S_3 for solar cells. Chemical bath deposition (CBD) is the most common method used to deposit

Sb_2S_3 thin films because of its simple operations, low cost, and potentials for scalable deposition. More details of CBD will be introduced in Section 2.5.3. The first attempt at synthesizing Sb_2S_3 via the CBD method employed $Na_2S_2O_3$ and Sb_2O_3 as the sulphur and antimony source, whereas 2,2',2",2"'-(ethane-1,2-diyldinitrilo)tetraacetic acid (EDTA) was used as a complexing agent[127]. A uniform and compact Sb_2S_3 thin film with an amorphous nature was obtained. Subsequently, Savadogo and Mandal used thioacetamide and potassium antimony tartrate as sulphur and antimony source, and 2,2′,2″-nitrilotri(ethan-1-ol), ammonium hydroxide, and silicotungstic acid (STA) as complexing agent. By adding a heat treatment step at 300 °C, the amorphous film was converted into polycrystalline film[128]. In their following studies, with identical methods and conditions, Sb_2S_3 solar cells with the PCE exceeding 5% were achieved[129,130], indicating the high quality of Sb_2S_3 thin films deposited by the CBD method. Inspired by the success, the CBD method has been widely applied for Sb_2S_3 thin film deposition, while different sulphur and antimony sources, complexing agents, as well as additives have been explored to tune the properties of Sb_2S_3.

In 2014, Choi *et al*. modified the surface of Sb_2S_3 by thioacetamide-based sulfurization and achieved a PCE of 7.5%, the record of Sb_2S_3 sensitized solar cells[131]. As for planar Sb_2S_3 solar cells, by employing multiple sulphur sources (sodium thiosulfate and thioacetamide), the processes of heterogeneous nucleation and S^{2-} release were enhanced, and the PCE reached 8%. This is the highest efficiency of all Sb_2S_3 solar cells so far[132]. On the other hand, by introducing Ce^{3+} into the precursor solution for Sb_2S_3 deposition, the nucleation and growth processes of Sb_2S_3 were modulated, which successfully reduced the grain boundary density. This grain

engineering achieved the highest V_{OC} of Sb_2S_3 solar cells (796 meV) and an impressive PCE of 7.66%[133]. In our recent work, we showed that the addition of 2-aminoethanol (MEA) into the precursor solution could also tune the nucleation and growth of Sb_2S_3 films, resulting in increased grain size and a higher deposition rate. Our MEA-modulated Sb_2S_3 solar cell gave a PCE of 7.22% under the AM1.5 G spectrum, and an IPV PCE of 17.55% under a 1000 lux WLED, which is the highest yet reported for Sb_2S_3 IPVs. We also constructed large-area Sb_2S_3 minimodules to power IoT wireless sensors, enabling long-term continuous monitoring of environmental parameters under office lighting[44]. These achievements demonstrate the abundant opportunities to optimise the deposition of Sb_2S_3 films and underscore the exceptional potential of Sb_2S_3 solar cells for harvesting indoor light.

In addition to improving the efficiency of Sb_2S_3 solar cells, efforts have also been made to develop more benign (*i.e.*, cadmium-free) Sb_2S_3 solar cells recently. However, as shown in Fig. 2.19, the main challenge is the non-uniform island growth of Sb_2S_3 on the surface of oxide ETLs (such as TiO_2 and SnO_2), which results in discontinuous Sb_2S_3 films, thus reducing efficiencies[134-139]. To overcome this limitation, either an interfacial layer (*e.g.*, ZnS[134-136,138] and In_2S_3[139,140]) or an Sb_2S_3 seed layer[137] has been inserted between Sb_2S_3 and oxide ETLs, facilitating the heterogeneous nucleation and compact growth of Sb_2S_3 films. On the one hand, the underlying mechanisms by which CdS or interfacial layers outperform oxides as substrates for Sb_2S_3 growth remain unclear. Identifying the critical properties of substrates that enable the growth of uniform and compact Sb_2S_3 films can facilitate the efficient development of Cd-free Sb_2S_3 solar cells, a crucial step toward their widespread application.

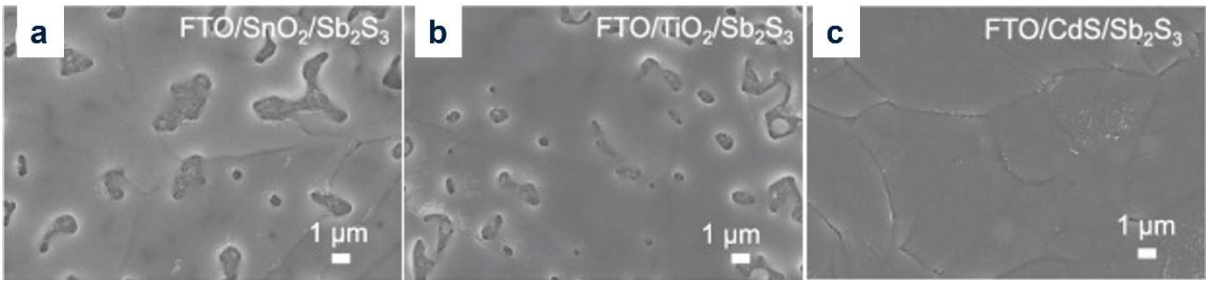

Fig. 2.19 | Top-view FE-SEM images of thermally treated a, FTO/SnO_2/Sb_2S_3; b, FTO/TiO_2/Sb_2S_3 and c, FTO/CdS/Sb_2S_3. Reproduced with permission from Ref. 138. Copyright 2022 Elsevier.

2.5 Thin film deposition

Thin films can exhibit a wide range of properties, depending on their composition, microstructure, thickness, and other influencing factors. These properties include ferromagnetism, superconductivity, high wear resistance, and resistive switching. Consequently, thin-film-based technologies play a vital role in the global economy, with applications spanning memory storage, optoelectronic devices, and surface coatings that protect structures from high-temperature oxidation. The properties of thin films are heavily influenced by the growth techniques and processing conditions employed, which also significantly impact their commercial viability. To accommodate varying demands for quality, cost, and scale, several techniques have been developed for depositing thin films, including solution processing, physical vapor deposition (PVD), and chemical vapor deposition (CVD), among others. The following sections will provide a detailed discussion of these techniques, with a particular focus on spin coating, CBD, and CVD.

2.5.1 Solution processing

Compared to other thin film deposition techniques, solution processing does not require vacuum systems or high processing temperatures, making it a cost- and energy-efficient choice, and offers scalability and flexibility in substrate choice. Among various solution processing methods, spin coating is the most common and simplest one used in the laboratory because it can be used to grow a wide range of materials fast, not requiring expensive equipment or vacuum systems. Spin coating can also grow some materials with complex structures that are difficult for other techniques, for example, the growth of polymers by PVD. It is also easier to explore the processing conditions of spin coating to quickly optimize thin film growth. Therefore, spin coating has been extensively used for organic[141,142] and perovskite solar cells[143-145], nanoplatelet light-emitting diodes[146-148], flexible thin film transistors[149], and other applications[150,151].

Thin film growth starts with nucleation. During spin coating, nuclei can form within the solvent (homogeneous nucleation) or on the surface of the substrate or other clusters in the solvent (heterogeneous nucleation). Nucleation requires supersaturation, which can be obtained by removing the solvent. Fig 2.20 shows three common methods to remove the solvent. Evaporation of solvent can be accelerated by heating the substrate or using a burst of nitrogen gas over the sample (gas-phase quenching). The antisolvent method involves dropping a solvent that does not dissolve the precursors (*i.e.*, "bad" solvent) to wash away the "good"

solvent and help nucleation. The degassing method removes the solvent by reducing the pressure (*e.g.*, by holding the film in a low vacuum chamber). These three methods all achieve supersaturation by removing the "good" solvent to increase the precursor concentration.

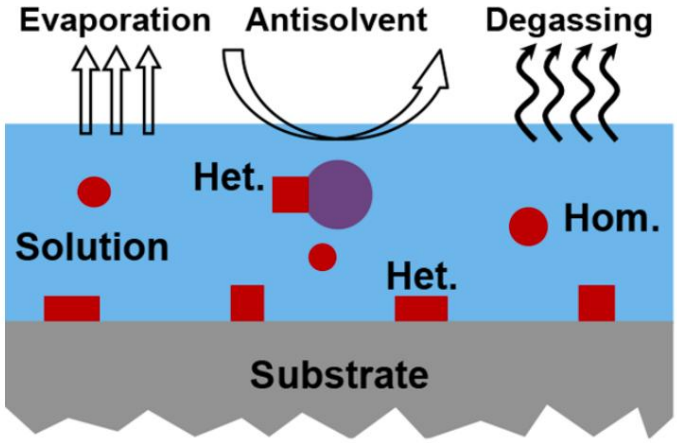

Fig. 2.20 | Schematic of homogeneous and heterogeneous nucleation during spin coating. The blue region is the residual solvent. Three common methods to accelerate solvent removal (evaporation, antisolvent and degassing) are also shown. Reproduced with permission from Ref. 122. Copyright 2019 American Chemical Society.

Homogeneous nucleation occurs when units of the nucleating phase cluster within the solvent. These "units" can be atoms, ions, molecules or formula-units, which are commonly referred to as monomers. To make the homogeneous nucleation process thermodynamically favourable, the change in Gibbs free energy (ΔG_{Hom}) should be negative, as given by this equation:

$$\Delta G_{Hom} = -V\Delta G_V + A\gamma_{NL} \tag{2.42}$$

where ΔG_V as the Gibbs free energy per unit volume change in monomers, V as the volume of the nucleus, A as the surface area of the nucleus and γ_{NL} as the energy associated with the creation of the solid-liquid interface. Since the creation of a new solid-liquid interface would

oppose nucleation, ΔG_V must be negative to make the nucleation happen. ΔG_V can be described by:

$$\Delta G_V = -\frac{RT}{V_m} RT \ln(S_P + 1). \tag{2.43}$$

In this equation, R is the Universal gas constant (8.314 J mol^{-1} K^{-1}), T the absolute temperature of the solution, V_m the molar volume of the nucleus, and S_P the supersaturation. As the nuclei are typically modelled as spheres, combining eq. (2.42) and (2.43) with the volume and area of a sphere, ΔG_{Hom} as a function of the nucleus radius can be derived:

$$\Delta G_{Hom} = \left(-\frac{4\pi r^3}{3V_m}\right) RT ln(S_P + 1) + 4\pi r^2 \gamma_{NL} \tag{2.44}$$

and plotted in Fig. 2.21. When the nucleus radius increases beyond a threshold value (r^*), ΔG_{Hom} starts decreasing, and nucleation becomes thermodynamically favourable when ΔG_{Hom} is negative. It can also be noted that the supersaturation S_P needs to be positive to facilitate the nucleation process, which is defined as:

$$S_P = \frac{C - C_S}{C_S} \tag{2.45}$$

where C is the solution concentration in the precursor concentration, and C_S the equilibrium solubility limit. Thus, supersaturation is necessary to make $S_P > 0$, which can be achieved by the three strategies (*i.e.*, evaporation, antisolvent and degassing) illustrated in Fig. 2.20.

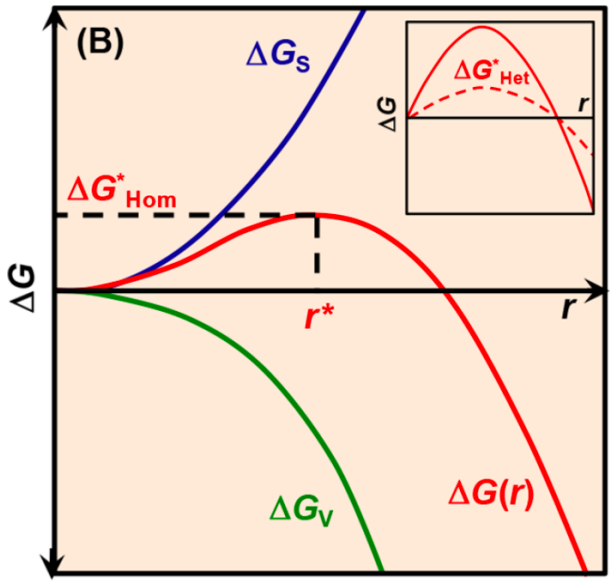

Fig. 2.21 | Free energy change (ΔG), sum of surface (ΔG_S), and volume (ΔG_V) free energy changes, as a function of nucleus radius (r) for homogeneous nucleation (inset: heterogeneous nucleation). Reproduced with permission from Ref. 122. Copyright 2019 American Chemical Society.

The key feature of heterogeneous nucleation is that the nuclei form on another surface, such as the substrate, instead of within the solvent. In heterogeneous nucleation, new interfaces between nucleus and liquid (NL), as well as nucleus and substrate (SN), are created, while the liquid-substrate interface (SL) is removed. The total interfacial energy in heterogeneous nucleation is lower than in homogeneous nucleation, so heterogeneous nucleation is more common. The change is the Gibbs free energy in heterogeneous nucleation (ΔG_{Het}) can be calculated by:

$$\Delta G_{\mathrm{Het}} = \left[\left(-\frac{4\pi r^3}{3V_m}\right) RT\ln\left(S_{\mathrm{p}}+1\right) + 4\pi r^2 \gamma_{NL}\right] f(\theta). \tag{2.46}$$

The parameter $f(\theta)$ depends on the contact angle θ of the nucleus on the substrates as

$f(\theta) = \frac{1}{4}(2 + cos\theta)(1 - cos\theta)^2$. The contact angle can be derived from Young's equation:

$$\gamma_{SL} = \gamma_{SN} + \gamma_{NL}cos\theta. \quad (2.47)$$

It can be seen that ΔG_{Het} would reach the lowest value when $\theta = 0$ (*i.e.*, full wetting). As θ approaches π, ΔG_{Het} gets closer to ΔG_{Hom}.

For thin films used in solar cells, larger grains are usually desired because grain boundaries can be the sites of dangling bonds and traps, which can be centres of non-radiative recombination. Grain boundaries can also scatter carriers and lower the mobility. Thus, larger grains are preferred due to the lower density of grain boundaries. Also, the thin films should be as compact as possible because pinholes penetrating the whole film can be the paths where other layers connect and affect device performance. To ensure compact films, compatible solvents and substrate should be used. For example, if the solvent is polar, the substrate should be treated with oxygen plasma or UV-ozone to remove organic residues on the surface. A high density of nuclei is also important for a compact film. The three strategies shown in Fig. 2.20 can be used to obtain a higher density of nuclei by increasing supersaturation. To promote the grain coarsening, some post-treatment, such as heat treatment, may be applied after spin coating. The morphology of thin films can be controlled by manipulating the density and uniformity of nucleation and grain coarsening.

The key challenge in depositing $CuSbSe_2$ thin films through solution processing is selecting appropriate solvents capable of effectively dissolving the chalcogenide precursors. Unfortunately, chalcogenides are generally insoluble in most traditional solvents such as *N*, *N*-

dimethylformamide (DMF), dimethyl sulfoxide (DMSO), and *N*-methylpyrrolidone (NMP)[152]. It has been reported that hydrazine can dissolve a wide range of chalcogenides and can be used to fabricate the absorber materials of solar cells, including $CuSbSe_2$[112,121,153-155]. However, hydrazine is highly toxic and explosive, preventing the practical application of this hydrazine-based solution processing method. In 2013, a binary solvent mixture of ethane-1,2-dithiol (EDT) and ethane-1,2-diamine (en) was reported to dissolve nine bulk V_2VI_3 chalcogenide materials at room temperature, ambient pressure, in air, and on the order of minutes[156]. This thiol-amine solvent system was applied to the dissolution of a wider range of chalcogenides, including Cu_2Se[157-160] and Sb_2Se_3[156,161]. This solvent system was also used to dissolve Cu_2Se and In_2Se_3 separately, then the two precursor solutions were mixed to spin coat $CuInSe_2$ thin films[160]. This study inspired us to use Cu_2Se and Sb_2Se_3 as precursors to spin-coat $CuSbSe_2$ thin films.

In 2017, Murria *et al.*[162] dissolved CuCl and $CuCl_2$ in the mixture of propane-1-thiol and butan-1-amine, then investigated the dissolution mechanism of this solvent system using mass spectrometry. The mechanism was reported to be initiated by proton transfer from the thiol to amine, then the thiolate ion dissolves the copper salts by coordinating with the copper cations, while the propylammonium cation coordinates with the chloride anions. So far, the thiol-amine solvent system has successfully dissolved a wide range of precursors, including elemental materials, oxides, chalcogenides and other metal salts, as listed in Fig. 2.22. Binary combinations of thiols and amines have become a useful solvent system for the solution processing of chalcogenide thin films.

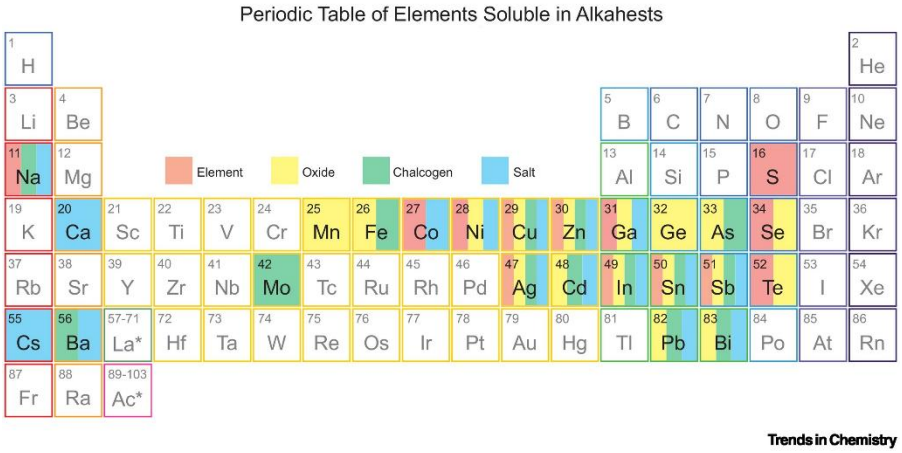

Fig. 2.22 | Periodic table of elements and their counterparts soluble in thiol-amine solvent systems. Reproduced with permission from Ref. 163. Copyright 2021 Elsevier.

2.5.2 Chemical vapour deposition (CVD)

In chemical vapour deposition (CVD), thin films are formed on a substrate through the reaction of gaseous precursors. Alternatively, some reactants can be pre-deposited on a substrate and subsequently react with gaseous precursors. CVD is widely used in both laboratory and industrial production because it can grow a wide range of materials with high purity and a rapid growth rate. The properties of grown materials can also be tuned by adjusting CVD conditions[164]. To make a chemical reaction thermodynamically feasible, a reduction in the Gibbs free energy is required, *i.e.*, $\Delta G < 0$. The ΔG of a reaction can be derived from:

$$\Delta G = \sum G_{products} - \sum G_{reactants}\,. \tag{2.48}$$

However, for a non-closed system with gas transport in or out, the effects of gas transport and kinetics need to be considered as well to determine whether a CVD reaction can happen.

A tube furnace is commonly used for CVD, where a quartz tube is held inside a horizontal

furnace. By heating the precursors and substrates, the precursors are vaporised, and the activation energy barrier for the chemical reaction is overcome. The gaseous precursor reacts with other reactants and is transported to other zones containing substrates via a flowing carrier gas (*e.g.*, Ar), then the solid products deposit in thin film form. Byproducts and other waste gases are carried out of the reactor. CVD typically involves five main steps. First, precursors are delivered to the substrate zone within the reactor. Next, reactants move across the boundary layer and adsorb onto the substrate. This is followed by surface diffusion and incorporation into the lattice through nucleation and growth. Gaseous waste products are then removed from the substrate via the boundary layer. Finally, the waste products are extracted from the reactor. Properties of CVD thin films can be tuned and optimised through variation of the parameters such as flow rates, pressure and growth temperatures[165-167].

Reactive close-spaced sublimation (RCSS), a technique similar to CVD, has been employed to deposit $CuSbSe_2$ thin films[118], as shown in Fig. 2.23. The bottom heater was kept at 500 °C to vaporise the Sb_2Se_3 powder, while the Cu substrate temperature was controlled by the top heater. By using a constant pressure, it was found that substrate temperature and reaction duration were the key factors influencing the phase purity and microscopic morphology of $CuSbSe_2$ thin films. Meanwhile, it was demonstrated that heated Sb_2Se_3 could be partially decomposed as:

$$Sb_2Se_3\ (s) \Leftrightarrow \frac{1}{4}Sb_4\ (g) + SbSe(g) + Se_2(g). \quad (2.49)$$

Both released Se and Sb_2Se_3 vapour could react with the Cu substrates to form Cu_2Se and $CuSbSe_2$. Meanwhile, formed Cu_2Se could further react with Sb_2Se_3 as:

$$Cu_2Se(s) + Sb_2Se_3\ (s) \Leftrightarrow 2CuSbSe_2(s). \quad (2.50)$$

This work shed light on the CVD technique for $CuSbSe_2$ thin films and highlighted the key parameters affecting the CVD film quality.

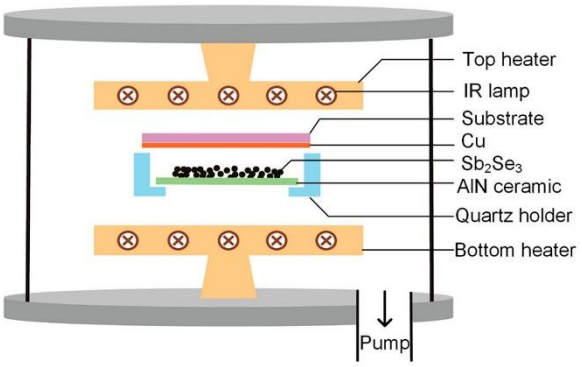

Fig. 2.23 | Schematic of the RCSS chamber for $CuSbSe_2$ deposition. Reproduced with permission from Ref. 118. Open access, CC BY.

2.5.3 Chemical bath deposition (CBD)

Chemical bath deposition (CBD) is a scalable solution processing method for thin film deposition. As illustrated in Fig. 2.24, in CBD, the substrates are immersed in a solution containing the precursors. The solution is heated to initiate reactions, which result in films being deposited onto the substrates, while constant stirring may be applied to ensure uniform deposition. Parameters such as ion concentrations, solution pH, temperature, and complexing agents can be adjusted to regulate the deposition process[168]. In addition to its simplicity and low cost, the CBD method offers several notable advantages. One significant benefit is the ability to easily introduce additives to the chemical bath to fine-tune the properties of deposited films. Moreover, during synthesis, the solution can penetrate porous structures, enabling

conformal film deposition within them, which is a critical aspect for sensitised solar cells[125]. On the other hand, CBD tends to waste a considerable amount of precursor solutions, and all available surface sites may be covered by films. In CBD, nuclei can form through either homogeneous or heterogeneous nucleation processes. To promote the formation of uniform and compact films on substrates, homogeneous nucleation within the precursor solution must be suppressed. This can be achieved by optimising parameters such as the additives in the solution, the selection and surface modification of substrates, and the incorporation of various complexing agents.

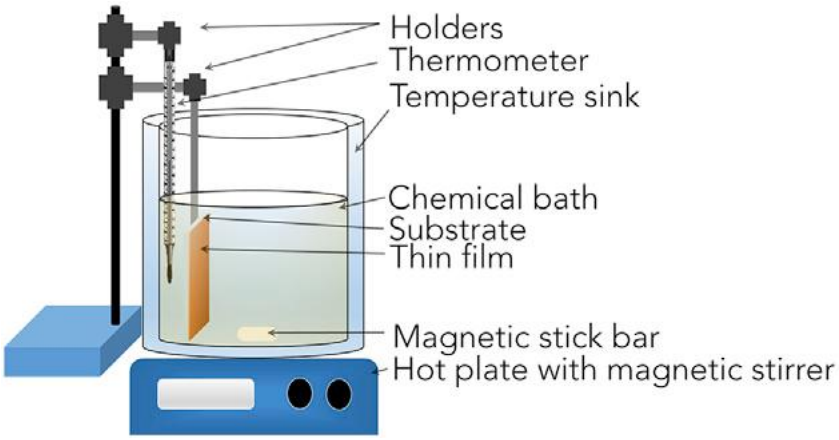

Fig. 2.24 | Schematic of chemical bath deposition. Reproduced with permission from Ref. 125. Copyright 2018 Elsevier.

The significant advancements of the CBD method for Sb_2S_3 solar cells are discussed in Section 2.4. A related technique, the hydrothermal (HT) method, has also been utilised for fabricating Sb_2S_3 solar cells. Unlike the ambient pressure and moderate temperatures of the CBD method, the HT method involves chemical reactions conducted in a sealed, high-pressure autoclave at elevated temperatures. Despite these differences, both techniques utilise similar precursors and

chemical reactions to synthesise Sb_2S_3. To date, CBD[131,132] and HT[43,44,133] methods have demonstrated comparable PCEs for Sb_2S_3 solar cells, suggesting that both methods can produce Sb_2S_3 films with similar quality. In addition to Sb_2S_3, the CBD method has been widely used for the deposition of other compounds, such as CdS[169,170] and SnO_2[171], which are also important for solar cells and involved in this thesis.

2.6 Overall aims of the thesis

Previous sections in this chapter discussed the fundamentals of semiconductors and solar cells, and then reviewed the progress and limitations in the fields of PIMs, $CuSbSe_2$ film deposition and Sb_2S_3 solar cells. In this section, I will highlight the key challenges that this thesis aims to address.

Chapter 4 focusses on understanding the ability of $CuSbSe_2$ to avoid charge-carrier localisation. Pnictogen-based semiconductors are regarded as promising lead-free alternatives to LHPs since Sb^{3+} and Bi^{3+} have similar electronic structures to Pb^{2+}. However, charge-carrier localisation has been prevalently observed in many Bi-based compounds, which severely reduces the mobility and sets the intrinsic limits of optoelectronic devices based on these materials. Inspired by the recent discovery of the band-like transport in BiOI, I investigated a related layered material, $CuSbSe_2$. This chapter aims to firstly examine the nature of charge-carriers in $CuSbSe_2$ through OPTP and temperature-dependent Hall effect measurements. After confirming the unusual large polarons in $CuSbSe_2$, detailed DFT calculations unravel the key

enabling factors. These key factors can provide valuable insights into how the limitation of charge-carrier localisation can be avoided by designing the structural and electronic features of semiconductors. This can be critical for developing efficient solar cells based on environmentally friendly PIMs.

Chapter 5 investigates two deposition techniques for $CuSbSe_2$ thin films, a thiol-amine-based solution processing method and a CVD method. These techniques exhibit improved safety compared to the reported hydrazine-based solution processing method and offer a scalable choice. After achieving phase-pure $CuSbSe_2$ thin films through the thiol-amine route in Chapter 4, this chapter analyses the parameters influencing the film properties, such as phase purity and microscopic morphology. Moreover, $CuSbSe_2$ solar cells based on these two techniques are fabricated and compared, suggesting the importance of selecting suitable deposition methods and device structures. This chapter aims to identify the main advancements and limitations of these novel techniques, providing suggestions on the development of $CuSbSe_2$ solar cells.

Chapter 6 focuses on the effects of buffer layers on Sb_2S_3 deposition. To achieve Cd-free solar cells, Sb_2S_3 has been deposited on various benign buffer layers (*e.g.*, TiO_2 and SnO_2). Even if the morphology of Sb_2S_3 thin films on different buffer layers has been compared, the underlying mechanisms of CdS outperforming others are still unclear. This chapter firstly reveals the effects of buffer layers on the nucleation and growth processes of Sb_2S_3, then investigates the chemical evolution of buffer layer/Sb_2S_3 interfaces carefully. By identifying the key properties of CdS enabling compact Sb_2S_3 films, insights into the design of benign

buffer layers for efficient Sb_2S_3 solar cells can be gained. This can contribute to the goal of Cd-free Sb_2S_3 solar cells and promote their wide applications. Moreover, the optical loss analysis of Sb_2S_3 solar cells sheds light on their future optimisation directions.

Overall, this thesis explores two chalcogenide materials, $CuSbSe_2$ and Sb_2S_3, for their potential in photovoltaic applications. By addressing fundamental charge-carrier properties, optimising deposition techniques, and enhancing device fabrication, it aims to advance the development of these materials. The findings provide valuable insights into designing materials with highly mobile charge carriers, achieving high-quality films through cost-effective methods, and promoting environmentally friendly solar cells. These contributions not only enhance the photovoltaic potential of chalcogenide materials but also pave the way for more sustainable and efficient solar energy technologies.

Chapter 3: Experimental methods

3.1 $CuSbSe_2$ thin film deposition

A few techniques have been used to grow $CuSbSe_2$ thin films, including one-step electrodeposition[172], selenization of Sb-Cu precursors[120], hydrazine-based solution spin coating[112,121], co-sputtering with Sb_2Se_3 and Cu_2Se[117], and close-space sublimation[118]. Spin coating is the most common and simplest solution processing method used in the laboratory because it can be used to grow a wide range of materials fast, not requiring expensive equipment or vacuum systems. In my projects on $CuSbSe_2$ (Chapter 4 and Chapter 5), $CuSbSe_2$ thin films were deposited via spin coating based on a novel thiol-amine route. Meanwhile, inspired by the reported close-space sublimation method[118], we also developed a CVD method to deposit $CuSbSe_2$ thin films, which is discussed in Chapter 5 as well.

3.1.1 Solution Processing

To deposit $CuSbSe_2$ thin films, a novel thiol-amine route was developed. Typically, 0.1585 g Sb_2Se_3 (99.99% trace metals basis, Merck) and 0.0680 g Cu_2Se (99.5% metals basis, Alfa Aesar) were mixed in an empty vial, then 1 mL ethane-1,2-diamine (en, for synthesis, Merck) and 0.1 mL ethane-1,2-dithiol (EDT, for synthesis, Merck) were added to the vial in a N_2-filled glovebox. The solution was firstly stirred at 70 °C for 10 min, then stirred at 30 °C overnight to fully dissolve precursors. Before spin coating, the solution was filtered with a 0.2 μm PTFE

filter, and a 1.2 cm × 1.2 cm substrate was cleaned by sonication in acetone and propan-2-ol for 15 min, respectively. After the sonication cleaning, the substrate was blown dry with N_2 then UV-ozone treated for 20 min. Then 40 μL solution was spread onto the substrate. Initially, a droplet of the solution was dispensed at the centre of the substrate and spread across the surface using the pipette tip, while the remaining solution was gradually applied to ensure full coverage. The substrate was then spin-coated at 2000 rpm for 60 seconds. Only one layer was spin-coated for each sample. After spin coating, the sample was thermally treated on a hot plate at 100 °C for 10 min (ramp rate 30 °C min^{-1} as indicated by the hotplate reading). The sample was subsequently cooled down naturally together with the hot plate. The cooling rate was estimated to be 5 °C min^{-1}. All of the above processes, except substrate cleaning, were performed in a N_2-filled glovebox, where the H_2O and O_2 levels were monitored and kept low (H_2O < 0.1 ppm; O_2 < 5 ppm). When the thermal treatment was completed, the sample was taken out of the glovebox and placed into a quartz tube for heat treatment. The tube was first pumped to a pressure of ≈50 mTorr, then filled with Ar to reach a pressure of ≈1200 mTorr. Then the sample was heated to 400 °C (ramp rate 60 °C min^{-1}) and kept for 2 min, then cooled down naturally (estimated cooling rate: 10 °C min^{-1}) to obtain phase-pure $CuSbSe_2$ thin films. The process of spin coating is illustrated in Fig. 3.1.

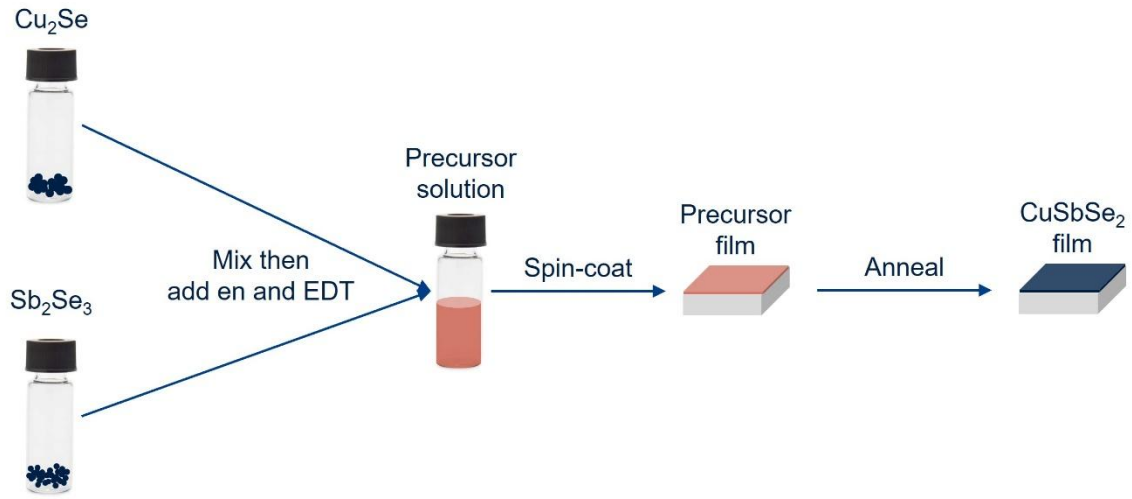

Fig. 3.1 | Schematic of the solution processing method to deposit $CuSbSe_2$ thin films.

3.1.2 Chemical Vapour Deposition

As it has been reported that the pre-sputtered Cu layer can react with evaporated Sb_2Se_3 to form $CuSbSe_2$ thin films using the traditional close-spaced sublimation method[118], we employed a conventional CVD setup to deposit $CuSbSe_2$ thin films based on the similar reactions. The setup is illustrated in Fig. 3.2. Firstly, the 1.2 × 1.2 cm^2 substrates (single crystal silicon or glass) were coated with 100 nm Cu films, then the substrates were mounted on glass slides using Ag paint (RS PRO Conductive Lacquer) with a 2-cm interval between neighbouring substrates. The CVD was carried out in a three-zone Carbolite Gero TG3 Gradient Tube Furnace, with the glass slides placed in the side zone 1 and 3 of the quartz tube. An alumina crucible loaded with 0.2 g Sb_2Se_3 precursor (99.99% trace metals basis, Merck) was placed in the centre zone 2 of the tube. Then the tube was sealed and pumped to a pressure of ≈50 mTorr, and filled with Ar as the carrier gas. When the target working pressure was reached, the centre zone and side zones were heated to 580 °C and 530 °C, respectively (ramp rate 30 °C

min^{-1} for all zones). When the target temperature of the centre zone was reached, the temperatures were kept for 4 to 5 min to investigate the effects of dwelling time. Afterwards, the heating was stopped and the samples were cooled down naturally to room temperature, then taken out of the tube for characterization (estimated cooling rate: 10 °C min^{-1}).

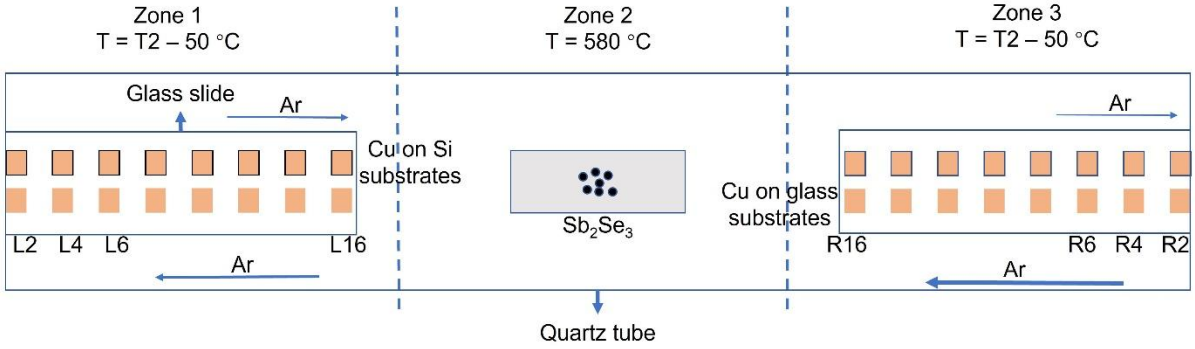

Fig. 3.2 | Schematic of the chemical vapour deposition (CVD) method to deposit $CuSbSe_2$ thin films. The temperature profiling of zones is illustrated in Fig. 5.5.

3.2 Sb_2S_3 thin film deposition

Different thin film deposition techniques have been developed to fabricate Sb_2S_3 solar absorbers, including hydrothermal[44,133], chemical bath deposition (CBD)[131,132], vapour transport deposition[173,174], rapid thermal evapouration[175], closed space sublimation[176] and so on. Among them, the CBD method has been widely used due to its simple operation, low cost and high production capacity[177]. So far, the highest power conversion efficiency (PCE) of Sb_2S_3 solar cells is achieved using the CBD method (8%)[132]. Therefore, CBD is recognized as the most feasible and successful method for Sb_2S_3 thin film deposition, and was employed in my project (Chapter 6).

To prepare the precursor solution, 1.2523 g antimony potassium tartrate trihydrate ($C_8H_4K_2O_{12}Sb_2 \cdot 3H_2O$, ACS, 99.0-103.0%, Thermo Scientific Chemicals) were firstly added to 50 mL deionized (DI) water in the reaction container and stirred until completely dissolved, then 2.4819 g sodium thiosulfate pentahydrate ($Na_2S_2O_3 \cdot 5H_2O$, 99.5+%, ACS reagent, Thermo Scientific Chemicals) were added to the solution as the S source. After the S source was fully dissolved and the mixture solution turned yellow, two 3 × 3 cm^2 substrates (FTO/CdS or FTO/SnO_2 or FTO/SnO_2/CdS) were immersed in the solution with the CdS surface facing down inside the container, and the edges of substrates covered with Kapton tapes. The substrates were tilted at an angle of $\approx 75°$ with respect to the horizontal plane. Then the container was sealed and kept at 95 °C for 6 h in a water bath. When the reaction finished and the contents cooled down, the substrates were taken out and rinsed with DI water then dried with N_2 flow. After removing the Kapton tapes, the as-deposited films were thermally treated at 380 °C for 10 min in a N_2-filled glovebox then cooled down naturally to room temperature.

3.3 Material characterisation

3.3.1 X-ray diffraction (XRD)

XRD measurements are based on Bragg's law:

$$n\lambda = 2dsin\theta \tag{3.1}$$

where n is an integer and λ is the X-ray source wavelength; d represents the distance between a set of crystal planes while θ is the angle between the incident X-ray and the crystal

plane. When Bragg's law is satisfied, the scattered X-ray will have constructive interference. In my projects, the XRD measurements were performed in air at room temperature on a Bruker D2 Phaser at Imperial College London, London, UK, or D8 Advance Eco instrument diffractometer at the University of Oxford, Oxford, UK. The beam path was optically aligned to the centre of the sample holder using the instrument's standard alignment routine, and the holder was secured in place using the stage's locking mechanism. A copper K_α X-ray source ($\lambda(K_{\alpha 1})$ = 1.5406 Å; $\lambda(K_{\alpha 2})$ = 1.5444 Å) was utilized. The $CuSbSe_2$ XRD samples were prepared via solution processing or chemical vapour deposition on 1.2 × 1.2 cm^2 single crystal silicon substrates, while Sb_2S_3 XRD samples were prepared via chemical bath deposition on 3 × 3 cm^2 substrates. Prior to measurement, each sample was mounted on a piece of plasticine positioned at the centre of the sample holder. The sample surface was then levelled with the holder surface using a glass microscope slide, and visually checked to ensure alignment with the edge of the holder. No additional height, tilt, or rotational alignment was applied. No sample spinning was used during measurements.

3.3.2 X-ray photoelectron spectroscopy (XPS)

XPS is a technique to analyse the surface chemistry of samples. When irradiating the sample surface with an X-ray beam, if the energy of the beam, $h\nu$, exceeds the binding energy of the electrons in the material, E_{BE}, then photoelectrons with the kinetic energy E_{KE} can be excited from core levels to the vacuum level, whose relationship can be described using the equation:

$$E_{KE} = h\nu - E_{BE} - \varphi \quad (3.2)$$

where φ is the work function of the Concentric Hemispherical Analyser (CHA). As XPS detects photoelectrons emitted from 1- 10 nm below the sample surface, it is a surface-sensitive technique. By analysing the XPS spectra, the information on both surface compositions of the sample and chemical states of surface atoms can be obtained, because the bonding environments of atoms can affect the electron core levels.

The probing depth of XPS is determined by how deep an electron can be generated and still escape without inelastically scattering. According to Beer's law, the intensity of electrons (I) emitted from depths deeper than d can be calculated by:

$$I = I_0 \exp(-d/\lambda), \quad (3.3)$$

where I_0 is the total number of generated electrons and the term λ is the attenuation length of the electron. The attenuation length is similar to the inelastic mean free path (IMFP) of the electrons, which is defined as the average length an electron with a certain kinetic energy can travel before inelastically scattering. Therefore, IMFP depends on the kinetic energy of the electron and the material through which it is traveling. To estimate IMFPs for different materials, the TPP-2M predictive equation has been developed[178-181]. The equation shows that IMFPs can be influenced by the number of valence electrons, the density, the atomic or molecular weight, the bandgap energy, as well as the electron energy. According to equation (3.2), when excited by the identical X-ray beam, core levels with different binding energies can have different kinetic energies, thus different IMFPs.

In my projects, the XPS data were acquired using a Kratos Axis SUPRA at Harwell, UK, with monochromated Al K_α (1486.69 eV) X-rays at 15 mA emission and 12 kV HT (180 W), and a spot size/analysis area of 700 × 300 μm^2. The instrument was calibrated to the Au 4*f* core level of a metal foil (83.95 eV), and dispersion adjusted to give a binding energy of 932.6 eV for the Cu $2p_{3/2}$ line of metallic copper. The Ag $3d_{5/2}$ line FWHM at 10 eV pass energy was 0.544 eV. The source resolution for monochromatic Al K_α X-rays is ~0.3 eV. The instrumental resolution was determined to be 0.29 eV at 10 eV pass energy using the Fermi edge of the valence band for metallic silver. Resolution with the charge compensation system on was <1.33 eV FWHM on PTFE. High resolution core line spectra were obtained using a pass energy of 40 eV, step size of 0.1 eV and sweep time of 60s, and for Auger-Meitner spectra with a pass energy of 40 eV, step size of 0.25 eV and sweep time of 60s, resulting in a line width of 0.696 eV for Au $4f_{7/2}$. Survey spectra were obtained using a pass energy of 160 eV. The samples were electrically grounded to the instrument using copper clips. A low-energy flood gun charge compensation system was used during the measurements, and a thermocouple was used to monitor the temperature on the sample stage at ~25 °C. All data were recorded at such a temperature and a base pressure of below 9 × 10^{-9} Torr.

CasaXPS software was used to fit all the spectra. All peaks were fit with a Shirley background[182] and the binding energies were calibrated relative to the adventitious C 1*s* at 284.8 eV. Peak fits were carried out for all 10 iterations to quantify the relative atomic percentages and to determine the oxidation states and chemical species. The spin−orbit splitting (SOS) constraints on the peak positions were based on the average published values from the

NIST X-ray photoelectron spectroscopy database[183]. For the Cu 2*p* doublet, a spin−orbit splitting of 19.8 eV was used[184-187]; for the Se 3*d* doublet, a spin−orbit splitting of 0.9 eV was used[118,184,186,187]. For the S 2*p* doublet, a spin−orbit splitting of 1.2 eV was used[188-190]; for the Sb 3*d* doublet, a spin−orbit splitting of 9.4 eV was used[118,133,191]. The doublet peak area was constrained as 1:2 for *p* core states and 2:3 for *d* core states, while the full width at half maximum (FWHM) was constrained to be equal for doublet peaks. Sum Gaussian/Lorentzian (SGL) line shape was used for peak fitting, and the Gaussian/Lorentzian ratio was adjusted to optimise the peak fitting. Kratos relative sensitivity factor (RSF) values were used for the quantification purpose.

3.3.3 Raman spectroscopy

Raman spectroscopy is an analytical technique that measures the vibrational energy modes of samples based on Raman scattering[192]. The sample is first excited to a higher vibrational energy state by the incident laser, and then the absorbed light will be almost immediately re-emitted as scattered light. If the sample gains energy during the scattering, the wavelength of the scattered light will be longer than that of the incident light, and this process is called Stokes Raman scattering. Inversely, the process where the scattered light gains energy during the scattering and exhibits a shorter wavelength than the incident light is called anti-Stokes Raman scattering. The comparison of the wavelengths of the incident and scattered light can provide information about the vibrational modes of the sample, as each molecule or chemical structure can have a unique spectral feature, which is shown as intensity peaks at certain Raman shift

values. Raman shift $\Delta\tilde{\nu}$ is defined as the difference of the wavenumbers of excitation laser and the scattered light:

$$\Delta\tilde{\nu} = \frac{1}{\lambda_{excitation}} - \frac{1}{\lambda_{scattered}}. \quad (3.3)$$

In my projects, Raman spectra were obtained in air at room temperature with a Renishaw Raman system at Imperial College London, London, UK, using a 532 nm wavelength continuous wave (cw) laser source. Before taking the measurements on $CuSbSe_2$, the equipment was calibrated by adjusting the characteristic Raman peak of the built-in silicon reference to 520 cm^{-1}. The final spectrum for each $CuSbSe_2$ sample was obtained by averaging 10 scans, where each scan took 5 s to collect. The $CuSbSe_2$ films were spin-coated onto 1.2 × 1.2 cm^2 glass substrates. The optical microscope built into the Raman spectrometer was used to focus the incident laser on the film surface before taking the Raman measurements.

3.3.4 Fourier-transform infrared (FTIR) spectroscopy

FTIR spectroscopy is another technique for chemical identification. A typical FTIR instrument applies a broadband mid-infrared (mid-IR, usually around 10000 to 100 cm^{-1}) radiation to the sample. As the radiation at certain wavenumbers can be absorbed by the sample and converted into the vibrational energy of chemical structures, while other radiation passes through the sample, the FTIR spectra can provide unique spectral fingerprints of different molecules or chemical structures.

In my projects, FTIR spectra were obtained in dry N_2 at atmospheric pressure at room temperature with a Bruker Vertex 80 FTIR Spectrometer at the University of Oxford, Oxford, UK. The light source was a mid-infrared glowbar, which is emissive from about 13000 to 40 cm^{-1}. The $CuSbSe_2$ films were deposited onto 7.5 × 2.5 cm^2 single crystal silicon substrates. Before taking the measurements on $CuSbSe_2$, the wavenumber was calibrated by the mirror position, which was determined using the interference pattern of the HeNe laser, and the absolute reflectivity was calibrated using the blank 7.5 × 2.5 cm^2 single crystal silicon substrate. The final spectrum for the $CuSbSe_2$ sample was obtained by averaging 3 scans, where each scan took 3176 s to collect.

3.3.5 Scanning electron microscopy (SEM) and energy-dispersive X-ray spectroscopy (EDX)

SEM uses a focused electron beam to excite the secondary electrons for imaging. Since the secondary electrons come from within a few nanometres of the sample surface, they are sensitive to the surface structure and morphology. The SEM images shown in my projects were acquired from Zeiss Auriga Cross Beam instrument (Imperial College London, London, UK), LEO Gemini 1525 FEGSEM (Imperial College London, London, UK), or FEI Quanta 600 FEG instrument (University of Oxford, Oxford, UK) with an acceleration voltage of 5-10 kV for the focused electron beams. The chamber pressure was maintained at ~10^{-4} – 10^{-5} Pa during measurements. The samples included spin-coated $CuSbSe_2$ thin films on different substrates and chemical-vapour-deposited $CuSbSe_2$ thin films on glass or ZnO substrates, as well as

chemical-bath-deposited Sb_2S_3 thin films on FTO/CdS or FTO/SnO_2 or FTO/SnO_2/CdS substrates. A thin layer of Cr (~10 nm) was coated onto the sample surface to improve the conductivity when necessary. Silver tapes were attached to the sample surface to avoid charge accumulation.

EDX/EDS is an elemental and compositional analysis tool that SEM is commonly equipped with. When an electron in the orbital of the inner shell is excited to a higher energy level by the electron beam and a vacancy is created, another electron from the outer shell will be transferred to the vacancy to stabilize the system and emit the X-ray with the corresponding energy, called characteristic X-rays. Since each element has a unique energy difference between the electron shells, the presence and fraction of each element can be analysed by detecting the specific energy of each characteristic X-ray. Compared with XPS, EDX has a larger detection volume since the X-rays can come from the bulk material, so EDX is more suitable for bulk composition analysis. The EDX results shown in my projects were acquired from the microscopes mentioned above with an acceleration voltage of 15-20 kV, depending on the investigated elements. The samples included spin-coated $CuSbSe_2$ thin films and chemical-bath-deposited Sb_2S_3 thin films on FTO/CdS or FTO/SnO_2 or FTO/SnO_2/CdS substrates. Prior to measurements, the system was calibrated using a cobalt (Co) standard sample to ensure quantification accuracy. Spectral fitting and quantification were conducted using Oxford Aztec software.

The quantification results presented in Section 5.2.1 include statistical errors derived from peak

fitting and counting statistics. However, these errors do not represent the total experimental uncertainty. Other sources of error include instrument calibration limitations, sample surface roughness and inhomogeneity, interaction volume effects leading to signal from underlying layers or adjacent phases, and potential spectral overlaps or background subtraction inaccuracies. These factors may contribute to additional uncertainties not captured in the tabulated error values.

3.3.6 Absorption coefficient (α) spectrum determination

The absorption coefficient α can be calculated from the equation:

$$\alpha = \frac{\ln\left(\frac{1-R}{T}\right)}{d} \tag{3.4}$$

where R and T are the reflectance and transmittance, respectively and d is the film thickness. To determine the absorption coefficient in both sub-bandgap and over-bandgap regions, ultraviolet-visible spectrophotometry (UV-Vis) and photothermal deflection spectroscopy (PDS) were combined, along with a Dektak® stylus profilometer to determine d.

In my projects, a Bruker Vertex 80v Fourier-Transform IR spectrometer at the University of Oxford with a reflection-transmission accessory was used to measure the absorption spectra. A silver mirror was used as a reflection reference, and the blank sample holder was used as a 100% transmission reference.

Compared to UV-vis, PDS can detect the absorbance in the sub-bandgap region more precisely. In PDS measurements, the sample is immersed in a fluid whose refractive index changes as temperature increases. When the incident pump beam is absorbed by the sample, the following non-radiative recombination processes will convert the energy of absorbed light into heat, then lead to a higher temperature on the sample surface. In this case, the fluid surrounding the sample will exhibit a refractive index gradient, which will cause the deflection of another probe beam grazing above the sample surface. Therefore, the relative absorbance spectrum of the sample can be obtained according to the deflected angle.

PDS measurements in my projects were taken at room temperature on a home-made setup detailed elsewhere[193]. $CuSbSe_2$ films were spin-coated on 2 mm thick circular quartz substrates with 1 cm diameter (Spectrosil® 2000). The samples were loaded into the sample holder chamber, then immersed in an inert liquid FC-72 Fluorinert™ (3M Company), which has a high thermo-optical coefficient. A monochromatic beam from a 250 W quartz tungsten halogen lamp (Newport-Oriel) integrated with a 250 mm focal length monochromator (CVI DK240) was illuminated perpendicularly to the sample surface, modulated with a mechanical chopper at a frequency of 13 Hz. A 670 nm CW diode laser beam passing through the immersive medium, parallel to the sample surface (the transverse configuration), changes its optical path synchronously with the modulating pump excitation. The probe beam deflection is detected by a quadrant photodiode, with the signal amplitude demodulated with a lock-in amplifier (Stanford Research Systems SR830). The relative absorbance spectrum measured by PDS was normalised to its highest signal value. We then mapped this maximum value of the absorbance,

found at 1.3 eV photon energy, onto the absolute absorption coefficient value obtained from UV-vis at the same photon energy. The whole absolute absorption coefficient spectrum could then be acquired.

3.3.7 Transient absorption (TA) spectroscopy

TA spectroscopy is a pump-probe technique for analysing the photo-excited states (energies and associated lifetimes) of materials. The sample is firstly irradiated by the pump pulse and photo-generated charge-carriers are excited to higher energy states, then a broadband probe pulse is applied to measure the absorption (or transmittance) change of the sample at a certain time after the pump pulse is removed (pump-probe delay). Therefore, TA spectra can record the TA signals as a function of wavelength and pump-probe delay. In my projects, TA signals were expressed as $\frac{\Delta T}{T} = \frac{T_{pump\ on} - T_{pump\ off}}{T_{pump\ off}}$, where $T_{pump\ on}$ and $T_{pump\ off}$ represent the transmission with and without the pumping, respectively.

In a typical TA spectrum, three main types of signals can be observed[194]:

i. Ground state bleaching (GSB, green in Fig. 3.3):

After the electrons in the ground state are excited to the first excited state by the pump pulse, fewer probe pulses can be absorbed as fewer electrons are left in the ground state compared to the case without the pump, which means $T_{pump\ on} > T_{pump\ off}$, so a positive $\Delta T/T$ signal can be observed in the spectrum. The energy of the GSB signal is usually close to the bandgap energy of the sample.

ii. Stimulated emission (SE, orange in Fig. 3.3):

In the case of the population of the excited state caused by the pump pulse, a photon from the probe pulse passing through the sample can induce the emission of another photon as an excited electron returns to the ground state. Since both the passing probe and the stimulated emission can be detected, a positive $\Delta T/T$ signal can be monitored.

iii. Photo-induced absorption (PIA, blue in Fig. 3.3):

Some electrons excited to the first excited state can be further excited to higher excited states by the pulse pump, which could not happen before the electrons in the ground state get excited by the pump. Thus, a negative $\Delta T/T$ signal will be observed. The energies of PIA signals depend on the energy difference between the first and higher excited states, so the PIA signals might overlap with GSB signals if they have similar energies, making it challenging to distinguish different signals and their mechanisms.

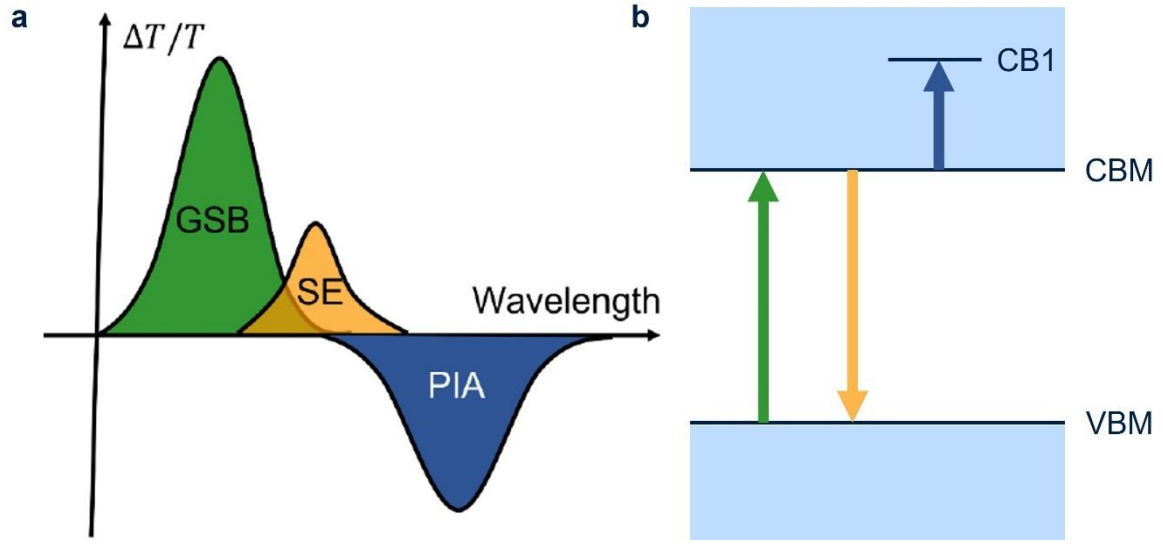

Fig. 3.3 | Typical TA signals and mechanisms. a, Contributions to a TA spectrum: ground-state bleach (green), stimulated emission (orange), and photo-induced absorption (blue). Figure courtesy of Dr. Yi-Teng Huang. **b,** Corresponding transition mechanisms represented by the

same colours. CB1 refers to the higher excited state.

In my projects, TA measurements were taken in air at room temperature at the University of Cambridge, Cambridge, UK. $CuSbSe_2$ films were spin-coated onto 1.2 × 1.2 cm^2 glass substrates. For long-time TA measurements, the third harmonic (355 nm) of an electronically controlled, Q-switched Nd:YVO_4 laser (Innolas Picolo 25) provided ~800 ps pump pulses. For short-time TA measurements, the fundamental Ti:Sapphire 800 nm wavelength laser provided ~150 fs pump pulses. Broad-band near-IR probe pulses ranging from 800 to 980 nm were provided by a noncolinear optical parametric amplifier (NOPA) setup. Probe pulses were split into two beams by a beamsplitter. The other reference beam can then be used to calibrate shot-to-shot noise coming from the NOPA setup itself. This allows very weak signals to be measured. Both the probe and reference beams were detected by a Si dual-line array detector read out by a custom-built board from Stresing Entwicklungsbüro.

3.3.8 Optical-pump-terahertz-probe (OPTP) spectroscopy

Similar to TA spectroscopy, OPTP spectroscopy also employs an optical pump to excite electrons in the ground state to excited states in the sample. However, OPTP spectroscopy utilises terahertz (THz) light instead of the visible-to-NIR light as the probe beam. THz light has a frequency of 10^{11} to 10^{13} Hz, which is close to the frequency of charge-carrier scattering in semiconductors. Therefore, THz light is suitable for analysing the properties of mobile charge-carriers. During OPTP measurements, the change in transmitted THz field amplitude

$-\Delta T/T$ is monitored. The measured $-\Delta T/T$ signal is proportional to the photoconductivity $\Delta\sigma$ of the sample according to the equation:

$$\Delta\sigma = \frac{\epsilon_0 c(n_{sub}+1)}{d}\left(-\frac{\Delta T}{T}\right) \tag{3.5}$$

where ϵ_0 is the vacuum permittivity, n_{sub} is the substrate refractive index and d is the sample thickness. Since the photoconductivity is proportional to charge-carrier mobility, which can be expressed as the following equation:

$$\Delta\sigma = \phi q \sum\mu \Delta n = \frac{\epsilon_0 c(n_{sub}+1)}{d}\left(-\frac{\Delta T}{T}\right) \tag{3.6}$$

with ϕ the photo-to-charge branching ratio, $\sum\mu$ the effective sum mobility (sum of the mobilities of electrons and holes) and Δn the photo-induced charge-carrier density. Based on equation 3.6, the measured $-\Delta T/T$ signal can provide information about the charge-carrier mobility, which is important for analysing the charge-carrier localisation.

In my first project, OPTP measurements were conducted at room temperature using a setup described in detail elsewhere (located at the University of Oxford, Oxford, UK)[27]. Briefly, an amplified Ti-Saph laser system (Spectra-Physics, Spitfire) provides 800 nm wavelength pulses of 35 fs pulse duration and 5 kHz repetition rate. Single-cycle THz radiation pulses were generated *via* the inverse spin Hall effect upon photoexcitation of a spintronic emitter with the fundamental laser output[195]. THz detection was achieved by using a fraction of the fundamental laser output to gate the THz signal by free-space electro-optic (EO) sampling with a 1 mm-thick ZnTe (110) crystal. Here, a Wollaston prism was used to separate different circularly polarized components of the gate, which were then measured by a pair of balanced photodiodes. Samples were excited by frequency-doubled 400 nm pulses, obtained by second-harmonic

generation in beta-barium-borate (BBO) crystal. During the OPTP measurements, the THz emitter, EO crystal, and samples are kept under vacuum at pressures below 10^{-1} mbar. Samples were spin-coated $CuSbSe_2$ thin films on 2 mm thick circular z-cut quartz substrates with a diameter of 1.3 cm.

3.3.9 Hall effect measurements

When an electric current flows through a material where an external magnetic field exists, the magnetic field will apply a force whose direction is perpendicular to that of the electric current to the moving charge carriers (Lorentz force). Therefore, the charge-carriers will accumulate on one side of the material and create a voltage which can balance the influence of the magnetic field. The production of this measurable voltage is called the Hall effect, as it was discovered by E. H. Hall[196]. The Hall voltage is given by

$$V_H = IB/ndq \tag{3.3}$$

where I is the current, B is the magnetic field, n is the charge-carrier density, d is the sample thickness, and q is the elementary charge.

To determine the resistivity of uniform samples, the van der Pauw technique is widely used, where thin film samples contain four very small ohmic contacts placed on the periphery[197]. After obtaining two characteristic resistances, R_A and R_B, by measuring the current and voltage from different contacts of the sample, the sheet resistance R_S can be derived through the van der Pauw equation:

$$\exp(-\pi R_A/R_S) + \exp(-\pi R_B/R_S) = 1. \quad (3.4)$$

Then the bulk resistivity can be calculated by

$$\rho = R_S d, \quad (3.5)$$

while the charge-carrier mobility can be derived from

$$\mu = |V_H|/IBR_S. \quad (3.6)$$

In my first project, samples for Hall effect measurements were prepared according to the van der Pauw method. 100 nm thick gold was evaporated onto four corners of each solution-processed $CuSbSe_2$ film sample as metal contacts (0.2 cm × 0.2 cm size). The substrate was a 1.2 × 1.2 cm^2 glass substrate. Then the gold contacts were wired to the system for measurements. Hall effect measurement at room temperature (300 K) was done in air with the Lake Shore 8400 Series at Imperial College London under a 1 T magnetic field. Ohmic check was run before the Hall effect measurements to make sure the quality of metal contacts and electric connections was good.

For Hall effect measurements at lower temperatures, the same sample geometry was used. The measurements were carried out at Université Grenoble Alpes, Grenoble, France, in a 16 T superconducting magnet with a temperature ranging from 1.3 to 300 K in a helium gas environment. The samples were mounted on the probe in the magnetic fields perpendicular to the ab-plane and glued with a GE-varnish. A combination of silver pastes and silver wires was used to make the electrical connection. After drying the pastes, it was confirmed that the contact resistances were acceptable within the order of a few ohms. The longitudinal (ρ_{xx}) and

transverse resistivity (ρ_{xy}) were obtained using the van der Pauw technique with a current amplitude of 0.1-1 mA, and an alternating frequency of 3-17 Hz with the help of SR830 digital lock-in amplifier. The perpendicular magnetic fields were swept at a rate of 0.5 T/min at a given temperature. All data were taken over a full range from -16 T to 16 T, averaged in positive and negative fields to remove a small longitudinal resistance contribution to the measured voltage, which may arise from the van der Pauw geometry, and retain only the antisymmetric voltage component due to the Hall effect.

3.4 Photovoltaic device fabrication

For photovoltaic devices based on solution-processed $CuSbSe_2$, the investigated device structures included:

ITO/compact TiO_2/$CuSbSe_2$/Spiro-OMeTAD/Au;

ITO/compact TiO_2/meso-porous TiO_2/$CuSbSe_2$/Spiro-OMeTAD/Au;

ITO/SnO_2/$CuSbSe_2$/Spiro-OMeTAD/Au;

ITO/NiO_x/$CuSbSe_2$/ZnO/Ag.

Before thin film deposition, the commercial 1.2 cm × 1.2 cm ITO substrates were cleaned by sonication in propanone and propan-2-ol for 15 min, respectively. After the sonication cleaning, the substrates were blown dry with N_2 then UV-ozone treated for 20 min. The procedure to deposit $CuSbSe_2$ thin films is described in Section 3.1.1. The methods of depositing other materials are listed below:

Compact TiO_2: 350 μL titanium(IV) isopropoxide (TTIP, 0.24 M, 99.999%, Merck) was first dissolved in 2.5 mL ethanol, then 2.5 mL solution of chlorane in absolute ethanol (prepared by adding 35 μL 2 M chlorane to 2.5 mL absolute ethanol) was added drop by drop into the TTIP solution with constant stirring. Before spin coating, the solution was filtered with a 0.2 μm PTFE filter, then 30 μL solution was spread onto the substrate, followed by spinning at 1500 rpm for 45 s (1500 rpm/s acceleration) in the fume hood. After spin coating, the sample was thermally treated on a hot plate at 150 °C for 10 min, then at 350 °C for 30 min, then at 540 °C for 1 h, then cooled to 350 °C and kept for 30 min, then cooled down overnight.

Meso-porous TiO_2: 100 μL 18NR-T Transparent Titania Paste (Greatcell Solar Materials) was spread onto ITO/compact TiO_2 substrate, followed by spinning at 4000 rpm for 10 s (2000 rpm/s acceleration) in the fume hood. After spin coating, the sample was thermally treated on a hot plate at 125 °C for 5 min, then at 325 °C for 5 min, then at 375 °C for 5 min, then at 450 °C for 30 min, then cooled down naturally.

SnO_2: the SnO_2 ETL was deposited by spin coating commercial SnO_2 colloidal dispersion (15% in H_2O, Alfa Aesar) that was diluted to 2.67% with DI water before spin coating. 30 μL diluted dispersion was spread onto the ITO substrate, followed by spinning at 3000 rpm for 30 s (3000 rpm/s acceleration) in the fume hood. After spin coating, the sample was thermally treated on a hot plate at 150 °C for 30 min, then cooled down naturally.

NiO_x: 1454 mg nickel nitrate hexahydrate (99.999%, Merck) was first dissolved in the mixture of 5 mL ethane-1,2-diol (anhydrous, 99.8%, Merck) and 334 µL ethane-1,2-diamine (for synthesis, Merck). Before spin coating, the solution was filtered with a 0.2 µm PTFE filter, then 40 µL solution was spread onto the substrate, followed by spinning at 5000 rpm for 45 s (5000 rpm/s acceleration) in the fume hood. After spin coating, the sample was thermally treated on a hot plate at 100 °C for 30 min, then at 300 °C for 1 h, then cooled down naturally and transferred into the glovebox.

Spiro-OMeTAD: the precursor solution was prepared by mixing 72 mg spiro-OMeTAD (Borun New Material), 29.8 µL tert-butylpyridine (TBP, 98%, Merck), and 17.5 µL 0.52 g/mL solution of lithium bis(trifluoromethylsyfonyl)imide salt (>98.0%, TCI) dissolved in ethanenitrile (≥99.5%, ACS reagent, Merck) with 1 mL chlorobenzene (anhydrous, 99.8%, Merck). Before spin coating, the solution was filtered with a 0.2 µm PTFE filter, then 40 µL solution was spread onto the substrate, followed by spinning at 3000 rpm for 30 s (500 rpm/s acceleration) in the glovebox. After spin coating, the sample was stored in the dry cabinet (relative humidity < 1%) overnight before further characterisation.

Au or Ag: 80 nm Au or 100 nm Ag was evaporated through a mask onto the surface of ETL or HTL, which defined the device area of 4.5 mm^2.

For photovoltaic devices based on chemical-vapour-deposited $CuSbSe_2$, the investigated device structure was ITO/ZnO/$CuSbSe_2$/Au.

The procedure to clean ITO substrates is described above. The procedure to deposit $CuSbSe_2$ thin films is described in Section 3.1.2. The methods of depositing other materials are listed below:

ZnO: 1 g zinc acetate dihydrate (99.999%, Merck) was dissolved in 10 ml 2-methoxyethanol (anhydrous, 99.8%, Merck) and 284 μL 2-aminoethanol (for synthesis, Merck) then 50 μL solution was spread onto the substrate, followed by spinning at 3000 rpm for 60 s (500 rpm/s acceleration) in the fume hood. After spin coating, the sample was thermally treated on a hot plate at 200 °C for 30 min, then the spin coating and heat treatment were repeated once again to deposit thicker films.

Au: 80 nm Au was evaporated through a mask onto the surface of ETL or HTL, which defined the device area of 4.5 mm^2.

For photovoltaic devices based on Sb_2S_3, the investigated device structure was ITO/CdS/ Sb_2S_3/spiro-OMeTAD/Au.

Before CdS deposition, the commercial 3 cm × 3 cm FTO substrates were cleaned by sonication in detergent, acetone and propan-2-ol, each for 15 min, respectively. After the sonication cleaning, the substrates were blown dry with N_2 then UV-ozone treated for 20 min. The procedure to deposit Sb_2S_3 thin films is described in Section 3.2. The methods of

depositing other materials are listed below:

CdS: CdS ETL was deposited via the CBD method. To prepare the precursor solution, 0.0925 g cadmium nitrate tetrahydrate ($Cd(NO_3)_2 \cdot 4H_2O$, 99.9%, Thermo Scientific Chemicals) was firstly dissolved in 20 mL DI water, then 25 mL ammonia solution (for analysis, 25%, Merck) and 153 mL DI water were added to the solution, then 1.1711 g thiourea (ACS reagent, ≥99.0%, Merck) was dissolved in the solution. FTO substrates were vertically immersed in the precursor solution and heated in a water bath for 13 min with continuous stirring (temperature gradually decreasing from 65 °C to 55 °C). Then the samples were taken out and rinsed with DI water then blown dry with N_2. The as-prepared CdS films were then treated by spin coating 200 µL $CdCl_2$ solution in methanol (concentration = 20 mg/mL) with the spin speed of 3000 rpm and the duration of 30 s. Afterwards, the treated CdS films were thermally treated at 400 °C for 10 min then cooled down naturally.

SnO_2: SnO_2 was used as an alternative buffer layer to compare the nucleation process of Sb_2S_3 on SnO_2 and CdS. SnO_2 was deposited using the CBD method, which was adjusted based on the method reported by Yoo *et. al.*[171]. Firstly, 330 mg $SnCl_2 \cdot 2H_2O$ (≥99.99%, Merck) was dissolved in 120 mL DI water, followed by adding 1500 mg urea (ACS reagent, 99.0-100.5%, Merck) and 30 µL sulfanylacetic acid (TGA, 98%, Merck) to the solution, then stirring for 5 minutes. Then 1500 µL chlorane (HCl, 37 wt.% in water, Merck) was added to the solution to obtain the clear precursor solution. After another 10-minute stirring, FTO substrates were vertically immersed in the precursor solution then heated in a water bath at 90 °C for 6 h, and

the deposition was stopped when the pH of the solution reached 1.5. Then the samples were taken out and rinsed with DI water then blown dry with N_2. The as-prepared SnO_2 films were then thermally treated at 170 °C for 1 h then cooled down naturally.

Spiro-OMeTAD: the precursor solution was prepared by mixing 36.6 mg spiro-OMeTAD (Borun New Material), 14.5 μL tert-butylpyridine (TBP, 98%, Merck), and 9.5 μL 0.52 g/mL solution of lithium bis(trifluoromethylsyfonyl)imide salt (>98.0%, TCI) dissolved in ethanenitrile (≥99.5%, ACS reagent, Merck) with 1 mL chlorobenzene (anhydrous, 99.8%, Merck). Before spin coating, the solution was filtered with a 0.2 μm PTFE filter, then 100 μL solution was spin-coated onto the substrate by dynamic spin coating with the spin speed of 4000 rpm, the duration of 40 s, and the acceleration of 4000 rpm/s. The solution was applied to the sample surface as fast as possible after the spin speed reached 4000 rpm. After spin coating, the sample was stored in the dry cabinet (relative humidity < 1%) overnight before further characterisation.

Au: 80 nm Au was evaporated through a mask onto the surface of ETL or HTL, which defined the device area of 0.25 cm^2 or 1 cm^2, depending on the mask geometry.

3.5 Photovoltaic device characterisation

3.5.1 J-V characterisation

$CuSbSe_2$-based photovoltaic devices:

Current density-voltage (J-V) and maximum power point measurements were conducted using a Keithley 2623A source measure unit (SMU) at Imperial College London at a scan rate of 50 mV/s in the ambient environment under AM1.5G spectrum and in the dark. The light source was a 450 W Oriel xenon lamp equipped with a Schott-K113 Tempax sunlight filter (Präzisions Glas & Optik GmbH), which provided the standard AM1.5G spectrum. Before J-V measurements, the spectrum was calibrated using a standard silicon photodiode.

Sb_2S_3-based photovoltaic devices:

Current density-voltage (J-V) and maximum power point measurements were conducted using a Keithley 2400 source meter at the University of Oxford in the ambient environment under AM1.5G spectrum and in the dark. AM1.5G spectrum was generated by a class AAA WaveLabs Sinus-220 solar simulator. The intensity of the solar simulator was set to produce 100 mW/cm^2 equivalent irradiance using a certified KG3-filtered Si reference photodiode (Fraunhofer ISE). The J-V sweeps were firstly a reverse scan (i.e., from forward bias to reverse bias), followed by a forward scan (i.e., from reverse bias to forward bias) at a scan rate of 10 mV/s. The bias ranged from -0.2 V to 0.8 V.

For indoor photovoltaic (IPV) characterisations, current-voltage (I-V) and maximum power point measurements were conducted using a Keithley 2400 source meter in the ambient environment under simulated indoor light and in the dark. The simulated indoor light was generated by a LightBox XL indoor light simulator developed by Lightricity Ltd, which

employed an 11 × 11 white LED array with the colour temperature of 3000 K as the light source. The illuminance ranged from 50 to 20000 lux, and the light intensities at 200, 500, 1000, 2000, and 20000 lux were calibrated using a III-V reference solar cell. When the illuminance was set as 1000 lux, the light intensity was 0.287 mW/cm^2. The J-V sweeps were first a forward scan, followed by a reverse scan at a scan rate of 10 mV/s. The bias ranged from -0.1 V to 0.8 V.

3.5.2 Optical loss analysis

To perform optical loss analysis on our Sb_2S_3 solar cells, external quantum efficiency (EQE) was first acquired. EQE measurements were performed using a custom-built Fourier transform photocurrent spectrometer based on a Bruker Vertex 80v Fourier Transform Interferometer. The Sb_2S_3 solar cells were illuminated with a 250 W quartz-tungsten halogen lamp. The light first passed through a monochromator (Princeton Instruments SP2150) with a filter wheel (Princeton Instruments FA2448), then was chopped with a Thorlabs MC2000B optical chopper at 280 Hz, and finally focused onto the sample with a smaller spot size than the pixel area (0.25 cm^2 defined by the metal aperture mask). The amplitude of the resulting AC current was measured with a lock-in amplifier (Stanford Research Systems SR830) as the voltage drop across a 50 Ohm resistor in series with the solar cell. Before measurements, the instrument was calibrated to a Newport-calibrated silicon reference solar cell (Thorlabs FDS100-CAL) with known external quantum efficiency.

After obtaining the EQE as a function of wavelength, $EQE(\lambda)$, the short circuit current density $J_{SC,EQE}$ can be derived via the equation:

$$J_{SC,EQE} = q \int EQE(\lambda)S(\lambda)d\lambda\,, \tag{3.7}$$

where q is the elementary charge and $S(\lambda)$ is the spectral response. The $J_{SC,EQE}$ value is expected to be close to the short circuit current density J_{SC} measured by the J-V characterisation. By replacing $EQE\,(\lambda)$ with other optical absorption curves, different theoretical limits of the current density of Sb_2S_3 solar cells can be analysed as below:

If assuming all generated charge-carriers in Sb_2S_3 can be collected, the current density limit $J_{SC,coll}$ is given by

$$J_{SC,coll} = q \int A(\lambda)S(\lambda)d\lambda\,, \tag{3.8}$$

where $A(\lambda)$ represents the absorptance of Sb_2S_3. Thus, the optical loss due to uncollected charge-carriers after the photons are absorbed by Sb_2S_3, J_{uncoll}, can be calculated by

$$J_{uncoll} = J_{SC,coll} - J_{SC,EQE}. \tag{3.9}$$

If assuming all photons arriving at Sb_2S_3 can be absorbed and all generated charge-carriers can be collected, the current density limit $J_{SC,abs}$ is given by

$$J_{SC,abs} = q \int (1 - A_{window}(\lambda))S(\lambda)d\lambda\,, \tag{3.10}$$

where $A_{window}(\lambda)$ represents the absorptance of the window layer (FTO/CdS). Thus, the optical loss due to photons which reach Sb_2S_3 but are not absorbed, J_{unabs}, can be calculated by

$$J_{unabs} = J_{SC,abs} - J_{SC,coll}. \tag{3.11}$$

Furthermore, if the reflection of the glass side of the device is the only mechanism of optical

loss, the theoretical limit of short circuit current density is given by

$$J_{SC,R} = q \int \left(1 - R_{device}(\lambda)\right) S(\lambda) d\lambda \,, \tag{3.12}$$

where $R_{device}(\lambda)$ is the reflection of the complete device. In this case, the optical loss caused by the parasitic absorption of the window layer can be calculated by

$$J_{window} = J_{SC,R} - J_{SC,abs}, \tag{3.13}$$

while the loss due to device reflection is given by

$$J_{loss,R} = q \int R_{device}(\lambda) S(\lambda) d\lambda \,. \tag{3.14}$$

3.6 Density functional theory (DFT) calculation

Density functional theory (DFT) is widely used for ab initio calculations of crystal structures, electronic characteristics and charge-carrier-lattice interactions within lattices, and various molecular or atomic systems. In a system containing *N* (valence) electrons, the many-body Schrödinger's equation is given by

$$\hat{H}\varphi = \left[\hat{T} + \hat{V} + \hat{U}\right]\varphi = \left[\sum_{i=1}^{N}\left(-\frac{\hbar^2}{2m_i}\nabla^2\right) + \sum_{i=1}^{N} V(r_i) + \sum_{i<j}^{N} U(r_i, r_j)\right]\varphi \tag{3.15}$$

where $\hat{H}$, $\hat{T}$, $\hat{V}$ and $\hat{U}$ is the operator of Hamiltonian, kinetic energy, external potential energy, and electron-electron correlation energy, respectively. m_i is the effective mass of the i^{th} electron. $\hat{V}$ in a crystal system is often treated as a potential built up by the fixed and positively charged nuclei, which is independent of the motion of surrounding electrons. When *N* is large, the computational costs for solving the many-body Schrödinger's equation will be extremely high. According to the Hohenberg-Kohn theorems[198], φ can be regarded as a functional of the position-dependent electron density $n(\boldsymbol{r})$. In this case, the 6*N*-dimensional

wavefunction φ can be simplified to a 3-dimensional problem, so the computational costs are significantly lower. With such simplification, solving DFT calculations will be used to search for the minimum of the system energy $E[n(\boldsymbol{r})]$ as

$$E[n(\boldsymbol{r})] = T[n(\boldsymbol{r})] + U[n(\boldsymbol{r})] + \int d^3\boldsymbol{r}V(\boldsymbol{r})n(\boldsymbol{r}) \quad (3.16)$$

where $V(\boldsymbol{r})$ is the potential distribution for the system, and the functional $T[n(\boldsymbol{r})] + U[n(\boldsymbol{r})]$ can be approximated by the Kohn-Sham equations[199].

In Chapter 4, crystal, electronic, and phonon structures were computed within the Kohn-Sham density functional theory (KS-DFT) framework[199], employing the projector augmented wave (PAW) method[200] as implemented in the Vienna ab initio Simulation Package (VASP)[201]. Calculations of the structural relaxation and deformation potentials were performed using the hybrid functional of Heyd, Scuseria, and Ernzerhof (HSE06)[202] hybrid functional using a 4 × 6 × 2 Γ-centred grid and a plane wave cut-off of 300 eV. The band structure between high-symmetry points was interpolated from a densely sampled, uniform band structure calculation performed using the zero-weighted **k**-point method on a weighted 4 × 6 × 2 grid. The dielectric function was computed within the single-particle approximation using the linear optics routine developed by Gajdos *et al.*, implemented in VASP (LOPTICS = .TRUE.)[200,201,203,204]. Convergence of the dielectric function to one decimal place was achieved by increasing the number of bands (NBANDS) to 204. The projection from plane waves to an orbital basis, along with subsequent COHP[205] analysis, was performed using the postprocessing, analysis, and plotting tools Lobster[206-208] and LobsterPy[209]. Sumo[210] was used to plot the DOS. Gaussian broadening of 0.12 eV was applied to both COHPs and DOS. Deformation potential

calculations were performed using the method developed by Wei and Zunger[20,211,212], with deformed structures generated and analysed using the ab initio scattering and transport (AMSET) package[21]. The finite displacement method[213] within the harmonic approximation was used to calculate the phonon band structure, as implemented in Phonopy using a displacement of 0.15 Å[214,215], where the r^{2}SCAN meta-GGA functional was employed[216]. Before conducting supercell calculations, the r^{2}SCAN functional was employed for a structural optimisation on a 6 × 8 × 2 Γ-centred grid with a plane wave cut-off of 500 eV. Force constants were calculated using 3 × 4 × 1 supercells over a commensurate 2 × 2 × 1 **k**-point grid. Phonon band structure and DOS plots were generated using the ThermoParser[217] utility. The static dielectric constants and Born effective charges (BECs) were determined through density functional perturbation theory (DFPT) (IBRION = 8, LEPSILON = .TRUE.), using the Perdew–Burke–Ernzerhof (PBE) functional[218], with a plane wave cut-off of 300 eV and an 8 × 14 × 3 **k**-point grid at a single *q*-point (Γ).

The ShakeNBreak method and package[219,220] were used to search for low-energy bulk polarons. A 64-atom supercell was employed for spin-polarised calculations (ISPIN = 2) with an unpaired electron or hole. Local distortions of ±30% and 0% were applied to atomic sites, followed by a stochastic rattle of all atoms in the cell with a standard deviation of 0.25 Å. An undistorted supercell was also evaluated. For holes, distortions were trialled centred on Cu, Se1, and Se2, while for electrons, distortions centred on Sb were investigated. Distorted supercells were relaxed using the Γ-point approximation in the Γ-only version of VASP. Energy data was visualised using ShakeNBreak tools.

Chapter 4: Rationalising band-like transport in $CuSbSe_2$

Heavy pnictogen-based inorganic semiconductors have emerged as promising nontoxic and stable alternatives to lead-halide perovskites for photovoltaic applications. However, a common problem that has been prevalently found in these families of compounds is charge-carrier localisation, which can significantly reduce the charge-carrier mobility and diffusion length. In this study, $CuSbSe_2$ is demonstrated to exhibit delocalised charge-carriers, experimentally proved by optical pump terahertz probe spectroscopy and temperature-dependent mobility measurements. Through combined experimental and theoretical analysis, three key factors enabling this behaviour are identified: (1) the layered structure, which accommodates acoustic wave-induced distortions within interlayer gaps, minimizing changes in bond length and reducing acoustic deformation potentials; (2) quasi-bonding interactions across the interlayer gap, leading to the higher electronic dimensionality; and (3) Born effective charges not being anomalously high, along with a small bandgap (≤1.2 eV), which lower the ionic contribution to the dielectric constant, thus reduce Fröhlich coupling strength. These findings provide valuable insights for the future exploration of perovskite-inspired materials with delocalised charge-carriers.

This chapter is adapted from my published paper "Fu, Y., Lohan, H., Righetto, M. *et al.* Structural and electronic features enabling delocalized charge-carriers in $CuSbSe_2$. *Nat Commun* **16**, 65 (2025)" with permission. Open access, CC-BY 4.0.

The contributions from other researchers include:

Hugh Lohan performed the density functional theory calculations and collected the data. Mark Isaacs performed the X-ray photoelectron spectroscopy and collected the data. Robert Jacobs performed the Fourier transform infrared spectroscopy and collected the data. Marcello Righetto performed the optical pump terahertz probe spectroscopy and UV-vis spectroscopy measurements and Elliott model fit and collected the data. Yi-Teng Huang performed transient absorption spectroscopy and collected the data. Chang-Woo Cho performed low-temperature Hall effect measurements and collected the data. Szymon J. Zelewski performed photothermal deflection spectroscopy measurements and collected the data. Yuchen Fu performed all other synthesis and measurements and analysed all data included in the chapter.

4.1 Introduction

To overcome the toxicity and stability limitations of LHPs, as well as replicating their ability to tolerate defects, heavy pnictogen-based (Sb^{3+}- and Bi^{3+}-based) semiconductors have received increasing interest[9,61,81,221-223]. However, even though early studies found some Bi-based materials to exhibit even longer lifetimes than LHPs[96,224-226], the performance of the PV devices based on these materials was far below the expectation[227]. Recently, it has been revealed that the long lifetimes are caused by charge-carrier localisation, resulting in reduced mobilities and diffusion lengths[14,18,96]. The prevalent observation of charge-carrier localisation in Bi-based semiconductors indicates that future exploration of pnictogen-based PIMs requires understanding how to avoid this limitation in these materials. Inspired by the recently

discovered band-like transport in BiOI[101,100], I studied a similar layered Sb-based semiconductor, $CuSbSe_2$. Via a novel thiol-amine-based solution processing route, phase-pure $CuSbSe_2$ thin films were achieved. The structural and vibrational properties were investigated through XRD and Raman and infrared (IR) spectroscopy. Then the properties of photo excitations in $CuSbSe_2$ were studied with spectroscopic tools (UV-vis, TA and OPTP spectroscopy). Along with temperature-dependent mobility measurements, it was confirmed that this material could avoid charge-carrier localisation. Furthermore, the strength of coupling with different types of phonons, as well as the key properties influencing the strength, were investigated through calculations to reveal the underlying mechanisms of the delocalised charge-carriers in $CuSbSe_2$. By understanding the factors leading to the absence of charge-carrier localisation in $CuSbSe_2$, the insights into designing novel heavy pnictogen-based semiconductors with band-like transport can be gained, which is important for the future development of promising lead-free solar absorbers.

4.2 Structural and vibrational properties of $CuSbSe_2$

As shown in Fig. 4.1a, $CuSbSe_2$ has a layered crystal structure, similar to chalcostibites (*Pnma* space group)[228,229]. The $CuSbSe_2$ layers are held together by *van der Waals* interactions. The bonding environments of the Sb and Cu atoms are illustrated in Fig. 4.1 as well. Each Sb atom is bonded to three Se atoms, forming a trigonal pyramidal geometry, while each Cu atom is bonded to four Se atoms as a tetrahedron. The $CuSe_4$ tetrahedra and $SbSe_3$ trigonal pyramids share corners (of Se). The Sb and Se atoms separated by the interlayer gap (distance = 3.26 Å)

are too far to form full covalent bonds. Previous studies on $CuSbS_2$ and Sb_2Se_3 have reported the stereochemical activities of the $5s^2$ lone pair on Sb^{3+} in these materials[103-107], indicating that the orbital energy levels of the Sb 5*s* and chalcogen 3*p* or 4*p* states are close enough in energy to interact. The crystal structure of $CuSbSe_2$ shows that the Sb 5s lone pair in this material is also stereochemically active, leading to a second-order Jahn-Teller distortion[106].

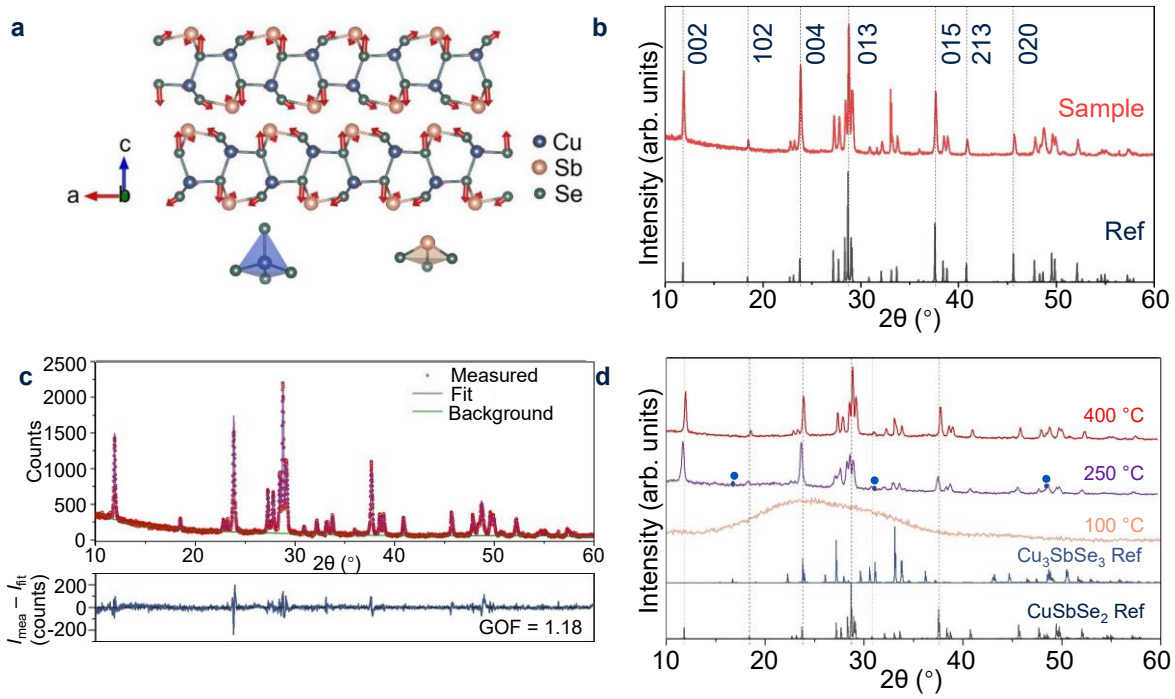

Fig. 4.1 | Structural properties of $CuSbSe_2$. a, Crystal structure of $CuSbSe_2$, viewed along the *b* axis, and with the dominant A_g Raman mode shown in red arrows. The bonding environments of Cu and Sb are illustrated below the crystal structure. **b,** X-ray diffraction (XRD) pattern of solution-processed thin films compared with the reference pattern of $CuSbSe_2$ (ICSD database, ID 418754. The Miller indices of the dominant peaks are indicated. **c,** Pawley fit of the XRD pattern shown in Fig. 4.1b. The goodness of fit (GOF) is given, along with the residuals (blue), measured data points (red), fit (purple) and background (green). Please note

that a profile fit was fit made to the measured pattern, and the silicon substrate peaks were removed in order to understand how well the reference pattern matches with the diffraction pattern from the thin film itself. Without removing these silicon substrate peaks, the GOF from Pawley fitting is 1.58, and the residuals are dominated by the silicon substrate peaks not fit. **d,** Comparison of the XRD patterns of films thermally treated at 400 ℃ for 2 min (red), 250 ℃ for 10 min (purple) and 100 ℃ for 10 min (pink) with the $CuSbSe_2$ reference pattern (black, ICSD database, coll. code 418754) and Cu_3SbSe_3 reference pattern (blue, ICSD database, coll. code 401095). The three XRD patterns were taken by the Bruker D2 Phaser system.

Since $CuSbSe_2$ is a promising solar absorber, different techniques have been employed to grow this material. However, these techniques all have some limitations, such as requiring vacuum-based equipment (*e.g.*, sputter deposition[117], close-space sublimation[118]) or long reaction times (*e.g.*, fusion method[119] or selenization of metal precursors[120]), or the use of toxic precursors (*e.g.*, hydrazine-based solution processing[112,121]). Among these methods, solution processing requires less expensive equipment[122,230,231], but the use of highly toxic hydrazine solvent is still a concern[232]. Inspired by the recent success of a more benign solvent system than hydrazine, a thiol-amine mixture, in dissolving chalcogenide precursors and depositing solar absorbers such as $Cu_2ZnSn(S, Se)_4$[157,233], $Cu(In, Ga)Se_2$[158,160] and $CuIn(S, Se)_2$[234], I develop this novel thiol-amine-based solution processing route to successfully deposit phase-pure $CuSbSe_2$ thin films for the first time, as detailed in Section 3.1.1. As shown in Fig. 4.1b, the XRD pattern of my $CuSbSe_2$ thin films matched with the reference pattern for $CuSbSe_2$ (ICSD database, coll. code 418754), indicating that phase-pure $CuSbSe_2$ thin films were obtained. The thickness of the

phase-pure $CuSbSe_2$ thin film was 520±10 nm, measured by a Dektak® stylus profilometer. Details of Pawley fitting of the XRD pattern are shown in Fig. 4.1c. After excluding the two silicon substrate peaks, all other measured peaks can match the reference pattern, and the residuals are featureless. Along with a goodness of fit (GOF) of 1.18, the Pawley fitting further confirms my $CuSbSe_2$ thin films to be phase-pure.

The effect of heat treatment temperature on the phase purity of solution-processed $CuSbSe_2$ thin films was also investigated, as shown in Fig. 4.1d. After being thermally treated in a N_2-filled glovebox at 100 ℃ for 10 min, the spin-coated $CuSbSe_2$ thin films showed an XRD pattern with no clear, sharp peaks, indicating amorphous films. When the heat treatment temperature was increased to 250 ℃ (also for 10 min), the measure XRD pattern had sharp peaks and most of them matched with the $CuSbSe_2$ reference pattern, but some minor peaks belonging to Cu_3SbSe_3 (ICSD database, coll. code 401095) also existed and marked by blue dots (2θ = 16.70°, 31.10° and 48.53°) in Fig. 4.1d. Finally, to remove the Cu_3SbSe_3 impurity phase, the $CuSbSe_2$ thin films were firstly dried at 100 ℃ for 2 min in a N_2-filled glovebox, then thermally treated at 400 ℃ for 2 min in an Ar-filled tube furnace. The XRD patterns of phase-pure $CuSbSe_2$ thin films measured by different X-ray diffractometers are shown in Fig. 4.1b and d, respectively.

To analyse the preferred orientation of the phase-pure $CuSbSe_2$ thin film, I calculated the texture coefficients of the main peaks. The texture coefficient of crystal plane hkl (TC_{hkl}) can be calculated using the equation[235]:

$$TC_{hkl} = \frac{\frac{I(hkl)}{I_0(hkl)}}{\frac{1}{N}\sum_{i=1}^{N}\frac{I(h_i k_i l_i)}{I_0(h_i k_i l_i)}} \quad (4.1)$$

where $I(h_i k_i l_i)$ is the measured peak intensity of the $h_i k_i l_i$ plane while $I_0(hkl)$ represents the standard peak intensity of the corresponding plane, and N is the number of peaks considered. In my calculations, the standard peak intensity was obtained from the reference pattern from the ICSD database, with crystal planes 002, 004, 013 and 015 analysed. As Table 4.1 shows, the texture coefficients of planes 002 and 004 are higher than 1, indicating that the solution-processed $CuSbSe_2$ films preferred the orientation along the *c*-axis. As stated in Section 3.3.1, while no additional tilt or height alignment was applied, the use of optical alignment, surface levelling, and standard measurement routines ensures reproducibility of peak positions and relative peak intensities. Texture coefficients reported here are intended for comparative analysis between different crystal planes, rather than for absolute quantification of preferred orientation.

Table 4.1 | Texture coefficients of crystal planes in solution-processed $CuSbSe_2$ thin film.

Crystal plane	Texture coefficient
002	1.93±0.03
004	1.30±0.07
013	0.37±0.02
015	0.40±0.08

Moreover, I also investigated the structural and chemical stability of the $CuSbSe_2$ thin films since it is important for solar absorbers to be stable in diverse environments. To examine the

structural stability in the ambient environment, XRD patterns of the as-prepared (as described in Section 3.1.1) and aged samples were obtained. As shown in Fig. 4.2a, after stored in the ambient environment (room temperature and approximately 80% relative humidity) for 3 weeks, the XRD pattern of the $CuSbSe_2$ thin films remained unchanged, indicating the ideal structural stability of $CuSbSe_2$ in the ambient environment. Another test of the structural stability of $CuSbSe_2$ thin films was carried out under 1-sun illumination at 85 °C and 85% relative humidity, as detailed in the reference[236]. After kept under such conditions for 3, 8 and 24 hours, the macroscopic appearance and XRD patterns of the $CuSbSe_2$ thin films were compared in Fig. 4.2b. The unchanged appearance and XRD patterns prove better structural stability of $CuSbSe_2$ under these conditions than triple-cation perovskite thin films, which began showing degradation products after only 8 h[236].

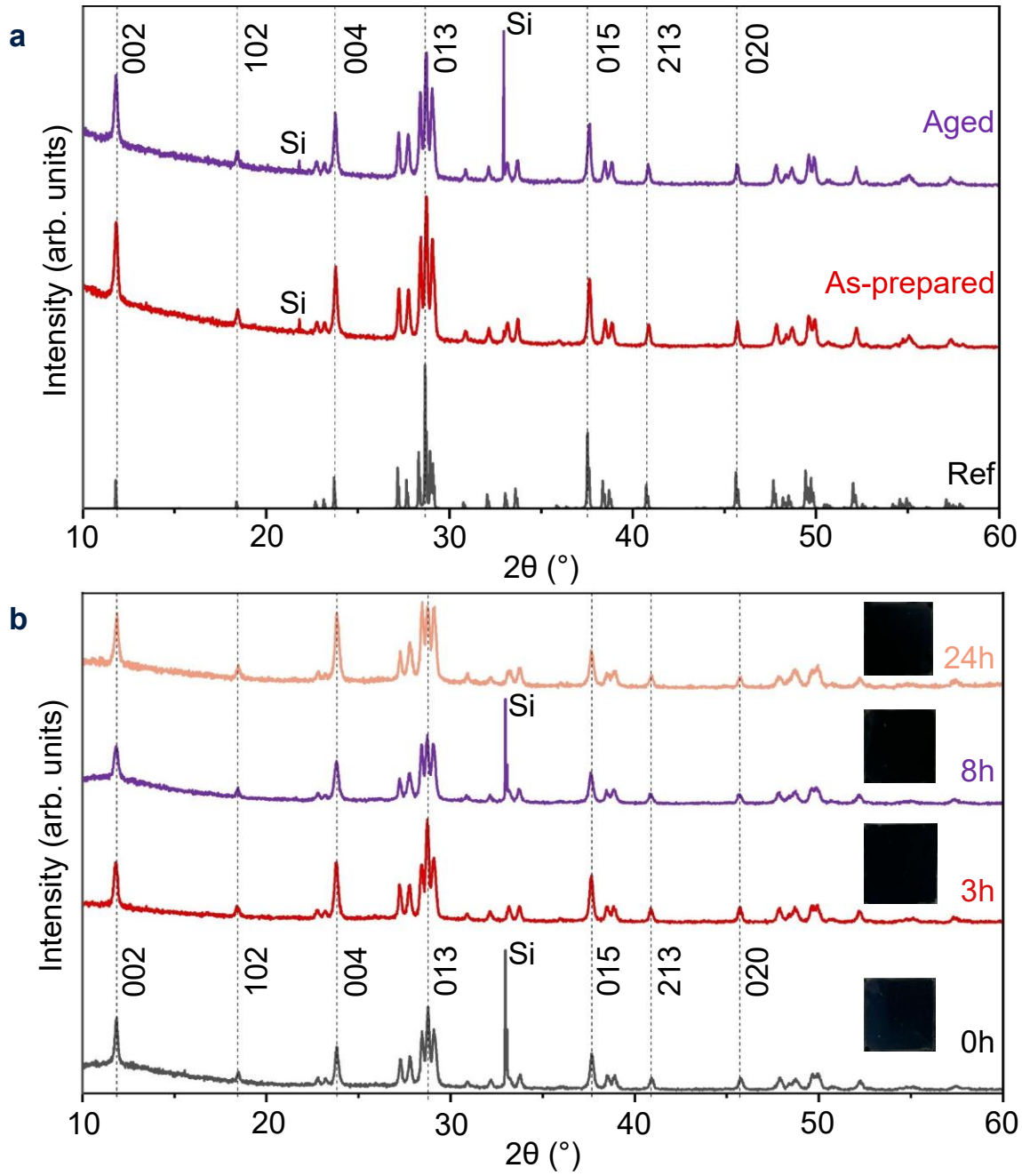

Fig. 4.2 | Phase stability of $CuSbSe_2$ thin films in diverse environments. a, XRD patterns of as-prepared (red) and aged $CuSbSe_2$ films (stored in ambient environment for 3 weeks, purple) with the $CuSbSe_2$ reference pattern (black, ICSD database, coll. code 418754). Main peaks are indicated by dashed lines along with the corresponding Miller indices. **b,** Evolution of the appearance and XRD patterns of $CuSbSe_2$ thin films under 1-sun illumination, at 85 °C and 85% relative humidity over 24 h. Main peaks are indicated by dashed lines along with the

corresponding Miller indices.

Considering that $CuSbSe_2$ contains Cu in the +1 oxidation state, which is typically less thermodynamically stable than the Cu +2 oxidation state under ambient conditions, it is worth checking the chemical stability of the cation species in the $CuSbSe_2$ films. Therefore, XPS measurements were conducted on the as-prepared and aged samples, and the results are illustrated in Fig. 4.3. After ageing in the ambient environment for 3 weeks, some peaks in the XPS survey spectra showed different intensities, but the peak positions and overall spectra were not significantly changed (Fig. 4.3a and b).

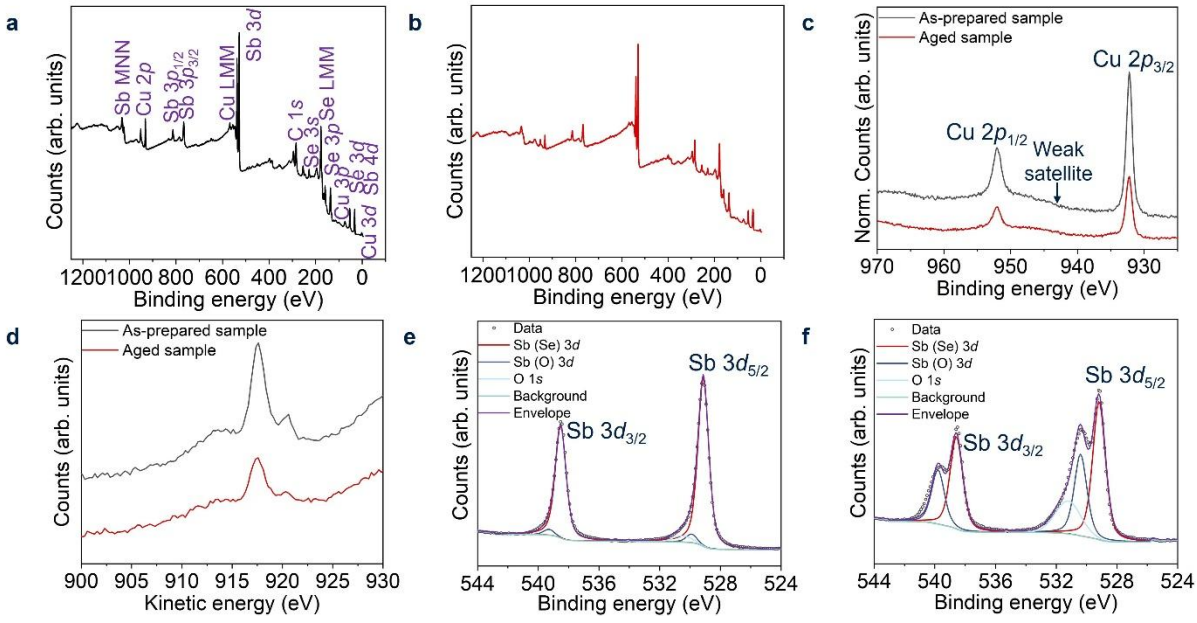

Fig. 4.3 | Chemical stability of $CuSbSe_2$ thin films in ambient environment. XPS survey spectra of **a,** as-prepared $CuSbSe_2$ thin films and **b,** aged $CuSbSe_2$ thin films. **c,** Cu 2*p* core levels and **d,** Cu $L_3M_{4,5}M_{4,5}$ Auger-Meitner spectra of as-prepared (black line) and aged $CuSbSe_2$ samples (red line). Spectra in Fig. 4.3c are normalised to the respective areas of the

Cu 2$p_{3/2}$ peak of the aged sample. Sb 3*d* core levels spectra and fitting of **e,** as-prepared $CuSbSe_2$ thin films and **f,** aged $CuSbSe_2$ thin films.

To analyse the oxidation states and bonding environments of the Cu^+ in $CuSbSe_2$ more precisely, the Cu 2*p* core levels and Cu $L_3M_{4,5}M_{4,5}$ Auger-Meitner spectra were obtained (Fig. 4.3c and d). After 3-week ageing, no obvious difference in the Cu 2*p* core levels and Cu $L_3M_{4,5}M_{4,5}$ Auger-Meitner spectra of the as-prepared and aged samples can be observed. Meanwhile, the satellite signal in the Cu 2*p* spectra is usually used to distinguish different oxidation states of Cu[237-240]. As indicated in Fig. 4.3c, the spectra of both as-prepared and aged samples exhibit weak satellite signals, which means that Cu remains in the +1 oxidation state after ageing. Also, as Fig. 4.3d shows, the Cu $L_3M_{4,5}M_{4,5}$ Auger-Meitner spectra of both as-prepared and aged samples were similar to the spectra of other Cu(I) species in different compounds[241]. The fitting of the peak gave a kinetic energy of 917.7±0.2 eV, close to the reported kinetic energy of Cu $L_3M_{4,5}M_{4,5}$ peaks in Cu_2Se (917.5 eV) and CuAgSe (917.6 eV)[186]. These results prove that the Cu(I) species in $CuSbSe_2$ can remain their oxidation states and bonding environments in the ambient environment over time.

Fig. 4.3e and f show the Sb 3*d* core level spectra. A doublet with binding energies 538.5 eV ($3d_{3/2}$, red line) and 529.1 eV ($3d_{5/2}$, red line) can be observed in each spectrum. These binding energies are consistent with the reported values of Sb(III)[242]. Similar Sb 3*d* doublets were also reported for $CuSbSe_2$ grown by close-space sublimation and hot injection[118,243].

Using the fitting methods stated in Section 3.3.2, we also found that the Sb 3*d* spectra for both the fresh and aged samples could be deconvoluted into the peaks of Sb bonded to Se (main peak, red line) and O (purple line). After aged in ambient air for 3 weeks, the Sb–O peak exhibited increased size. A more intense O 1*s* peak also appeared in the Sb 3*d* spectra for the aged samples, indicating the formation of Sb–O species at the surface of the $CuSbSe_2$ film. The Sb-O species in the Sb $3d_{3/2}$ peak has a binding energy of 539.6 eV, which is closer to the Sb $3d_{3/2}$ peak reported for Sb_2O_3 (539.8 eV) than for Sb_2O_5 (540.4 eV)[244]. This comparison confirms that the Sb species in the $CuSbSe_2$ films can remain in the +3 oxidation state in the ambient environment, with Sb_2O_3 forming on the film surface.

Finally, Raman and Fourier transform infrared (FTIR) spectroscopy were employed to detect the dominant optical phonon modes present in $CuSbSe_2$. For the *Pnma* space group (D_{2h}^{16}), there are four Raman active mode symmetries (A_g, B_{1g}, B_{2g}, and B_{3g}), along with three IR active mode symmetries (B_{1u}, B_{2u}, and B_{3u})[112,245]. Three obvious peaks at 105.7±0.2 cm^{-1} (A_g), 141.7±0.6 cm^{-1} (B_{3g}), and 213.7±0.2 cm^{-1} (A_g) can be observed in the Raman spectrum of spin-coated $CuSbSe_2$ thin film (Fig. 4.4a), and all of them have been reported in previous studies assigning them to the příbramite phase of $CuSbSe_2$[117,246-248]. Our calculated phonon spectrum for $CuSbSe_2$ also found phonon modes at similar positions (Fig. 4.4d and Table 4.2). The measured FTIR spectrum showed two relatively strong peaks positioned at 182.8 ± 0.2 cm^{-1} and 223.1±0.1 cm^{-1} (Fig. 4.4b). While no FTIR spectrum of $CuSbSe_2$ has been reported yet, according to our calculations, these two peaks can be assigned to the B_{2u} and B_{3u} modes based on their energies, respectively. These Raman and FTIR measurements agree with the previous

analysis of the phase purity of $CuSbSe_2$ thin films based on XRD measurements.

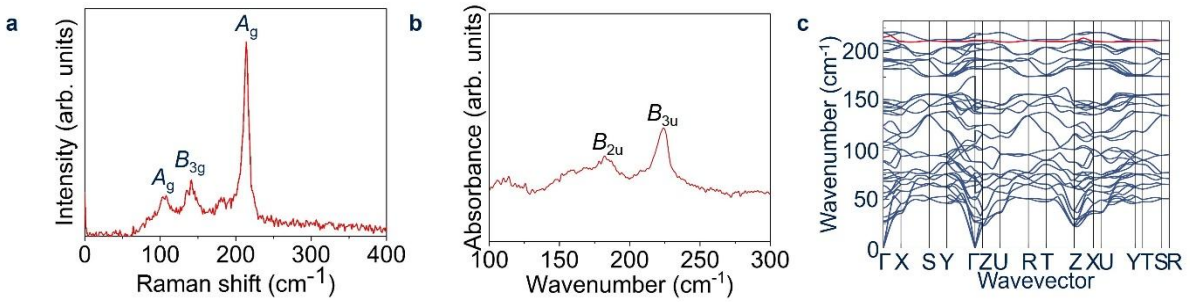

Fig. 4.4 | Vibrational properties of solution-processed $CuSbSe_2$ thin films. a, Raman spectrum (average of 10 scans) and **b,** FTIR spectrum of spin-coated $CuSbSe_2$ thin film with phonon modes of the most intense peaks labelled. **c,** Phonon dispersion curve of $CuSbSe_2$. The band containing the dominant A_g mode is highlighted in red.

Table 4.2 | Calculated symmetry operations and wavenumbers of all phonon modes of $CuSbSe_2$ excluding B_{1u}, B_{2u}, and B_{3u} translational modes. Phonon modes observed in Raman and FTIR measurements are highlighted in bold.

	Symmetry	Wavenumber (cm^{-1})			
Raman active	A_g	49.5	63.9	88.3	**104.4**
		152.0	185.6	209.2	**212.9**
	B_{1g}	27.7	76.8	149.3	192.2
	B_{2g}	52.4	68.5	103.2	125.5
		145.1	194.4	202.1	211.7
	B_{3g}	31.9	71.8	**137.8**	192.6
IR active	B_{1u}	41.2	108.9	123.2	143.4
		191.4	201.6	215.9	
	B_{2u}	56.6	141.1	**183.0**	
	B_{3u}	79.4	88.4	106.4	147.5
		185.7	208.2	**220.1**	
Inactive	A_u	26.4	70.8	139.6	183.7

It should also be noted that a Raman peak with much higher intensity than other peaks can be observed in the spectrum (Fig. 4.4a). Based on reported results and our calculations, this dominant peak at $\approx$213 cm^{-1} was found to be an A_g mode, of which the band is highlighted in red in our calculated phonon dispersion curve (Fig. 4.4c). The calculated wavenumber was 213.7$\pm$0.2 cm^{-1}, consistent with the measured result. Also, our calculations found this phonon

mode to be an intra-layer breathing mode, and the vibrations associated with this mode are illustrated by the red arrows in Fig. 4.1a.

4.3 Optoelectronic properties of $CuSbSe_2$

4.3.1 Absorption coefficient measurement

For solar absorbers, a high absorption coefficient is a critical property. Meanwhile, by analysing the absorption coefficient curve, insights into the nature of the excitations in materials can be gained. By combining photothermal deflection spectroscopy (PDS) measurements for photon energies below 1.3 eV, and UV-visible (UV-vis) spectrophotometry measurements for photon energies above 1.3 eV, the absorption coefficient curve of $CuSbSe_2$ thin film was established as shown in Fig. 4.5a (detailed methods in Section 3.3.6). Since PDS is more suitable for detecting absorption at the sub-bandgap region, while UV-vis can provide the absolute absorption coefficients, combining these two techniques can allow us to determine the absolute absorption coefficients within both sub- and above-bandgap regions. It can be seen that $CuSbSe_2$ exhibits the optical absorption coefficients around 8×10^{-4} cm^{-1} at around 1.4 eV, enabling it to absorb most of the AM 1.5G spectrum within a thin film, which is promising for photovoltaic applications.

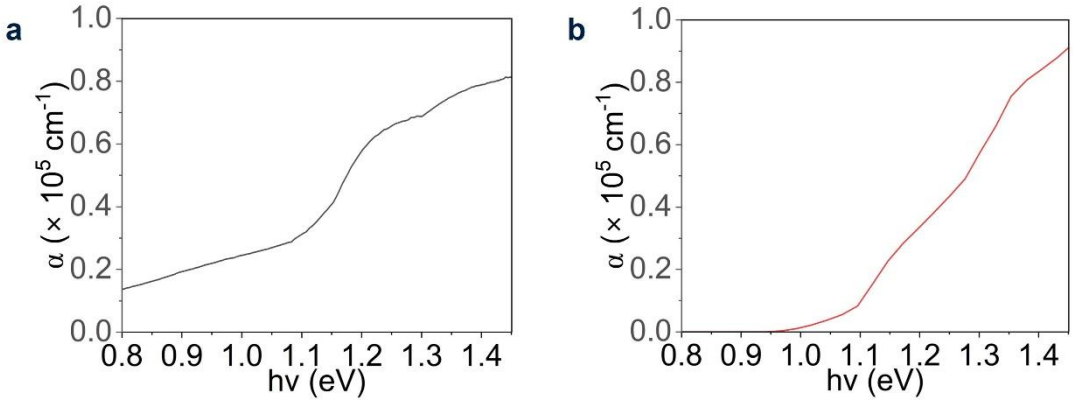

Fig. 4.5 | Optical absorption coefficient curves of $CuSbSe_2$. The curves were determined by **a,** experiments and **b,** calculations.

In literature, $CuSbSe_2$ has experimentally- and computationally-determined bandgaps in the range of 0.9–1.2 eV[108-110,112], while our calculation indicates an indirect bandgap of 1.16 eV. Meanwhile, it has been reported that the energy of the first direct transition of $CuSbSe_2$ is close to its indirect bandgap (0.09 – 0.11 eV)[111,113], which explains its high optical absorption coefficient. Besides, it is worth noting that the absorption spectrum shows a shoulder at approximately 1.4 eV, which can be caused by either the formation of excitons or the density of states in $CuSbSe_2$. Since whether the excitons can form in these materials is important for understanding the charge-carrier kinetics, it is necessary to confirm the cause of the shoulder in the absorption spectrum. Therefore, we calculated the absorption coefficient curve of $CuSbSe_2$ from the frequency-dependent dielectric tensor using hybrid DFT (HSE06 functional)[202], as Fig. 4.5b shows. A similar shoulder is also observed in the calculated absorption coefficient curve. Since our calculations were carried out in the independent particle approximation[249], phonon-assisted transitions and polaronic/excitonic effects were not

considered. Thus, the shoulder observed in both absorption coefficient spectra is believed to arise because of the electronic structure of $CuSbSe_2$.

To better understand the nature of excitations in $CuSbSe_2$, the optical absorbance curve of $CuSbSe_2$ was fitted based on Elliott's theory[29], following a previously-reported procedure[250]. As the black solid and red dashed line in Fig. 4.6a show, the fit matches the measured spectrum well, despite a significant lineshape broadening ($\Gamma \sim 90$ meV). Meanwhile, the deconvolution of the excitonic and continuum contributions gives a weak and broad excitonic contribution (purple area in Fig. 4.6a), along with a low exciton binding energy (E_b) of 9 ± 4 meV. This fit is close to the value obtained from our DFT calculations using the Wannier-Mott hydrogenic model[251], 8.7 meV. Given that these E_b values are well below kT at room temperature (26 meV), the excitations in $CuSbSe_2$ are expected to be predominantly free charge-carriers rather than bound excitons.

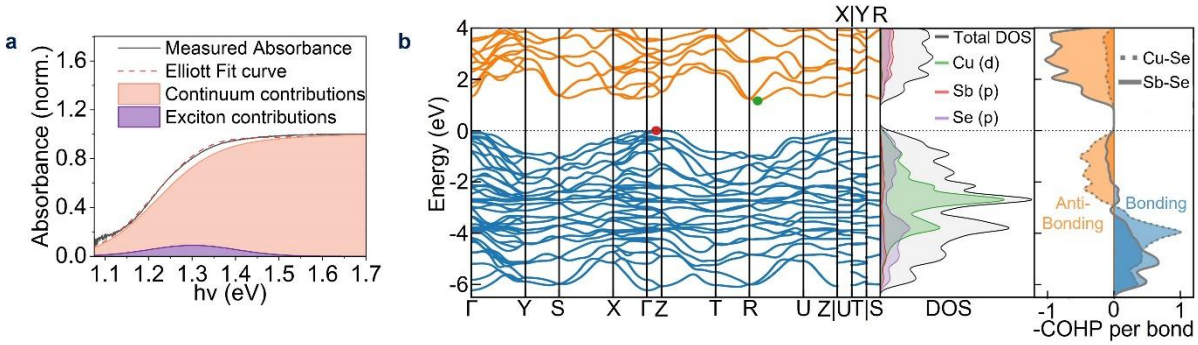

Fig. 4.6 | Optical and electronic properties of $CuSbSe_2$. a, Comparison between the measured optical absorbance curve (black solid line) and fit with the Elliott model (red dashed line). The contributions from the exciton and continuum to the optical absorption spectrum are represented by the areas shaded purple and pink, respectively. **b,** Electronic band structure of

$CuSbSe_2$ (left panel; the highest occupied state set to 0 eV), along with electronic density of states curves (middle panel), and crystal orbital Hamilton population (COHP) diagram (right panel). The bonding and anti-bonding interactions are represented by blue and orange, respectively.

The electronic structure of $CuSbSe_2$ is presented in Fig. 4.6b. From the electronic band diagram (left panel), it can be seen that the lowest bandgap is indirect with a value of 1.17 eV, which is consistent with the less steep absorption onsets in the optical absorbance spectra. The middle panel of Fig. 4.6b illustrates the electronic density of states (DoS) curves of $CuSbSe_2$, with contributions from different orbitals. It can be seen that VB mainly consists of Cu(d)-Se(p) interactions, while CB is mainly from Sb(s, p)-Se(p) interactions.

4.3.2 Short-time and long-time TA measurements

Short-time and long-time transient absorption (TA) measurements were conducted to understand the kinetics of the free charge-carriers in $CuSbSe_2$. In short-time TA measurements, an 800nm wavelength laser pulse was used to excite the sample. After excitation, a broadband near-IR probe pulse was employed to detect the relative change in transmittance ($\Delta T/T$) of the sample with the pump-probe delays from 1 to 1000 ps. As introduced in Section 3.3.7, the positive ground state bleach (GSB) signal describes the transition from ground state to the first excited state. Therefore, the decay in the GSB signal can be used to analyse the depopulation process near the band edges. Meanwhile, negative photo-induced absorption (PIA) signals may also exist and interfere with the GSB signal if they have similar energies. The PIA signals can

be caused by the transitions to different energy states rather than the first excited state, whose origins can be self-trapping, defect-related energy states, or excitation to higher energy states.

As Fig. 4.7b shows, the short-time TA spectrum exhibited a broadband GSB signal centred at approximately 1.36 eV. However, a strong PIA signal pulled down this GSB signal within 5-10 ps. The interference between the GSB and PIA signals can also be observed in the normalised TA signal kinetics (Fig. 4.7c). As for the long-time TA measurements (pump-probe delays ranging from 1 to 1000 ns), as Fig. 4.7d-f shows, no GSB signal can be observed due to the strong PIA signals. Thus, it is difficult to estimate the charge-carrier lifetime according to the TA results, and different techniques are required to understand the charge-carrier kinetics in $CuSbSe_2$. Whereas the broad GSB signal observed in the short-time TA spectrum also supports that the dominant species of charge-carriers in $CuSbSe_2$ are free carriers instead of excitons.

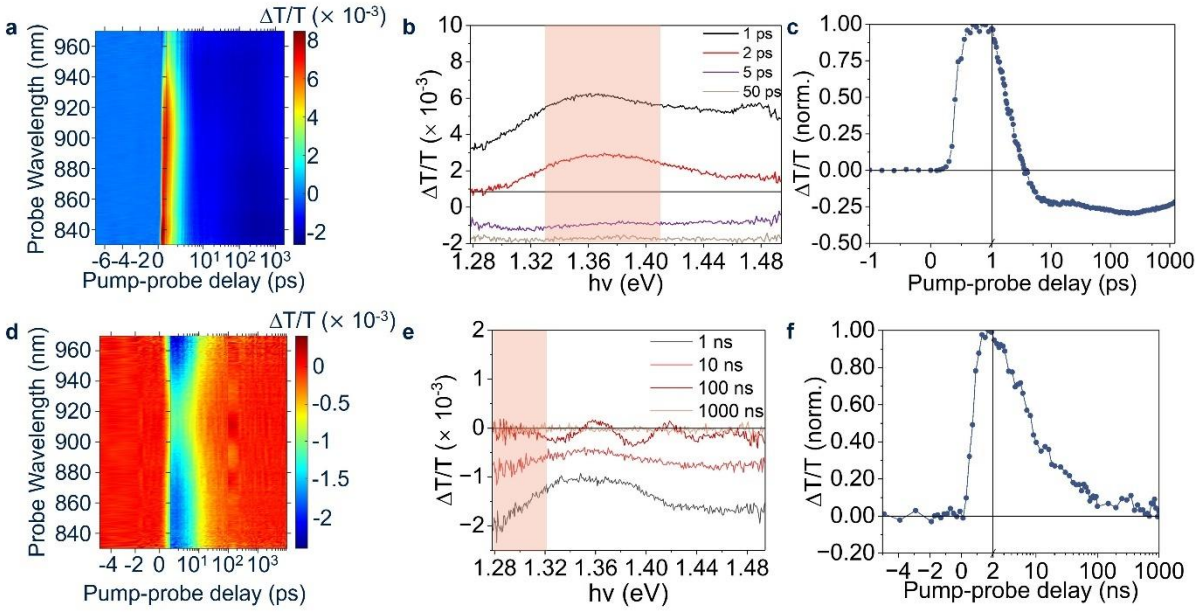

Fig. 4.7 | TA measurements of $CuSbSe_2$. a, Short-time transient absorption (TA) signal colour map of $CuSbSe_2$ films excited by a 800 nm wavelength pump (150 fs pulse width, 41 mJ cm^{-2} $pulse^{-1}$ fluence, with 500 Hz repetition rate), along with **b,** short-time TA spectra for pump-probe delays of 1, 2, 5 and 50 ps, and **c,** its normalized ground state bleach (GSB) signal kinetics. The GSB kinetics were acquired by averaging the signals from 1.33 to 1.41 eV (pink shaded area in **b**) and normalized to the maximum $\Delta T/T$ value. Data shown for parts **b** and **c** are the average of 5 scans. **d,** Long-time TA signal colour map of $CuSbSe_2$ films excited by 355 nm pump (800 ps pulse width, 21 μJ cm^{-2} $pulse^{-1}$ fluence, 500 Hz repetition rate), along with **e,** TA spectra for different pump-probe delays from 1 to 1000 ns, and **f,** its normalized PIA signal kinetics. Please note that the signal in part **f** is normalized and is therefore not shown as negative values, as would be conventionally the case. The PIA kinetics were acquired by averaging the signals from 1.28 to 1.32 eV (pink shaded area in **e**) and normalized to the maximum $\Delta T/T$ value.

4.4 Investigating charge-carrier-phonon coupling of $CuSbSe_2$

4.4.1 OPTP measurements

As the strong PIA signals in TA spectra made it difficult to investigate the charge-carrier kinetics in $CuSbSe_2$, optical pump terahertz probe (OPTP) spectroscopy was employed to gain more insights into the photo-generated charge-carriers in $CuSbSe_2$. After the sample is excited

by a 400-nm pump pulse, the fractional change in transmitted terahertz (THz) probe $-\Delta T/T$ is detected. As introduced in Section 3.3.8, the measured $-\Delta T/T$ is proportional to the photoconductivity of the sample, which can provide information on both population and mobility of charge-carriers. The OPTP measurements on several Bi-based materials have shown similar decays of the photoconductivity within a sub-picosecond timescale after the excitation[27,28,96], caused by the reduced mobilities of localised charge-carriers. Compared to charge-carrier localisation, defect-assisted trapping can also reduce the mobilities of charge-carriers, but the photoconductivity decay is slower since charge-carriers have to diffuse to the defect sites before getting trapped or recombining non-radiatively[28], while charge-carrier localisation can happen immediately after generation, resulting in the faster photoconductivity decay. Therefore, the photoconductivity decay timescale can provide insights into the mechanisms of charge-carrier trapping in different materials. It should also be noted that the formation of excitons can also influence the photoconductivity transients, so the nature of excitations (*i.e.*, free charge-carriers or excitons) should be considered when analysing the OPTP spectrum. As discussed in Section 4.3.1, $CuSbSe_2$ exhibits free charge-carriers rather than excitons.

As Fig. 4.8a shows, the original OPTP signal of the $CuSbSe_2$ sample decreased by 50% over a period of 6.7 ps, while 92% of the original signal was lost over 50 ps. This decay is slower than the decay of the GSB signal measured by short-time TA spectroscopy (Fig. 4.7c), which can be attributed to the interference between GSB and PIA signals, obscuring the real depopulation process of photogenerated charge-carriers in $CuSbSe_2$. Compared to the photoconductivity

decays reported for other Bi-based materials, the decay observed in the OPTP measurements on $CuSbSe_2$ shows a much slower timescale. As listed in Table 4.3, $Cs_2AgBiBr_6$, Cu_2AgBiI_6, $NaBiS_2$ and as-prepared $AgBiS_2$ all lost 50% of their original OPTP signals after only 0.5–2 ps[27,28,96,252]. The charge-carrier kinetics of $CuSbSe_2$ obtained from OPTP measurements prove that $CuSbSe_2$ can avoid charge-carrier localisation, while defect-assisted trapping is the main trapping mechanism.

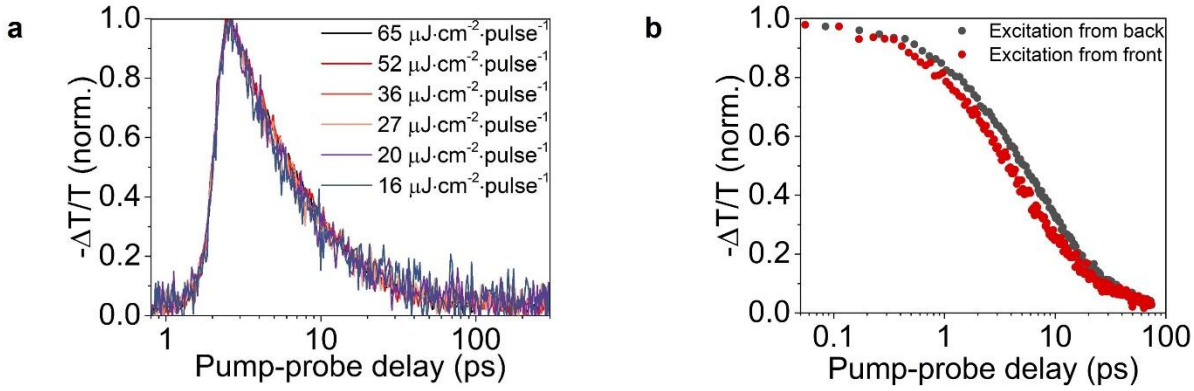

Fig. 4.8 | Optical pump terahertz probe (OPTP) measurements on $CuSbSe_2$. a, Normalised comparison between fluence-dependent OPTP transients measured for $CuSbSe_2$ thin films following 400 nm wavelength pulsed excitation. **b,** Normalised comparison between OPTP transients measured from the back side ($CuSbSe_2$ film-quartz substrate interface, black) and front side ($CuSbSe_2$ film surface, red) of $CuSbSe_2$ sample. The fluence is 65 μJ/cm^2 per pulse. The origin point of the pump-probe delay was adjusted to only show the photoconductivity decay process.

Table 4.3 | Comparison of key properties of $CuSbSe_2$ with other Sb- and Bi-based

compounds. These are the charge-carrier mobility at room temperature, effective mass, bandgap and dielectric constants, along with the time taken for the photoconductivity signals to decay by 50% from the initial peak value. The charge-carrier mobilities shown are extracted from the photoconductivity spectra measured by OPTP. t_{50} refers to the time taken for the photoconductivity to decay to 50% of the initial peak value in OPTP measurements.

Material	OPTP Mobility ($cm^2 \cdot V^{-1} \cdot s^{-1}$)	Effective mass (m_h^*/m_0; m_e^*/m_0)	Bandgap (eV)	Dielectric constant (ϵ_∞; ϵ_{stat})	t_{50} (ps)
Polycrystalline $CuSbSe_2$	4.7±0.2 (this work)	1.60; 0.43 (this work)	0.9-1.2[108-110,114]	11.3; 23.0 (this work)	6.7 (this work)
Single crystal $CuSbSe_2$[108]	87 (measured by Hall effect measurements)				
$NaBiS_2$[96]	0.29 (delocalized); 0.03 (localized)	1.04; 0.24	1.4	ϵ_∞ = 8.1; ϵ_{stat} = 43.7	~0.5
$AgBiS_2$[94,253]	As-prepared: 0.43 ± 0.05 (delocalized), 0.11 ± 0.05 (localized); thermally treated: 2.70 ± 0.10 (delocalized), 2.20 ± 0.10 (localized)	0.51; 0.24	1.45	19.43(x/y), 12.44(z); 115.61(x/y), 35.08(z)	<1 (as-prepared); 20-30 (heat-treated)
$Cs_2AgSbBr_6$[254,255]	0.5 (delocalized); 0.1 (localized)	0.234-0.969; 0.289-0.431	1.64	4.82; 13.69	1-2
$Cs_2AgBiBr_6$[28,102,256-258]	3 (delocalized); 1.3 (localized)	0.14; 0.37	2-2.25	4.60; 12.76	1-2
Polycrystalline BiOI[100,101]	~3	0.26; 0.23	1.93	8.60; 43.33	200-300
Single crystal BiOI[101]	26 (perpendicular),				

	83 (parallel), measured by time of flight measurements				
Sb_2S_3[98,107]	0.9±0.1	0.64; 0.40	1.7-1.8	11.55(x), 10.97(y), 8.25(z); 98.94(x), 94.21(y), 13.14(z)	10-20
$MA_3Bi_2I_9$[259-261]	Not reported	0.95; 0.54	2.1-2.2	5.43(x), 4.67 (z); 39.89(x), 9.62(z)	Not reported
$Cs_3Bi_2I_9$[262,263]	Not reported	0.94 (perpendicular to (100)), 2.14 (perpendicular to (001)); 0.33 (perpendicular to (100)), 3.22 (perpendicular to (001))	1.95	5.38 (perpendicular to (100)), 4.09 (perpendicular to (001)); 9.90 (perpendicular to (100)), 7.85 (perpendicular to (001))	Not reported
BiSI[264-267]	Not reported	0.95; 0.53	1.57	8.03; 37.81	Not reported
BiI_3[268-271]	Not reported	2.01; 0.68	1.8	7.1 (in plane), 6.4 (out of plane); 54 (in plane), 8.6 (out of plane)	Not reported

4.4.2 Temperature-dependent Hall effect measurements

Another effect of charge-carrier localisation is the different temperature dependence of the mobilities of free and localised charge-carriers. For large polarons, as the temperature increases, there will be more phonons that charge-carriers can be coupled to, thus leading to the lower overall mobility[12,14,17,21]. By comparison, since small polarons are transported by hopping between lattice sites, the increased temperature can provide more thermal energy for the

hopping of small polarons, therefore leading to higher mobility[12,17,27,28]. Such different temperature dependence can be another scope to examine the strength of charge-carrier localisation in $CuSbSe_2$. Through Hall effect measurements, the Drude mobilities of charge-carriers in $CuSbSe_2$ were measured at temperatures ranging from 120 to 300 K. As Fig. 4.9a shows, as the temperature increased, a clear decrease in mobility was observed, which indicates the existence of large polarons in $CuSbSe_2$. By performing a power law fit, the relationship between the mobility and temperature was found to be $\mu \propto T^{-1.2}$, which agreed with the behaviour of large polarons. At room temperature (300 K), the mobility given by Hall effect measurements was 1.01±0.01 $cm^2 \cdot V^{-1} \cdot s^{-1}$ while the value found by OPTP measurements was 4.7±0.2 $cm^2 \cdot V^{-1} \cdot s^{-1}$. The different values of mobilities can be attributed to the measured length scales of these two characterisation techniques. Hall effect measurement is a macroscopic technique investigating the overall charge-carrier mobility throughout the whole film, while the photoconductivity measured by OPTP spectroscopy describes the transport within a shorter range, usually within one grain[14,27,97,227].

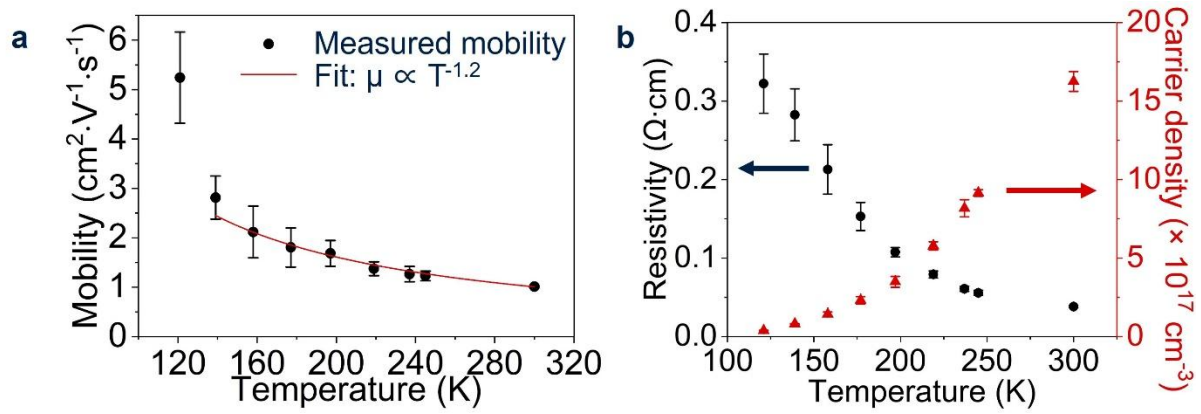

Fig. 4.9 | Temperature-dependent Hall effect measurements on $CuSbSe_2$. a, Temperature-dependent mobility of $CuSbSe_2$ thin films determined using Hall effect measurements, along

with the power law fit, indicating $\mu \propto T^{-1.2}$. The point at the lowest temperature (121 K) is not included in the fit due to its higher standard deviation than the other data points. **b,** Temperature-dependent resistivity (black circles, plotted to the left y-axis) and charge-carrier density (red triangles, plotted to the right y-axis) of $CuSbSe_2$ thin films determined using Hall effect measurements.

Importantly, the mobility values obtained from both measurements are higher than the typical values of materials undergoing charge-carrier localisation. As listed in Table 4.3, OPTP measurements on those materials (*i.e.*, $NaBiS_2$, $Cs_2AgSbBr_6$, $Cs_2AgBiBr_6$ and as-prepared $AgBiS_2$) found the localised mobilities to range from 0.1 to 1.3 $cm^2 \cdot V^{-1} \cdot s^{-1}$, which were all lower than the OPTP mobility of $CuSbSe_2$, even though $CuSbSe_2$ showed a high effective mass. Meanwhile, BiOI, another pnictogen-based semiconductor which has been proven to be able to avoid charge-carrier localisation, exhibited a peak OPTP mobility of ~3 $cm^2 \cdot V^{-1} \cdot s^{-1}$ at 295 K. The comparison between $CuSbSe_2$ and other pnictogen-based semiconductors also supports that $CuSbSe_2$ can avoid charge-carrier localisation.

The temperature-dependent resistivity and charge-carrier density were also found through Hall effect measurements. As shown in Fig. 4.9b, the increasing temperature resulted in higher charge-carrier density as more charge-carriers were thermally excited to the conduction band. The increase in the charge-carrier density also led to lower resistivity at higher temperatures.

4.4.3 Calculations of properties related to charge-carrier-phonon coupling

After experimentally demonstrating the absence of charge-carrier localisation in $CuSbSe_2$, computational tools were also employed to further analyse the properties related to charge-carrier-phonon coupling and understand the underlying factors enabling the band-like transport in $CuSbSe_2$.

To describe the strength of coupling of charge-carriers to acoustic phonons, a dimensionless constant, known as the acoustic coupling constant (g_{ac}), is given by the equation:

$$g_{ac} = \frac{E_d^2}{C a_0} . \frac{m}{3\pi\hbar^2} \tag{4.2}$$

where E_d is the acoustic deformation potential, C the elastic constant, m the mass of the charge-carrier considered and $\hbar$ the reduced Planck's constant. Materials with the value much lower than one are expected to avoid charge-carrier localization. Firstly, in my project, deformation potential theory[272] was used to analyse the acoustic deformation potential E_d. This theory assumes that the propagating acoustic wave has the wavelength larger than the size of the unit cell, therefore the acoustic wave can be regarded as a homogenous strain to the unit cell. Based on this assumption, the deformation potential due to long-wavelength acoustic phonons can be quantitatively analysed as the change in band edge position when a strain is applied to the structure, as described by this equation:

$$E_{\mathrm{d}}^{\mathbf{nk}} = \frac{\delta \mathcal{E}_{n\boldsymbol{k}}}{\delta S_{\alpha\beta}} \tag{4.3}$$

In this equation, $\mathcal{E}_{n\boldsymbol{k}}$ is the energy of band n at wavevector $\mathbf{k}$, while $S_{\alpha\beta}$ is the uniform stress tensor[21]. As shown in Table 4.4, our calculations gave the acoustic deformation potentials of 1.73 eV and 6.51 eV for the VBM and CBM of $CuSbSe_2$, respectively. For comparison,

$Cs_2AgBiBr_6$, which undergoes charge-carrier localisation, was found to exhibit much higher acoustic deformation potentials (13.7 eV for VBM; 14.7 eV for CBM), while $CsPbBr_3$, which can avoid charge-carrier localisation, has comparable values (2.2 eV for VBM; 6.3 eV for CBM) to those of $CuSbSe_2$[28]. The calculations of acoustic deformation potential provide more evidence on the absence of charge-carrier localisation in $CuSbSe_2$. To further verify this, the acoustic coupling constants (g_{ac}) of $CuSbSe_2$ were also calculated and listed in Table 4.4. The average acoustic coupling constants on the order of 10^{-3} are consistent with our experimental findings that $CuSbSe_2$ does not undergo charge-carrier localisation.

Table 4.4 | Calculated properties related to carrier-phonon coupling in $CuSbSe_2$ along different principal axes. a_o: lattice parameter; E_d^{VBM}: acoustic deformation potential of the valence band maximum; E_d^{CBM}: acoustic deformation potential of the conduction band minimum; g_{ac}: acoustic coupling constant; C_{iii}: Diagonal component of the elastic tensor; ϵ_∞: dielectric constant at high frequency; ϵ_{stat}: static dielectric constant; m_h^*: effective mass of holes (related to electronic conductivity); m_h^*: effective mass of electrons (related to electronic conductivity); α_h: Fröhlich coupling constant of holes; α_e: Fröhlich coupling constant of electrons. E_b: Wannier-Mott binding energies. Average: to arrive at the average shown in Table 4.4, a tensor averaging scheme was employed for each tensor, and these values were used in the relevant formula. For rank 2 tensors, each tensor was diagonalized, and the average of their eigenvalues was taken. For elastic constants, the Reuss average scheme was employed, calculated via the Elate web app[273]. Simple means were used for rank 1 tensors, except for the effective masses, for which the harmonic mean was taken. Once a tensor average

for each quantity in each formula was found, these were used in the relevant equations to find the average values. More details of the data processing steps are available in the raw data file of the published paper[274].

	a	*b*	*c*	Average
a_o (Å)	6.457	4.034	14.929	
E_d^{VBM}(eV)	1.16	1.93	2.11	1.73
E_d^{CBM} (eV)	6.60	6.32	6.62	6.51
C_{iii} (GPa)	75.5	81.7	60.4	41.6
g_{ac}^{VBM}	1×10^{-3}	3×10^{-3}	3×10^{-3}	2×10^{-3}
g_{ac}^{CBM}	7×10^{-3}	1.0×10^{-2}	1.0×10^{-2}	9×10^{-3}
ϵ_∞	10.1	12.5	11.4	11.3
ϵ_{stat}	12.0	40.4	16.5	23.0
m_h^*	1.44	1.30	2.38	1.60
m_e^*	0.29	0.41	0.94	0.43
α_h	0.55	1.77	1.17	1.59
α_e	0.25	0.99	0.73	0.82
E_b (meV)	22.3	2.6	33.6	8.7

Besides coupling to acoustic phonons, another possible cause of charge-carrier localisation is strong coupling between charge-carriers and longitudinal optical (LO) phonons. To describe the strength of such coupling, the Fröhlich coupling constant, α, is derived from the equation:

$$\alpha = \frac{q^2}{4\pi\epsilon_0}\left(\frac{1}{\epsilon_\infty} - \frac{1}{\epsilon_{\text{stat}}}\right)\sqrt{\frac{m^*}{2\omega_{\text{LO}}\hbar^3}} \quad (4.4)$$

where ϵ_0 is the vacuum permittivity while ϵ_∞ and ϵ_{stat} are the calculated optical and static dielectric constants, respectively. m^* is the effective mass of the free charge-carrier, while ω_{LO} is the effective longitudinal optical (LO) phonon frequency, and $\hbar$ is the reduced Planck's constant. ω_{LO} (138 cm^{-1}) was determined by weight-averaging all Γ-point phonon modes according to their dipole moments since Fröhlich coupling investigates the coupling between charge-carriers and LO phonon modes, which can produce local dipoles[21]. The average Fröhlich coupling constants of holes and electrons in $CuSbSe_2$ (α_h = 1.59, α_e = 0.82) both fall in the weak regime and are lower than the values of other ABZ_2 materials such as $NaBiS_2$ (α_h = 2.92, α_e = 1.40)[96], $AgBiS_2$ (α_h = 1.63, α_e = 1.09)[93], as well as methylammonium lead iodide perovskites (2-3)[18]. The low Fröhlich coupling constants of $CuSbSe_2$ indicate the weak interactions between charge-carriers and LO phonons, enabling this material to avoid charge-carrier localisation due to strong Fröhlich coupling.

4.4.4 Understanding the mechanisms of weak charge-carrier-phonon coupling of $CuSbSe_2$

Having confirmed that $CuSbSe_2$ can avoid charge-carrier localisation through both experimental and computational methods, which is quite unusual compared to many other heavy pnictogen-based semiconductors, it is worth to further understanding the underlying mechanisms of the weak charge-carrier-phonon coupling of $CuSbSe_2$ and reveal the critical

factors enabling this behaviour.

As discussed in the previous section, the low acoustic deformation potential E_d of $CuSbSe_2$ is the main property resulting in the low acoustic coupling constants g_{ac} since g_{ac} is proportional to the square of E_d. Considering that E_d describes the change in band edge positions caused by lattice distortion, which is determined by the bonding interactions between atoms, insights into the reason for low acoustic deformation potential can be gained by analysing the change in bonding environments when the lattice is distorted. To understand the bonding environments in $CuSbSe_2$, the crystal orbital Hamilton population (COHP) calculations were first performed, and the results are illustrated as the COHP diagram (right panel of Fig. 4.6b). With –COHP set as the horizontal axis, positive values represent bonding interactions, while negative values indicate anti-bonding interactions between atoms, and values near the centre line indicate non-bonding interactions. For bonding interactions, Sb-Se bonds show a more positive -COHP value per bond than Cu-Se bonds, indicating stronger covalent bonds between Sb and Se atoms. It can also be seen from Fig. 4.6 that the VBM of $CuSbSe_2$ mainly consists of Cu(d)-Se(p) anti-bonding states, with much weaker contributions from Sb(s, p)-Se(p) interactions, which are approximately non-bonding. Such non-bonding interactions are caused by the stereochemical activity of the lone electron pair of the Sb atom, which is projected into the interlayer gap. The CBM has more contributions from Sb-Se antibonding interactions, while having fewer from Cu-Se antibonding states.

After understanding the interactions contributing to the band edges, we simulated the lattice

distortion by applying a strain along the *c*-axis (*i.e.*, perpendicular to $CuSbSe_2$ layers), then allowed the structure to relax to its local energy minimum and calculated the change in bond lengths to examine the change in bonding environment of $CuSbSe_2$. The bonds studied are highlighted in Fig. 4.10a and represented with the corresponding colours in Fig. 4.10b. In Fig. 4.10b, the change in the lengths of studied bonds is illustrated as a function of the applied strain. When the strain reached $\pm$5%, most bonds exhibited minor length changes (below 1%), while the maximum bond length change, observed in Cu1-Se3 bond, was also only about 2%. On the contrary, a significant change around $\pm$20% under $\pm$5% *c*-axis strain was shown for the interlayer distance, defined as the perpendicular distance between Sb2 and Sb3 atoms. The phenomenon that Cu-Se bonds show more length changes than Sb-Se bonds is consistent with the overall stronger covalent bonds between Sb and Se atoms found by our COHP calculations, which can be attributed to the filled Cu-Se antibonding states near the VBM[275]. Our analysis of the effects of *c*-axis strain on bonding environment reveals that most lattice strain can be absorbed by modulating the interlayer distance, while the lengths of the in-layer bonds are not changed significantly.

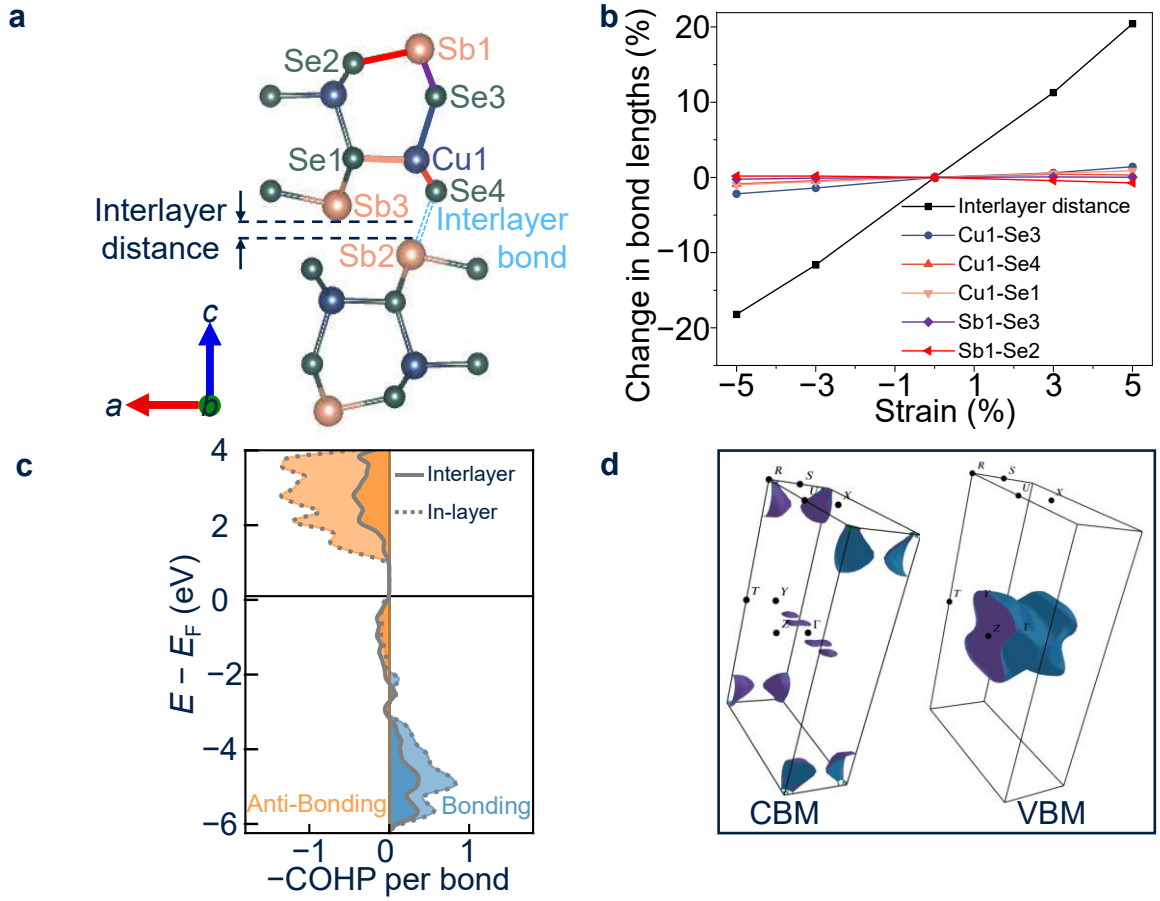

Fig. 4.10 | Computational analysis of $CuSbSe_2$. a, Structure of $CuSbSe_2$, with key atoms labelled, and the interlayer distance defined as the perpendicular distance between Sb2 and Sb3. **b,** Percentage changes in bond lengths and interlayer distance of $CuSbSe_2$ as a function of strain along the *c*-axis. All calculated bond lengths shown are after relaxation of the atoms in the structure after distortion, *i.e.*, calculations for equilibrated structures as shown. A disproportionally large change in the interlayer distance is observed as compared to bond lengths for a given strain. **c,** Calculated crystal orbital Hamilton population (COHP) per bond of in-layer (dashed line) and interlayer (solid line) Sb-Se bonds. The bonding and anti-bonding interactions are represented by blue and orange, respectively. **d,** Fermi iso-surface 0.1 eV below the VBM (top figure) and above the CBM (bottom figures).

To better compare the in-layer and interlayer bonding interactions, we also performed COHP calculation on the interlayer Sb-Se bond (highlighted in light blue in Fig. 4.10a) and derived an integrated crystal orbital Hamilton population (ICOHP) value to compare the covalent bonding strength with the in-layer Sb-Se bond. As Fig. 4.10c shows, in-layer Sb-Se bonds exhibit much higher ICOHP values than the interlayer case, indicating much weaker interlayer Sb-Se bonding, so no formal covalent bonds can form between $CuSbSe_2$ layers, and this material can be regarded as a layered material. Based on our computational analysis of the in-layer and interlayer bonding environments under lattice distortion, the underlying mechanism of the low acoustic deformation potential of $CuSbSe_2$ has been revealed. When the lattice is distorted due to the propagation of an acoustic wave, most distortion can be absorbed by the interlayer space (via changing the interlayer distance), while the lengths of in-layer bonds are not affected significantly. Due to the much weaker interlayer bonding interactions, the obvious change in the interlayer distance will not affect the overall bonding environment significantly. Meanwhile, even though in-layer bonds exhibit stronger interactions, the minor change in the bond lengths results in less significant influence on the bonding environment. Therefore, the electronic structure of $CuSbSe_2$ can resist the effect of lattice distortion, leading to its low acoustic deformation potential.

Besides acoustic deformation potential, electronic dimensionality can also influence charge-carrier-phonon coupling. As described by the continuum model of Toyozawa, which considers both acoustic and optical phonon fields[15,276], a 3D electronic structure exhibits an energy barrier against charge-carrier localisation, which is an advantage over lower electronic dimensionality,

but the energy barrier height should also be considered[19,27]. For materials with a 2D electronic structure, the acoustic coupling constant g_{ac} determines their tendency to undergo charge-carrier localisation or not. For g_{ac} higher than 1, charge-carrier localisation is energetically favourable with no energy barrier. However, when g_{ac} < 1, free charge-carriers tend to have lower energy than localised charge-carriers, so charge-carrier localisation should not occur[19]. As for electronically 1D materials, charge-carrier localisation is predicted to occur spontaneously. To investigate the electronic dimensionality of $CuSbSe_2$, we calculated the Fermi surfaces slightly above and below the CBM and VBM (0.1 eV energy difference), which are represented by the states occupied by free charge-carriers with the same energies, as shown in Fig. 4.10d. For Fermi surfaces, planar or columnar motifs indicate electronically 1D and 2D structures, respectively, which exhibit weak dispersion along the flat planar/axial direction(s). By comparison, motifs with closed surfaces show dispersion in all directions, therefore represent 3D electronic structures[107]. For the VBM of $CuSbSe_2$, the Fermi surface shows a columnar feature with weak dispersion along the *c*-axis, indicating a 2D electronic structure, while the CBM shows a number of ellipsoidal and rod-like structures with closed surfaces, suggesting the electronic structure as 3D. The different dimensionalities of VBM and CBM can be understood based on the main bonding interactions between atoms, which contribute to the band edges, as shown in Fig. 4.6b. The VBM of $CuSbSe_2$ is dominated by Cu-Se interactions, which mostly occur within each layer. On the contrary, the CBM mainly consists of interactions between Sb and Se atoms. As discussed previously, besides the Sb-Se interactions within each layer, the weak interactions between the Sb and Se species across the interlayer gaps also contribute to the CBM, resulting in its higher electronic dimensionality. The electronic 3D

CBM makes it more difficult for electrons to be localised. Meanwhile, even though the VBM of $CuSbSe_2$ is 2D, due to its low g_{ac} (Table 4.4), free charge-carriers are energetically favourable. Both the relatively high electronic dimensionality and the low acoustic coupling constant result in the band-like transport in $CuSbSe_2$.

Our analysis also shows that the structural and electronic dimensionalities of $CuSbSe_2$ are different. The electronic dimensionality of the VBM of $CuSbSe_2$ matches its quasi-2D crystal structure, but its CBM shows 3D features. Actually, such deviation has also been observed in other pnictogen-based semiconductors. For example, $Cs_2AgBiBr_6$ was found to exhibit an electronic structure close to 0D, despite its 3D crystal structure[277]. The significantly lower electronic dimensionality contributes to the charge-carrier localisation in this material. Moreover, Sb_2Se_3 and Sb_2S_3 both have the same quasi-1D crystal structure. It has been reported that they have a 2D and 3D VBM, respectively[107]. These observations emphasise the importance of analysing the electronic dimensionality carefully instead of simply predicting it according to the crystal structure of materials. Our study on CuSbSe2, along with those on $Cs_2AgBiBr_6$ and antimony chalcogenides, suggests that electronic dimensionality is an important property influencing charge-carrier localisation and is worth considering with other properties, such as the acoustic and Fröhlich coupling constants, in order to properly understand the nature of charge-carrier-phonon interactions.

In addition to the weak coupling between charge-carriers and acoustic phonons, the weak Fröhlich interaction of $CuSbSe_2$ also contributes to its band-like transport. According to Table

4.4 and Eq. 4.4, the low Fröhlich coupling constant of $CuSbSe_2$ is primarily determined by the small difference between the electronic and static dielectric constants, ϵ_∞ and ϵ_{stat}, which means the ionic dielectric contribution is low compared to electronic contributions. As shown in Table 4.4, the electronic dielectric contribution is relatively high along all principal axes, while close ϵ_∞ and ϵ_{stat} (low ionic contributions) can be observed, especially along the *a*- and *c*-axes. The high electronic contribution can be attributed to the small bandgap and high refractive index of $CuSbSe_2$, since the electronic dielectric constant ϵ_∞ is related to the bandgap E_g and refractive index n as $\epsilon_\infty \propto E_{\text{g}}^{-0.5}$ and $\epsilon_\infty \propto n^{0.5}$ [278]. The high refractive index can be understood by the high density of states near the band edges of $CuSbSe_2$, which leads to a stronger interaction between electrons and light, thus a higher refractive index. To find the mechanism of the low ionic dielectric contribution, the Born effective charge (BEC) tensors for the different atoms in $CuSbSe_2$ were calculated and listed in Fig. 4.11. The Born effective charges ($Z^*_{\alpha,ij}$), also known as dynamical charges, describe the change in polarization in direction i when the sublattice of atoms (α) is displaced along direction j[279,280], as given by this equation:

$$Z^*_{\alpha,ij} = \frac{\partial P_i}{\partial u_{\alpha,j}}. \tag{4.5}$$

$$Z^*_{\mathrm{Cu1(I)}} = \begin{matrix} \overbrace{}^{\text{displacement direction}} \\ a \quad b \quad c \end{matrix} \begin{pmatrix} 0.87 & 0 & -0.07 \\ 0 & 1.23 & 0 \\ 0.28 & 0 & 1.18 \end{pmatrix} \quad \Sigma = [1.14 \quad 1.23 \quad 1.12]$$

$$Z^*_{\mathrm{Sb1(III)}} = \begin{matrix} \overbrace{}^{\text{displacement direction}} \\ a \quad b \quad c \end{matrix} \begin{pmatrix} 2.53 & 0 & -0.62 \\ 0 & 5.65 & 0 \\ -1.50 & 0 & 2.06 \end{pmatrix} \quad \Sigma = [1.03 \quad 5.65 \quad 1.44]$$

$$Z^*_{\mathrm{Se1(II)}} = \begin{pmatrix} -1.06 & 0 & -0.21 \\ 0 & -4.18 & 0 \\ -0.45 & 0 & -1.08 \end{pmatrix} \quad \Sigma = [-1.51 \quad -4.18 \quad -1.29]$$

$$Z^*_{\mathrm{Se2(II)}} = \begin{pmatrix} -2.34 & 0 & 0.04 \\ 0 & -2.71 & 0 \\ 0.67 & 0 & -2.16 \end{pmatrix} \quad \Sigma = [-1.67 \quad -2.71 \quad -2.12]$$

Fig. 4.11 | Calculated Born effective charge (BEC) of atoms in $CuSbSe_2$. The BEC values represent the induced polarization when atoms are displaced, in this case, along the principal crystallographic axis directions. The net BEC values for displacements in the direction of each axis (*a*, *b* or *c*) are shown below each tensor in square brackets.

The values of the Born effective charges can provide insights into the bonding interactions in materials. For example, materials with strong ionic-covalent bonds tend to have the Born effective charges of cations significantly larger than the formal oxidation states. As shown in Fig. 4.11, the BECs for Cu1 in $CuSbSe_2$ are close to the formal oxidation state of the species. However, BEC values higher than the formal oxidation states have been observed for Sb1 and Se1 atoms when they are displaced along the *b* direction, while the net BECs for displacements along *a* and *c* directions are lower than their oxidation states (first and third value in square brackets). The low net BEC values of Sb1 and Se1 atoms for *a*- and *c*-direction displacements are consistent with their close ϵ_∞ and ϵ_{stat} values along these directions, and contribute to the low Fröhlich coupling constants in these directions (Table 4.4). As for the anomalously

large contributions of the Sb1 and Se1 atoms along the *b*-axis, the possible cause can be either a change in the polarization of the Sb1 and Se1 atoms upon displacement, or a direct transfer of charge between them, but further studies are required to distinguish these reasons[280]. It has been reported that the lone electron pair of Sb atoms leads to a symmetry-breaking interaction between hybridized Sb-*s*, *p* orbitals and Se *p* orbitals[106]. In this case, the sub-lattice displacement can influence the expression of the Sb lone electron pair and result in strong deviations of the BEC from the oxidation state. Importantly, the Fröhlich coupling constant of $CuSbSe_2$ along the *b*-axis is still lower than 2, despite the relatively larger ionic dielectric contributions along this direction.

Moreover, we also compare the BEC value of Sb atoms in $CuSbSe_2$ with those of other pnictogen-based materials, as well as $CH_3NH_3PbI_3$, as listed in Table 4.5. For Pb atoms in $CH_3NH_3PbI_3$, where the $6s^2$ lone electron pair is expressed, BEC values anomalously higher than the oxidation state of Pb^{2+} are observed, which lead to high ionic dielectric constants (ϵ_∞ = 6.1; ϵ_{stat} = 25.7[281]), thus stronger Fröhlich interactions (α = 2-3 for $CH_3NH_3PbI_3$[18]) than $CuSbSe_2$. Also, nearly all Sb and Bi atoms in the materials shown in Table 4.5 have higher BEC values than their formal oxidation states, indicating higher ionic dielectric contributions, even though anisotropy does exist. Compared to these atoms, the Sb in $CuSbSe_2$ exhibits significantly lower BEC values along the *a* and *c* directions, resulting in low ionic dielectric contributions, therefore weak Fröhlich interaction.

Table 4.5 | Born effective charge (BEC) of pnictogen atoms in Sb- and Bi-based compounds, along with the BEC value of the Pb atom in $CH_3NH_3PbI_3$. The labels a, b and c refer to principal crystallographic axes, while xx, yy and zz refer to diagonal components of the Born effective charge tensors.

Material	Born effective charge
$CuSbSe_2$ (this work)	Sb: 1.03 (a), 5.65 (b), 1.44 (c)
$Cs_2AgBiBr_6$[282]	Bi: 4.79 (average)
BiOI[283]	Bi: 5.87 (a); 5.87 (b); 3.08 (c)
Sb_2S_3[284]	Sb1: 2.89 (xx); 5.62 (yy); 7.36 (zz); Sb2: 3.33 (xx); 7.25 (yy); 4.50 (zz)
$Cs_3Bi_2I_9$[285]	Bi: 3.9 (xx), 3.9 (zz)
BiSI[286]	Bi: 6.42 (a); 3.04 (b); 4.01 (c)
BiI_3[271]	Bi: 5.2 (a); 5.2 (b), 2.8 (c)
$CH_3NH_3PbI_3$[65]	Pb: 5.22 (a), 3.54 (b), 4.86 (c)

4.5 Conclusions

In conclusion, through experimental and computational investigations, I found that $CuSbSe_2$, as a heavy pnictogen-based chalcogenide, can avoid charge-carrier localisation. A novel thiol-amine-based solution processing method was developed to deposit phase-pure $CuSbSe_2$ thin films. By analysing the optical absorption curves and calculated exciton binding energy, the charge-carriers in $CuSbSe_2$ were found to be free charge-carriers instead of excitons. OPTP measurements revealed that $CuSbSe_2$ lost 50% initial photoconductivity over 6.7 ps, much slower than other materials undergoing charge-carrier localisation. The temperature dependence of charge-carrier mobility found through temperature-dependent Hall effect measurements further confirmed that large polarons are dominant in $CuSbSe_2$. DFT calculations revealing the low acoustic and Fröhlich coupling constants of $CuSbSe_2$ also supported that this material can avoid charge-carrier localisation. To understand the critical enabling properties, detailed computational studies on the bonding/anti-bonding nature of the crystal orbitals at the band extrema, and changes in bond lengths and interlayer spacing as a function of distortions, as well as the Born effective charges of ions were performed. In particular, $CuSbSe_2$ was found to be able to minimize the acoustic deformation potentials via relaxing the lattice distortion by modulating the interlayer space while keeping the change in bond lengths low. Another important factor was that having groups of atoms contributing to the orbitals at band extrema (*e.g.*, $CuSe_4$ tetrahedra) oriented at an angle to the principal axes, such that distortions are relaxed as changes in bond angles rather than bond length. Moreover, the electronic coupling between species across the interlayer gaps results in higher electronic

dimensionality, thus strong coupling to acoustic phonons is avoided. Meanwhile, both high electronic contribution (mostly due to the small bandgap) and low ionic contribution to the dielectric constants lead to the weak Fröhlich coupling. The low ionic contribution can be explained by the Born effective charges of Sb, Cu and Se not substantially deviating from their formal oxidation states (in contrast to lead-halide perovskites)[287]. Overall, this work provides valuable insights into the future design and screening of novel solar absorber materials with band-like transport.

4.6 Future work

Based on these findings, I propose that free volumes in the structure can mitigate the impact of structural distortions on the bonding environment and reduce the deformation potential. This can be achieved by not only a layered structure but also motifs featuring regular soft layers of species that do not contribute to orbitals at the band extrema. Simultaneously, quasi-bonding across these regular gaps plays a crucial role in enhancing electronic dimensionality if the quasi-bonding contributes to the band-edge density of states, thereby reducing the likelihood of charge-carrier localisation. A family of materials exhibiting these properties is the bismuth- and sulphide-based alternatives for $CuSbSe_2$ (*e.g.*, $CuSbS_2$[114], $CuBiS_2$[104] and $CuBiSe_2$[288]) as they have a similar crystal structure and the stereochemical activity of the pnictogen cation has been predicted, allowing quasi-bonding across the interlayer gaps. Therefore, an important future work will be to investigate the charge-carrier-phonon coupling in these materials, which can help examine the wider generalizability of the proposed design rules for materials with

delocalised charge-carriers. On the other hand, materials without free volumes in their structures (*e.g.*, Cu_3SbSe_3) should also be studied to examine the criteria from the opposite perspective. I have demonstrated that combined experimental (*e.g.*, photoconductivity transients and temperature-dependent mobility measurements) and computational studies can give a comprehensive analysis of the charge-carrier localisation of materials. By further testing and modifying the principles put forward from this work, simple descriptors for wider sets of semiconductors with band-like transport can be finally established, which is believed to help accelerate the screening of efficient solar absorbers.

Chapter 5: Photovoltaic devices based on solution-processed and chemical-vapour-deposited $CuSbSe_2$

In the previous chapter, it was found that $CuSbSe_2$ avoids carrier localisation, which is critical for achieving long diffusion lengths. In addition, $CuSbSe_2$ has high absorption coefficients exceeding 8×10^5 cm^{-1} at 1.4 eV or higher energies. As such, the absorption profile of $CuSbSe_2$ is well matched to the solar spectrum. These factors, along with the composition of low-toxicity elements, make $CuSbSe_2$ promising for development as photovoltaic devices. But in contrast to preparing materials for the optical and in-plane electrical characterisation made in the previous chapter, realising these materials in photovoltaic devices requires thin films without pinholes. Ideally, the thin film processing method should be scalable and have low embedded energy.

This chapter investigates the development of two approaches with the goal of achieving pinhole-free $CuSbSe_2$ thin films for photovoltaic devices: 1) a novel solution processing method using a thiol-amine alkahest solvent, and 2) a chemical vapour deposition (CVD) approach. For solution processing, different heat treatment parameters and underlayers are explored, leading to improvements in film morphology, which highlights the importance of careful control of solvent removal and substrate selection. CVD, on the other hand, yields films with better coverage, fewer structural defects and larger grain sizes. My work revealed that substrate temperature, working pressure, and evaporation time are critical to the phase purity of CVD-grown $CuSbSe_2$ thin films. Since the substrate temperature can influence the phase

purity and morphology of $CuSbSe_2$ thin films significantly, a sharp temperature gradient (35 °C cm^{-1}) in the furnace results in a narrow region where phase-pure and compact films can be achieved. Therefore, the sharp temperature gradient is identified as the main limitation of the CVD setup. Moreover, solar cells based on solution-processed films showed resistor-like J-V curves while some pixels based on CVD films exhibited diode-like J-V curves. However, no photovoltaic devices with measurable PCE were achieved, which can be caused by structural defects of $CuSbSe_2$ films or a sub-optimal device structure. Since devices fabricated using these two techniques involve different $CuSbSe_2$ film thicknesses and device structures, a direct comparison between the two techniques may not be appropriate. To more effectively evaluate the quality of solution-processed and CVD $CuSbSe_2$ films and device performance, these parameters should be more carefully controlled in future studies. This chapter demonstrates that moderate thermal energy input at the beginning of the heat treatment can improve the morphology of the solution-processed $CuSbSe_2$ thin films. Meanwhile, the layer under $CuSbSe_2$ also has significant effects on the film morphology. For the CVD method, the temperature gradient within the deposition region should be carefully controlled to grow phase-pure $CuSbSe_2$ films effectively.

The contributions from other researchers include:

Hugh Lohan performed the chemical vapor deposition of $CuSbSe_2$, mentored by Yuchen Fu, and the sputtering of Cu, mentored by Daniel Darvill Price. Ben Bowers performed ALD to deposit ZnO for $CuSbSe_2$ solar cells. Pengjun Liu evaporated metal contacts for all

photovoltaic devices and performed the J-V characterisation. Yuchen Fu performed all other synthesis and measurements and analysed all data included in the chapter.

5.1 Introduction

As concluded in Chapter 4, $CuSbSe_2$ can avoid charge-carrier localisation, which is the main challenge of many other heavy-pnictogen-based semiconductors[14,18,96]. Meanwhile, $CuSbSe_2$ is regarded as a promising photovoltaic material due to its composition of elements which are not restricted for use in commercial electronics[291], high optical absorption coefficient, and predicted defect tolerance. Therefore, various techniques have been employed to deposit $CuSbSe_2$ films, such as sputter deposition[117], reactive close-space sublimation (RCSS)[118], selenization of metal precursors[120], and solution processing[112,121]. Among these methods, solution processing can be more cost-effective than vacuum-based approaches, and has the advantage of allowing the processing parameter space to be explored faster on the lab-scale[122,230,231]. However, the previously-reported solution processing method for $CuSbSe_2$ is limited by the use of hazardous hydrazine as the solvent[232]. On the other hand, a more benign solvent system than hydrazine, a thiol-amine mixture, has successfully dissolved chalcogenide precursors and deposited thin films such as $Cu_2ZnSn(S, Se)_4$[233,292], $Cu(In, Ga)Se_2$[158,160], and $CuIn(S, Se)_2$[234]. Using this thiol-amine-based solution processing method, $CuSbSe_2$ thin films were grown. To optimise the film morphology, the heat treatment parameters and the layer under $CuSbSe_2$ were modulated.

Besides the solution processing method, a CVD deposition method was also developed in this chapter. To achieve phase-pure $CuSbSe_2$ thin films, the deposition parameters, including substrate temperature, working pressure and reaction duration were investigated. After establishing the optimal parameters, the effects of the underlayers (glass or ZnO) on the morphology of CVD $CuSbSe_2$ thin films were studied. Moreover, I fabricated $CuSbSe_2$ solar cells with both thiol-amine-based solution processing and CVD methods. This project highlights the factors influencing the quality of $CuSbSe_2$ thin films grown by CVD, as well as the more novel thiol-amine solution processing method..

5.2 Characterisation of solution-processed $CuSbSe_2$ thin film

5.2.1 Phase purity and composition of $CuSbSe_2$ thin films

The experimental methods to prepare phase-pure $CuSbSe_2$ thin films via spin coating are detailed in Section 3.1.1, while the effect of heat treatment temperature on the phase purity of solution-processed $CuSbSe_2$ thin films is shown in Fig. 4.1d. By increasing the heat treatment temperature from 100 °C to 400 °C, crystallised $CuSbSe_2$ thin films without any impurity phases are achieved. It should also be noted that the films thermally treated at 250 °C for 10 min show some peaks belonging to Cu_3SbSe_3 (ICSD database, coll. code 401095) with only minor intensities, as shown by blue dots in Fig. 4.1d. The low intensity of these peaks indicates that the main phase of the films thermally treated at 250 °C is $CuSbSe_2$, and with only a small fraction of Cu_3SbSe_3 impurity phase. Therefore, in the following Sections 5.2.2 and 5.4.1, all

characterisation is performed on solution-processed $CuSbSe_2$ thin films thermally treated at 250 ℃ instead of 400 ℃ due to the simpler heat treatment procedure, which could be carried out on a hotplate inside a glovebox, rather than requiring taking to a separate tube furnace. Also, when the temperature exceeds 200 ℃, the increasing resistivity of ITO as temperature increases can be detrimental to the device performance[296]. Thus, a lower heat treatment temperature is preferred for devices.

The surface and bulk compositions of solution-processed $CuSbSe_2$ thin films were measured by XPS and EDX, respectively. XPS was also employed to determine the chemical species present, their oxidation state and coordination environment. Fig. 5.1 shows the survey spectrum, Cu 2*p*, Sb 3*d* and Se 3*d* core levels with the fitting of peaks. Due to the weak satellite signals near the Cu $2p_{1/2}$ peak, only the Cu $2p_{3/2}$ peak was fitted for the quantification purpose. Also, since the Sb $3d_{5/2}$ peak overlaps with the O 1*s* peak, the Sb $3d_{3/2}$ peak was used for quantification. Table 5.1 shows the XPS peak positions and separations between split peaks of Cu, Sb and Se, as well as the comparison with the reported values from literature[118]. In Ref. 118, $CuSbSe_2$ films were deposited via the reactive close-spaced sublimation method. The similar values of the BE peak positions and separations of my solution-processed $CuSbSe_2$ thin films to the reported values indicate similar chemical environments of the elements. Moreover, as shown in Fig. 4.3c and d, and discussed in Section 4.2, the weak satellite signals in the Cu 2*p* spectra, as well as the kinetic energy of Cu $L_3M_{4,5}M_{4,5}$ Auger-Meitner peak, confirm the oxidation state of Cu in the solution-processed $CuSbSe_2$ thin films to be +1. The deconvolution of Sb 3*d* spectra also demonstrates the +3 oxidation state of Sb species in the $CuSbSe_2$ thin

films.

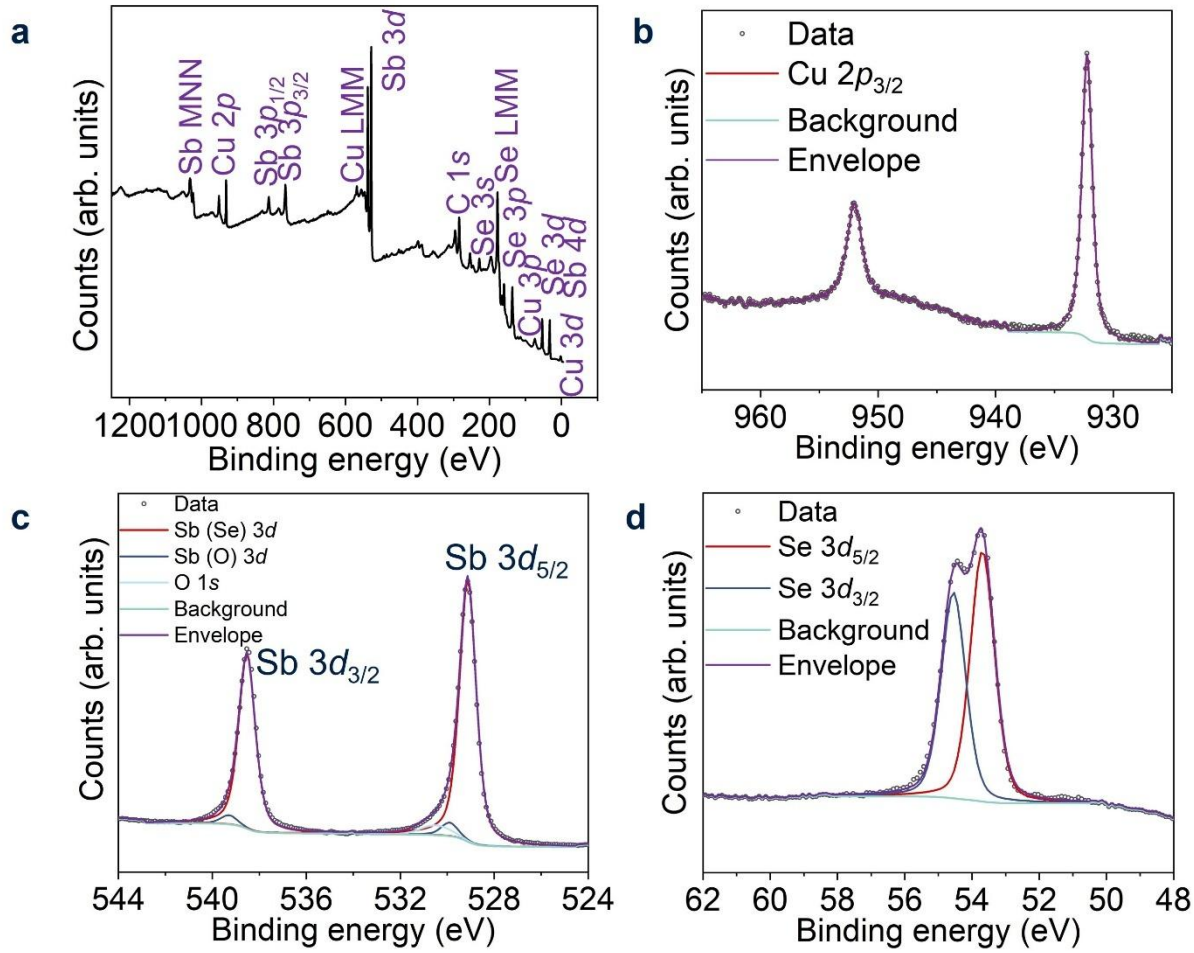

Fig. 5.1 | XPS analysis of the solution-processed $CuSbSe_2$ thin films. a, XPS survey spectrum. The Se LMM, Cu LMM and Sb MNN signals are Se $L_3M_{4,5}M_{4,5}$, Cu $L_3M_{4,5}M_{4,5}$ and Sb $M_{4,5}N_{4,5}N_{4,5}$, respectively; **b,** Cu 2*p* core levels with the fitting of the Cu $2p_{3/2}$ peak; **c,** Sb 3*d* core levels with the fitting; **d,** Se 3*d* core levels with the fitting.

Table 5.1 | XPS results of solution-processed $CuSbSe_2$ thin films. Measured binding energy peak positions (BE) of each core level are listed on the left, and compared with reported results (right).

Core level	This work	Reported results[118]
Cu $2p_{3/2}$	932.2	932.0
Cu $2p_{1/2}$	952.0	951.8
Sb $3d_{5/2}$	529.1	528.8
Sb $3d_{3/2}$	538.5	538.2
Se $3d_{5/2}$	53.7	53.5
Se $3d_{3/2}$	54.6	54.4

Table 5.2 compares the composition of the solution-processed $CuSbSe_2$ thin films measured by XPS and EDX. XPS measurement shows an Sb-rich surface of the $CuSbSe_2$ films, which can be attributed to the formation of the Sb_2O_3 layer on the surface. Meanwhile, a possible reason for the deficient Cu is the formation energy of the Cu vacancy in $CuSbSe_2$ being the lowest among all defects[112], which may lead to the evaporation of Cu from the surface during the heat treatment process. On the other hand, the bulk composition measured by EDX shows the atomic ratio Cu:Sb:Se to be 1.34:1.00:2.60, which is closer to the stoichiometric value.

The error bars shown for atomic ratios represent the standard deviation across three separate

EDX mapping regions on each sample, reflecting the degree of compositional variation across the surface. Care was taken to select representative regions free of visible defects or contamination. These values capture spatial inhomogeneity but do not account for other sources of experimental uncertainty described in Section 3.3.5, such as instrumental calibration errors, peak fitting uncertainty, or interaction volume effects. Therefore, the total quantification error may be larger than the standard deviation reported. Considering the measurement precision and uncertainty associated with EDX, the atomic ratio was rounded to 2 decimal places.

Table 5.2 | Composition of solution-processed $CuSbSe_2$ thin films measured by XPS and EDX. The atomic ratios are calculated by setting the Sb fraction as 1.00. XPS quantification is based on peak areas (Cu $2p_{3/2}$, Sb $3d_{3/2}$, Se $3d$) and RSFs for Kratos system (Cu $2p_{3/2}$: 3.55, Sb $3d_{3/2}$: 3.45, Se $3d$: 0.85).

Elements	Atomic % (XPS)	Cu:Sb:Se	Atomic % (EDX)	Cu:Sb:Se
Cu	16.39	0.39:1.00:1.00	27.13 ± 0.96	1.34:1.00:2.60
Sb	41.91		20.24 ± 0.63	
Se	41.70		52.63 ± 0.38	

5.2.2 $CuSbSe_2$ thin film morphology observation and optimisation

5.2.2.1 Effects of heat treatment parameters

Heat treatment is commonly applied after solution processing thin films, and is used to remove

the remaining solvent to create supersaturation, promoting the nucleation and thin film growth and coarsening the grains[122]. Heat treatment can have significant effects on the morphology of solution-processed thin films[121,297], which is critical to the performance of photovoltaic devices. In my project, $CuSbSe_2$ samples were initially prepared by placing the spin-coated films on a hotplate preheated at 250 ℃, and keeping them on the hotplate for 10 min. As shown in Fig. 5.2a, a high density of pinholes and clusters of grains can be observed. This can be attributed to the rapid removal of the remaining solvents from the film by directly placing these samples on the hotplate immediately after spin coating. When a substantial amount of residual solvent is present, solutes exhibit high mobility, enabling rapid diffusion across the substrate surface during the initial stage of heat treatment. The fast diffusion of solutes can favour the formation of distinct islands when these solutes bind more strongly to each other than to the substrate[122,298]. This limitation could be addressed by removing more of the solvent before heat treatment or decreasing the rate of solvent removal.

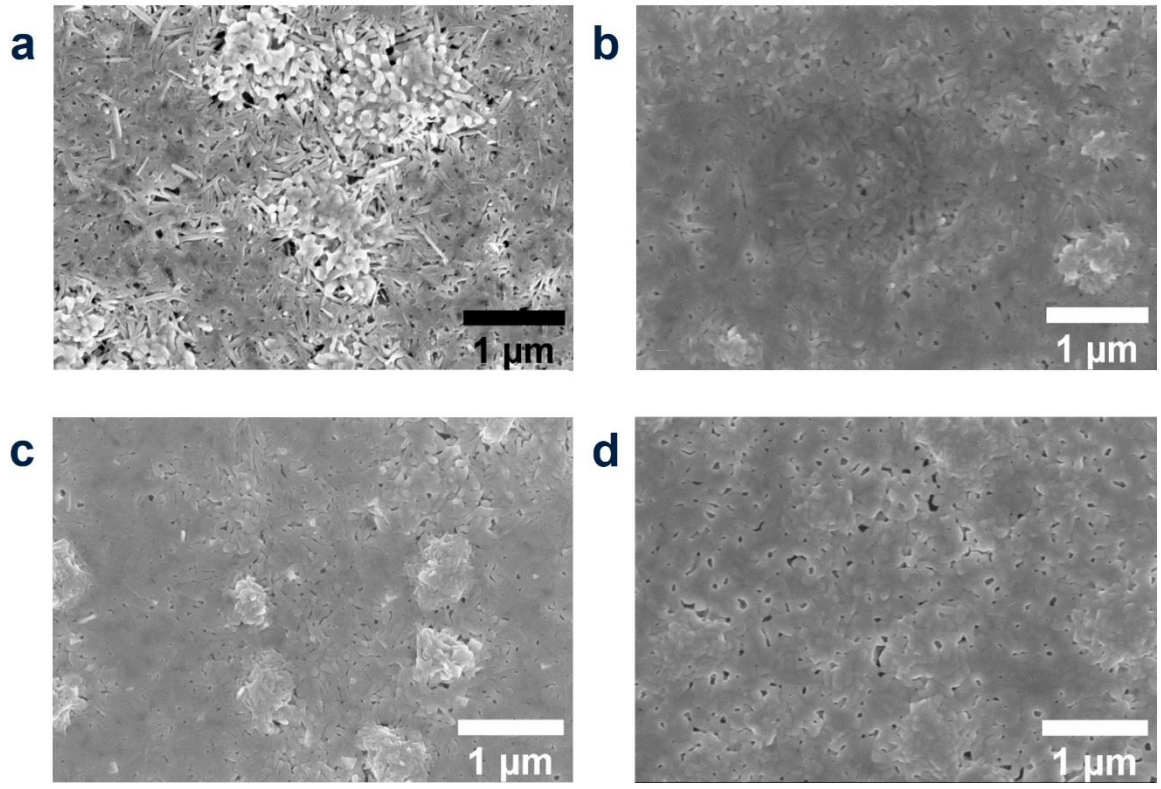

Fig. 5.2 | Top-view SEM images of the solution-processed $CuSbSe_2$ thin films on glass substrates thermally treated with different parameters. The target heat treatment temperature is 250 °C for all samples. **a,** $CuSbSe_2$ thin film thermally treated on a preheated hotplate (250 °C) for 10 min. **b-d,** $CuSbSe_2$ thin films heated together with a cool hotplate from room temperature to 250 °C then kept for different durations. The duration is **b,** 10 min; **c,** 1 min; **d,** 50 min.

To pursue the latter strategy, I placed the samples on the hotplate at room temperature, before ramping up the temperature to 250 °C (ramp rate 30 °C min^{-1} as indicated by the hotplate reading), and keeping at this temperature for 10 min. The morphology of the samples treated with such "mild" heat treatment is presented in Fig. 5.2b, where the pinhole density is evidently lower than the original process (Fig. 5.2a). This comparison suggests that moderate thermal energy input is more suitable for the heat treatment of the solution-processed $CuSbSe_2$

thin films, and this mild heat treatment was adopted for all subsequent films.

In addition to the initial temperature of the hotplate, another studied parameter is the duration at the target temperature (250 °C). The morphology of $CuSbSe_2$ thin films thermally treated for 10, 1 and 50 minutes is illustrated in Fig. 5.2b-d, respectively. Compared to the sample thermally treated for 10 minutes (Fig. 5.2b), the film thermally treated for 1 min (Fig. 5.2c) exhibits more grain clusters, indicating that more time is needed for diffusion, grain growth and homogenisation of the film morphology. On the contrary, the 50-minute heat treatment (Fig. 5.2d) results in the complete absence of clusters, as well as more pinholes, which can be caused by the evaporation of the film during the long heat treatment period. Combining these observations, it can be concluded that moderate thermal energy input at the beginning of heat treatment and restriction of the heat treatment duration (10 min in my study) can lead to $CuSbSe_2$ thin films with the lowest density of grain clusters and pinholes. These heat treatment parameters are applied to all $CuSbSe_2$ thin films involved in the following studies.

5.2.2.2 Effects of underlayers

To fabricate solar cells, the absorber layer is usually deposited on electron or hole transport layers. It has been reported that the substrates used, or any surface modifications made on the substrates, can have a significant effect on the morphology and quality of spin-coated thin films[122,299-301]. Therefore, it is important to examine the morphology of the solution-processed $CuSbSe_2$ thin films on different underlayers. In this study, I compared the effects of three

potential ETLs: compact TiO_2 (c-TiO_2), mesoporous TiO_2 (mp-TiO_2) and SnO_2 nanocrystal thin films, as well as one HTL: NiO_x made by solution processing. As displayed in Fig. 5.3a, the $CuSbSe_2$ thin film on c-TiO_2 exhibits the highest density of pinholes and grain clusters. The pinholes can be the paths where the ETL and HTL contact each other and shunt the devices. Thus, the density of pinholes and other structural defects should be minimised to achieve better device performance. mp-TiO_2, as a common interlayer to improve the morphology of the absorber layer in solar cells, can form a porous scaffold and act as a host matrix into which the upper material can be embedded. For the mp-TiO_2/$CuSbSe_2$ sample (Fig. 5.3b), a rougher surface can be observed, which can be attributed to the structure of mp-TiO_2. Its density of pinholes is lower than the c-TiO_2/$CuSbSe_2$ sample, but some pinholes penetrating through the $CuSbSe_2$ layer could still be observed from scanning electron microscopy. On the other hand, the $CuSbSe_2$ thin film on SnO_2 shows fewer pinholes than the c-TiO_2/$CuSbSe_2$ sample and more large flake grains. The flake grains reflect the quasi-2D crystal structure of $CuSbSe_2$, and the overlap between these grains may prevent the contact of ETL and HTL through pinholes penetrating the whole $CuSbSe_2$ film.

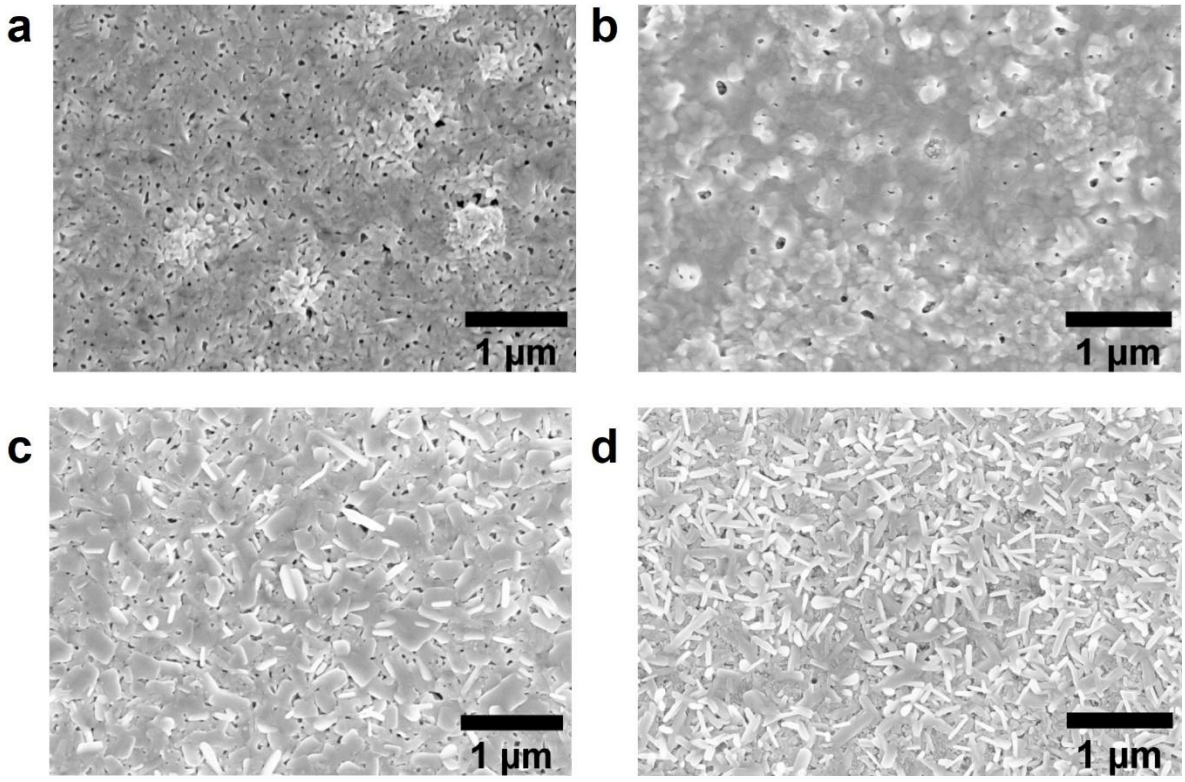

Fig. 5.3 | Top-view SEM images of the solution-processed $CuSbSe_2$ thin films deposited on different underlayers. All samples were thermally treated at 250 ℃ for 10 min. The layer under $CuSbSe_2$ is **a,** compact TiO_2 (c-TiO_2); **b** meso-porous TiO_2 (mp-TiO_2); **c,** SnO_2; **d,** NiO_x.

Alternatively, a p-i-n device structure can also be utilized by depositing $CuSbSe_2$ films onto HTLs, such as NiO_x. The microscopic morphology of NiO_x/$CuSbSe_2$ is illustrated in Fig. 5.3d. Compared with the SnO_2/$CuSbSe_2$ sample, the $CuSbSe_2$ film on NiO_x has fewer pinholes, indicating that devices with this structure may be less likely to be shunted. Therefore, the structure of ITO/NiO_x/$CuSbSe_2$/ETL/metal contact is selected for the solar cells based on the solution-processed $CuSbSe_2$ thin films. To explore a suitable ETL, PCBM was first spin-coated onto $CuSbSe_2$. However, due to the rod-like $CuSbSe_2$ grains making a rough surface, PCBM could not cover the whole surface. To deposit a compact ETL on the rough $CuSbSe_2$ surface,

atomic layer deposition (ALD) was finally employed to deposit ZnO as the ETL of the p-i-n structured $CuSbSe_2$ solar cells. ALD was chosen because it is able to meet the needs for atomic layer control and conformal deposition on complex surfaces[302].

5.2.2.3 Other methods to optimise film morphology

After confirming the effects of heat treatment parameters and underlayers on the morphology of the solution-processed $CuSbSe_2$ thin films, I explored other methods to optimise film morphology. Firstly, as discussed in Section 5.2.1, the relatively moderate thermal energy input at the beginning of the heat treatment process can improve the film morphology. To further modulate the thermal energy input, two more heat treatment steps were added prior to the 250 ℃ treatment: heat treatment at 60 ℃ for 0 or 5 min, followed by 100 ℃ for 0 or 2 or 5 min. The final heat treatment step was still at 250 ℃ for 10 min for all samples. The morphology of the films is compared in Fig. 5.4a-d. It can be noticed that all samples show similar morphology despite the different durations of each heat treatment step. The density of pinholes and grain size of these samples have no significant differences, reflecting that the even lower rate of the thermal energy input cannot further optimise the morphology of the solution-processed $CuSbSe_2$ thin films.

Moreover, the antisolvent method was utilized to improve the $CuSbSe_2$ film morphology. Antisolvent treatment is a common method to optimise the morphology of solution-processed thin films, as introduced in Section 2.5.1. By dripping a “bad” solvent onto the spinning sample,

the “good” solvent is driven out much faster than simply through solvent evaporation during spinning, and the precursor solubility in the remaining solution is reduced upon mixing the antisolvent into it. In this case, rapid supersaturation can be achieved, hence forming a high density of nuclei simultaneously[122,303,304]. This can result in a uniform and dense film. In this project, I dripped 75 μL methylbenzene onto the spinning film 20 s before the end, then placed the sample on a hotplate at room temperature. The sample and the hotplate were heated together to 250 ℃, then kept for 10 min. As shown in Fig. 5.4e, the $CuSbSe_2$ film treated with methylbenzene antisolvent exhibits a similar morphology to the sample displayed in Fig. 5.2a. Since the latter was obtained by thermal treatment on a preheated hotplate after the spin coating, the similar morphology of these two samples can be caused by the rapid removal of the remaining solvent. Also, Fig. 5.4f shows the morphology of the $CuSbSe_2$ film on SnO_2 treated with propan-2-ol as the antisolvent. The antisolvent volume and dripping time are the same as the methylbenzene-treated sample. Compared to the untreated SnO_2/$CuSbSe_2$ sample (Fig. 5.3c), using the propan-2-ol antisolvent results in some larger pinholes and grain clusters. Such comparisons indicate that extremely fast removal of the remaining solvent is not favourable for solution-processed $CuSbSe_2$ thin films based on our thiol-amine route.

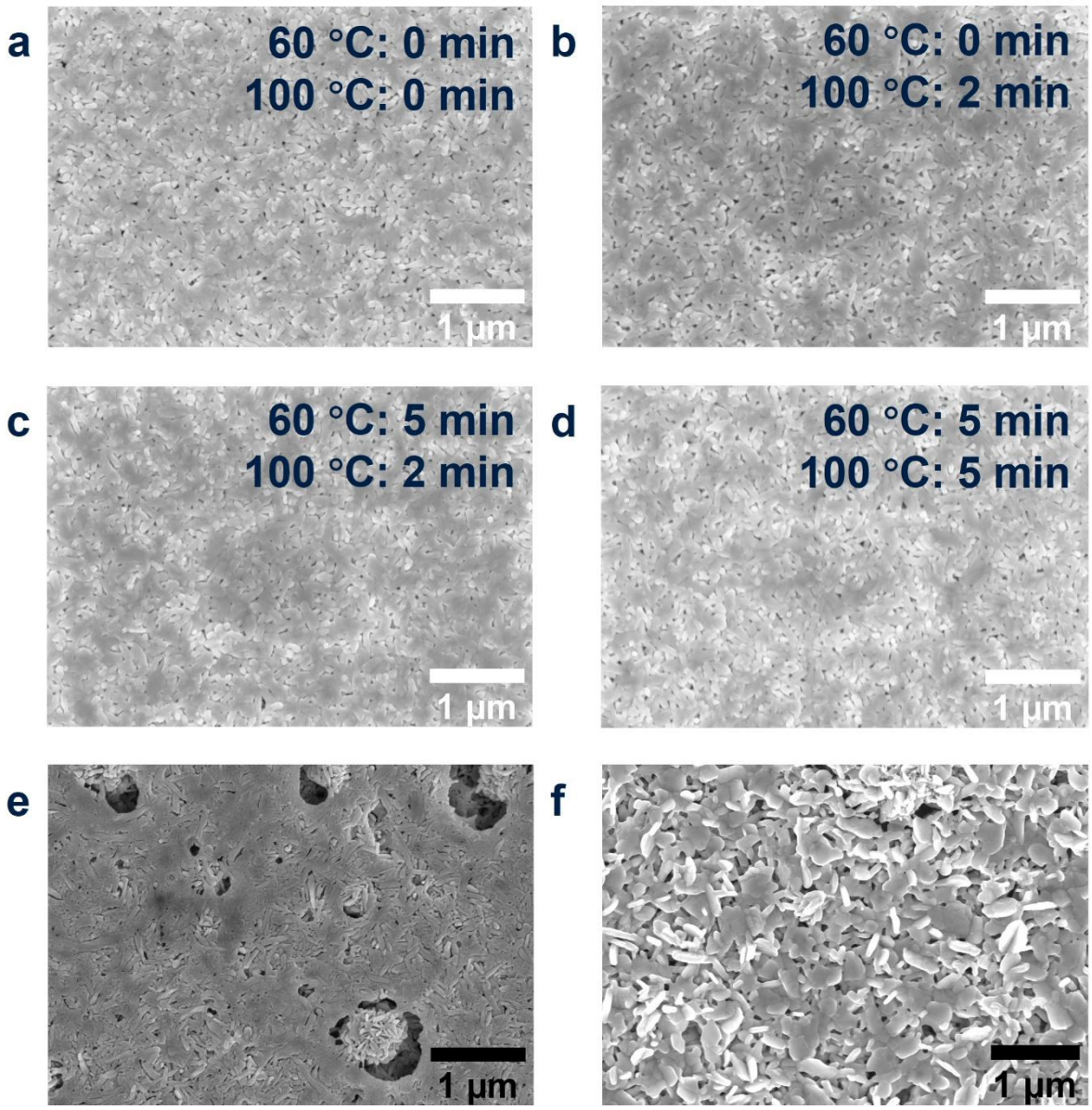

Fig. 5.4 | Top-view SEM images of the solution-processed $CuSbSe_2$ thin films prepared with multi-step heat treatment or antisolvent treatment. a-d, multi-step heat treatment. The durations for the heat treatment at 60 ℃ and 100 ℃ are labelled in the figures. The final step for all samples is heat treatment at 250 ℃ for 10 min. Samples are **a,** 0 0; **b,** 0 2; **c,** 5 2; **d,** 5 5. **e and f,** antisolvent treatment. 75 µL antisolvent of **e,** methylbenzene or **f,** propan-2-ol is applied 20 seconds before the spin coating ends. Both samples are thermally treated at 250 ℃ for 10 min after the spin coating.

5.3 Characterisation of chemical-vapour-deposited $CuSbSe_2$ thin film

5.3.1 Exploring the optimal CVD parameters

As discussed in the prior work on the RCSS of $CuSbSe_2$ films[118], the parameters that can influence the deposited films include the substrate temperature and the evaporation time of the Sb_2Se_3 precursor. For our CVD setup, by setting different temperatures for the centre and sides zones, a downward temperature gradient from the centre to the edges of the tube can be created. Thus, the substrates placed at different positions inside the tube exhibit different substrate temperatures. Another difference between the reported RCSS method and our CVD method is the use of carrier gas. The smaller RCSS chamber does not require any carrier gas, while our setup needs Ar as the carrier gas to transfer the Sb_2Se_3 vapour to different positions in the tube. Therefore, the working pressure during the deposition, which determines the flow rate of the Sb_2Se_3 vapour, can also affect the quality of the CVD $CuSbSe_2$ films.

Table 5.3 | Summary of parameters used for the CVD growth of $CuSbSe_2$ thin films. Investigated parameters include the substrate temperature (controlled by the sample position), the evaporation time and the working pressure. The temperatures of zones were set identically for all samples (*i.e.*, the centre zone at 580 ℃; the side zones at 530 ℃).

Batch ID	Sample position	Evaporation time (min)	Working pressure (mTorr)
0713	R8	5	600
	R10		
	R12		
	L8		
	L10		
	L12		
0704	L8	4	600
0721			317
0727			50
0704	R10	4	600
0713		5	

In this study, I explored the optimal experimental parameters by examining the phase purity of CVD $CuSbSe_2$ thin films. The conditions of the investigated samples are summarized in Table 5.3. The first investigated parameter is the substrate temperature. As illustrated in Fig. 3.2, a series of glass or silicon substrates coated with Cu were positioned at 2-16 cm away from the edge of the side zones with a 2-cm interval between adjacent samples. The positions were labelled as R2, R4 … R16 for the right size zone, and L2, L4 … L16 for the left side zone. All samples for XRD measurements were deposited on Si substrates. To analyse the effect of substrate temperature, the evaporation time of 5 min and the working pressure of 600 mTorr were employed (batch ID 0713). The XRD patterns of the samples in the right zone containing

$CuSbSe_2$ phase are compared in Fig. 5.5a, where the peaks belonging to impurity phase Cu_3SbSe_3 are indicated by blue dots.

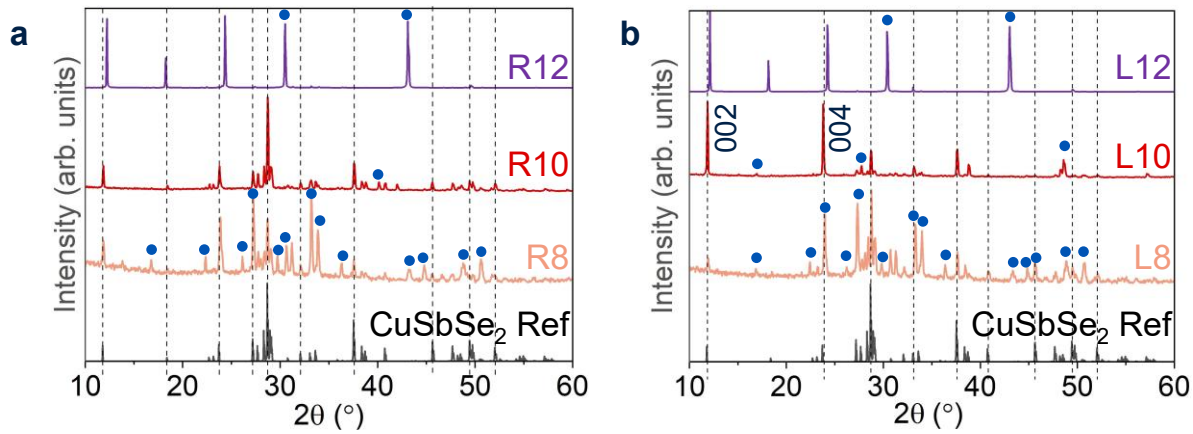

Fig. 5.5 | XRD patterns of the CVD $CuSbSe_2$ thin films deposited with different substrate temperatures. Substrates at different positions exhibited different temperatures due to the temperature gradient within the tube. Comparison between the $CuSbSe_2$ reference pattern (black, ICSD database, coll. code 418754) and the XRD patterns of the samples in **a,** the right zone, denoted as RX; **b,** the left zone, denoted as LX. Main peaks belonging to.$CuSbSe_2$ are indicated by dashed lines, while peaks from Cu_3SbSe_3 are highlighted by blue dots.

For R12 (purple line), which is the closest to the centre, the peaks belonging to Cu_3SbSe_3 have high intensities, indicating its large amount. The other two strong peaks (2θ = 12.23° and 24.34°) might come from $Cu_{2-x}Se$ polymorph or other impurity phases[118]. In comparison, most peaks of sample R10 (red line), which is 2 cm further away from the centre than R12, better match with the $CuSbSe_2$ reference pattern (black, ICSD database, coll. code 418754), with only one peak coming from the Cu_3SbSe_3 phase (2θ = 40.14°). When moving another 2 cm away from the centre, the sample R8 (pink line) exhibits the mixture of $CuSbSe_2$ and Cu_3SbSe_3

phases. The different XRD patterns of the samples with different substrate temperatures can be explained by the evaporation process of Sb_2Se_3. As previously reported, Sb_2Se_3 is partially decomposed and releases Se vapour during the evaporation process[118,305], which firstly reaches and selenizes the nearest Cu film. Therefore, $Cu_{2-x}Se$ polymorph can be observed in the R12 sample. Meanwhile, since Sb_2Se_3 and Se both have much higher vapour pressure than Sb, the Sb reactant can only be transferred to the Cu films in the form of Sb_2Se_3 vapour. After Se vapour reacts with the Cu film at position R12, Sb_2Se_3 vapour can be carried to further positions and react with subsequent Cu films. Thus, at the position R10, the Sb_2Se_3 vapour reacts with the Cu film to form the desired $CuSbSe_2$ phase. Also, the lower substrate temperature of R10 than R12 results in more Sb_2Se_3 vapour condensed onto the Cu film surface. Due to the condensation of Sb_2Se_3 vapour at R10, the Cu film at the further position R8 may undergo a deficiency of the Sb source, even if its substrate temperature is lower, which explains the co-existence of $CuSbSe_2$ and Cu_3SbSe_3 phases.

Similar results are also observed in the left zone. As shown in Fig. 5.5b, the optimal film with the lowest content of impurity phases is obtained at position L10, while the sample L12 shows strong Cu_3SbSe_3 and $Cu_{2-x}Se$ peaks, and sample L8 contains both $CuSbSe_2$ and Cu_3SbSe_3 phases. Moreover, the stronger peaks of the 002 and 004 crystal planes in the sample L10 demonstrate its preferred *c*-axis orientation compared to the sample R10, even though these two samples have the same sample-precursor distance, indicating that the depositions in the left and right zones are not strictly symmetric. Among all samples mentioned above, the sample R12 shows the best phase purity, which is deposited with an evaporation time of 5 min, a

working pressure of 600 mTorr, and a distance to the right zone edge of 10 cm.

It should also be noted that the distance between the adjacent samples in the same zone is only 2 cm, but they possess distinct XRD patterns, which suggests the significant effect of substrate temperature on the phase purity of CVD $CuSbSe_2$ thin films, as well as the sharp temperature gradient within the deposition region. To better verify this, I performed temperature profiling at different positions in the tube while employing the identical temperature setting for each zone (580 °C for the centre zone while 530 °C for the side zones). As displayed in Fig. 5.6, the temperature across zone 2, where the Sb_2Se_3 precursor is placed, does not have significant changes. By contrast, a sharp temperature gradient is observed in the left side zone. Especially in the region where films containing $CuSbSe_2$ phase are deposited (about 8-12 cm), a temperature gradient of 35 °C cm^{-1} was obtained. A similarly sharp temperature gradient is also found in the right side zone. Such large changes in the substrate temperature result in distinct changes in the phase purity of adjacent samples. To improve the scalability of the CVD method, a less steep temperature gradient is required across the deposition region.

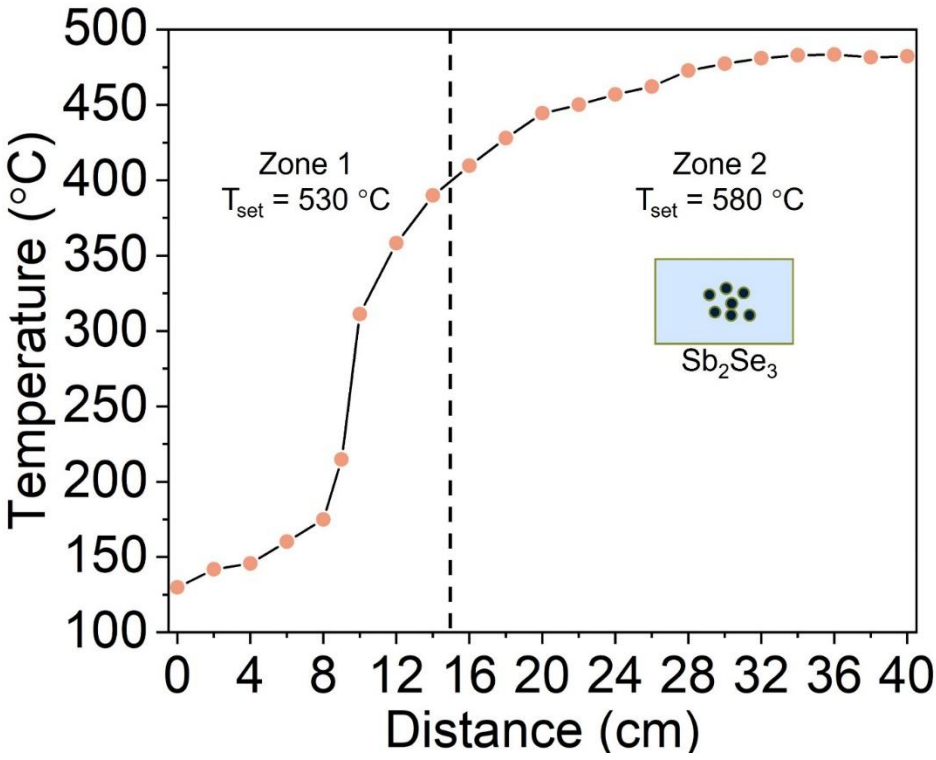

Fig. 5.6 | Temperature profiling of the tube furnace used for CVD of $CuSbSe_2$. The temperature of each zone is set identically as the deposition process (*i.e.*, T_{set} for zone 1 and 2 is 530 °C and 580 °C, respectively). The origin point of the distance is the edge of zone 1, and the Sb_2Se_3 precursor is positioned at 30 cm. The length of zone 1 (and 3) is 15 cm. The region where films containing the $CuSbSe_2$ phase are deposited is at a distance of 8-12 cm.

After examining the effect of the substrate temperature, other parameters, including the working pressure and evaporation time, are also investigated. Fig. 5.7a compares the XRD patterns of three samples at position L8 (batch ID 0704, 0721, 0727). An evaporation time of 4 min and different working pressures are employed. With a relatively low working pressure (49 or 317 mTorr), films containing the $CuSbSe_2$ phase were obtained. When the working pressure is increased to 600 mTorr, no obvious $CuSbSe_2$ peak can be observed in the XRD pattern. At higher working pressures, there was a higher flow rate of the carrier gas. Thus,

600 mTorr working pressure may lead to the fast flow of the Sb_2Se_3 vapour, and thus the insufficient reaction between the Cu film and Sb_2Se_3. This explains the absence of the $CuSbSe_2$ phase in the 600-mTorr sample, while the other two samples show a mixture of $CuSbSe_2$ and Cu_3SbSe_3 phases. This comparison indicates that the working pressure also has a significant effect on the phase purity of the CVD films. It should be noted that all samples deposited with a 4-minute evaporation time exhibit Cu_3SbSe_3 (indicated by blue dots) or Cu_3SbSe_4 (indicated by blue triangles) impurity phases, regardless of the variations in working pressure and substrate temperature. Therefore, the effect of evaporation time should be considered as well.

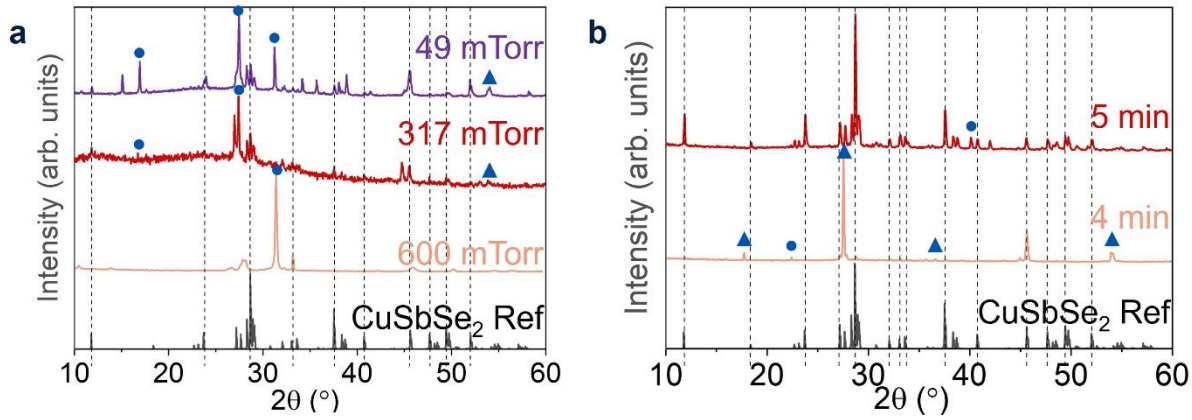

Fig. 5.7 | Effects of the working pressure and evaporation time on the phase purity of the CVD $CuSbSe_2$ thin films. a, XRD patterns of the samples deposited with the working pressure of 600 (pink), 317 (red) and 49 mTorr (purple), along with the $CuSbSe_2$ reference pattern (black, ICSD database, coll. code 418754). All samples are positioned at L8 and employ the evaporation time of 4 minutes; **b,** XRD patterns of the samples deposited with the evaporation time of 4 (pink) and 5 minutes (red), along with the $CuSbSe_2$ reference pattern (black). Both samples are positioned at R10 and employ the working pressure of 600 mTorr. In both figures, main peaks belonging to $CuSbSe_2$ are indicated by dashed lines, while peaks from Cu_3SbSe_3

and Cu_3SbSe_4 are marked by blue dots and triangles, respectively.

Fig. 5.7b shows the XRD patterns of the films deposited with evaporation times of 4 and 5 minutes (batch ID 0704, 0713). For both samples, a working pressure of 600 mTorr and substrate position of R10 are employed. Most peaks in the XRD pattern of the 4-min sample come from Cu_3SbSe_3 (indicated by blue dots) or Cu_3SbSe_4 (indicated by blue triangles) phases, while $CuSbSe_2$ is the dominant phase of the 5-min sample, with only one minor peak belonging to the Cu_3SbSe_3 phase ($2\theta = 40.14°$). Such differences demonstrate that the 4-minute evaporation cannot provide sufficient Sb_2Se_3 vapour to react with the Cu film, leading to the formation of Cu-rich impurities. With longer evaporation time, more generated Sb_2Se_3 vapour can further react with the impurity phases to form the desired $CuSbSe_2$ phase. Overall, by considering samples deposited with various parameters, we can confirm the optimal CVD parameters to be the substrate position of R10, the working pressure of 600 mTorr, and the evaporation time of 5 minutes. Combining these parameters, nearly phase-pure $CuSbSe_2$ thin films can be obtained via our CVD method. The thickness of the nearly phase-pure $CuSbSe_2$ thin film was 2000 ± 190 nm, measured by a Dektak® stylus profilometer.

5.3.2 $CuSbSe_2$ thin film morphology

After confirming the optimal parameters to obtain nearly phase-pure $CuSbSe_2$ thin films by CVD, the morphology of the films with $CuSbSe_2$ as the dominant phase is observed. As discussed in the previous section, the main limitation of the CVD setup is the steep temperature

gradient within the deposition region. Therefore, to maximize the number of samples with the desired phase purity in each deposition process, another substrate is positioned right next to position R10 (*i.e.*, the sample interval is 1 cm instead of 2 cm), which is labelled as R11. The morphology of the CVD $CuSbSe_2$ films deposited on glass substrates at position R10 and R11 is compared in Fig. 5.8a and b. Compared to the sample at R10 (Fig. 5.8a), the one at R11 (Fig. 5.8b) exhibits significantly larger grains. This can be explained by the higher substrate temperature at R11 than R10, as R11 is closer to the high-temperature zone 2, which facilitates the grain coarsening.

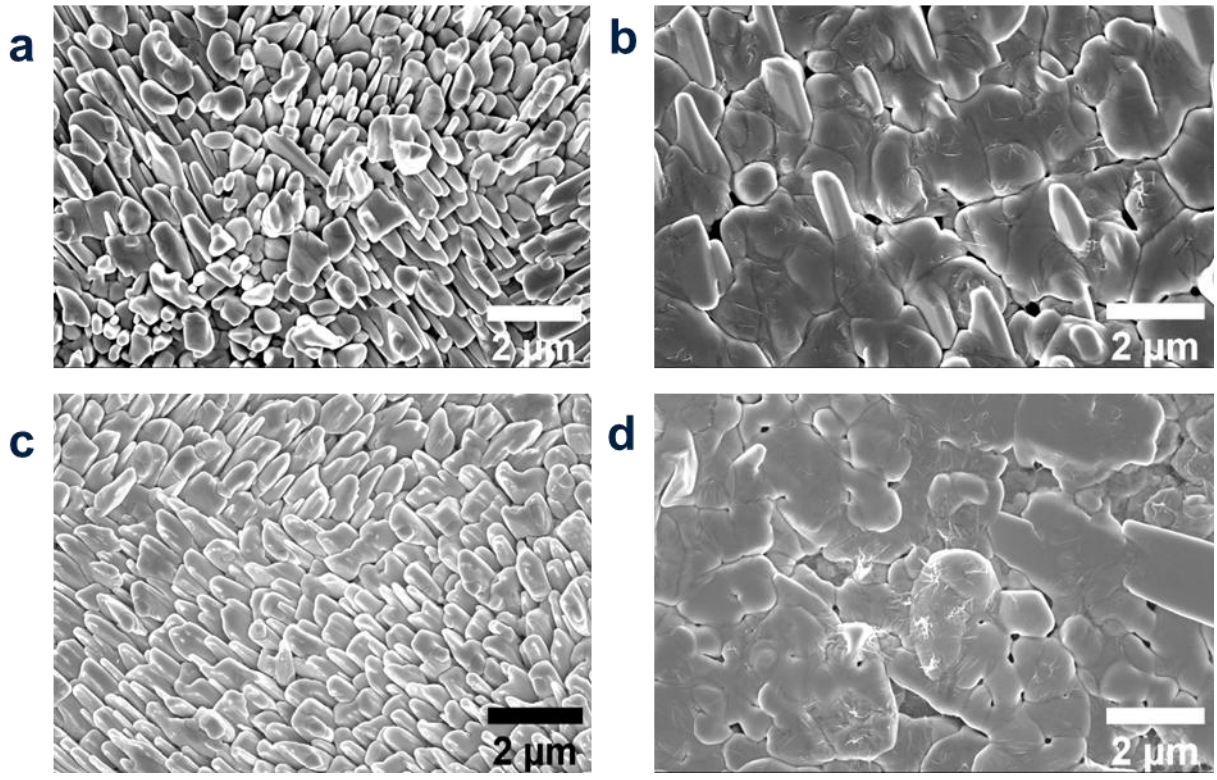

Fig. 5.8 | Top-view SEM images of the CVD $CuSbSe_2$ thin films deposited with different substrate temperatures and underlayers. The film is deposited on glass (**a** and **b**) or glass/ZnO (**c** and **d**) substrates at position R10 (**a** and **c**) or R11 (**b** and **d**).

In addition to the different grain sizes, it is also noticed that the films deposited at lower substrate temperature (R10, Fig. 5.8a) show more randomly oriented grains, while the grains in the sample with higher substrate temperature (R11, Fig. 5.8b) exhibit more planar features parallel to the substrate surface. To investigate the change in the crystal orientation, XRD patterns of these samples are compared in Fig. 5.9a. An obviously enhanced orientation of the (001) planes can be observed when moving from R10 to R11. As a quantitative analysis, the texture coefficients of the main crystal planes are calculated and displayed in Fig. 5.9b. Since the texture coefficients higher than 1 indicate texturing towards this orientation, it can be concluded that the sample at R10 is slightly *c*-axis oriented, and such a preferred orientation is substantially enhanced in the sample at R11. The alignment for the XRD measurements is described in Section 3.3.1. It should be clarified that the texture coefficients reported here reflect relative differences in texturing between samples, and are not intended as absolute values of preferred orientation. The changes in the texture coefficients as the substrate temperature increases agree with the previous study on the heat treatment of $CuSbSe_2$ thin films. As reported by Yang *et al.*, the texture coefficient of (001) planes increases with higher heat treatment temperature, which can be rationalised by the lower surface energy of (001) planes than other crystal planes[121]. By enhancing the *c*-axis orientation, the total energy of the system can be reduced, which provides the driving force for crystal growth[306]. Thus, both larger grain size and stronger *c*-axis orientation are observed in the CVD $CuSbSe_2$ thin films at R11, because the higher substrate temperature facilitates atomic diffusion and realignment by delivering more thermal energy.

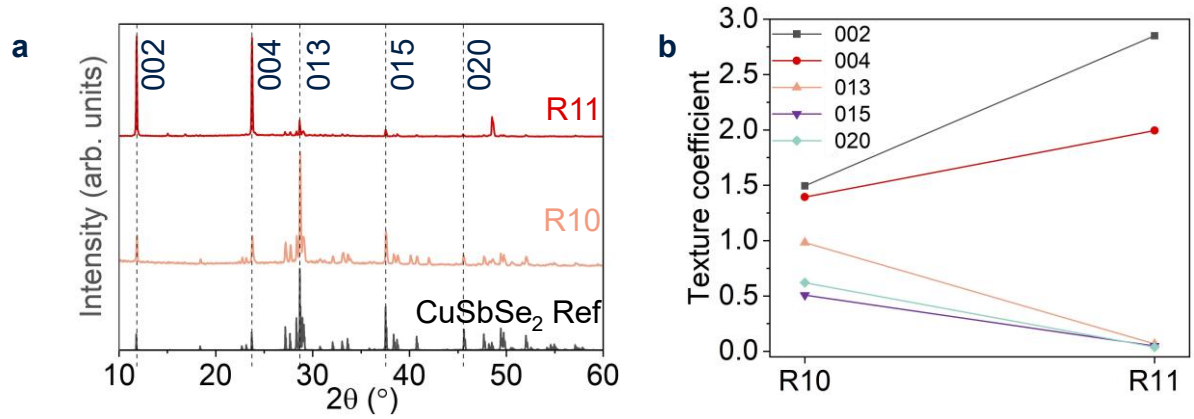

Fig. 5.9 | Comparison of the XRD patterns and preferred crystal orientation of the CVD $CuSbSe_2$ thin films. a, comparison of the XRD patterns of the nearly phase-pure CVD $CuSbSe_2$ thin films deposited at position R10 (pink) and R11 (red), along with the $CuSbSe_2$ reference pattern (black). The crystal planes investigated for texture coefficients are indicated by dashed lines with their Miller indices. Both samples were deposited on Si substrates. **b,** texture coefficients of the crystal planes in the CVD $CuSbSe_2$ thin films deposited at position R10 (left) and R11 (right).

As analysed in Section 5.2.2.2, the underlayer can influence the morphology of solution-processed $CuSbSe_2$ thin films. Similar observations have also been found for CVD $CuSbSe_2$ thin films, which are shown in Fig. 5.8. The samples deposited on either glass (Fig. 5.8a and c) or glass/ZnO (Fig. 5.8b and d) substrates show similar macrostructural features, demonstrating the negligible effect of the underlayer on the film morphology. The difference between the solution-processed and CVD $CuSbSe_2$ thin films can be attributed to the deposition mechanisms of the two methods. During solution processing, nucleation takes place within the solution or on the solution-substrate interface. Therefore, properties such as surface energy and roughness of the surface onto which the precursor solution is spin-coated can influence the

nucleation and growth of the thin film. By contrast, the CVD $CuSbSe_2$ thin films are formed via the reaction between the pre-sputtered Cu films and Sb_2Se_3 vapour. In this case, the substrates are all covered with Cu despite different layers under the Cu films, so the underlayer has minimal effects on the film morphology. Meanwhile, compared to the solution-processed $CuSbSe_2$ thin films, the CVD $CuSbSe_2$ films exhibit improved coverage, increased thickness and larger grains.

5.4 Characterisation of $CuSbSe_2$-based photovoltaic devices

5.4.1 Characterisation of solution-processed $CuSbSe_2$ photovoltaic devices

After optimising the morphology of the solution-processed $CuSbSe_2$ thin films by modulating the heat treatment parameters and underlayers, I found that the best morphology was obtained from $CuSbSe_2$ deposited onto ITO/NiO_x. I therefore proceeded to fabricate a device with the structure ITO/NiO_x/$CuSbSe_2$/ZnO/Ag. The schematic of the device structure is given in Fig. 5.10a, and the typical J-V curves of the solar cell based on the solution-processed $CuSbSe_2$ thin films under dark and illumination conditions are shown in Fig. 5.10b. Even though the illuminated solar cell has a slightly higher current density, resistor-like J-V curves are observed under both conditions, demonstrating the shunting problem of the device. It should be noted that more than 20 pixels with such a structure are tested, as well as solar cells with other structures as listed in Section 3.4, but all of them show resistor-like J-V curves. The shunted devices can be attributed to the high density of pinholes in the solution-processed $CuSbSe_2$ thin

films. Another possible reason is the intrinsic p-type conductivity of $CuSbSe_2$, making the n-i-p or p-i-n device structures unsuitable. This may also explain why CdS/$CuSbSe_2$ is the most used device structure so far[112,117,307].

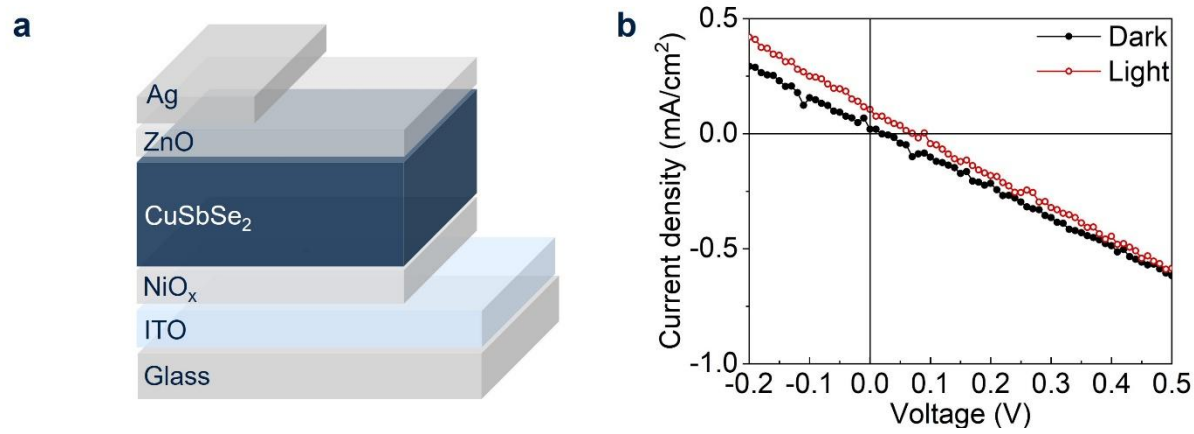

Fig. 5.10 | Device structure and IV curves of the solar cells based on solution-processed $CuSbSe_2$ thin films. a, Schematic of the employed device structure. The pixel area is 0.045 cm^2. **b,** J-V curves of one pixel under dark (black) and illumination (red) conditions.

5.4.2 Characterisation of chemical-vapour-deposited $CuSbSe_2$ photovoltaic devices

Considering the results that $CuSbSe_2$ solar cells with p-i-n or n-i-p structures were shunted and all reported studies on $CuSbSe_2$ solar cells used the simpler p-n structure[112,117,118], a p-n device structure, ITO/ZnO/$CuSbSe_2$/Au, is used for the CVD $CuSbSe_2$-based solar cells (Fig. 5.11a). According to Section 5.3.2, the films deposited at positions R10 and R11 are nearly phase-pure and have no obvious pinholes penetrating through the whole films, so these films are used to fabricate solar cells. Out of 12 pixels with a device area of 4.5 mm^2, two pixels show rectifying behaviour in their J-V curves, as displayed in Fig. 5.11b. However, these *J-V* curves pass

through the origin, indicating that there was no photocurrent extracted from these devices. This can arise due to shunting still being present in these devices, high rates of non-radiative recombination within the bulk or at interfaces, or poor charge-carrier extraction. Meanwhile, the different performance of solar cells based on solution-processed and CVD $CuSbSe_2$ thin films cannot be solely attributed to variations in device structure, as the two techniques yield films with distinct coverage, thickness, and grain size. Therefore, further investigation is required to identify the key factors influencing device performance.

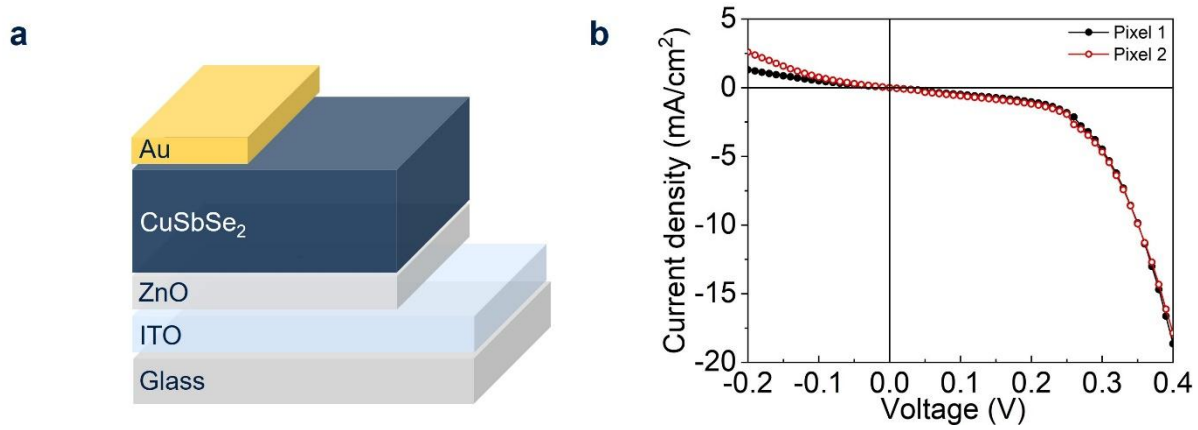

Fig. 5.11 | Device structure and IV curves of the solar cells based on CVD $CuSbSe_2$ thin films. a, Schematic of the employed device structure. The pixel area is 0.045 cm^2. **b,** J-V curves of two different pixels under illumination (AM 1.5G) condition.

5.5 Conclusions

In conclusion, two novel deposition methods, thiol-amine-based solution processing and CVD, have been developed to deposit $CuSbSe_2$ thin films, which are subsequently used to fabricate solar cells. For the solution-processed $CuSbSe_2$ thin films, XPS is used to confirm the chemical

states of elements, while EDX is used to measure the bulk composition. By investigating the factors influencing film morphology, it has been found that too rapid removal of the remaining solvent, achieved by either intense thermal energy input during the heat treatment process or applying antisolvent during the spin coating, results in a high density of structural defects. By tuning the thermal energy input at the beginning of the heat treatment process and the total heat treatment duration, the morphology of solution-processed $CuSbSe_2$ thin films has been optimised. Moreover, the underlayer has been found as another factor significantly affecting the film morphology, suggesting the important role of the surface energy of the substrate. By contrast, the exploration of the optimal CVD parameters to deposit phase-pure $CuSbSe_2$ thin films demonstrates that the substrate temperature, as well as the working pressure and evaporation time to be the main factors determining the properties of the CVD $CuSbSe_2$ thin films. The distinct XRD patterns of adjacent samples imply a sharp temperature gradient within the deposition region, which is further confirmed to be about 35 °C cm^{-1} through temperature profiling. This is a key limitation of the CVD setup, since this results a only a narrow region in the furnace for achieving phase-pure $CbSbSe_2$ thin films. Compared to solution processing, CVD yields $CuSbSe_2$ thin films with better coverage, increased thickness and larger grains.

After establishing the optimal parameters of both methods to deposit $CuSbSe_2$ thin films with ideal phase purity and morphology, $CuSbSe_2$-based solar cells have been fabricated and characterised. Solar cells based on solution-processed $CuSbSe_2$ thin films show resistor-like J-V curves despite the various device structures, indicating shunting to be prevalent, due to the unsatisfactory film morphology. As for the solar cells based on CVD $CuSbSe_2$ thin films which

employ a simpler device structure, diode-like J-V curves have been observed for two pixels. However, since $CuSbSe_2$ films deposited with these two methods exhibit different coverage, thickness and grain size, the key factors to enhance the performance of $CuSbSe_2$-based solar cells may need further investigation.

Overall, this work explores two techniques for depositing $CuSbSe_2$ thin films, offering enhanced safety compared to the previously-reported hydrazine-based solution processing method. The analysis of deposition and post-treatment parameters provides valuable insights into optimising $CuSbSe_2$ thin film quality. To enable a more effective comparison of deposition techniques for $CuSbSe_2$ thin films and to better understand the factors governing the performance of $CuSbSe_2$-based solar cells, properties such as $CuSbSe_2$ film thickness, grain size, and device structure should be examined independently.

5.6 Future work

For the thiol-amine route, pinholes and small grains in the $CuSbSe_2$ films, caused by rapid solvent removal, are key limitations. A "softer" heat treatment process with gradual solvent removal could improve film morphology. For example, solvent heat treatment in a solvent-vapour atmosphere has improved grain size and compactness in perovskite films[157,308,309], suggesting similar strategies may benefit the thiol-amine route. Moreover, besides EDT and en used in this work, various thiols (*e.g.*, 2-sulfanylethan-1-ol [115]) and amines (*e.g.*, hexan-1-amine [292], propan-1-amine [310]) with different thiol/amine ratios[156,310] have been employed to dissolve

chalcogenide precursors. This offers more parameter space to explore the optimal recipe for depositing $CuSbSe_2$ thin films.

As for the CVD method, the film quality and scalability are predominantly limited by the steep temperature gradient. To overcome this issue, either a furnace with better temperature control or a different temperature setup (*e.g.*, temperature continuously decreasing from one side zone to the other) is needed. By achieving a gentler temperature gradient, along with tuning other parameters (working pressure, evaporation time, etc.) accordingly, scalable deposition of phase-pure $CuSbSe_2$ thin films can be expected.

Regarding $CuSbSe_2$ solar cells, proper device structure and optimised film quality are the potential directions of investigation proposed from this work. Considering that some solar cells based on $ZnO/CuSbSe_2$ show diode-like J-V curves, the development of $CuSbSe_2$ solar cells using benign ETLs rather than CdS is also worth more efforts.

Chapter 6: Investigating effects of buffer layers on chemical bath deposited Sb_2S_3

One key limitation of Sb_2S_3 solar cells is the toxicity of the Cd used in the CdS buffer layer, which is widely used in these devices. This study investigates the use of SnO_2 as a benign alternative to CdS for Sb_2S_3 solar cells. Deposition of Sb_2S_3 on SnO_2 resulted in discontinuous Sb_2S_3 films with pinholes, attributed to the different nucleation behaviour of Sb_2S_3 on SnO_2 compared to CdS. EDX mapping confirmed that isolated spherical Sb_2S_3 nuclei form on the surface of SnO_2, indicating the difficulty of heterogeneous nucleation of Sb_2S_3. XPS analysis indicated that Sb predominantly bonds with oxygen on SnO_2, forming Sb_2O_3 and hindering Sb_2S_3 nucleation. Moreover, using CdS as an interfacial layer (~30 nm) between SnO_2 and Sb_2S_3 enabled compact Sb_2S_3 film morphology while reducing the Cd content by ~50%. This highlights the potential of other sulphide interfacial layers to optimise Sb_2S_3 film morphology and achieve solar cells with reduced Cd content. Our Sb_2S_3 solar cells also demonstrated impressive performance under 1-sun illumination, with V_{OC} values comparable to the highest reported (0.796 V[133]). Optical loss analysis identified device reflection and window layer parasitic absorption as key challenges, suggesting anti-reflection coatings and more transparent buffer layers as future improvement strategies. Overall, this work elucidates the mechanisms by which CdS outperforms SnO_2 as a buffer layer for Sb_2S_3 solar cells and proves the promising potential of Sb_2S_3 solar cells for indoor light harvesting. Our study also offers valuable guidance for developing more environmentally benign buffer layers and optimising Sb_2S_3 solar cell performance.

The contributions from other researchers include:

Chia-Yu Chang and Yi-Teng Huang helped with the operation of the scanning electron microscope and energy dispersive X-ray spectroscopy, and collected the data. Mark Isaacs performed the X-ray photoelectron spectroscopy and collected the data. Xiaoyu Guo and Huimin Zhu performed the J-V characterisation and external quantum efficiency measurements and collected the data. Emma Setzer developed the script for optical loss analysis. Yuchen Fu performed all other synthesis and measurements and analysed all data included in the chapter.

6.1 Introduction

Sb_2S_3 is regarded as a promising absorber material for solar cells due to its composition of benign elements, and high optical absorption coefficient (> 10^4 cm^{-1} when $\lambda < 700$ nm)[125,311]. The wide bandgap of Sb_2S_3 (1.7 eV) also makes it a suitable candidate for the top cell of tandem photovoltaics, or for harvesting energy from indoor light sources, which commonly emit within the visible wavelength range[42]. As discussed in Section 3.2, various techniques have been employed to deposit Sb_2S_3 thin films. Chemical bath deposition (CBD) is one of the most used methods due to its simple operation, low cost and potential for scalable production[177]. Meanwhile, different device structures have been developed for Sb_2S_3 solar cells. One of the earliest device architectures was the meso-superstructured device, consisting of a compact TiO_2 and mesoporous TiO_2 buffer layer. However, with this design, the highest device performance with CBD-grown Sb_2S_3 has remained at 7.5% PCE since 2014 [131]. Similarly, planar Sb_2S_3 solar

cells using compact TiO_2 as the buffer layer also presented unsatisfactory performance with the highest PCE of 4.61%[312]. Subsequent efforts replaced compact TiO_2 with a CdS buffer layer (or oxide/CdS double buffer layer), a material widely used for planar thin film solar cells. This adjustment successfully increased the record PCE to 8.00%[132]. However, the high toxicity of Cd hinders the widespread commercial applications of Sb_2S_3 solar cells with such a structure[42,290], leading to the development of more benign buffer layers, such as TiO_2 and SnO_2, to fabricate safer Sb_2S_3 solar cells. Previous studies have reported that the growth of Sb_2S_3 onto TiO_2 or SnO_2 can result in discontinuous Sb_2S_3 films with a high density of structural defects, significantly limiting the device performance. On the contrary, Sb_2S_3 films grown on CdS buffer layer (or oxide/CdS double buffer layer) exhibit a dense and flat surface morphology, resulting in a higher PCE [134,137,138]. Understanding the mechanism by which the CdS buffer layer enables compact Sb_2S_3 films can provide insights for designing benign alternatives, which is crucial for developing environmentally friendly Sb_2S_3 solar cells.

In this work, Sb_2S_3 thin films were deposited on different buffer layers (*i.e.*, CdS, SnO_2 and SnO_2/CdS) via chemical bath deposition. By observing the surface morphology of Sb_2S_3 thin films at the beginning stage of chemical bath deposition (*i.e.*, nucleation stage of Sb_2S_3), the effects of buffer layers on the nucleation process were elucidated. This, in turn, determined the final morphology of Sb_2S_3 thin films. Using EDX and XPS analysis, the interfacial chemistry between Sb_2S_3 and the buffer layers was investigated, and the critical factors facilitating the compact Sb_2S_3 thin films were proposed. My work provides insights into the strategies to develop non-hazardous buffer layers for Cd-free Sb_2S_3 solar cells and accelerate their practical

applications.

6.2 Preparation of buffer layers

As described in Sections 3.2 and 3.4, the Sb_2S_3 absorber layer and the CdS buffer layer were deposited using the CBD method. Although TiO_2 has been widely employed as the buffer layer for Sb_2S_3 solar cells, the performance has shown slight improvement over the past decade. Thus, SnO_2, rather than TiO_2, was selected as the candidate for forming a benign buffer layer in this study. Moreover, the lower processing temperature of SnO_2 made it a cost- and energy-efficient choice[313]. Spin coating is the most common deposition technique for the SnO_2 buffer layer[44,133,313], but it is not suitable for scalable fabrication. In contrast, the CBD method for depositing SnO_2 thin films has shown greater potential for scalability and successfully improved the performance of perovskite solar cells[171,314]. Therefore, in my project, the CBD method reported by Yoo *et al.*[171] was adopted to deposit SnO_2 buffer layer onto FTO substrates. During the CBD of SnO_2, the pH of the precursor solution gradually increased, accompanied by an evolution of the surface morphology. In halide perovskite solar cells, SnO_2 obtained at pH=1.5 (starting from an initial pH of 1) gave the best performance[171]. A similar increase in solution pH and morphology evolution was also observed in this project. After a 4-hour reaction, the pH remained at approximately 1 and the surface morphology of SnO_2 film (Fig. 6.1b) resembled that of blank FTO substrate (Fig. 6.1a), which could be attributed to the very thin SnO_2 film conforming to the underlying FTO layer. Extending the reaction time to 6 hours increased the solution pH to 1.5, which is the reported optimal condition for SnO_2 deposition.

The morphology of the deposited SnO_2 buffer layer was then more distinct from that of the FTO substrate, and is shown in Fig. 6.1c. The chemical bath deposition was stopped once the pH reached 1.5. The reaction time of 6 h was employed for all SnO_2 buffer layers studied in this project.

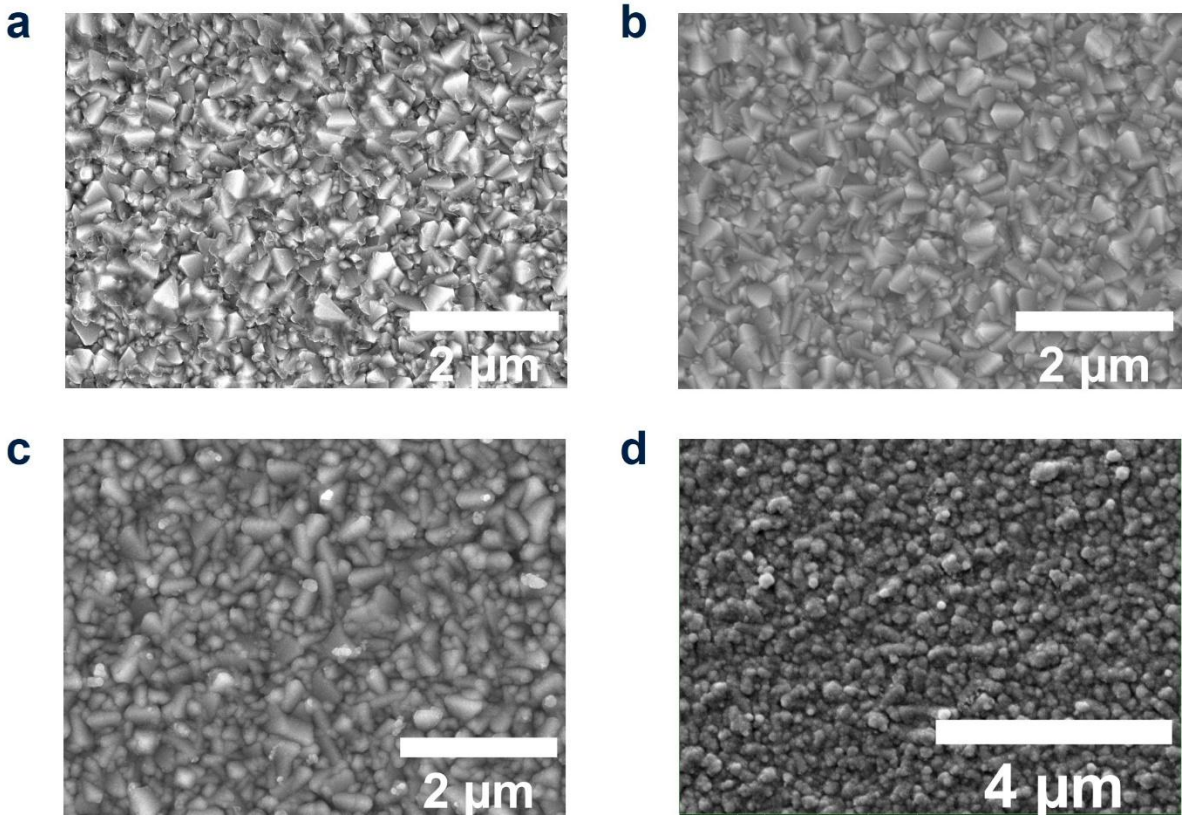

Fig. 6.1 | Top-view SEM images of FTO substrate and different buffer layers. a, Surface morphology of blank FTO substrate. **b,** Surface morphology of CBD SnO_2 after a 4-h reaction (pH $\approx$ 1). **c,** Surface morphology of CBD SnO_2 after a 6-h reaction (pH = 1.5). **d,** Surface morphology of CdS.

Besides the single buffer layer (SnO_2 or CdS), I also investigated a double buffer layer by stacking CdS on top of SnO_2. SnO_2 was deposited using the method introduced in Section 3.4.

Different reaction times (13, 10 or 7 min) were employed to deposit CdS on top with different thicknesses. After obtaining the buffer layer(s) on FTO substrates, a Sb_2S_3 absorber layer was deposited according to the procedure described in Section 3.2. Identical deposition parameters were used for all Sb_2S_3 absorber layers, regardless of the underlying buffer layers.

6.3 Effects of the buffer layers on Sb_2S_3 thin films

Firstly, Sb_2S_3 thin films were deposited on CdS and SnO_2 buffer layers, respectively. After heat treatment, different macroscopic appearances of Sb_2S_3 thin films were observed, as shown in Fig. 6.2a and b. The FTO/CdS/Sb_2S_3 sample exhibited a uniform and shiny surface (Fig. 6.2a), whereas the surface of the FTO/SnO_2/Sb_2S_3 sample showed different features at the edges and centre, with significantly less shiny area (Fig. 6.2b) compared to the FTO/CdS/Sb_2S_3 sample. This comparison suggests that the underlying buffer layer can have significant effects on the morphology of Sb_2S_3 thin films.

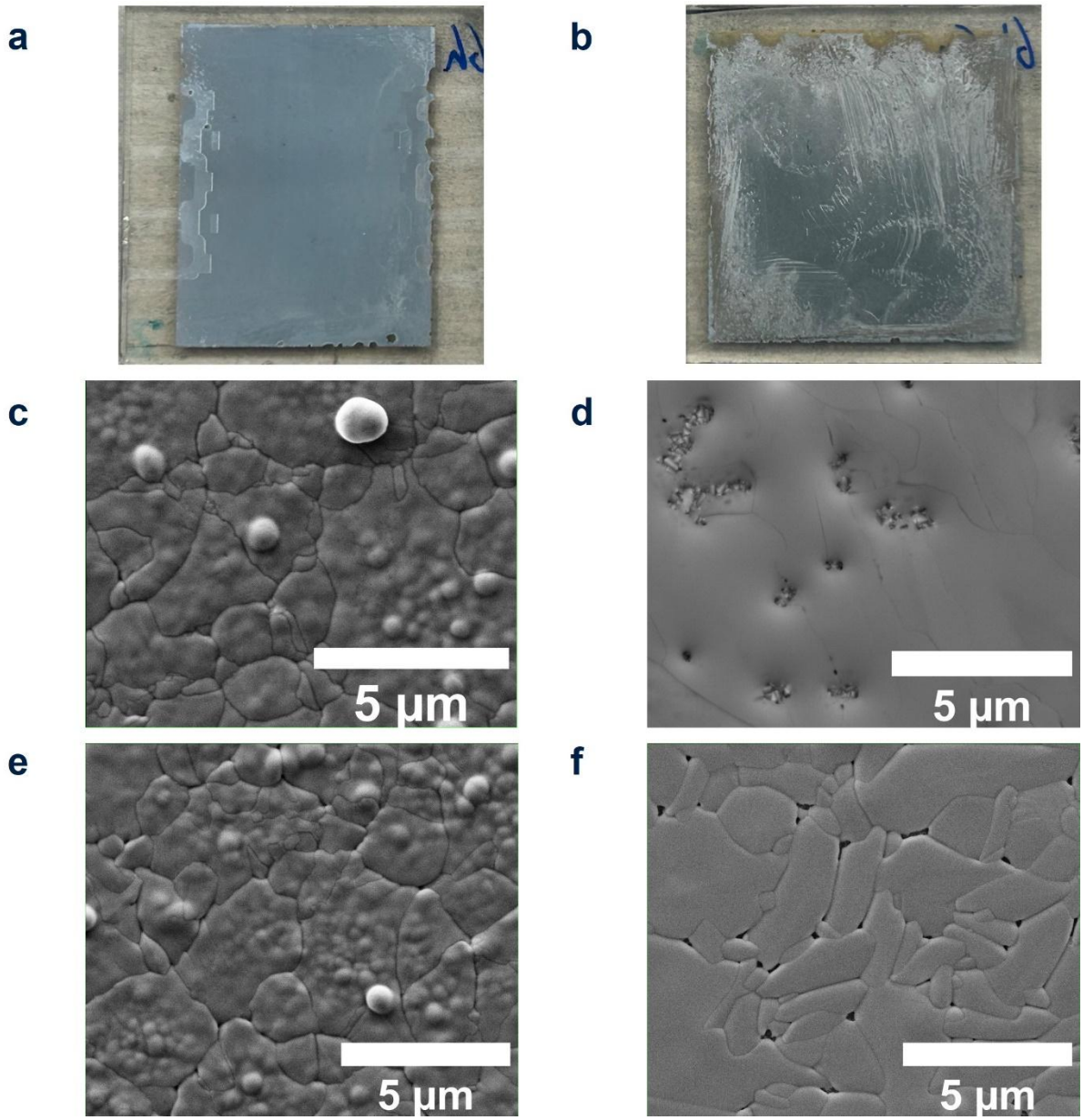

Fig. 6.2 | Macroscopic appearance and microscopic morphology of Sb_2S_3 thin films on different buffer layers. Macroscopic appearance of Sb_2S_3 thin film on **a,** FTO/CdS substrate and **b,** FTO/SnO_2 substrate. Microscopic morphology of Sb_2S_3 thin film on **c,** FTO/CdS substrate and **d,** FTO/SnO_2 substrate. Microscopic morphology of Sb_2S_3 thin film on SnO_2/CdS double buffer layer with **e,** standard-thickness CdS (13-min reaction) or **f,** thinner CdS (7-min reaction).

To investigate further, SEM was employed to observe the microscopic surface morphology. As shown in Fig. 6.2c, Sb_2S_3 thin film on CdS exhibited compact morphology with no visible pinholes. Similar microscopic morphology of Sb_2S_3 thin films has been reported in previous studies, and the spherical bright particles were identified as Sb_2S_3 clusters formed via homogeneous nucleation in solution and deposited on the sample surface[43,132]. On the contrary, Sb_2S_3 thin film deposited directly on SnO_2 displayed pinholes, and the morphology of the exposed areas was similar to that of the underlying SnO_2 buffer layer (Fig. 6.1c). This superior ability of CdS to promote the formation of compact and uniform Sb_2S_3 thin films explained why Sb_2S_3 solar cells with CdS buffer layers outperform those employing oxide buffer layers and give the currently highest PCE.

Furthermore, to confirm that the interface between the buffer layer and Sb_2S_3 is the critical factor determining the morphology of Sb_2S_3 thin films, a SnO_2/CdS double buffer layer was deposited onto the FTO substrate. Firstly, CdS with the standard thickness was prepared via a 13-minute reaction, followed by the deposition of Sb_2S_3 thin film. As shown in Fig. 6.2e, the Sb_2S_3 thin film on SnO_2/CdS double buffer layer also exhibited compact morphology with no pinholes, similar to the Sb_2S_3 thin film on a single CdS buffer layer. These observations indicate that the morphology of Sb_2S_3 thin films is predominantly determined by the surface characteristics of the underlying buffer layer. By modulating the properties of the buffer layer surface, Sb_2S_3 thin films can be deposited onto more benign buffer layers while preserving their compact and uniform morphology.

6.4 Nucleation of Sb_2S_3 on different buffer layers

Nucleation is the most important initial phenomenon in thin film formation, which can determine the subsequent thin film growth and the ultimate film quality[122]. Therefore, to better understand the mechanism of the different morphology of Sb_2S_3 thin films on different buffer layers, I investigated the nucleation behaviour of Sb_2S_3 by observing its evolution in morphology during the initial stages of CBD (0.5 to 1 h after the deposition started). Fig. 6.3a and d compare the surface morphology of Sb_2S_3 thin films on CdS and SnO_2 buffer layer after 0.5 hours of chemical bath deposition. At the initial stage of chemical bath deposition of Sb_2S_3, the CdS/Sb_2S_3 sample (Fig. 6.3a) had a similar morphology to the bare CdS buffer layer (Fig. 6.1d), while spherical particles, identified as Sb_2S_3 nuclei, were observed on the surface of the SnO_2 buffer layer. Similar comparison of surface morphology was also seen in samples undergoing 1-h chemical bath deposition (Fig. 6.3b and e). By the end of the deposition process (6 h), the whole surface of both samples was covered by Sb_2S_3 nuclei (Fig. 6.3 c and f). However, the SnO_2/Sb_2S_3 sample still possessed more spherical nuclei than the CdS/Sb_2S_3 sample. The different evolution in the microscopic morphology of these two samples highlights the effect of the underlying buffer layer on the nucleation behaviour of Sb_2S_3, which ultimately leads to distinct morphologies of Sb_2S_3 thin films.

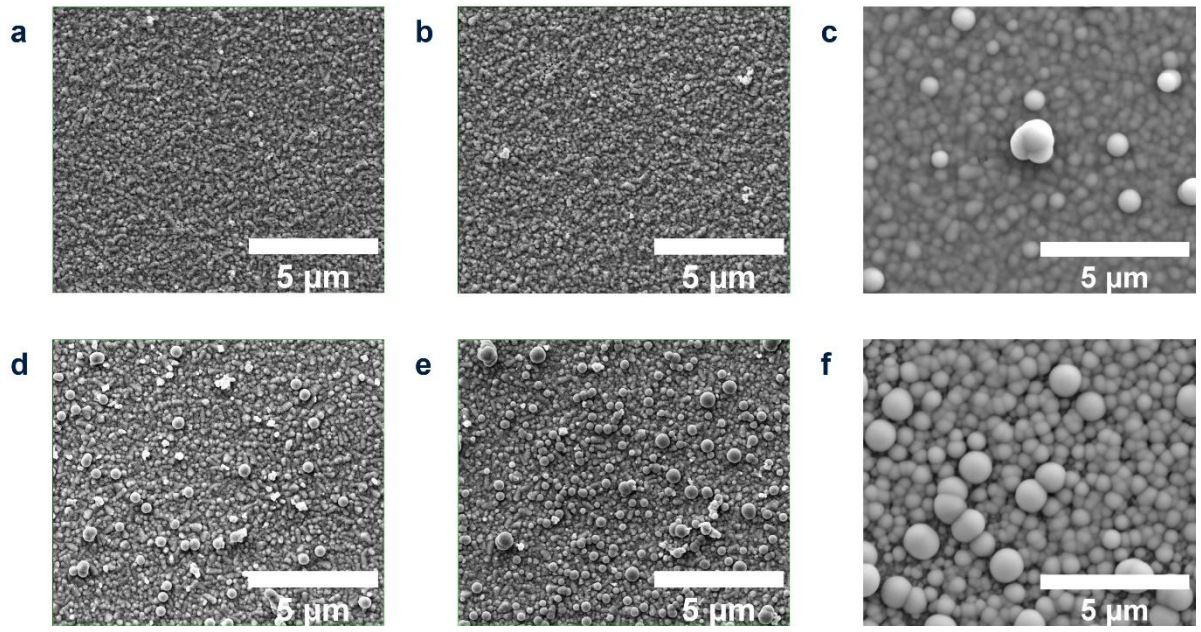

Fig. 6.3 | Microscopic morphology evolution of Sb_2S_3 thin film on different buffer layers as deposition proceeds. The deposition lasts for **a** and **d,** 0.5 h; **b** and **e,** 1 h; **c** and **f,** 6 h. The underlying buffer layers are **a-c,** CdS; **d-f,** SnO_2.

The unobvious change in surface morphology of the CdS/Sb_2S_3 sample during the first hour of Sb_2S_3 deposition can be explained by either the difficulty of Sb_2S_3 nucleating on CdS or the Sb_2S_3 being very thin and conformal to the underlying CdS. Considering the compact morphology of the Sb_2S_3 thin film that ultimately forms on CdS (Fig. 6.2c), the latter explanation is more plausible. To further confirm this hypothesis, EDX mapping was employed to analyse the distribution of elements across the sample surface. As shown in Fig. 6.4 a-c, both Sb and S elements were uniformly distributed on the entire surface. However, due to the similar energies of characteristic X-rays of Sb and Sn, the mapping of Sb might be affected by Sn in the underlying FTO substrates. Also, since the interaction depth for EDX is usually on the micrometre scale, the characteristic X-rays of S were possibly from both Sb_2S_3 nuclei and the underlying CdS.

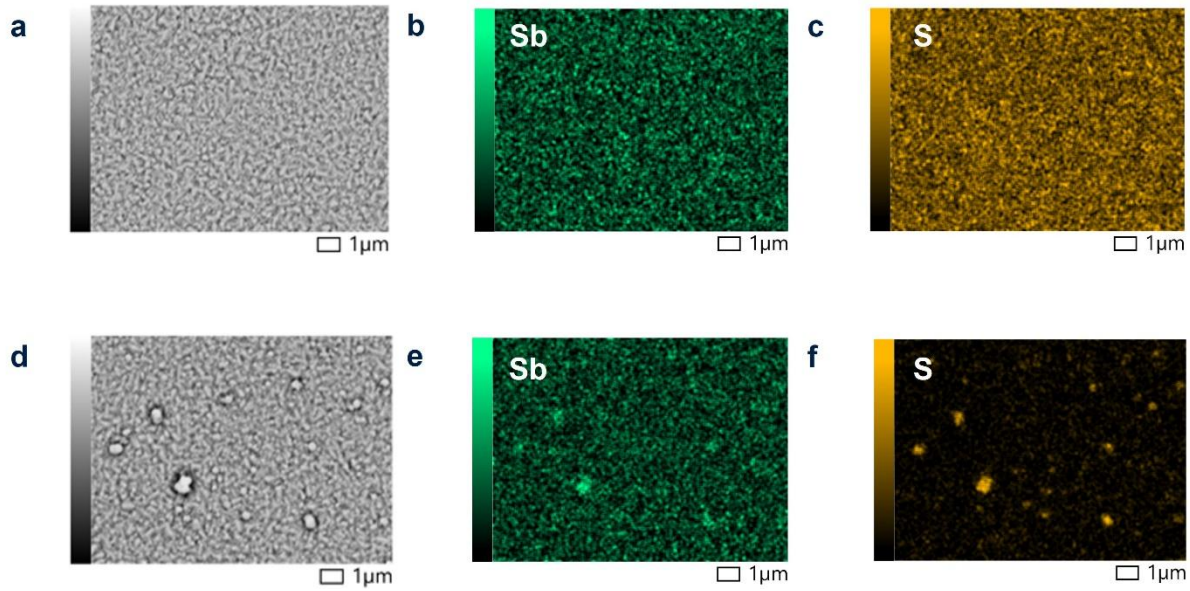

Fig. 6.4 | EDX analysis of Sb_2S_3 thin films on different buffer layers after 0.5-h Sb_2S_3 deposition. a and **d,** SEM images; **b** and **e,** Sb element mapping; **c** and **f,** S element mapping. The underlying buffer layers are **a-c,** CdS; **d-f,** SnO_2. Colour bars are individually adjusted to optimise contrast. Comparisons focus on spatial distribution rather than absolute intensity.

Despite the limitations of EDX mapping, the comparison of Sb_2S_3 thin films on CdS and SnO_2 still shows the effects of buffer layers on Sb_2S_3 deposition. As observed in Fig. 6.4d-f, when deposited onto SnO_2, S elements were detected primarily at the sites of the spherical particles. Although the Sb signal is less localised than S, it also appears brighter at these particle sites.. This indicates that the spherical particles correspond to Sb_2S_3 nuclei.

It should be noted that the purpose of this comparison is not to quantitatively assess the absolute S content between the two samples, but rather to examine the spatial distribution of S within each sample. Although the colour/intensity scales were independently adjusted for visual clarity, the pronounced localisation of the S signal in the Sb_2S_3 film on SnO_2 would remain visible

regardless of scale adjustment. This supports the interpretation that the nucleation of Sb_2S_3 on SnO_2 is less uniform, with the spherical Sb_2S_3 particles more likely formed via homogeneous nucleation in the precursor solution, due to the difficulty of heterogeneous nucleation on the SnO_2 surface.

It should also be considered that due to the relatively large interaction volume of EDX (typically on the order of 1 μm), X-rays generated within the Sb_2S_3 particles may contribute to signals detected in nearby regions. Therefore, the presence of Sb and S signals outside the particle locations does not necessarily indicate the existence of a continuous Sb_2S_3 phase beyond the particles themselves.

Besides EDX analysis, XPS measurements were also performed to investigate the change in the surface chemistry of the samples from Sb_2S_3 deposition. The XPS spectra of two types of samples, pristine CdS and CdS coated with a thin layer of Sb_2S_3 (hereafter referred to as CdS/thin-Sb_2S_3), were compared. Similar to the EDX analysis above, the thin layer of Sb_2S_3 was deposited onto the CdS surface by performing CBD for 0.5 h. According to the calculation from the TPP-2M formula[178-181] using QUASES, when applying Al K_α (1486.69 eV) X-ray, the IMFPs of CdS and Sb_2S_3 are 27.59 Å and 28.89 Å, respectively. Firstly, I compared the XPS spectra of pristine CdS and CdS/thin-Sb_2S_3 to confirm the successful deposition of Sb_2S_3. As illustrated in Fig. 6.5a, the main changes in the XPS survey spectrum after the deposition of Sb_2S_3 were the appearance of high-intensity Sb 3*d* signals and weaker Cd 3*d* signals. The Cl 2*s* and 2*p* core states observed in the CdS survey spectrum can be attributed to the $CdCl_2$ used

to treat the CdS surface. Similarly, in the low binding energy spectra (Fig. 6.5b), pristine CdS exhibited a strong Cd 4*d* peak, which was less obvious in the spectrum of CdS/thin-Sb_2S_3 sample. The appearance of Sb 3*d* signals confirmed that Sb_2S_3 was successfully deposited onto CdS. Meanwhile, as compared in Fig. 6.5c, the weaker intensity of Cd 3*d* signals after Sb_2S_3 deposition indicated that the thickness of Sb_2S_3 was well-controlled, enabling the X-ray to penetrate through the thin Sb_2S_3 layer and reach the CdS surface. Therefore, the chemical environment of both Sb_2S_3 and the underlying CdS was probed.

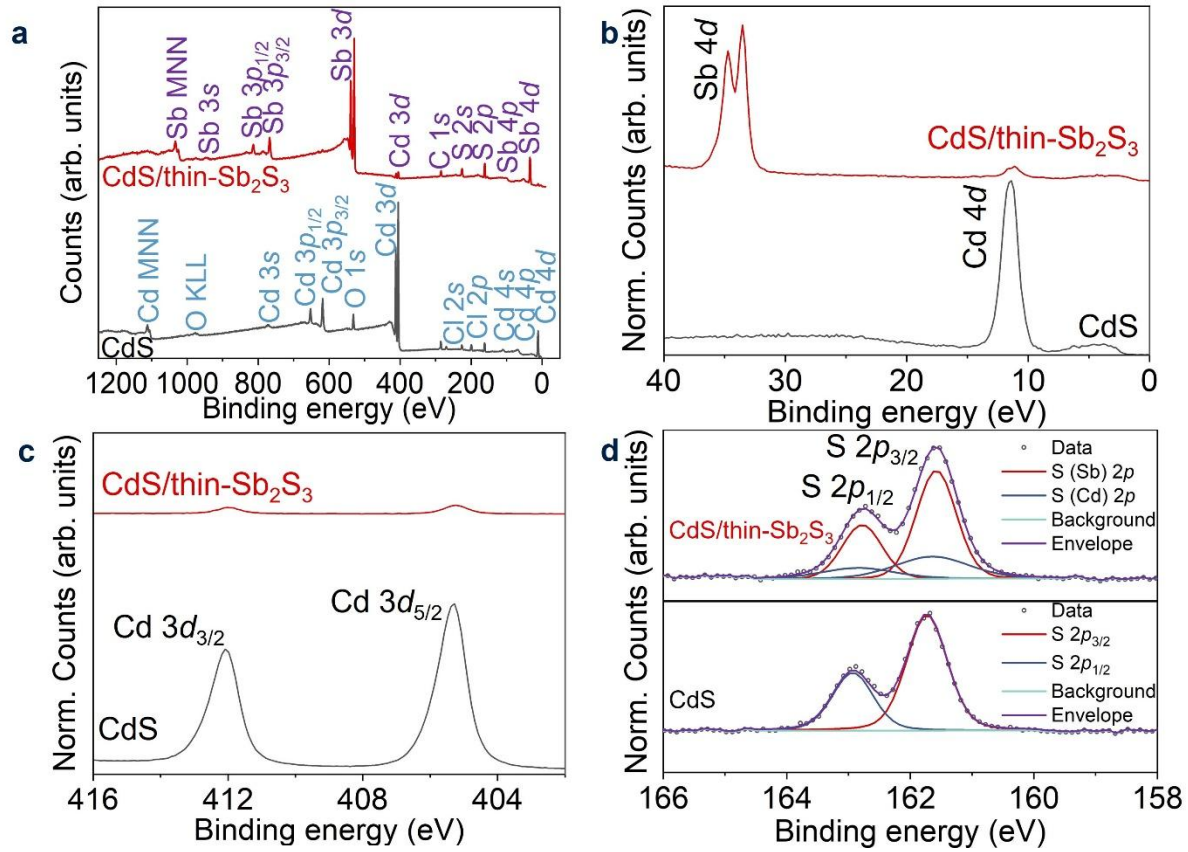

Fig. 6.5 | XPS analysis of pristine CdS buffer layer and CdS/thin-Sb_2S_3 sample. The CdS/thin-Sb_2S_3 sample was obtained by depositing Sb_2S_3 onto CdS for 0.5 h. Comparison of XPS spectra of CdS (black lines) and CdS/thin-Sb_2S_3 sample (red lines) includes **a,** survey spectra. The Cd MNN, O KLL and Sb MNN signals are Cd $M_{4,5}N_{4,5}N_{4,5}$, O $KL_{2,3}L_{2,3}$ and Sb

$M_{4,5}N_{4,5}N_{4,5}$, respectively; **b,** low binding energy spectra. Spectra are normalised to the respective areas of the Cd 4*d* peak; **c,** Cd 3*d* spectra. Spectra are normalised to the respective areas of the Cd $3d_{5/2}$ peak; **d,** S 2*p* spectra with fitting. Spectra are normalised to the respective areas of the S $2p_{3/2}$ peak of CdS sample.

Moreover, by fitting the S 2*p* spectra, one chemical state of S was found for CdS, with the binding energies of 161.7 eV and 162.9 eV for S $2p_{3/2}$ and $2p_{1/2}$ peaks, respectively (lower panel of Fig. 6.5d). The peak positions were close to prior reports for CdS[190]. On the contrary, for the CdS/thin-Sb_2S_3 sample (upper panel of Fig. 6.5d), more complicated chemical environments for S atoms were observed. According to the peak positions, the major S 2*p* doublet was assigned to S atoms bonded with Sb (red curve denoted as S (Sb) 2*p*, S $2p_{3/2}$ at 161.6 eV and $2p_{1/2}$ at 162.8 eV), while the minor peaks were attributed to S atoms bonded to Cd (blue curves denoted as S (Cd) 2*p*). The major components due to S atoms bonded to Sb were consistent with the significantly reduced intensities of Cd 3*d* and 4*d* signals observed in Fig. 6.5a-c. Also, the shift of S 2*p* peaks towards lower binding energies in Sb_2S_3 compared to CdS agrees with previous studies[43,132,133,315]. However, a comparison of the S (Cd) 2*p* doublets in the CdS and CdS/thin-Sb_2S_3 samples reveals that the doublet in the CdS/thin-Sb_2S_3 sample exhibits a broader FWHM of 1.4 eV, compared to 0.8 eV in the CdS only sample. The broader FWHM suggests that the minor S 2*p* doublet in the CdS/thin-Sb_2S_3 sample cannot be attributed solely to S atoms in pure CdS. Instead, it is likely that some S atoms are simultaneously bonded to both Cd and Sb, contributing to the increased peak broadening. To more effectively deconvolute the contributions from different chemical states, XPS measurements with higher

energy resolution may be necessary to enable more precise peak fitting.

Next, to investigate the effects of different buffer layers on the chemical environment of Sb_2S_3, XPS spectra of CdS/thin-Sb_2S_3 and SnO_2/thin-Sb_2S_3 samples were compared. The SnO_2/thin-Sb_2S_3 samples were prepared by depositing Sb_2S_3 onto SnO_2 with a duration of 0.5 h. According to the calculation from the TPP-2M formula using QUASES, when applying Al K_α (1486.69 eV) X-ray, the IMFPs of SnO_2 are 29.40 Å. Following the deposition of Sb_2S_3, Sb 3*d* signals were detected, while the intensity of Sn 3*d* signals was reduced, indicating the X-ray penetrated through Sb_2S_3 and probed the underlying SnO_2 layer. As shown in Fig. 6.6a, compared to the SnO_2/thin-Sb_2S_3 sample, the S 2*p* signals in the survey spectrum of the CdS/thin-Sb_2S_3 sample exhibit higher intensities. Fig 6.6b focused on the S 2*p* region of the survey spectra of CdS/thin-Sb_2S_3 (black) and SnO_2/thin-Sb_2S_3 (pink) samples, as well as the pristine SnO_2 (red). While clear S 2*p* peaks were observed in the CdS/thin-Sb_2S_3 sample, the SnO_2/thin-Sb_2S_3 sample exhibited much weaker S 2*p* signals, indicating significantly lower nucleation and deposition rates of Sb_2S_3 on the SnO_2 surface compared to the CdS surface.

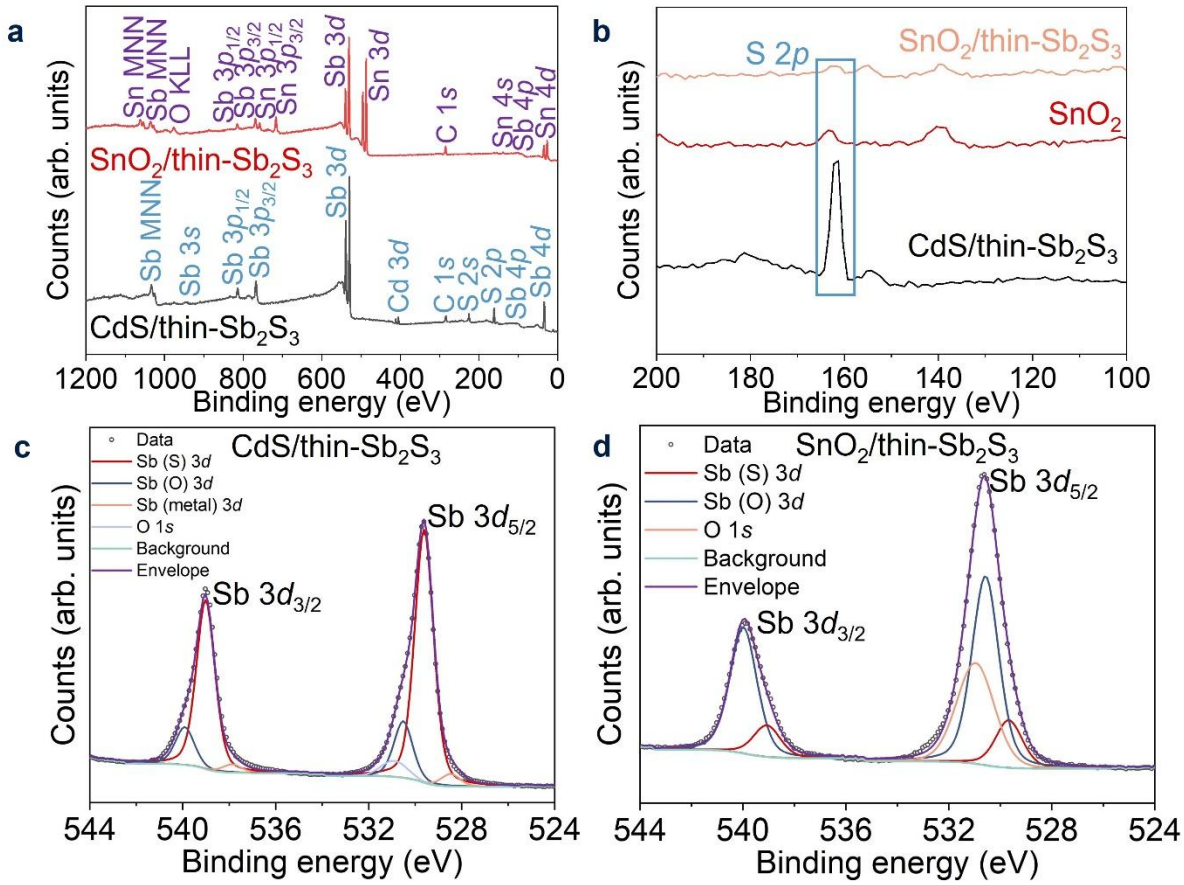

Fig. 6.6 | XPS analysis of CdS/thin-Sb_2S_3 and SnO_2/thin-Sb_2S_3 sample. The samples were both obtained by depositing Sb_2S_3 onto CdS or SnO_2 with a duration of 0.5 h. XPS spectra include **a,** survey spectra of CdS-thin Sb_2S_3 (black) and SnO_2-thin Sb_2S_3 (red). The Sn MNN, O KLL and Sb MNN signals are Sn $M_{4,5}N_{4,5}N_{4,5}$, O $KL_{2,3}L_{2,3}$ and Sb $M_{4,5}N_{4,5}N_{4,5}$, respectively; **b,** zoomed-in S 2*p* region in the survey spectra of CdS-thinSb_2S_3 (black), pure SnO_2 (red) and SnO_2-thin Sb_2S_3 interface. Spectra are normalised to the respective areas of the S 2*p* peak of CdS-thin Sb_2S_3 sample; **c,** Sb 3*d* spectrum of CdS-thin Sb_2S_3 with fitting and **d,** Sb 3*d* spectrum of SnO_2-thin Sb_2S_3 with fitting.

The different nucleation behaviour of Sb_2S_3 on CdS and SnO_2 was further supported by detailed

analysis of the Sb 3*d* spectra. For the CdS/thin-Sb_2S_3 sample (Fig. 6.6c), the major components (red curves) with the binding energies of 539.0 eV (Sb $3d_{3/2}$) and 529.6 eV (Sb $3d_{5/2}$) were assigned to Sb_2S_3 according to their peak positions, which are close to the reported results[43,44,132,133]. Two weaker peaks (blue curves) at 539.9 eV (Sb $3d_{3/2}$) and 530.5 eV (Sb $3d_{5/2}$) were believed to come from antimony oxide. It should be noted that the Sb $3d_{3/2}$ peak position of the Sb-O species was closer to that reported for Sb_2O_3 (539.8 eV) rather than Sb_2O_5 (540.4 eV)[244]. This confirmed that Sb in our Sb_2S_3 films remained in the +3 oxidation state, with a small amount of Sb_2O_3 impurity formed in the films, which has been observed in Sb_2S_3 fabricated through different techniques[132,133,315]. At the low binding energy tails, the fitting also gives two minor peaks (pink curves) whose positions were close to the Sb metal. Similar Sb metal peaks have been reported in the previous study, where Sb metal was detected at the Sb_2S_3 surface fractured in the vacuum[316] or etched by Ar^+ before XPS measurements. For our CdS/thin-Sb_2S_3 sample, the Sb metal is more likely to form due to X-ray damage during the measurements. According to the peak deconvolution of the Sb 3*d* spectrum, Sb-S species were the dominant component (78.52 at.%), while Sb_2O_3 and Sb metal content are much lower (17.66% and 3.82 at.%, respectively) in the CdS/thin-Sb_2S_3 sample.

In comparison, for the SnO_2/thin-Sb_2S_3 sample, a significantly higher fraction of Sb-O species was observed (Fig. 6.6d). The fitting showed that Sb_2O_3 became the main constituent (79.85 at.%), while the rest Sb species was assigned to Sb_2S_3 (20.15 at.%). No Sb metal component was detected. This can be attributed to the higher electronegativity of O (3.44) compared to S (2.58), leading to stronger Sb-O bonds than Sb-S bonds. It should be noted that Sb 3*d* and O1*s*

spectra can directly overlap, making the peak fitting more challenging. In my analysis, identical line shape and FWHM are used for different Sb species (*i.e.*, Sb_2S_3, Sb_2O_3 and Sb metal) in each sample to simplify the peak deconvolution. However, the Sb 3*d* peaks in the CdS/thin-Sb_2S_3 sample are narrower (FWHM = 1.0 eV) than those in the SnO_2/thin-Sb_2S_3 sample (FWHM = 1.2 eV), indicating that XPS measurements with better energy resolution might be required to facilitate more accurate peak fitting.

The analysis of the Sb 3*d* spectrum of the SnO_2/thin-Sb_2S_3 sample shows that Sb^{3+} in the precursor solution preferentially bonded with O on the SnO_2 surface rather than bonding with S to form Sb_2S_3 nuclei. This is consistent with the EDX mapping shown in Fig. 6.4 e and f, where most S elements were detected only in Sb-rich regions, such as the spherical clusters. This distribution explained the low intensity of S 2*p* XPS signals detected in the SnO_2/thin-Sb_2S_3 sample (Fig. 6.6b). In this case, the homogeneous nucleation process occurring in the precursor solution is likely the primary pathway to form Sb_2S_3 nuclei, followed by the nuclei deposition onto the SnO_2 surface via the Sb-O bonds, which is considered to be the origin of the spherical particles observed in Fig. 6.3 d-f.

Combining the SEM observations, EDX mapping analysis and XPS measurements, it can be concluded that Sb_2S_3 deposited on SnO_2 tends to form more isolated Sb_2S_3 nuclei, leading to a discontinuous film. The isolated Sb_2S_3 nuclei on the SnO_2 surface are caused by the stronger bonding interaction between Sb and O atoms than S atoms, making the heterogeneous nucleation of Sb_2S_3 on SnO_2 difficult, and isolating spherical Sb_2S_3 nuclei via the homogeneous

nucleation process. Our investigation indicates that the challenges in growing high-quality Sb_2S_3 films on oxide surfaces include unsatisfying film morphology and the ease of Sb_2O_3 impurity formation. Both factors can significantly limit the performance of Sb_2S_3 solar cells.

As shown in Fig. 6.2 e and f, the use of CdS as an interfacial layer between SnO_2 and Sb_2S_3 enabled the formation of compact Sb_2S_3 films, despite the CdS layer being thin. Similar EDX mapping was performed on SnO_2/CdS/Sb_2S_3 samples (Fig. 6.7). To investigate the nucleation behaviour of Sb_2S_3 on the double buffer layer, three types of SnO_2/CdS substrates with varying CdS layer thicknesses were prepared, followed by Sb_2S_3 deposition for 0.5 h. In all cases, a uniform distribution of Sb and S elements was observed, similar to the results for CdS/Sb_2S_3 samples shown in Fig. 6.4.

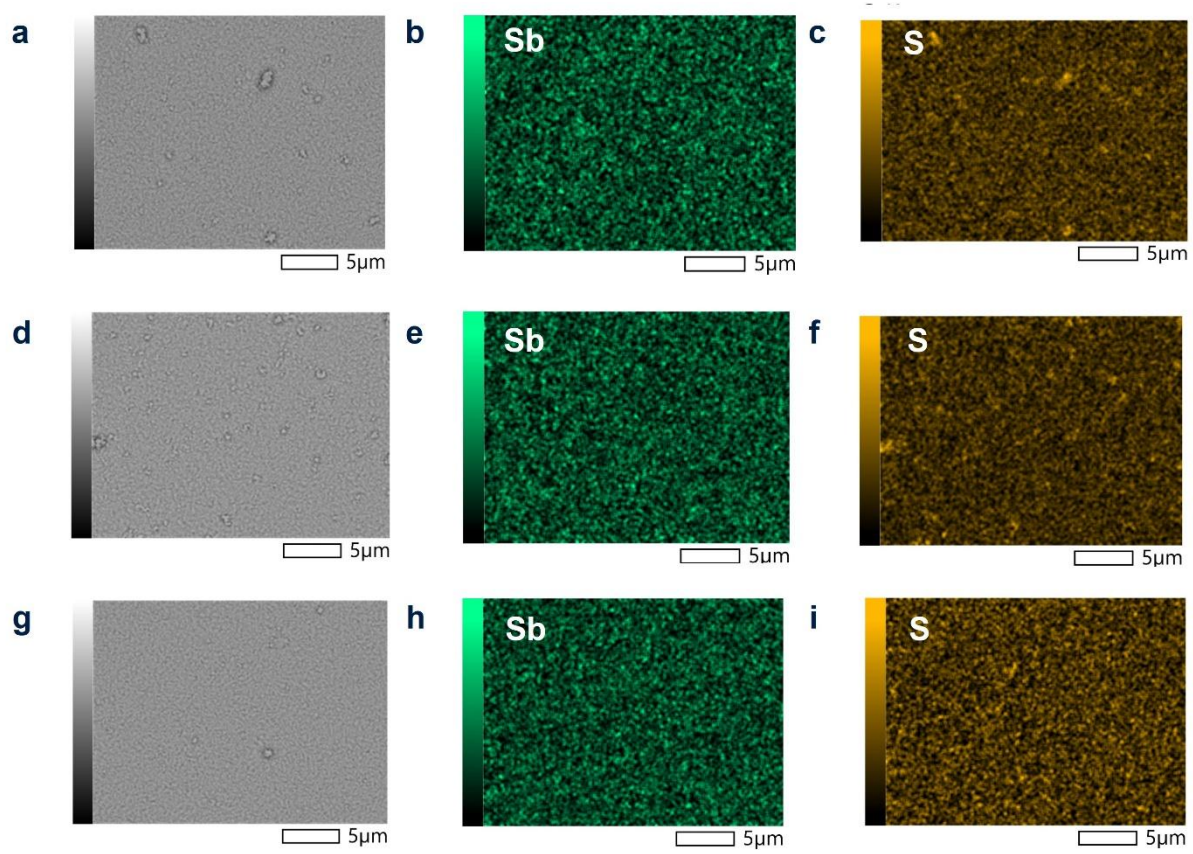

Fig. 6.7 | EDX analysis of Sb_2S_3 thin films on SnO_2/CdS double buffer layers after 0.5-h

Sb_2S_3 deposition. a, d and **g,** SEM images; **b, e** and **h,** Sb element mapping; **c, f** and **i,** S element mapping. The underlying buffer layers were **a-c,** SnO_2/CdS (13-min deposition); **d-f,** SnO_2/CdS (10-min deposition); **g-i,** SnO_2/CdS (7-min deposition).

The introduction of a CdS interfacial layer between the SnO_2 buffer layer and Sb_2S_3 not only maintained the compact morphology of the Sb_2S_3 film, but also reduced the Cd content when using a thinner CdS layer. By decreasing the CBD duration of CdS from 13 min to 7 min, the thickness of CdS reduced from ~60 nm to ~30 nm. In this case, the Cd content was lowered from ~0.0030 wt.% to ~0.0015 wt.% for a complete Sb_2S_3 solar cell weighing 5 g. Our analysis has proven that the sulphide surface is critical to facilitate the compact morphology of Sb_2S_3, while the oxide surface is detrimental due to the formation of Sb_2O_3 impurity, as well as making the heterogeneous nucleation of Sb_2S_3 on the surface difficult. To fabricate Cd-free Sb_2S_3 solar cells, novel sulphide buffer layers with the ability to improve the Sb_2S_3 film morphology and effectively extract photo-generated charge-carriers are worth further exploration.

6.5 Sb_2S_3-based photovoltaic devices

In my project, the performance of Sb_2S_3 solar cells was also characterised, along with the analysis of the optical loss mechanisms. The device structure achieving the current record PCE of Sb_2S_3 solar cells (*i.e.*, FTO/CdS/Sb_2S_3/Spiro-OMeTAD/Au) was employed in this project, with an active area of 0.25 cm^2 per pixel. The distribution statistics of the PCE of Sb_2S_3 solar cells under standard 1 sun (30 pixels analysed) and indoor (1000 lux white LED with the colour

temperature of 3000 K; 20 pixels analysed) illumination are shown in Fig. 6.8a and b, respectively. Under 1 sun illumination, the champion device gave a V_{OC} of 0.748 V, a J_{SC} of 13.3 mA/cm^2, and a PCE of 5.52% (reverse scan). Although the device area was larger than the typical active area used in previous studies on Sb_2S_3 solar cells, the PCE is comparable to some early results[43,131,133], indicating that our deposition technique and device structure are promising. On the other hand, under 1000 lux WLED illumination, the same device achieved a peak PCE of 10.4%, with a V_{OC} of 0.549 V and a J_{SC} of 88.8 μA/cm^2. The higher PCE under the WLED illumination demonstrated the great potential of Sb_2S_3 solar cells for indoor light harvesting.

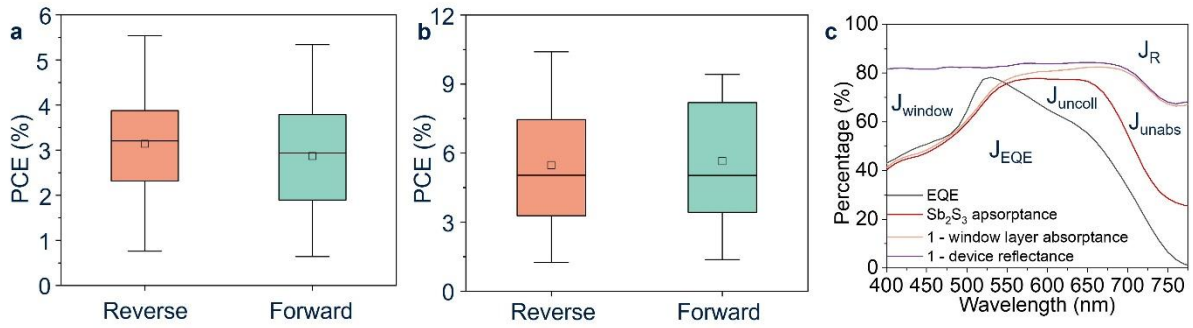

Fig. 6.8 | Device performance and optical loss analysis of Sb_2S_3 solar cells. a and **b,** the distribution statistics of the PCE of the Sb_2S_3 solar cell under 1-sun (AM 1.5G) illumination (Fig. 6.8a) and 1000 lux WLED illumination (Fig. 6.8b). For 1-sun illumination, only pixels with V_{OC} > 0.3 eV were analysed. For 1000 lux illumination, only pixels with V_{OC} > 0.1 eV were analysed; **c,** optical loss analysis of the Sb_2S_3 solar cell.

It should be noted that our Sb_2S_3 solar cell exhibited a V_{OC} of 0.748 V, which is among the highest reported V_{OC} values of Sb_2S_3 solar cells (refer to Figure 5g and Table S6 in Ref. 133). However, the relatively low J_{SC} remains the main factor limiting device performance. The

possible reasons for optical loss include unabsorbed photons, parasitic absorption of the window layer (*i.e.*, FTO/CdS), and failure to collect photo-generated charge-carriers in the absorber layer. To analyse the contributions of each mechanism, we obtained the absorptance of the window layer and the Sb_2S_3 layer through UV-vis spectroscopy (measured with an integrating sphere), the external quantum efficiency (EQE) measurements of the champion device, and the optical loss analysis. The experimental details of EQE measurements and optical loss calculations are introduced in Section 3.5.2. As shown in Fig. 6.8c, the area below the EQE curve (black line) represents the current density derived by integrating $EQE(\lambda)$ from 400 nm to 800 nm ($J_{SC,EQE}$ = 11.98 mA/cm^2). This value differed slightly from the current density measured by J-V characterisation (13.14 mA/cm^2), likely attributed to the smaller illuminated area or the narrower wavelength range used for integration for EQE measurements. The area between the EQE curve and the Sb_2S_3 absorptance curve (red line) represents optical loss due to uncollected charge-carriers after the photons are absorbed by Sb_2S_3, denoted as J_{uncoll} (J_{uncoll} = 2.43 mA/cm^2). The optical loss caused by photons not absorbed by Sb_2S_3 was marked as J_{unabs} (J_{unabs} = 2.15 mA/cm^2), which is the area between the red and pink curves (1 – window layer absorptance). The loss due to the window layer parasitic absorption, denoted as J_{window} (J_{window} = 2.80 mA/cm^2), was viewed as the area between the pink and purple curves (1 – device reflectance). The final optical loss mechanism was caused by the reflectance of the device when the illumination was applied from the glass side. Thus, the area above the purple curve in Fig. 6.8c represents the photons reflected by the complete device, and the lost current density $J_{loss,R}$ = 4.60 mA/cm^2. Since it is difficult to deposit Sb_2S_3 on low-reflectance glass substrates, the reflectance of Sb_2S_3 layer was measured using FTO/CdS/Sb_2S_3

samples. This inaccurate measurement of reflectance can be the reason why EQE values were abnormally higher than the absorptance of Sb_2S_3 at wavelengths below 550 nm. The optical loss analysis has suggested that the reflectance of the device makes the most contribution to the current loss, indicating that applying an anti-reflection coating on the glass side of devices could effectively improve the device performance. The second mechanism of optical loss is the parasitic absorption of the window layer, reflecting the necessity of reducing the thickness of CdS or replacing CdS with other more transparent ETLs. The insights from our previous sections regarding the effects of buffer layers on Sb_2S_3 growth have provided valuable guidance for developing alternative ETLs to further improve Sb_2S_3 solar cells.

6.6 Conclusions

In conclusion, this study explores the use of SnO_2 as a more benign alternative to CdS as the buffer layer for Sb_2S_3 solar cells. However, when deposited onto SnO_2, discontinuous Sb_2S_3 films with pinholes were observed. Microscopic morphology at the nucleation stage demonstrated different nucleation behaviour of Sb_2S_3 on CdS and SnO_2. EDX mapping showed that S was uniformly distributed in the CdS-thin Sb_2S_3 sample. In contrast, S was only detected at Sb-rich regions at the SnO_2-thin Sb_2S_3 sample, forming spherical Sb_2S_3 clusters. XPS analyses revealed that Sb tends to firstly bond with O on the surface of SnO_2 to form Sb_2O_3 as the dominant species instead of Sb_2S_3, making the heterogeneous nucleation of Sb_2S_3 on the SnO_2 surface difficult. Moreover, by employing CdS as an interfacial layer between SnO_2 and Sb_2S_3, compact Sb_2S_3 films were successfully deposited, and similar nucleation of Sb_2S_3 was

observed. Reducing the CdS layer thickness significantly lowered the total Cd content. The findings highlighted that the ease of forming antimony oxide was the main reason hindering the deposition of high-quality Sb_2S_3 films on oxide surfaces, and a sulphide interfacial layer was a promising method to optimise Sb_2S_3 film morphology and achieve Cd-free Sb_2S_3 solar cells. Furthermore, our Sb_2S_3 solar cells showed impressive performance under 1 sun illumination, especially the V_{OC} value that was comparable to the highest reported values[133]. The optical loss analysis revealed that most current loss was caused by the reflection of devices and the parasitic absorption of the window layer, suggesting the potential of using anti-reflection coatings and transparent buffer layers to further improve the performance of Sb_2S_3 solar cells. Additionally, the characterisation under WLED illumination demonstrated the promising ability of Sb_2S_3 to harvest indoor lighting, owing to its suitable bandgap value. Overall, this project revealed the underlying mechanisms of CdS outperforming SnO_2 as a buffer layer for Sb_2S_3 solar cells. It provided valuable guidance about the future exploration of benign buffer layers, as well as methods to optimise Sb_2S_3 solar cells.

6.7 Future work

As I experimentally demonstrated that when depositing Sb_2S_3, Sb_2O_3 was the dominant species on the SnO_2 surface, while Sb_2S_3 formed directly on the CdS surface, it is worth performing some first principles calculations to further examine the findings. For example, comparing the interfacial energy and adhesion work of the SnO_2/Sb_2S_3 and CdS/Sb_2S_3 heterointerface could offer an understanding of the stability of heterointerfaces[133]. Also, by investigating the

interfaces between Sb_2S_3 and other oxide ETLs, such as TiO_2 and ZnO, it is possible to evaluate whether these oxides form stable interfaces with Sb_2S_3 while improving its morphology. Meanwhile, the properties of the Sb_2O_3/Sb_2S_3 interface should also be studied to better explain the challenges associated with Sb_2S_3 deposition onto Sb_2O_3, as reflected by the observed spherical Sb_2S_3 clusters and localised S detection at Sb-rich regions on the SnO_2 surface.

Since we proved that the CdS interfacial layer effectively optimised Sb_2S_3 film morphology, various sulphide ETLs are worth exploring to achieve Cd-free Sb_2S_3 solar cells. ZnS and In_2S_3 have been successfully applied as ETLs for Sb_2S_3 solar cells, but further research is still required to optimise their deposition techniques and enhance the overall performance of Sb_2S_3 solar cells[134-136,140]. Additionally, various sulphide materials, such as SnS_2[317,318], Bi_2S_3[319] and MoS_2[320,321], have emerged as promising ETLs for solar cells or photodetectors, offering valuable opportunities to improve the performance and sustainability of Sb_2S_3 solar cells. Moreover, the wide bandgap of Sb_2S_3 makes it a promising candidate for both indoor light harvesting[43,44] and top cells for tandem solar cells[322], which deserves more attention in the future.

Chapter 7: Conclusions and outlook

This thesis advances the understanding of the fundamental properties, synthesis techniques, and device development of chalcogenide solar absorbers, highlighting their potential for photovoltaic applications. The first project identified the key factors enabling delocalised charge-carriers in $CuSbSe_2$, addressing the prevalent challenge of charge-carrier localisation in pnictogen-based semiconductors. This is critical for efficient solar cells. The second project investigated two deposition techniques, a thiol-amine-based solution processing and a chemical vapour deposition (CVD) method, for depositing $CuSbSe_2$ thin films. This study identified their strengths, limitations, and the challenges for $CuSbSe_2$ solar cells. The third project examined the influence of buffer layers on Sb_2S_3 thin films, revealing the limitations of SnO_2 as a benign buffer layer and demonstrating how a CdS interfacial layer can improve film morphology. Strategies to improve the performance of Sb_2S_3 solar cells were also proposed through optical loss analysis. Collectively, these findings promote the future development of chalcogenide materials for photovoltaic technologies.

Meanwhile, these findings also open some future research directions to optimise chalcogenide solar absorbers. First, the design rules proposed in the first project for semiconductors that avoid charge-carrier localisation require further investigation to assess their generalisability. A promising starting point would be the bismuth- and sulphide-based analogues of $CuSbSe_2$, like $CuSbS_2$ and $CuBiSe_2$, along with non-layered compounds, such as Cu_3SbSe_3. Another class of materials deserving attention is those with quasi-1D crystal structures, such as BiSBr, as they

also exhibit free volumes in the structures. Investigating charge-carrier–phonon coupling in these materials will help validate the proposed design principles for band-like transport. Following this, the broader family of semiconductors can be explored to refine these principles and ultimately establish simple descriptors for materials that avoid charge-carrier localisation, which is the key to discovering semiconductors with efficient band-like transport. Second, the two deposition techniques for $CuSbSe_2$ thin films developed in this work offer opportunities for further optimisation. For the thiol-amine route, gradually removing the remaining solvents may address the issue of structural defects. Therefore, strategies such as solvent heat treatment and multi-step spin coating are worth exploring for $CuSbSe_2$ thin film deposition. Also, the variation of thiols and amines offers additional parameter space for optimising the film quality. As the steep temperature gradient is the primary limitation of our CVD method, improving temperature control to achieve a gentler gradient could enhance film quality and scalability. After addressing this issue, the CVD technique is expected to deposit large-area $CuSbSe_2$ thin films with fewer structural defects and grain boundaries, which can enhance solar cell performance.

As for Sb_2S_3 solar cells, considering that the interfaces between Sb_2S_3 and buffer layers have been experimentally investigated, first-principles calculations would be an important step to further examine the stability of heterointerfaces, particularly between Sb_2S_3 and oxide ETLs like TiO_2 and ZnO, in comparison with the CdS/Sb_2S_3 interface. Similar computational studies can also be conducted for alternative sulphide ETLs, such as ZnS, In_2S_3, SnS_2, Bi_2S_3, and MoS_2, to identify the most promising buffer layer for Cd-free Sb_2S_3 solar cells. Through careful

selection of buffer layers and optimisation of Sb_2S_3/buffer layer interfaces, efficient Cd-free Sb_2S_3 solar cells can be realised, enabling broader applications. Additionally, the wide bandgap of Sb_2S_3 makes it highly promising as an indoor light absorber and as a top cell in tandem solar cells. These areas represent key directions for the future development of Sb_2S_3 solar cells.

Among all PIMs, chalcogenide materials offer exceptional stability and optoelectronic properties, positioning them as attractive lead-free alternatives to LHPs. This thesis demonstrates the ability of $CuSbSe_2$ to avoid charge-carrier localisation, as well as the potential of Sb_2S_3 solar cells for Cd-free improvements and efficient indoor light harvesting. These findings should inspire further research into both materials and the broader family of chalcogenides, advancing more efficient and sustainable solar technologies to address global energy challenges.

References

1 Zhang, J., Raufer, R. & Liu, L. Solar Home Systems for Clean Cooking: A Cost–Health Benefit Analysis of Lower-Middle-Income Countries in Southeast Asia. *Sustainability* **12**, 3909 (2020). https://doi.org/10.3390/su12093909

2 Ritchie, H., Rosado, P. & Roser, M. Energy. *Our world in data* (2024).

3 Nelson, J. A. *The Physics Of Solar Cells*. (Imperial College Press, 2003).

4 Needleman, D. B. *et al.* Economically sustainable scaling of photovoltaics to meet climate targets. *Energy & Environmental Science* **9**, 2122-2129 (2016). https://doi.org/10.1039/C6EE00484A

5 Philipps, S. & Warmuth, W. Photovoltaics Report. (Freiburg, 2024).

6 Blakesley, J. C. *et al.* Roadmap on established and emerging photovoltaics for sustainable energy conversion. *Journal of Physics: Energy* **6**, 041501 (2024). https://doi.org/10.1088/2515-7655/ad7404

7 Niewelt, T. *et al.* Reassessment of the intrinsic bulk recombination in crystalline silicon. *Solar Energy Materials and Solar Cells* **235**, 111467 (2022). https://doi.org/10.1016/j.solmat.2021.111467

8 Richter, A., Hermle, M. & Glunz, S. W. Reassessment of the Limiting Efficiency for Crystalline Silicon Solar Cells. *IEEE Journal of Photovoltaics* **3**, 1184-1191 (2013). https://doi.org/10.1109/JPHOTOV.2013.2270351

9 Huang, Y. T., Kavanagh, S. R., Scanlon, D. O., Walsh, A. & Hoye, R. L. Z. Perovskite-inspired materials for photovoltaics and beyond-from design to devices. *Nanotechnology* **32**, 132004 (2021). https://doi.org/10.1088/1361-6528/abcf6d

10 Sze, S. M. *Semiconductor Devices: Physics and Technology*. (John Wiley & Sons Singapore Pte. Limited, 2012).

11 Richter, J. M. *et al.* Enhancing photoluminescence yields in lead halide perovskites by photon recycling and light out-coupling. *Nature Communications* **7**, 13941 (2016). https://doi.org/10.1038/ncomms13941

12 Franchini, C., Reticcioli, M., Setvin, M. & Diebold, U. Polarons in materials. *Nature Reviews Materials* **6**, 560-586 (2021). https://doi.org/10.1038/s41578-021-00289-w

13 Herz, L. M. Charge-Carrier Mobilities in Metal Halide Perovskites: Fundamental Mechanisms and Limits. *ACS Energy Letters* **2**, 1539-1548 (2017). https://doi.org/10.1021/acsenergylett.7b00276

14 Buizza, L. R. V. & Herz, L. M. Polarons and Charge Localization in Metal-Halide Semiconductors for Photovoltaic and Light-Emitting Devices. *Advanced Materials* **33**, e2007057 (2021). https://doi.org/10.1002/adma.202007057

15 Toyozawa, Y. Self-Trapping of an Electron by the Acoustical Mode of Lattice Vibration. I. *Progress of Theoretical Physics* **26**, 29-44 (1961). https://doi.org/10.1143/ptp.26.29

16 Morrissey, F. X. & Dexheimer, S. L. Coherent acoustic phonon generation in exciton self-trapping. *Physical Review B* **81** (2010). https://doi.org/10.1103/PhysRevB.81.094302
17 Song, K. & Williams, R. T. *Self-Trapped Excitons*. (Springer, 1993).
18 Rondiya, S. R., Jagt, R. A., MacManus-Driscoll, J. L., Walsh, A. & Hoye, R. L. Z. Self-trapping in bismuth-based semiconductors: Opportunities and challenges from optoelectronic devices to quantum technologies. *Applied Physics Letters* **119**, 220501 (2021). https://doi.org/10.1063/5.0071763
19 Hoye, R. L. Z. *et al.* The Role of Dimensionality on the Optoelectronic Properties of Oxide and Halide Perovskites, and their Halide Derivatives. *Advanced Energy Materials* **12**, 2100499 (2021). https://doi.org/10.1002/aenm.202100499
20 Wei, S. H. & Zunger, A. Predicted band-gap pressure coefficients of all diamond and zinc-blende semiconductors: Chemical trends. *Physical Review B* **60**, 5404-5411 (1999). https://doi.org/10.1103/PhysRevB.60.5404
21 Ganose, A. M. *et al.* Efficient calculation of carrier scattering rates from first principles. *Nature Communications* **12**, 2222 (2021). https://doi.org/10.1038/s41467-021-22440-5
22 Zheng, F. & Wang, L.-w. Large polaron formation and its effect on electron transport in hybrid perovskites. *Energy & Environmental Science* **12**, 1219-1230 (2019). https://doi.org/10.1039/C8EE03369B
23 Besancon, R. *The encyclopedia of physics*. (Springer Science & Business Media, 2013).
24 Baranowski, M. & Plochocka, P. Excitons in Metal-Halide Perovskites. *Advanced Energy Materials* **10**, 1903659 (2020). https://doi.org/10.1002/aenm.201903659
25 Sendner, M. *et al.* Optical phonons in methylammonium lead halide perovskites and implications for charge transport. *Materials Horizons* **3**, 613-620 (2016). https://doi.org/10.1039/C6MH00275G
26 Hu, C. M., Batke, E., Köhler, K. & Ganser, P. Resonant Polaron Coupling of High Index Electron Landau Levels in GaAs Heterostructures. *Physical Review Letters* **76**, 1904-1907 (1996). https://doi.org/10.1103/PhysRevLett.76.1904
27 Buizza, L. R. V. *et al.* Charge-Carrier Mobility and Localization in Semiconducting Cu_2AgBiI_6 for Photovoltaic Applications. *ACS Energy Letters* **6**, 1729-1739 (2021). https://doi.org/10.1021/acsenergylett.1c00458
28 Wu, B. *et al.* Strong self-trapping by deformation potential limits photovoltaic performance in bismuth double perovskite. *Science Advances* **7**, eabd3160 (2021). https://doi.org/10.1126/sciadv.abd3160
29 Elliott, R. J. Intensity of Optical Absorption by Excitons. *Physical Review* **108**, 1384-1389 (1957). https://doi.org/10.1103/PhysRev.108.1384
30 Shockley, W. & Queisser, H. J. Detailed Balance Limit of Efficiency of p-n Junction Solar Cells. *Journal of Applied Physics* **32**, 510-519 (1961). https://doi.org/10.1063/1.1736034
31 Rühle, S. Tabulated values of the Shockley–Queisser limit for single junction solar cells. *Solar Energy* **130**, 139-147 (2016). https://doi.org/10.1016/j.solener.2016.02.015

32 Peng, Y. *et al.* Lead-Free Perovskite-Inspired Absorbers for Indoor Photovoltaics. *Advanced Energy Materials* **11**, 2002761 (2021). https://doi.org/10.1002/aenm.202002761
33 Marques Lameirinhas, R. A., Torres, J. P. N. & de Melo Cunha, J. P. A Photovoltaic Technology Review: History, Fundamentals and Applications. *Energies* **15**, 1823 (2022). https://doi.org/10.3390/en15051823
34 O'Regan, B. & Grätzel, M. A low-cost, high-efficiency solar cell based on dye-sensitized colloidal TiO_2 films. *Nature* **353**, 737-740 (1991). https://doi.org/10.1038/353737a0
35 Kamat, P. V. Quantum Dot Solar Cells. Semiconductor Nanocrystals as Light Harvesters. *The Journal of Physical Chemistry C* **112**, 18737-18753 (2008). https://doi.org/10.1021/jp806791s
36 Kojima, A., Teshima, K., Shirai, Y. & Miyasaka, T. Organometal Halide Perovskites as Visible-Light Sensitizers for Photovoltaic Cells. *Journal of the American Chemical Society* **131**, 6050-6051 (2009). https://doi.org/10.1021/ja809598r
37 NREL. *Best Research-Cell Efficiency Chart*, <https://www.nrel.gov/pv/assets/pdfs/best-research-cell-efficiencies.pdf> (accessed October 2024).
38 Saravanapavanantham, M., Mwaura, J. & Bulović, V. Printed Organic Photovoltaic Modules on Transferable Ultra-thin Substrates as Additive Power Sources. *Small Methods* **7**, 2200940 (2023). https://doi.org/10.1002/smtd.202200940
39 Wang, X. *et al.* Ultrathin (~30 μm) flexible monolithic perovskite/silicon tandem solar cell. *Science Bulletin* **69**, 1887-1894 (2024). https://doi.org/10.1016/j.scib.2024.04.022
40 Liu, W. *et al.* Flexible solar cells based on foldable silicon wafers with blunted edges. *Nature* **617**, 717-723 (2023). https://doi.org/10.1038/s41586-023-05921-z
41 Sureshkumar Jayakumari, S. D. *et al.* Energy and Daylighting Performance of Kinetic Building-Integrated Photovoltaics (BIPV) Façade. *Sustainability* **16**, 9739 (2024). https://doi.org/10.3390/su16229739
42 Pecunia, V., Occhipinti, L. G. & Hoye, R. L. Z. Emerging Indoor Photovoltaic Technologies for Sustainable Internet of Things. *Advanced Energy Materials* **11**, 2100698 (2021). https://doi.org/10.1002/aenm.202100698
43 Zheng, J. *et al.* Enhanced hydrothermal heterogeneous deposition with surfactant additives for efficient Sb_2S_3 solar cells. *Chemical Engineering Journal* **446**, 136474 (2022). https://doi.org/10.1016/j.cej.2022.136474
44 Chen, X. *et al.* Additive engineering for Sb_2S_3 indoor photovoltaics with efficiency exceeding 17%. *Light: Science & Applications* **13**, 281 (2024). https://doi.org/10.1038/s41377-024-01620-0
45 Michaels, H. *et al.* Dye-sensitized solar cells under ambient light powering machine learning: towards autonomous smart sensors for the internet of things. *Chemical Science* **11**, 2895-2906 (2020). https://doi.org/10.1039/c9sc06145b
46 Mathews, I., Kantareddy, S. N., Buonassisi, T. & Peters, I. M. Technology and Market Perspective for Indoor Photovoltaic Cells. *Joule* **3**, 1415-1426 (2019). https://doi.org/10.1016/j.joule.2019.03.026

47 Mathews, I. *et al.* Self-Powered Sensors Enabled by Wide-Bandgap Perovskite Indoor Photovoltaic Cells. *Advanced Functional Materials* **29** (2019). https://doi.org/10.1002/adfm.201904072

48 Min, J. *et al.* An autonomous wearable biosensor powered by a perovskite solar cell. *Nature Electronics* **6**, 630-641 (2023). https://doi.org/10.1038/s41928-023-00996-y

49 Li, T.-T. *et al.* Photo-rechargeable all-solid-state lithium-sulfur batteries based on perovskite indoor photovoltaic modules. *Chemical Engineering Journal* **455**, 140684 (2023). https://doi.org/10.1016/j.cej.2022.140684

50 Müller, D. *et al.* Indoor Photovoltaics for the Internet-of-Things – A Comparison of State-of-the-Art Devices from Different Photovoltaic Technologies. *ACS Applied Energy Materials* **6**, 10404-10414 (2023). https://doi.org/10.1021/acsaem.3c01274

51 Yan, B. *et al.* Indoor photovoltaics awaken the world's first solar cells. *Science Advances* **8**, eadc9923 (2022). https://doi.org/10.1126/sciadv.adc9923

52 Reich, N. H., van Sark, W. G. J. H. M. & Turkenburg, W. C. Charge yield potential of indoor-operated solar cells incorporated into Product Integrated Photovoltaic (PIPV). *Renewable Energy* **36**, 642-647 (2011). https://doi.org/10.1016/j.renene.2010.07.018

53 De Rossi, F., Pontecorvo, T. & Brown, T. M. Characterization of photovoltaic devices for indoor light harvesting and customization of flexible dye solar cells to deliver superior efficiency under artificial lighting. *Applied Energy* **156**, 413-422 (2015). https://doi.org/10.1016/j.apenergy.2015.07.031

54 Lizin, S. *et al.* Life cycle analyses of organic photovoltaics: a review. *Energy & Environmental Science* **6**, 3136-3149 (2013). https://doi.org/10.1039/C3EE42653J

55 Cao, Y., Liu, Y., Zakeeruddin, S. M., Hagfeldt, A. & Grätzel, M. Direct Contact of Selective Charge Extraction Layers Enables High-Efficiency Molecular Photovoltaics. *Joule* **2**, 1108-1117 (2018). https://doi.org/10.1016/j.joule.2018.03.017

56 Ma, L.-K. *et al.* High-Efficiency Indoor Organic Photovoltaics with a Band-Aligned Interlayer. *Joule* **4**, 1486-1500 (2020). https://doi.org/10.1016/j.joule.2020.05.010

57 Noh, Y. W., Jin, I. S., Kim, K. S., Park, S. H. & Jung, J. W. Reduced energy loss in SnO_2/ZnO bilayer electron transport layer-based perovskite solar cells for achieving high efficiencies in outdoor/indoor environments. *Journal of Materials Chemistry A* **8**, 17163-17173 (2020). https://doi.org/10.1039/D0TA04721J

58 Ma, Q. *et al.* One-step dual-additive passivated wide-bandgap perovskites to realize 44.72%-efficient indoor photovoltaics. *Energy & Environmental Science* **17**, 1637-1644 (2024). https://doi.org/10.1039/D3EE04022D

59 Dong, C. *et al.* Lycopene-Based Bionic Membrane for Stable Perovskite Photovoltaics. *Advanced Functional Materials* **31**, 2011242 (2021). https://doi.org/10.1002/adfm.202011242

60 Brandt, R. E., Stevanović, V., Ginley, D. S. & Buonassisi, T. Identifying defect-tolerant semiconductors with high minority-carrier lifetimes: beyond hybrid lead halide perovskites. *MRS Communications* **5**, 265-275 (2015). https://doi.org/10.1557/mrc.2015.26

61 Ganose, A. M., Savory, C. N. & Scanlon, D. O. Beyond methylammonium lead iodide: prospects for the emergent field of ns^2 containing solar absorbers. *Chemical Communications* **53**, 20-44 (2016). https://doi.org/10.1039/C6CC06475B

62 Hoye, R. L. Z. *et al.* Strongly Enhanced Photovoltaic Performance and Defect Physics of Air-Stable Bismuth Oxyiodide (BiOI). *Advanced Materials* **29**, 1702176 (2017). https://doi.org/10.1002/adma.201702176
63 Walsh, A. & Zunger, A. Instilling defect tolerance in new compounds. *Nature Materials* **16**, 964-967 (2017). https://doi.org/10.1038/nmat4973
64 Yin, W.-J., Shi, T. & Yan, Y. Unusual defect physics in $CH_3NH_3PbI_3$ perovskite solar cell absorber. *Applied Physics Letters* **104**, 063903 (2014). https://doi.org/10.1063/1.4864778
65 Du, M. H. Efficient carrier transport in halide perovskites: theoretical perspectives. *Journal of Materials Chemistry A* **2**, 9091-9098 (2014). https://doi.org/10.1039/C4TA01198H
66 Mosquera-Lois, I. *et al.* Multifaceted nature of defect tolerance in halide perovskites and emerging semiconductors. *Nature Reviews Materials* (2025). https://doi.org/10.1038/s41570-025-00702-w
67 Wang, N. *et al.* Heterojunction-Depleted Lead-Free Perovskite Solar Cells with Coarse-Grained B-γ-$CsSnI_3$ Thin Films. *Advanced Energy Materials* **6**, 1601130 (2016). https://doi.org/10.1002/aenm.201601130
68 Xu, F., Wei, H. & Cao, B. A hot phonon bottleneck observed upon incorporation of SnF_2 to $MASnI_3$ films and its possible role in increasing photocarrier diffusion length. *Journal of Applied Physics* **135**, 133102 (2024). https://doi.org/10.1063/5.0194851
69 Ji, L. *et al.* Regulating crystallization dynamics and crystal orientation of methylammonium tin iodide enables high-efficiency lead-free perovskite solar cells. *Nanoscale* **14**, 1219-1225 (2022). https://doi.org/10.1039/D1NR06802D
70 Wang, P. *et al.* Ion Exchange/Insertion Reactions for Fabrication of Efficient Methylammonium Tin Iodide Perovskite Solar Cells. *Advanced Science* **7**, 1903047 (2020). https://doi.org/10.1002/advs.201903047
71 Meng, X. *et al.* Surface-Controlled Oriented Growth of $FASnI_3$ Crystals for Efficient Lead-free Perovskite Solar Cells. *Joule* **4**, 902-912 (2020). https://doi.org/10.1016/j.joule.2020.03.007
72 Dixit, H., Punetha, D. & Pandey, S. K. Improvement in performance of lead free inverted perovskite solar cell by optimization of solar parameters. *Optik* **179**, 969-976 (2019). https://doi.org/10.1016/j.ijleo.2018.11.028
73 Zakutayev, A. *et al.* Defect Tolerant Semiconductors for Solar Energy Conversion. *The Journal of Physical Chemistry Letters* **5**, 1117-1125 (2014). https://doi.org/10.1021/jz5001787
74 Zhang, S. B., Wei, S.-H., Zunger, A. & Katayama-Yoshida, H. Defect physics of the $CuInSe_2$ chalcopyrite semiconductor. *Physical Review B* **57**, 9642-9656 (1998). https://doi.org/10.1103/PhysRevB.57.9642
75 Walsh, A., Scanlon, D. O., Chen, S., Gong, X. G., & Wei, S. H. Self-Regulation Mechanism for Charged Point Defects in Hybrid Halide Perovskites. *Angewandte Chemie* **127**, 1811-1814 (2014). https://doi.org/10.1002/ange.201409740
76 Miyata, K. *et al.* Large polarons in lead halide perovskites. *Science Advances* **3**, e1701217 (2017). https://doi.org/10.1126/sciadv.1701217
77 Miyata, K. & Zhu, X. Y. Ferroelectric large polarons. *Nature Materials* **17**, 379-381

(2018). https://doi.org/10.1038/s41563-018-0068-7
78 Zhu, H. *et al.* Screening in crystalline liquids protects energetic carriers in hybrid perovskites. *Science* **353**, 1409-1413 (2016). https://doi.org/10.1126/science.aaf9570
79 Zhou, Z. *et al.* Methylamine-Gas-Induced Defect-Healing Behavior of $CH_3NH_3PbI_3$ Thin Films for Perovskite Solar Cells. *Angewandte Chemie International Edition* **54**, 9705-9709 (2015). https://doi.org/10.1002/anie.201504379
80 Rakita, Y., Lubomirsky, I. & Cahen, D. When defects become 'dynamic': halide perovskites: a new window on materials? *Materials Horizons* **6**, 1297-1305 (2019). https://doi.org/10.1039/C9MH00606K
81 Brandt, R. E. *et al.* Searching for "Defect-Tolerant" Photovoltaic Materials: Combined Theoretical and Experimental Screening. *Chemistry of Materials* **29**, 4667-4674 (2017). https://doi.org/10.1021/acs.chemmater.6b05496
82 U. S. Geological Survey. Mineral commodity summaries 2023. Report No. 2023, 210 (U. S. Geological Survey, Reston, VA, 2023).
83 Huq, T. N. *et al.* Electronic Structure and Optoelectronic Properties of Bismuth Oxyiodide Robust against Percent-Level Iodine-, Oxygen-, and Bismuth-Related Surface Defects. *Advanced Functional Materials* **30**, 1909983 (2020). https://doi.org/10.1002/adfm.201909983
84 Song, T.-B. *et al.* Piperazine Suppresses Self-Doping in $CsSnI_3$ Perovskite Solar Cells. *ACS Applied Energy Materials* **1**, 4221-4226 (2018). https://doi.org/10.1021/acsaem.8b00866
85 Meggiolaro, D., Ricciarelli, D., Alasmari, A. A., Alasmary, F. A. S., & De Angelis, F. Tin versus Lead Redox Chemistry Modulates Charge Trapping and Self-Doping in Tin/Lead Iodide Perovskites. *The Journal of Physical Chemistry Letters* **11**, 3546-3556 (2020). https://doi.org/10.1021/acs.jpclett.0c00725
86 Wang, J., Li, K., Tang, J. & Chen, C. A Perspective of Antimony Chalcogenide Photovoltaics toward Commercialization. *Solar RRL* **7**, 2300436 (2023). https://doi.org/10.1002/solr.202300436
87 Oh, J. T. *et al.* Post-deposition in situ passivation of $AgBiS_2$ nanocrystal inks for high-efficiency ultra-thin solar cells. *Energy & Environmental Science* **17**, 8885-8892 (2024). https://doi.org/10.1039/D4EE03266G
88 Huang, P.-C., Yang, W.-C. & Lee, M.-W. $AgBiS_2$ Semiconductor-Sensitized Solar Cells. *The Journal of Physical Chemistry C* **117**, 18308-18314 (2013). https://doi.org/10.1021/jp4046337
89 Pai, N. *et al.* Spray deposition of $AgBiS_2$ and Cu_3BiS_3 thin films for photovoltaic applications. *Journal of Materials Chemistry C* **6**, 2483-2494 (2018). https://doi.org/10.1039/C7TC05711C
90 Burgués-Ceballos, I., Wang, Y. & Konstantatos, G. Mixed $AgBiS_2$ nanocrystals for photovoltaics and photodetectors. *Nanoscale* **14**, 4987-4993 (2022). https://doi.org/10.1039/D2NR00589A
91 Bernechea, M. *et al.* Solution-processed solar cells based on environmentally friendly $AgBiS_2$ nanocrystals. *Nature Photonics* **10**, 521-525 (2016). https://doi.org/10.1038/nphoton.2016.108
92 Hu, L. *et al.* Enhanced optoelectronic performance in $AgBiS_2$ nanocrystals obtained

via an improved amine-based synthesis route. *Journal of Materials Chemistry C* **6**, 731-737 (2018). https://doi.org/10.1039/C7TC05366E

93 Wang, Y. *et al.* Cation disorder engineering yields $AgBiS_2$ nanocrystals with enhanced optical absorption for efficient ultrathin solar cells. *Nature Photonics* **16**, 235-241 (2022). https://doi.org/10.1038/s41566-021-00950-4

94 Righetto, M. *et al.* Cation-Disorder Engineering Promotes Efficient Charge-Carrier Transport in $AgBiS_2$ Nanocrystal Films. *Advanced Materials*, e2305009 (2023). https://doi.org/10.1002/adma.202305009

95 Kim, C., Kozakci, I., Kim, J., Lee, S. Y., & Lee, J. Y. Highly Efficient (>9%) Lead-Free $AgBiS_2$ Colloidal Nanocrystal/Organic Hybrid Solar Cells. *Advanced Energy Materials* **12**, 2200262 (2022). https://doi.org/10.1002/aenm.202200262

96 Huang, Y. T. *et al.* Strong absorption and ultrafast localisation in $NaBiS_2$ nanocrystals with slow charge-carrier recombination. *Nature Communications* **13**, 4960 (2022). https://doi.org/10.1038/s41467-022-32669-3

97 Huang, Y. T. *et al.* Elucidating the Role of Ligand Engineering on Local and Macroscopic Charge-Carrier Transport in $NaBiS_2$ Nanocrystal Thin Films. *Advanced Functional Materials* **34**, 2310283 (2024). https://doi.org/10.1002/adfm.202310283

98 Jia, Z. *et al.* Charge-Carrier Dynamics of Solution-Processed Antimony- and Bismuth-Based Chalcogenide Thin Films. *ACS Energy Letters* **8**, 1485-1492 (2023). https://doi.org/10.1021/acsenergylett.3c00140

99 Kentsch, R. *et al.* Exciton Dynamics and Electron–Phonon Coupling Affect the Photovoltaic Performance of the $Cs_2AgBiBr_6$ Double Perovskite. *The Journal of Physical Chemistry C* **122**, 25940-25947 (2018). https://doi.org/10.1021/acs.jpcc.8b09911

100 Lal, S. *et al.* Bandlike Transport and Charge-Carrier Dynamics in BiOI Films. *The Journal of Physical Chemistry Letters* **14**, 6620-6629 (2023). https://doi.org/10.1021/acs.jpclett.3c01520

101 Jagt, R. A. *et al.* Layered BiOI single crystals capable of detecting low dose rates of X-rays. *Nature Communications* **14**, 2452 (2023). https://doi.org/10.1038/s41467-023-38008-4

102 Pan, W. *et al.* $Cs_2AgBiBr_6$ single-crystal X-ray detectors with a low detection limit. *Nature Photonics* **11**, 726-732 (2017). https://doi.org/10.1038/s41566-017-0012-4

103 Temple, D. J., Kehoe, A. B., Allen, J. P., Watson, G. W. & Scanlon, D. O. Geometry, Electronic Structure, and Bonding in $CuMCh_2$(M = Sb, Bi; Ch = S, Se): Alternative Solar Cell Absorber Materials? *The Journal of Physical Chemistry C* **116**, 7334-7340 (2012). https://doi.org/10.1021/jp300862v

104 Dufton, J. T. *et al.* Structural and electronic properties of $CuSbS_2$ and $CuBiS_2$: potential absorber materials for thin-film solar cells. *Physical Chemistry Chemical Physics* **14**, 7229-7233 (2012). https://doi.org/10.1039/c2cp40916j

105 Whittles, T. J. *et al.* Core Levels, Band Alignments, and Valence-Band States in $CuSbS_2$ for Solar Cell Applications. *ACS Applied Materials & Interfaces* **9**, 41916-41926 (2017). https://doi.org/10.1021/acsami.7b14208

106 Walsh, A., Payne, D. J., Egdell, R. G. & Watson, G. W. Stereochemistry of post-transition metal oxides: revision of the classical lone pair model. *Chemical Society*

Reviews **40**, 4455-4463 (2011). https://doi.org/10.1039/C1CS15098G

107 Wang, X., Ganose, A. M., Kavanagh, S. R. & Walsh, A. Band versus Polaron: Charge Transport in Antimony Chalcogenides. *ACS Energy Letters* **7**, 2954-2960 (2022). https://doi.org/10.1021/acsenergylett.2c01464

108 Chen, T. *et al.* Ultralow Thermal Conductivity and Enhanced Figure of Merit for $CuSbSe_2$ via Cd-Doping. *ACS Applied Energy Materials* **4**, 1637-1643 (2021). https://doi.org/10.1021/acsaem.0c02820

109 Zhou, J. *et al.* Solvothermal crystal growth of $CuSbQ_2$ (Q=S, Se) and the correlation between macroscopic morphology and microscopic structure. *Journal of Solid State Chemistry* **182**, 259-264 (2009). https://doi.org/10.1016/j.jssc.2008.10.025

110 Goyal, D., Goyal, C. P., Ikeda, H. & Malar, P. Role of growth temperature in photovoltaic absorber $CuSbSe_2$ deposition through e-beam evaporation. *Materials Science in Semiconductor Processing* **108**, 104874 (2020). https://doi.org/10.1016/j.mssp.2019.104874

111 Maeda, T. & Wada, T. First-principles study of electronic structure of $CuSbS_2$ and $CuSbSe_2$ photovoltaic semiconductors. *Thin Solid Films* **582**, 401-407 (2015). https://doi.org/10.1016/j.tsf.2014.11.089

112 Xue, D. J. *et al.* $CuSbSe_2$ as a potential photovoltaic absorber material: studies from theory to experiment. *Advanced Energy Materials* **5**, 1501203 (2015). https://doi.org/10.1002/aenm.201501203

113 Yu, L., Kokenyesi, R. S., Keszler, D. A. & Zunger, A. Inverse Design of High Absorption Thin-Film Photovoltaic Materials. *Advanced Energy Materials* **3**, 43-48 (2012). https://doi.org/10.1002/aenm.201200538

114 Yang, B. *et al.* $CuSbS_2$ as a Promising Earth-Abundant Photovoltaic Absorber Material: A Combined Theoretical and Experimental Study. *Chemistry of Materials* **26**, 3135-3143 (2014). https://doi.org/10.1021/cm500516v

115 McCarthy, C. L. *et al.* Earth abundant $CuSbS_2$ thin films solution processed from thiol–amine mixtures. *Journal of Materials Chemistry C* **4**, 6230-6233 (2016). https://doi.org/10.1039/C6TC02117D

116 Banu, S., Ahn, S. J., Ahn, S. K., Yoon, K., & Cho, A. Fabrication and characterization of cost-efficient $CuSbS_2$ thin film solar cells using hybrid inks. *Solar Energy Materials and Solar Cells* **151**, 14-23 (2016). https://doi.org/10.1016/j.solmat.2016.02.013

117 Welch, A. W. *et al.* Trade-Offs in Thin Film Solar Cells with Layered Chalcostibite Photovoltaic Absorbers. *Advanced Energy Materials* **7**, 1601935 (2017). https://doi.org/10.1002/aenm.201601935

118 Wang, C. *et al.* Reactive close-spaced sublimation processed $CuSbSe_2$ thin films and their photovoltaic application. *APL Materials* **6**, 084801 (2018). https://doi.org/10.1063/1.5028415

119 Li, D. & Qin, X. Y. Thermoelectric properties of $CuSbSe_2$ and its doped compounds by Ti and Pb at low temperatures from 5 to 310K. *Journal of Applied Physics* **100** (2006). https://doi.org/10.1063/1.2218592

120 Colombara, D., Peter, L. M., Rogers, K. D., Painter, J. D., & Roncallo, S. Formation of $CuSbS_2$ and $CuSbSe_2$ thin films via chalcogenisation of Sb–Cu metal precursors.

Thin Solid Films **519**, 7438-7443 (2011). https://doi.org/10.1016/j.tsf.2011.01.140

121 Yang, B. *et al.* Hydrazine solution processed $CuSbSe_2$: Temperature dependent phase and crystal orientation evolution. *Solar Energy Materials and Solar Cells* **168**, 112-118 (2017). https://doi.org/10.1016/j.solmat.2017.04.030

122 Dunlap-Shohl, W. A., Zhou, Y., Padture, N. P. & Mitzi, D. B. Synthetic Approaches for Halide Perovskite Thin Films. *Chemical Reviews* **119**, 3193-3295 (2019). https://doi.org/10.1021/acs.chemrev.8b00318

123 Polizzotti, A., Repins, I. L., Noufi, R., Wei, S.-H. & Mitzi, D. B. The state and future prospects of kesterite photovoltaics. *Energy & Environmental Science* **6** (2013). https://doi.org/10.1039/c3ee41781f

124 Ghosh, C. & Varma, B. P. Optical properties of amorphous and crystalline Sb_2S_3 thin films. *Thin Solid Films* **60**, 61-65 (1979). https://doi.org/10.1016/0040-6090(79)90347-X

125 Kondrotas, R., Chen, C. & Tang, J. Sb_2S_3 solar cells. *Joule* **2**, 857-878 (2018). https://doi.org/10.1016/j.joule.2018.04.003

126 Wang, K. *et al.* Both Free and Trapped Carriers Contribute to Photocurrent of Sb_2Se_3 Solar Cells. *The Journal of Physical Chemistry Letters* **10**, 4881-4887 (2019). https://doi.org/10.1021/acs.jpclett.9b01817

127 Lokhande, C. D. Chemical deposition of metal chalcogenide thin films. *Materials Chemistry and Physics* **27**, 1-43 (1991). https://doi.org/10.1016/0254-0584(91)90158-Q

128 Savadogo, O. & Mandal, K. C. Studies on new chemically deposited photoconducting antimony trisulphide thin films. *Solar Energy Materials and Solar Cells* **26**, 117-136 (1992). https://doi.org/10.1016/0927-0248(92)90131-8

129 Savadogo, O. & Mandal, K. C. Low Cost Schottky Barrier Solar Cells Fabricated on CdSe and Sb_2S_3 Films Chemically Deposited with Silicotungstic Acid. *Journal of The Electrochemical Society* **141**, 2871 (1994). https://doi.org/10.1149/1.2059248

130 Savadogo, O. & Mandal, K. C. Low-cost technique for preparing n-Sb_2S_3/p-Si heterojunction solar cells. *Applied Physics Letters* **63**, 228-230 (1993). https://doi.org/10.1063/1.110349

131 Choi, Y. C., Lee, D. U., Noh, J. H., Kim, E. K. & Seok, S. I. Highly Improved Sb_2S_3 Sensitized-Inorganic–Organic Heterojunction Solar Cells and Quantification of Traps by Deep-Level Transient Spectroscopy. *Advanced Functional Materials* **24**, 3587-3592 (2014). https://doi.org/10.1002/adfm.201304238

132 Wang, S. *et al.* A Novel Multi-Sulfur Source Collaborative Chemical Bath Deposition Technology Enables 8%-Efficiency Sb_2S_3 Planar Solar Cells. *Advanced Materials* **34**, 2206242 (2022). https://doi.org/10.1002/adma.202206242

133 Liu, X. *et al.* Grain Engineering of Sb_2S_3 Thin Films to Enable Efficient Planar Solar Cells with High Open-Circuit Voltage. *Advanced Materials* **36**, 2305841 (2024). https://doi.org/10.1002/adma.202305841

134 Büttner, P. *et al.* Adjusting Interfacial Chemistry and Electronic Properties of Photovoltaics Based on a Highly Pure Sb_2S_3 Absorber by Atomic Layer Deposition. *ACS Applied Energy Materials* **2**, 8747-8756 (2019). https://doi.org/10.1021/acsaem.9b01721

135 Jaramillo-Quintero, O. A., Baron-Jaimes, A., Miranda-Gamboa, R. A., & Rincon, M. E. Cadmium-free ZnS interfacial layer for hydrothermally processed Sb_2S_3 solar cells. *Solar Energy* **224**, 697-702 (2021). https://doi.org/10.1016/j.solener.2021.06.037

136 Kumar, P. *et al.* Cadmium-free electron transport layers for hydrothermally processed semitransparent Sb_2S_3 solar cells. *Nano Energy* **134**, 110539 (2025). https://doi.org/10.1016/j.nanoen.2024.110539

137 Zhang, L. *et al.* Sb_2S_3 Seed-Mediated Growth of Low-Defect Sb_2S_3 on a TiO_2 Substrate for Efficient Solar Cells. *ACS Applied Energy Materials* **3**, 12417-12422 (2020). https://doi.org/10.1021/acsaem.0c02400

138 Pawar, P. S. *et al.* Atomic-layer-deposited TiO_2 and SnO_2 coupled with CdS as double buffer layers for HTL-free Sb_2S_3 thin-film solar cells. *Solar Energy* **246**, 141-151 (2022). https://doi.org/10.1016/j.solener.2022.09.044

139 Shi, J. *et al.* Enhanced interface properties of solution-processed antimony sulfide planar solar cells with n-type indium sulfide buffer layer. *Electrochimica Acta* **376**, 138031 (2021). https://doi.org/10.1016/j.electacta.2021.138031

140 Wang, C. *et al.* Interfacial defect healing of $In_2S_3/Sb_2(S, Se)_3$ heterojunction solar cells with a novel wide-bandgap InOCl passivator. *Journal of Materials Chemistry A* **11**, 19914-19924 (2023). https://doi.org/10.1039/D3TA01736B

141 Liu, Y. *et al.* Spin-Coated Small Molecules for High Performance Solar Cells. *Advanced Energy Materials* **1**, 771-775 (2011). https://doi.org/10.1002/aenm.201100230

142 Li, G. *et al.* High-efficiency solution processable polymer photovoltaic cells by self-organization of polymer blends. *Nature Materials* **4**, 864-868 (2005). https://doi.org/10.1038/nmat1500

143 Liu, C. *et al.* Bimolecularly passivated interface enables efficient and stable inverted perovskite solar cells. *Science* **382**, 810-815 (2023). https://doi.org/10.1126/science.adk1633

144 Lee, M. M., Teuscher, J., Miyasaka, T., Murakami, T. N. & Snaith, H. J. Efficient Hybrid Solar Cells Based on Meso-Superstructured Organometal Halide Perovskites. *Science* **338**, 643-647 (2012). https://doi.org/10.1126/science.1228604

145 Stranks, S. D. *et al.* Electron-Hole Diffusion Lengths Exceeding 1 Micrometer in an Organometal Trihalide Perovskite Absorber. *Science* **342**, 341-344 (2013). https://doi.org/10.1126/science.1243982

146 Giovanella, U. *et al.* Efficient Solution-Processed Nanoplatelet-Based Light-Emitting Diodes with High Operational Stability in Air. *Nano Letters* **18**, 3441-3448 (2018). https://doi.org/10.1021/acs.nanolett.8b00456

147 Ye, J. *et al.* Direct linearly polarized electroluminescence from perovskite nanoplatelet superlattices. *Nature Photonics* **18**, 586-594 (2024). https://doi.org/10.1038/s41566-024-01398-y

148 Ye, J. *et al.* Elucidating the Role of Antisolvents on the Surface Chemistry and Optoelectronic Properties of $CsPbBr_xI_{3-x}$ Perovskite Nanocrystals. *Journal of the American Chemical Society* **144**, 12102-12115 (2022). https://doi.org/10.1021/jacs.2c02631

149 Park, J. W., Kang, B. H. & Kim, H. J. A Review of Low-Temperature Solution-

Processed Metal Oxide Thin-Film Transistors for Flexible Electronics. *Advanced Functional Materials* **30**, 1904632 (2020). https://doi.org/10.1002/adfm.201904632

150 Purwidyantri, A. *et al.* Spin-coated Au-nanohole arrays engineered by nanosphere lithography for a *Staphylococcus aureus* 16S rRNA electrochemical sensor. *Biosensors and Bioelectronics* **77**, 1086-1094 (2016). https://doi.org/10.1016/j.bios.2015.10.094

151 Moreira, J., Vale, A. C. & Alves, N. M. Spin-coated freestanding films for biomedical applications. *Journal of Materials Chemistry B* **9**, 3778-3799 (2021). https://doi.org/10.1039/D1TB00233C

152 McCarthy, C. L. & Brutchey, R. L. Solution processing of chalcogenide materials using thiol-amine "alkahest" solvent systems. *Chemical Communications* **53**, 4888-4902 (2017). https://doi.org/10.1039/c7cc02226c

153 Mitzi, D. B. *et al.* A High-Efficiency Solution-Deposited Thin-Film Photovoltaic Device. *Advanced Materials* **20**, 3657-3662 (2008). https://doi.org/10.1002/adma.200800555

154 Mitzi, D. B., Kosbar, L. L., Murray, C. E., Copel, M. & Afzali, A. High-mobility ultrathin semiconducting films prepared by spin coating. *Nature* **428**, 299-303 (2004). https://doi.org/10.1038/nature02389

155 Mitzi, D. B. Solution Processing of Chalcogenide Semiconductors via Dimensional Reduction. *Advanced Materials* **21**, 3141-3158 (2009). https://doi.org/10.1002/adma.200802027

156 Webber, D. H. & Brutchey, R. L. Alkahest for V_2VI_3 chalcogenides: dissolution of nine bulk semiconductors in a diamine-dithiol solvent mixture. *Journal of the American Chemical Society* **135**, 15722-15725 (2013). https://doi.org/10.1021/ja4084336

157 Sun, X. *et al.* Mixed-solvent-vapor annealing of perovskite for photovoltaic device efficiency enhancement. *Nano Energy* **28**, 417-425 (2016). https://doi.org/10.1016/j.nanoen.2016.08.055

158 Zhao, X., Lu, M., Koeper, M. J. & Agrawal, R. Solution-processed sulfur depleted Cu(In, Ga)Se_2 solar cells synthesized from a monoamine–dithiol solvent mixture. *Journal of Materials Chemistry A* **4**, 7390-7397 (2016). https://doi.org/10.1039/c6ta00533k

159 Liu, F. *et al.* Low-temperature, solution-deposited metal chalcogenide films as highly efficient counter electrodes for sensitized solar cells. *Journal of Materials Chemistry A* **3**, 6315-6323 (2015). https://doi.org/10.1039/C5TA00028A

160 Arnou, P. *et al.* Solution processing of $CuIn(S,Se)_2$ and $Cu(In,Ga)(S,Se)_2$ thin film solar cells using metal chalcogenide precursors. *Thin Solid Films* **633**, 76-80 (2017). https://doi.org/10.1016/j.tsf.2016.10.011

161 Buckley, J. J., Greaney, M. J. & Brutchey, R. L. Ligand Exchange of Colloidal CdSe Nanocrystals with Stibanates Derived from Sb_2S_3 Dissolved in a Thiol-Amine Mixture. *Chemistry of Materials* **26**, 6311-6317 (2014). https://doi.org/10.1021/cm503324k

162 Murria, P. *et al.* Speciation of CuCl and $CuCl_2$ Thiol-Amine Solutions and Characterization of Resulting Films: Implications for Semiconductor Device

Fabrication. *Inorganic Chemistry* **56**, 14396-14407 (2017). https://doi.org/10.1021/acs.inorgchem.7b01359

163 Koskela, K. M., Strumolo, M. J. & Brutchey, R. L. Progress of thiol-amine 'alkahest' solutions for thin film deposition. *Trends in Chemistry* **3**, 1061-1073 (2021). https://doi.org/10.1016/j.trechm.2021.09.006

164 Sun, L. *et al.* Chemical vapour deposition. *Nature Reviews Methods Primers* **1**, 5 (2021). https://doi.org/10.1038/s43586-020-00005-y

165 Chen, X.-D. *et al.* Fast Growth and Broad Applications of 25-Inch Uniform Graphene Glass. *Advanced Materials* **29**, 1603428 (2017). https://doi.org/10.1002/adma.201603428

166 Deng, B., Liu, Z. & Peng, H. Toward Mass Production of CVD Graphene Films. *Advanced Materials* **31**, 1800996 (2019). https://doi.org/10.1002/adma.201800996

167 Tang, L. *et al.* Vertical Chemical Vapor Deposition Growth of Highly Uniform 2D Transition Metal Dichalcogenides. *ACS Nano* **14**, 4646-4653 (2020). https://doi.org/10.1021/acsnano.0c00296

168 Schneller, T., Waser, R., Kosec, M. & Payne, D. *Chemical solution deposition of functional oxide thin films*. (Springer, 2013).

169 Larramona, G. *et al.* Nanostructured Photovoltaic Cell of the Type Titanium Dioxide, Cadmium Sulfide Thin Coating, and Copper Thiocyanate Showing High Quantum Efficiency. *Chemistry of Materials* **18**, 1688-1696 (2006). https://doi.org/10.1021/cm052819n

170 Contreras, M. A. *et al.* Optimization of CBD CdS process in high-efficiency Cu(In,Ga)Se_2-based solar cells. *Thin Solid Films* **403-404**, 204-211 (2002). https://doi.org/10.1016/S0040-6090(01)01538-3

171 Yoo, J. J. *et al.* Efficient perovskite solar cells via improved carrier management. *Nature* **590**, 587-593 (2021). https://doi.org/10.1038/s41586-021-03285-w

172 Tang, D. *et al.* One-step electrodeposition and annealing of $CuSbSe_2$ thin films. *Electrochemical and Solid-State Letters* **15**, D11-D13 (2011). https://doi.org/10.1149/2.007202esl

173 Wang, R. *et al.* Improving the performance of Sb_2S_3 thin-film solar cells by optimization of VTD source-substrate proximity. *Solar Energy* **220**, 942-948 (2021). https://doi.org/10.1016/j.solener.2021.03.052

174 Zeng, Y. *et al.* Quasi-Vertically-Orientated Antimony Sulfide Inorganic Thin-Film Solar Cells Achieved by Vapor Transport Deposition. *ACS Applied Materials & Interfaces* **12**, 22825-22834 (2020). https://doi.org/10.1021/acsami.0c02697

175 Deng, H. *et al.* Quasiepitaxy Strategy for Efficient Full-Inorganic Sb_2S_3 Solar Cells. *Advanced Functional Materials* **29**, 1901720 (2019). https://doi.org/10.1002/adfm.201901720

176 Xie, Y. *et al.* Fabrication of Sb_2S_3 solar cells by close space sublimation and enhancing the efficiency via co-selenization. *Materials Science in Semiconductor Processing* **142**, 106451 (2022). https://doi.org/10.1016/j.mssp.2022.106451

177 Hodes, G. Semiconductor and ceramic nanoparticle films deposited by chemical bath deposition. *Physical Chemistry Chemical Physics* **9**, 2181-2196 (2007). https://doi.org/10.1039/B616684A

178 Powell, C. J. & Jablonski, A. Evaluation of electron inelastic mean free paths for selected elements and compounds. *Surface and Interface Analysis* **29**, 108-114 (2000). https://doi.org/10.1002/(SICI)1096-9918(200002)29:2%3C108::AID-SIA700%3E3.0.CO;2-4
179 Powell, C. J. & Jablonski, A. Evaluation of Calculated and Measured Electron Inelastic Mean Free Paths Near Solid Surfaces. *Journal of Physical and Chemical Reference Data* **28**, 19-62 (1999). https://doi.org/10.1063/1.556035
180 Tanuma, S., Powell, C. J. & Penn, D. R. Calculations of electron inelastic mean free paths. III. Data for 15 inorganic compounds over the 50–2000 eV range. *Surface and Interface Analysis* **17**, 927-939 (1991). https://doi.org/10.1002/sia.740171305
181 Tanuma, S., Powell, C. J. & Penn, D. R. Calculations of electron inelastic mean free paths. V. Data for 14 organic compounds over the 50–2000 eV range. *Surface and Interface Analysis* **21**, 165-176 (1994). https://doi.org/10.1002/sia.740210302
182 Shirley, D. A. High-Resolution X-Ray Photoemission Spectrum of the Valence Bands of Gold. *Physical Review B* **5**, 4709-4714 (1972). https://doi.org/10.1103/PhysRevB.5.4709
183 Wagner, C. D. NIST X-ray photoelectron spectroscopy database. *NIST Standarad Reference Database 20* (2000). https://doi.org/10.5334/dsj-2024-045
184 Cahen, D., Ireland, P. J., Kazmerski, L. L. & Thiel, F. A. X-ray photoelectron and Auger electron spectroscopic analysis of surface treatments and electrochemical decomposition of $CuInSe_2$ photoelectrodes. *Journal of Applied Physics* **57**, 4761-4771 (1985). https://doi.org/10.1063/1.335341
185 Nakai, I., Sugitani, Y., Nagashima, K. & Niwa, Y. X-ray photoelectron spectroscopic study of copper minerals. *Journal of Inorganic and Nuclear Chemistry* **40**, 789-791 (1978). https://doi.org/10.1016/0022-1902(78)80152-3
186 Romand, M., Roubin, M. & Deloume, J. P. ESCA studies of some copper and silver selenides. *Journal of Electron Spectroscopy and Related Phenomena* **13**, 229-242 (1978). https://doi.org/10.1016/0368-2048(78)85029-4
187 Sobol, P. E., Nelson, A. J., Schwerdtfeger, C. R., Stickle, W. F. & Moulder, J. F. Single Crystal $CuInSe_2$ Analysis by High Resolution XPS. *Surface Science Spectra* **1**, 393-397 (1992). https://doi.org/10.1116/1.1247638
188 Smart, R. S. C., Skinner, W. M. & Gerson, A. R. XPS of sulphide mineral surfaces: metal-deficient, polysulphides, defects and elemental sulphur. *Surface and Interface Analysis* **28**, 101-105 (1999). https://doi.org/10.1002/(SICI)1096-9918(199908)28:1%3C101::AID-SIA627%3E3.0.CO;2-0
189 Birchall, T., Connor, J. A. & Hillier, L. H. High-energy photoelectron spectroscopy of some antimony compounds. *Journal of the Chemical Society, Dalton Transactions*, 2003-2006 (1975). https://doi.org/10.1039/DT9750002003
190 Poirier, D. M. & Weaver, J. H. CdS by XPS. *Surface Science Spectra* **2**, 249-255 (1993). https://doi.org/10.1116/1.1247706
191 Wagner, C. D. Chemical shifts of Auger lines, and the Auger parameter. *Faraday Discussions of the Chemical Society* **60**, 291-300 (1975). https://doi.org/10.1039/DC9756000291
192 Raman, C. V. & Krishnan, K. S. A New Type of Secondary Radiation. *Nature* **121**,

501-502 (1928). https://doi.org/10.1038/121501c0
193 Sadhanala, A. *et al.* Preparation of Single-Phase Films of $CH_3NH_3Pb(I_{1-x}Br_x)_3$ with Sharp Optical Band Edges. *The Journal of Physical Chemistry Letters* **5**, 2501-2505 (2014). https://doi.org/10.1021/jz501332v
194 Berera, R., van Grondelle, R. & Kennis, J. T. M. Ultrafast transient absorption spectroscopy: principles and application to photosynthetic systems. *Photosynthesis Research* **101**, 105-118 (2009). https://doi.org/10.1007/s11120-009-9454-y
195 Horton, M. K., Montoya, J. H., Liu, M. & Persson, K. A. High-throughput prediction of the ground-state collinear magnetic order of inorganic materials using Density Functional Theory. *npj Computational Materials* **5**, 64 (2019). https://doi.org/10.1038/s41524-019-0199-7
196 Hall, E. H. On a New Action of the Magnet on Electric Currents. *American Journal of Mathematics* **2**, 287-292 (1879). https://doi.org/10.2307/2369245
197 van der Pauw, L. J. *A Method of Measuring Specific Resistivity and Hall Effect of Discs of Arbitrary Shape*. in *Semiconductor Devices: Pioneering Papers* 174-182 (WORLD SCIENTIFIC, 1991).
198 Hohenberg, P. & Kohn, W. Inhomogeneous Electron Gas. *Physical Review* **136**, B864-B871 (1964). https://doi.org/10.1103/PhysRev.136.B864
199 Kohn, W. & Sham, L. J. Self-Consistent Equations Including Exchange and Correlation Effects. *Physical Review* **140**, A1133-A1138 (1965). https://doi.org/10.1103/PhysRev.140.A1133
200 Kresse, G. & Joubert, D. From ultrasoft pseudopotentials to the projector augmented-wave method. *Physical Review B* **59**, 1758-1775 (1999). https://doi.org/10.1103/PhysRevB.59.1758
201 Kresse, G. & Furthmüller, J. Efficiency of *ab-initio* total energy calculations for metals and semiconductors using a plane-wave basis set. *Computational Materials Science* **6**, 15-50 (1996). https://doi.org/10.1016/0927-0256(96)00008-0
202 Heyd, J., Scuseria, G. E. & Ernzerhof, M. Hybrid functionals based on a screened Coulomb potential. *The Journal of Chemical Physics* **118**, 8207-8215 (2003). https://doi.org/10.1063/1.1564060
203 Kresse, G. & Hafner, J. *Ab initio* molecular-dynamics simulation of the liquid-metal-amorphous-semiconductor transition in germanium. *Physical Review B* **49**, 14251-14269 (1994). https://doi.org/10.1103/physrevb.49.14251
204 Kresse, G. & Hafner, J. *Ab initio* molecular dynamics for liquid metals. *Physical Review B* **47**, 558-561 (1993). https://doi.org/10.1103/PhysRevB.47.558
205 Dronskowski, R. & Bloechl, P. E. Crystal orbital Hamilton populations (COHP): energy-resolved visualization of chemical bonding in solids based on density-functional calculations. *The Journal of Physical Chemistry* **97**, 8617-8624 (2002). https://doi.org/10.1021/j100135a014
206 Nelson, R. *et al.* LOBSTER: Local orbital projections, atomic charges, and chemical-bonding analysis from projector-augmented-wave-based density-functional theory. *Journal of Computational Chemistry* **41**, 1931-1940 (2020). https://doi.org/10.1002/jcc.26353
207 Maintz, S., Deringer, V. L., Tchougreeff, A. L. & Dronskowski, R. Analytic projection

from plane-wave and PAW wavefunctions and application to chemical-bonding analysis in solids. *Journal of Computational Chemistry* **34**, 2557-2567 (2013). https://doi.org/10.1002/jcc.23424

208 Deringer, V. L., Tchougreeff, A. L. & Dronskowski, R. Crystal orbital Hamilton population (COHP) analysis as projected from plane-wave basis sets. *The Journal of Physical Chemistry A* **115**, 5461-5466 (2011). https://doi.org/10.1021/jp202489s

209 George, J. *et al.* Automated Bonding Analysis with Crystal Orbital Hamilton Populations. *Chempluschem* **87**, e202200123 (2022). https://doi.org/10.1002/cplu.202200123

210 M Ganose, A., J Jackson, A. & O Scanlon, D. sumo: Command-line tools for plotting and analysis of periodic *ab initio* calculations. *Journal of Open Source Software* **3** (2018). https://doi.org/10.21105/joss.00717

211 Franceschetti, A., Wei, S. H. & Zunger, A. Absolute deformation potentials of Al, Si, and NaCl. *Physical Review B* **50**, 17797-17801 (1994). https://doi.org/10.1103/physrevb.50.17797

212 Li, Y.-H., Gong, X. G. & Wei, S.-H. *Ab initio* all-electron calculation of absolute volume deformation potentials of IV-IV, III-V, and II-VI semiconductors: The chemical trends. *Physical Review B* **73**, 245206 (2006). https://doi.org/10.1103/PhysRevB.73.245206

213 Kresse, G., Furthmüller, J. & Hafner, J. *Ab initio* Force Constant Approach to Phonon Dispersion Relations of Diamond and Graphite. *Europhysics Letters* **32**, 729 (1995). https://doi.org/10.1209/0295-5075/32/9/005

214 Togo, A., Chaput, L., Tadano, T. & Tanaka, I. Implementation strategies in phonopy and phono3py. *Journal of Physics: Condensed Matter* **35** (2023). https://doi.org/10.1088/1361-648X/acd831

215 Togo, A. First-principles Phonon Calculations with Phonopy and Phono3py. *Journal of the Physical Society of Japan* **92** (2023). https://doi.org/10.7566/jpsj.92.012001

216 Furness, J. W., Kaplan, A. D., Ning, J., Perdew, J. P. & Sun, J. Accurate and Numerically Efficient r^2SCAN Meta-Generalized Gradient Approximation. *The Journal of Physical Chemistry Letters* **11**, 8208-8215 (2020). https://doi.org/10.1021/acs.jpclett.0c02405

217 Spooner, K. B., Einhorn, M., Davies, D. W. & Scanlon, D. O. ThermoParser: Streamlined Analysis of Thermoelectric Properties. *Journal of Open Source Software* **9** (2024). https://doi.org/10.21105/joss.06340

218 Perdew, J. P., Burke, K. & Ernzerhof, M. Generalized Gradient Approximation Made Simple. *Physical Review Letters* **77**, 3865-3868 (1996). https://doi.org/10.1103/PhysRevLett.77.3865

219 Mosquera-Lois, I., Kavanagh, S. R., Walsh, A. & Scanlon, D. O. Identifying the ground state structures of point defects in solids. *npj Computational Materials* **9**, 25 (2023). https://doi.org/10.1038/s41524-023-00973-1

220 Mosquera-Lois, I., Kavanagh, S. R., Walsh, A. & Scanlon, D. O. ShakeNBreak: Navigating the defect configurational landscape. *Journal of Open Source Software* **7** (2022). https://doi.org/10.21105/joss.04817

221 Sun, S. *et al.* Accelerated Development of Perovskite-Inspired Materials via High-

Throughput Synthesis and Machine-Learning Diagnosis. *Joule* **3**, 1437-1451 (2019). https://doi.org/10.1016/j.joule.2019.05.014

222 Chakraborty, A. *et al.* Rudorffites and Beyond: Perovskite-Inspired Silver/Copper Pnictohalides for Next-Generation Environmentally Friendly Photovoltaics and Optoelectronics. *Advanced Functional Materials* **32**, 2203300 (2022). https://doi.org/10.1002/adfm.202203300

223 Glück, N. & Bein, T. Prospects of lead-free perovskite-inspired materials for photovoltaic applications. *Energy & Environmental Science* **13**, 4691-4716 (2020). https://doi.org/10.1039/d0ee01651a

224 Slavney, A. H., Hu, T., Lindenberg, A. M. & Karunadasa, H. I. A Bismuth-Halide Double Perovskite with Long Carrier Recombination Lifetime for Photovoltaic Applications. *Journal of the American Chemical Society* **138**, 2138-2141 (2016). https://doi.org/10.1021/jacs.5b13294

225 Hoye, R. L. Z. *et al.* Fundamental Carrier Lifetime Exceeding 1 µs in $Cs_2AgBiBr_6$ Double Perovskite. *Advanced Materials Interfaces* **5**, 1800464 (2018). https://doi.org/10.1002/admi.201800464

226 Jaramillo, R. *et al.* Transient terahertz photoconductivity measurements of minority-carrier lifetime in tin sulfide thin films: Advanced metrology for an early stage photovoltaic material. *Journal of Applied Physics* **119** (2016). https://doi.org/10.1063/1.4940157

227 Longo, G. *et al.* Understanding the Performance-Limiting Factors of $Cs_2AgBiBr_6$ Double-Perovskite Solar Cells. *ACS Energy Letters* **5**, 2200-2207 (2020). https://doi.org/10.1021/acsenergylett.0c01020

228 Skoug, E. J. & Morelli, D. T. Role of lone-pair electrons in producing minimum thermal conductivity in nitrogen-group chalcogenide compounds. *Physical Review Letters* **107**, 235901 (2011). https://doi.org/10.1103/PhysRevLett.107.235901

229 Ramasamy, K. *et al.* Layered ternary sulfide $CuSbS_2$ nanoplates for flexible solid-state supercapacitors. *Journal of Materials Chemistry A* **3**, 13263-13274 (2015). https://doi.org/10.1039/c5ta03193a

230 Dai, X. *et al.* Solution-processed, high-performance light-emitting diodes based on quantum dots. *Nature* **515**, 96-99 (2014). https://doi.org/10.1038/nature13829

231 Lin, X., Kavalakkatt, J., Lux-Steiner, M. C. & Ennaoui, A. Inkjet-Printed $Cu_2ZnSn(S, Se)_4$ Solar Cells. *Advanced Science* **2**, 1500028 (2015). https://doi.org/10.1002/advs.201500028

232 Vidal, R. *et al.* Assessing health and environmental impacts of solvents for producing perovskite solar cells. *Nature Sustainability* **4**, 277-285 (2021). https://doi.org/10.1038/s41893-020-00645-8

233 Tian, Q. *et al.* Versatile and Low-Toxic Solution Approach to Binary, Ternary, and Quaternary Metal Sulfide Thin Films and Its Application in $Cu_2ZnSn(S,Se)_4$ Solar Cells. *Chemistry of Materials* **26**, 3098-3103 (2014). https://doi.org/10.1021/cm5002412

234 Arnou, P. *et al.* Hydrazine-Free Solution-Deposited $CuIn(S,Se)_2$ Solar Cells by Spray Deposition of Metal Chalcogenides. *ACS Applied Materials & Interfaces* **8**, 11893-11897 (2016). https://doi.org/10.1021/acsami.6b01541

235 Prabhakar, T. *et al.* Effects of growth process on the optical and electrical properties in Al-doped ZnO thin films. *Journal of Applied Physics* **115** (2014). https://doi.org/10.1063/1.4866997

236 Guo, X. *et al.* Air-stable bismuth sulfobromide (BiSBr) visible-light absorbers: optoelectronic properties and potential for energy harvesting. *Journal of Materials Chemistry A* **11**, 22775-22785 (2023). https://doi.org/10.1039/D3TA04491B

237 Otamiri, J. C., Andersson, S. L. T. & Andersson, A. Ammoxidation of toluene by $YBa_2Cu_3O_{6+x}$ and copper oxides: Activity and XPS studies. *Applied Catalysis* **65**, 159-174 (1990). https://doi.org/10.1016/S0166-9834(00)81595-X

238 Velásquez, P. *et al.* A Chemical, Morphological, and Electrochemical (XPS, SEM/EDX, CV, and EIS) Analysis of Electrochemically Modified Electrode Surfaces of Natural Chalcopyrite ($CuFeS_2$) and Pyrite (FeS_2) in Alkaline Solutions. *The Journal of Physical Chemistry B* **109**, 4977-4988 (2005). https://doi.org/10.1021/jp048273u

239 Poulston, S., Parlett, P. M., Stone, P. & Bowker, M. Surface Oxidation and Reduction of CuO and Cu_2O Studied Using XPS and XAES. *Surface and Interface Analysis* **24**, 811-820 (1996). https://doi.org/10.1002/(SICI)1096-9918(199611)24:12%3C811::AID-SIA191%3E3.0.CO;2-Z

240 Wang, D., Miller, A. C. & Notis, M. R. XPS Study of the Oxidation Behavior of the Cu_3Sn Intermetallic Compound at Low Temperatures. *Surface and Interface Analysis* **24**, 127-132 (1996). https://doi.org/10.1002/(SICI)1096-9918(199602)24:2%3C127::AID-SIA110%3E3.0.CO;2-Z

241 Biesinger, M. C. Advanced analysis of copper X-ray photoelectron spectra. *Surface and Interface Analysis* **49**, 1325-1334 (2017). https://doi.org/10.1002/sia.6239

242 Qiu, X., Ji, S., Chen, C., Liu, G. & Ye, C. Synthesis, characterization, and surface-enhanced Raman scattering of near infrared absorbing Cu_3SbS_3 nanocrystals. *CrystEngComm* **15**, 10431-10434 (2013). https://doi.org/10.1039/C3CE41861H

243 Hsiang, H.-I., Yang, C.-T. & Tu, J.-H. Characterization of $CuSbSe_2$ crystallites synthesized using a hot injection method. *RSC Advances* **6**, 99297-99305 (2016). https://doi.org/10.1039/C6RA20692A

244 Delobel, R., Baussart, H., Leroy, J.-M., Grimblot, J. & Gengembre, L. X-ray photoelectron spectroscopy study of uranium and antimony mixed metal-oxide catalysts. *Journal of the Chemical Society, Faraday Transactions 1: Physical Chemistry in Condensed Phases* **79**, 879-891 (1983). https://doi.org/10.1039/F19837900879

245 Rani, N., Gohel, V. B., Gupta, H. C., Singh, M. K. & Tiwari, L. M. A lattice dynamical investigation of the zone center frequencies of the orthorhombic $NdGaO_3$ perovskite. *Journal of Physics and Chemistry of Solids* **62**, 1003-1006 (2001). https://doi.org/10.1016/s0022-3697(00)00253-5

246 Tiwari, K. J., Vinod, V., Subrahmanyam, A. & Malar, P. Growth and characterization of chalcostibite $CuSbSe_2$ thin films for photovoltaic application. *Applied Surface Science* **418**, 216-224 (2017). https://doi.org/10.1016/j.apsusc.2017.01.279

247 Penezko, A., Kauk-Kuusik, M., Volobujeva, O., Traksmaa, R. & Grossberg, M. Observation of photoluminescence edge emission in $CuSbSe_2$ absorber material for

photovoltaic applications. *Applied Physics Letters* **115**, 092101 (2019). https://doi.org/10.1063/1.5114893

248 Penezko, A., Kauk-Kuusik, M., Volobujeva, O. & Grossberg, M. Properties of Cu-Sb-Se thin films deposited by magnetron co-sputtering for solar cell applications. *Thin Solid Films* **740**, 139004 (2021). https://doi.org/10.1016/j.tsf.2021.139004

249 Gajdoš, M., Hummer, K., Kresse, G., Furthmüller, J. & Bechstedt, F. Linear optical properties in the projector-augmented wave methodology. *Physical Review B* **73**, 045112 (2006). https://doi.org/10.1103/PhysRevB.73.045112

250 Davies, C. L. *et al.* Bimolecular recombination in methylammonium lead triiodide perovskite is an inverse absorption process. *Nature Communications* **9**, 293 (2018). https://doi.org/10.1038/s41467-017-02670-2

251 Wannier, G. H. The Structure of Electronic Excitation Levels in Insulating Crystals. *Physical Review* **52**, 191-197 (1937). https://doi.org/10.1103/PhysRev.52.191

252 Wright, A. D. *et al.* Ultrafast Excited-State Localization in $Cs_2AgBiBr_6$ Double Perovskite. *The Journal of Physical Chemistry Letters* **12**, 3352-3360 (2021). https://doi.org/10.1021/acs.jpclett.1c00653

253 Liu, X., Xiao, H., Zang, Z. & Li, R. Atomic periodic engineering enabled ultrathin high-efficiency $AgBiS_2$ solar cells. *Chemical Communications* **58**, 12066-12069 (2022). https://doi.org/10.1039/D2CC04610E

254 Wei, F. *et al.* Enhanced visible light absorption for lead-free double perovskite $Cs_2AgSbBr_6$. *Chemical Communications* **55**, 3721-3724 (2019). https://doi.org/10.1039/C9CC01134J

255 Righetto, M. *et al.* Alloying Effects on Charge-Carrier Transport in Silver–Bismuth Double Perovskites. *The Journal of Physical Chemistry Letters* **14**, 10340-10347 (2023). https://doi.org/10.1021/acs.jpclett.3c02750

256 Bartesaghi, D. *et al.* Charge Carrier Dynamics in $Cs_2AgBiBr_6$ Double Perovskite. *The Journal of Physical Chemistry C* **122**, 4809-4816 (2018). https://doi.org/10.1021/acs.jpcc.8b00572

257 Li, Z. *et al.* Bandgap lowering in mixed alloys of $Cs_2Ag(Sb_xBi_{1-x})Br_6$ double perovskite thin films. *Journal of Materials Chemistry A* **8**, 21780-21788 (2020). https://doi.org/10.1039/D0TA07145E

258 Bellakhdar, T., Nabi, Z., Bouabdallah, B., Benichou, B. & Saci, H. *Ab initio* study of structural, electronic, mechanical and optical properties of the tetragonal $Cs_2AgBiBr_6$ halide double perovskite. *Applied Physics A* **128**, 155 (2022). https://doi.org/10.1007/s00339-022-05276-8

259 Park, B.-W. *et al.* Bismuth Based Hybrid Perovskites $A_3Bi_2I_9$ (A: Methylammonium or Cesium) for Solar Cell Application. *Advanced Materials* **27**, 6806-6813 (2015). https://doi.org/10.1002/adma.201501978

260 Pazoki, M. *et al.* Bismuth Iodide Perovskite Materials for Solar Cell Applications: Electronic Structure, Optical Transitions, and Directional Charge Transport. *The Journal of Physical Chemistry C* **120**, 29039-29046 (2016). https://doi.org/10.1021/acs.jpcc.6b11745

261 Zheng, X. *et al.* Ultrasensitive and stable X-ray detection using zero-dimensional lead-free perovskites. *Journal of Energy Chemistry* **49**, 299-306 (2020).

https://doi.org/10.1016/j.jechem.2020.02.049
262 Sun, Q. *et al.* Optical and electronic anisotropies in perovskitoid crystals of $Cs_3Bi_2I_9$ studies of nuclear radiation detection. *Journal of Materials Chemistry A* **6**, 23388-23395 (2018). https://doi.org/10.1039/C8TA09525F
263 Sun, Q. *et al.* Anisotropic dielectric behavior of layered perovskite-like $Cs_3Bi_2I_9$ crystals in the terahertz region. *Physical Chemistry Chemical Physics* **22**, 24555-24560 (2020). https://doi.org/10.1039/D0CP04485G
264 Tiwari, D., Cardoso-Delgado, F., Alibhai, D., Mombrú, M. & Fermín, D. J. Photovoltaic Performance of Phase-Pure Orthorhombic BiSI Thin-Films. *ACS Applied Energy Materials* **2**, 3878-3885 (2019). https://doi.org/10.1021/acsaem.9b00544
265 Sasaki, Y. Photoconductivity of a Ferroelectric Photoconductor BiSI. *Japanese Journal of Applied Physics* **4**, 614 (1965). https://doi.org/10.1143/JJAP.4.614
266 Demartin, F., Gramaccioli, C. M. & Campostrini, I. Demicheleite-(I), BiSI, a new mineral from La Fossa Crater, Vulcano, Aeolian Islands, Italy. *Mineralogical Magazine* **74**, 141-145 (2010). https://doi.org/10.1180/minmag.2010.074.1.141
267 Ran, Z. *et al.* Bismuth and antimony-based oxyhalides and chalcohalides as potential optoelectronic materials. *npj Computational Materials* **4**, 14 (2018). https://doi.org/10.1038/s41524-018-0071-1
268 Liu, P. *et al.* Electronic structures and band alignments of monolayer metal trihalide semiconductors MX_3. *Journal of Materials Chemistry C* **5**, 9066-9071 (2017). https://doi.org/10.1039/C7TC03003G
269 Brandt, R. E. *et al.* Investigation of Bismuth Triiodide (BiI_3) for Photovoltaic Applications. *The Journal of Physical Chemistry Letters* **6**, 4297-4302 (2015). https://doi.org/10.1021/acs.jpclett.5b02022
270 Lintereur, A. T., Qiu, W., Nino, J. C. & Baciak, J. Characterization of bismuth tri-iodide single crystals for wide band-gap semiconductor radiation detectors. *Nuclear Instruments and Methods in Physics Research Section A: Accelerators, Spectrometers, Detectors and Associated Equipment* **652**, 166-169 (2011). https://doi.org/10.1016/j.nima.2010.12.013
271 Du, M.-H. & Singh, D. J. Enhanced Born charges in III-VII, IV-VII_2, and V-VII_3 compounds. *Physical Review B* **82**, 045203 (2010). https://doi.org/10.1103/PhysRevB.82.045203
272 Shockley, W. & Bardeen, J. Energy Bands and Mobilities in Monatomic Semiconductors. *Physical Review* **77**, 407-408 (1950). https://doi.org/10.1103/PhysRev.77.407
273 Gaillac, R., Pullumbi, P. & Coudert, F.-X. ELATE: an open-source online application for analysis and visualization of elastic tensors. *Journal of Physics: Condensed Matter* **28**, 275201 (2016). https://doi.org/10.1088/0953-8984/28/27/275201
274 Fu, Y. *et al.* Structural and electronic features enabling delocalized charge-carriers in $CuSbSe_2$. *Nature Communications* **16**, 65 (2025). https://doi.org/10.1038/s41467-024-55254-2
275 Das, A. *et al.* Strong Antibonding I (p)–Cu (d) States Lead to Intrinsically Low Thermal Conductivity in $CuBiI_4$. *Journal of the American Chemical Society* **145**, 1349-1358 (2023). https://doi.org/10.1021/jacs.2c11908

276 Toyozawa, Y. & Shinozuka, Y. Stability of an Electron in Deformable Lattice –Force Range, Dimensionality and Potential Barrier–. *Journal of the Physical Society of Japan* **48**, 472-478 (1980). https://doi.org/10.1143/jpsj.48.472
277 Xiao, Z., Meng, W., Wang, J., Mitzi, D. B. & Yan, Y. Searching for promising new perovskite-based photovoltaic absorbers: the importance of electronic dimensionality. *Materials Horizons* **4**, 206-216 (2017). https://doi.org/10.1039/C6MH00519E
278 Penn, D. R. Wave-Number-Dependent Dielectric Function of Semiconductors. *Physical Review* **128**, 2093-2097 (1962). https://doi.org/10.1103/PhysRev.128.2093
279 Born, M., Huang, K. & Lax, M. Dynamical Theory of Crystal Lattices. *American Journal of Physics* **23**, 474-474 (1955). https://doi.org/10.1119/1.1934059
280 Ghosez, P., Michenaud, J. P. & Gonze, X. Dynamical atomic charges: The case of ABO_3 compounds. *Physical Review B* **58**, 6224-6240 (1998). https://doi.org/10.1103/PhysRevB.58.6224
281 Brivio, F., Walker, A. B. & Walsh, A. Structural and electronic properties of hybrid perovskites for high-efficiency thin-film photovoltaics from first-principles. *APL Materials* **1** (2013). https://doi.org/10.1063/1.4824147
282 Klarbring, J., Hellman, O., Abrikosov, I. A. & Simak, S. I. Anharmonicity and Ultralow Thermal Conductivity in Lead-Free Halide Double Perovskites. *Physical Review Letters* **125**, 045701 (2020). https://doi.org/10.1103/PhysRevLett.125.045701
283 Yin, G.-X., Lv, S.-J. & Wang, H.-Y. First principles study of the electronic, elastic and vibrational properties of BiOI. *Solid State Communications* **336**, 114419 (2021). https://doi.org/10.1016/j.ssc.2021.114419
284 Liu, Y., Eddie Chua, K. T., Sum, T. C. & Gan, C. K. First-principles study of the lattice dynamics of Sb_2S_3. *Physical Chemistry Chemical Physics* **16**, 345-350 (2014). https://doi.org/10.1039/C3CP53879F
285 Lehner, A. J. *et al.* Crystal and Electronic Structures of Complex Bismuth Iodides $A_3Bi_2I_9$ (A = K, Rb, Cs) Related to Perovskite: Aiding the Rational Design of Photovoltaics. *Chemistry of Materials* **27**, 7137-7148 (2015). https://doi.org/10.1021/acs.chemmater.5b03147
286 Shi, H., Ming, W. & Du, M.-H. Bismuth chalcohalides and oxyhalides as optoelectronic materials. *Physical Review B* **93**, 104108 (2016). https://doi.org/10.1103/PhysRevB.93.104108
287 Ming, W., Shi, H. & Du, M.-H. Large dielectric constant, high acceptor density, and deep electron traps in perovskite solar cell material $CsGeI_3$. *Journal of Materials Chemistry A* **4**, 13852-13858 (2016). https://doi.org/10.1039/C6TA04685A
288 Förster, H.-J., Bindi, L. & Stanley, C. J. Grundmannite, $CuBiSe_2$, the Se-analogue of emplectite, a new mineral from the El Dragón mine, Potosí, Bolivia. *European Journal of Mineralogy* **28**, 467-477 (2016). https://doi.org/10.1127/ejm/2016/0028-2513
289 Albarède, F. *The properties of elements*. in *Geochemistry: An Introduction* 5-24 (Cambridge University Press, 2009).
290 Health and Safety Executive. *EH40/2005 Workplace Exposure Limits. Limits for Use with the Control of Substances*. 4th edn (TSO, 2020).
291 European Parliament & Council of the European Union.*Directive 2011/65/EU on the*

restriction of the use of certain hazardous substances in electrical and electronic equipment (RoHS) in *Official Journal of the European Union* Vol. L174,88-110 (European Union, Brussels, 2011).

292 Zhang, R. *et al.* Metal-metal chalcogenide molecular precursors to binary, ternary, and quaternary metal chalcogenide thin films for electronic devices. *Chemical Communications* **52**, 5007-5010 (2016). https://doi.org/10.1039/C5CC09915C

293 Creighton, J. & Ho, P. *Introduction to chemical vapor deposition (CVD)*. in *Chemical Vapor Deposition* 1-19 (ASM International, 2001).

294 Hossain, M. K. *et al.* Mechanism of non-catalytic chemical vapor deposition growth of all-inorganic $CsPbX_3$ (X = Br, Cl) nanowires. *Journal of Materials Chemistry C* **9**, 3229-3238 (2021). https://doi.org/10.1039/d1tc00077b

295 Baig, N., Kammakakam, I. & Falath, W. Nanomaterials: a review of synthesis methods, properties, recent progress, and challenges. *Materials Advances* **2**, 1821-1871 (2021). https://doi.org/10.1039/d0ma00807a

296 Li, F. *et al.* Semitransparent inverted polymer solar cells employing a sol-gel-derived TiO_2 electron-selective layer on FTO and MoO_3/Ag/MoO_3 transparent electrode. *Nanoscale Research Letters* **9**, 579 (2014). https://doi.org/10.1186/1556-276X-9-579

297 Zhu, W. *et al.* Coarsening of one-step deposited organolead triiodide perovskite films via Ostwald ripening for high efficiency planar-heterojunction solar cells. *Dalton Transactions* **45**, 7856-7865 (2016). https://doi.org/10.1039/C6DT00900J

298 Rusanen, M., Koponen, I., Heinonen, J. & Sillanpää, J. The effects of island diffusion and breakup in island growth during ion-beam assisted deposition. *Nuclear Instruments and Methods in Physics Research Section B: Beam Interactions with Materials and Atoms* **148**, 116-120 (1999). https://doi.org/10.1016/S0168-583X(98)00754-X

299 Lee, J. *et al.* Achieving Large-Area Planar Perovskite Solar Cells by Introducing an Interfacial Compatibilizer. *Advanced Materials* **29**, 1606363 (2017). https://doi.org/10.1002/adma.201606363

300 Singh, T. *et al.* Sulfate-Assisted Interfacial Engineering for High Yield and Efficiency of Triple Cation Perovskite Solar Cells with Alkali-Doped TiO_2 Electron-Transporting Layers. *Advanced Functional Materials* **28**, 1706287 (2018). https://doi.org/10.1002/adfm.201706287

301 Yang, G. *et al.* Interface engineering in planar perovskite solar cells: energy level alignment, perovskite morphology control and high performance achievement. *Journal of Materials Chemistry A* **5**, 1658-1666 (2017). https://doi.org/10.1039/C6TA08783C

302 George, S. M. Atomic Layer Deposition: An Overview. *Chemical Reviews* **110**, 111-131 (2010). https://doi.org/10.1021/cr900056b

303 Jeon, N. J. *et al.* Solvent engineering for high-performance inorganic–organic hybrid perovskite solar cells. *Nature Materials* **13**, 897-903 (2014). https://doi.org/10.1038/nmat4014

304 Jeon, N. J. *et al.* A fluorene-terminated hole-transporting material for highly efficient and stable perovskite solar cells. *Nature Energy* **3**, 682-689 (2018). https://doi.org/10.1038/s41560-018-0200-6

305 Ghosh, G. The Sb-Se (antimony-selenium) system. *Journal of Phase Equilibria* **14**, 753-763 (1993). https://doi.org/10.1007/BF02667889
306 Thompson, C. V. Grain Growth in Thin Films. *Annual Review of Materials Research* **20**, 245-268 (1990). https://doi.org/10.1146/annurev.ms.20.080190.001333
307 Peccerillo, E. & Durose, K. Copper—antimony and copper—bismuth chalcogenides—Research opportunities and review for solar photovoltaics. *MRS Energy & Sustainability* **5** (2018). https://doi.org/10.1557/mre.2018.10
308 Xiao, Z. *et al.* Solvent Annealing of Perovskite-Induced Crystal Growth for Photovoltaic-Device Efficiency Enhancement. *Advanced Materials* **26**, 6503-6509 (2014). https://doi.org/10.1002/adma.201401685
309 Liu, J. *et al.* Improved Crystallization of Perovskite Films by Optimized Solvent Annealing for High Efficiency Solar Cell. *ACS Applied Materials & Interfaces* **7**, 24008-24015 (2015). https://doi.org/10.1021/acsami.5b06780
310 Deshmukh, S. D., Ellis, R. G., Sutandar, D. S., Rokke, D. J. & Agrawal, R. Versatile Colloidal Syntheses of Metal Chalcogenide Nanoparticles from Elemental Precursors Using Amine-Thiol Chemistry. *Chemistry of Materials* **31**, 9087-9097 (2019). https://doi.org/10.1021/acs.chemmater.9b03401
311 Shah, U. A., Chen, S., Khalaf, G. M. G., Jin, Z. & Song, H. Wide bandgap Sb_2S_3 solar cells. *Advanced Functional Materials* **31**, 2100265 (2021). https://doi.org/10.1002/adfm.202100265
312 Zhang, Y. *et al.* Phosphotungstic Acid Regulated Chemical Bath Deposition of Sb_2S_3 for High-Efficiency Planar Heterojunction Solar Cell. *Energy Technology* **6**, 2126-2131 (2018). https://doi.org/10.1002/ente.201800238
313 Ke, W. *et al.* Low-Temperature Solution-Processed Tin Oxide as an Alternative Electron Transporting Layer for Efficient Perovskite Solar Cells. *Journal of the American Chemical Society* **137**, 6730-6733 (2015). https://doi.org/10.1021/jacs.5b01994
314 Barbé, J. *et al.* Amorphous Tin Oxide as a Low-Temperature-Processed Electron-Transport Layer for Organic and Hybrid Perovskite Solar Cells. *ACS Applied Materials & Interfaces* **9**, 11828-11836 (2017). https://doi.org/10.1021/acsami.6b13675
315 Liu, R. *et al.* Space-Charging Interfacial Layer by Illumination for Efficient Sb_2S_3 Bulk-Heterojunction Solar Cells with High Open-Circuit Voltage. *ACS Applied Materials & Interfaces* **15**, 24583-24594 (2023). https://doi.org/10.1021/acsami.3c02843
316 Zakaznova-Herzog, V. P. *et al.* High resolution XPS study of the large-band-gap semiconductor stibnite (Sb_2S_3): Structural contributions and surface reconstruction. *Surface Science* **600**, 348-356 (2006). https://doi.org/10.1016/j.susc.2005.10.034
317 Reza, M. S. *et al.* Design and Optimization of High-Performance Novel $RbPbBr_3$-Based Solar Cells with Wide-Band-Gap S-Chalcogenide Electron Transport Layers (ETLs). *ACS Omega* **9**, 19824-19836 (2024). https://doi.org/10.1021/acsomega.3c08285
318 Rui, Y., Li, T., Li, B., Wang, Y. & Müller-Buschbaum, P. Two-dimensional SnS_2 nanosheets as electron transport and interfacial layers enable efficient perovskite solar

cells. *Journal of Materials Chemistry C* **10**, 12392-12401 (2022). https://doi.org/10.1039/D2TC02452G

319 Yang, J. *et al.* Bi_2S_3 Electron Transport Layer Incorporation for High-Performance Heterostructure HgTe Colloidal Quantum Dot Infrared Photodetectors. *ACS Photonics* **10**, 2226-2233 (2023). https://doi.org/10.1021/acsphotonics.2c01145

320 Abd Malek, N. A. *et al.* Ultra-thin MoS_2 nanosheet for electron transport layer of perovskite solar cells. *Optical Materials* **104**, 109933 (2020). https://doi.org/10.1016/j.optmat.2020.109933

321 Shin, D. H., Ko, J. S., Kang, S. K. & Choi, S.-H. Enhanced Flexibility and Stability in Perovskite Photodiode–Solar Cell Nanosystem Using MoS_2 Electron-Transport Layer. *ACS Applied Materials & Interfaces* **12**, 4586-4593 (2020). https://doi.org/10.1021/acsami.9b18501

322 Zhang, J. *et al.* All Antimony Chalcogenide Tandem Solar Cell. *Solar RRL* **4** (2020). https://doi.org/10.1002/solr.202000048